

Quantifying lahar hazard and vulnerability

By

Stuart Mead

A thesis submitted to Macquarie University
for the degree of Doctor of Philosophy
Department of Environmental Sciences
July 2017



Except where acknowledged in the customary manner, the material presented in this thesis is, to the best of my knowledge, original and has not been submitted in whole or part for a degree in any university.

Stuart Mead

Acknowledgements

This thesis was made possible with help from the following people and organisations.

For guidance, support, trust, teaching me about volcanoes and fixing my grammar: My supervisor, Dr. Christina Magill, who would fill the page if I was to list all the support she provided.

For additional support, supervision and help along the journey: My co-supervisors, Dr. Mahesh Prakash, CSIRO and Prof. John McAneney.

My co-authors; for valuable suggestions, reviews and code: Vincent Lemiale, James Hilton, Jean-Claude Thouret and Matt Bolger.

For providing a support base in Sydney and supply of wine, cheese and biscuits: The Risk Frontiers staff past and present. John, Carol, Tetsuya, Emma, Kevin, Andrew, Foster, Valentina, Rob, Felipe, James, Ryan, Thomas L., Thomas M., Mingzhu, Lucinda, Deirdre, Niyas, Keping, Paul, Kat, Deanne, Anto and Matt.

For providing a support base in Melbourne: The CSIRO/Data61 staff past and present. Gary, Kate, Simon, Claire, Lachlan, Chris, Sharen, Matt B., Matt S., Ray, Phil, Damien, James, Vincent and Sophia.

For administrative, personal and educational support: Department of Environmental Sciences staff and students. Particular thanks to the administration team.

For support with ideas, fieldwork, data, feedback or coffee breaks: Colleagues at home and around the world. Liliane Thouret for protection from dogs in Arequipa. The Smithsonian Institution Global Volcanism Program for early access to the Volcanoes of the World catalogue. Melanie Froude for teaching me all I needed to know about lahars. Environmental Science students Danielle, Marek, Emma, Tetsuya, Dean, Paul, Stacy, Louise and Chenyin for providing the often needed break.

For continuous support and encouragement: Family, friends and housemates too numerous to mention.

Financial support was provided by an Australian Postgraduate Award (APA) and top-up scholarship from the Commonwealth Scientific and Industrial Research Organisation (CSIRO). Drones, wine and cheese were funded by Risk Frontiers. This thesis was typeset in L^AT_EX using a modified version of Alexei Gilchrist's template.

Abstract

Lahars are a class of gravity driven mass flows containing a mixture of volcanic debris and water which can cause severe damage to exposed populations in their path. They are generated through a range of initiation mechanisms during both eruptive and quiescent phases of volcanic activity. Lahars also vary in composition from hyper-concentrated streamflows to large, water saturated debris avalanches. Flow behaviour, volume and erosional processes differ as a consequence of this variability, affecting robust estimates of lahar hazard and destructive effects. Qualitative and semi-quantitative hazard estimates often rely on geologic and historic records to prescribe lahar volume, type and frequency. This is an important limitation on hazard estimates, as historic data is often incomplete and can be irrelevant under different environmental conditions or when eruptions alter topography and hydrology of volcanic slopes. Lahar risk assessment, which relies on a quantification of lahar hazard and damage, is therefore difficult to estimate.

In this thesis, new approaches to quantify the hazard and vulnerability components of lahar risk are developed. For lahar hazard assessment, change points in volcanic eruption record completeness are systematically calculated, along with estimations of uncertainty in the date. The frequency and composition of rain-triggered lahars estimated through a lahar susceptibility model that accounts for the mechanics of lahar initiation. This susceptibility is combined with lahar flow models in a new methodology to determine lahar hazard. The primary cause of building losses is identified using detailed numerical modelling in urban areas. This quantification of vulnerability identified that exposure may have a larger effect on lahar risk than vulnerability. The approaches presented here, while limited at times by scarce input data, can be applied to better understand and quantify lahar risk.

List of publications and thesis structure

This thesis is presented as a thesis-by-publication, containing six publications with an introduction and conclusion to summarise the background, aims and purpose of this study.

These publications are works where I have been the lead author and provided the most significant contributions. Macquarie University policy requires that: (1) these papers form a coherent body of work, and (2) the contribution of myself and others to each publication is specified.

To meet point 1, each part of the thesis contains an overview providing additional explanation that forms the bridge between publications. The text, images and tables of the publications are reformatted for consistency in style and referencing, but the content of each publication has not changed.

To address point 2, and reduce distraction of the reader by administrative details, a description of each chapter, authors' contributions and affiliations are provided in the following list.

List of publications

Chapter 2: Stuart Mead and Christina Magill¹ *Determining changepoints in data completeness for the Holocene eruption record*. Bulletin of Volcanology **76**, 864 (2014)

¹Risk Frontiers, Faculty of Science and Engineering, Macquarie University, Sydney

This paper was jointly conceived by Stuart Mead and Christina Magill. Stuart Mead developed the statistical model, analysed results and wrote the manuscript. Christina Magill reviewed and modified parts of the manuscript and provided advice on interpretation of results.

Chapter3: Stuart Mead, Christina Magill¹ and James Hilton² *Rain-triggered lahar susceptibility using a shallow landslide and surface erosion model*. Geomorphology **273**, pp. 168-177 (2016)

¹Risk Frontiers, Faculty of Science and Engineering, Macquarie University, Sydney

²Commonwealth Scientific and Industrial Research Organisation (CSIRO), Clayton, Victoria
Stuart Mead was responsible for the concept, susceptibility model development, analysis and preparation of the manuscript. Christina Magill reviewed the manuscript and contributed to model development concepts. James Hilton was responsible for writing the shallow-water solver on which the overland erosion model is based.

Chapter 4: Stuart Mead and Christina Magill¹ *Probabilistic hazard modelling of rain-triggered lahars*. Journal of Applied Volcanology **6:8**, pp. 1-7 (2017)

¹Risk Frontiers, Faculty of Science and Engineering, Macquarie University, Sydney

Stuart Mead wrote the manuscript, modified the Titan2D code, ran simulations and analysed results. Christina Magill advised on the generation of probabilistic hazard maps, reviewed and edited the manuscript.

Chapter 5: Stuart Mead, Mahesh Prakash², Christina Magill¹, Matt Bolger² and Jean-Claude Thouret³ *A distributed computing workflow for modelling environmental flows in complex terrain*. Environmental Software Systems. Infrastructures, Services and Applications IFIP AICT **448**, pp. 321-332 (2015)

¹Risk Frontiers, Faculty of Science and Engineering, Macquarie University, Sydney

²Commonwealth Scientific and Industrial Research Organisation (CSIRO), Clayton, Victoria

³Laboratoire Magmas et Volcans, University Blaise Pascal

Stuart Mead wrote the manuscript and developed the concept in discussions with Christina Magill. Structure-from-Motion and point cloud processing software was developed primarily by Stuart Mead with the assistance of Matt Bolger. Mahesh Prakash reviewed and contributed to the numerical modelling sections. Christina Magill contributed to manuscript review and field data collection. Jean-Claude Thouret assisted with fieldwork and manuscript review.

Chapter 6: Stuart Mead, Christina Magill¹, Vincent Lemiale², Jean-Claude Thouret³ and Mahesh Prakash² *Quantifying lahar damage using numerical modelling*. Natural Hazards and Earth System Sciences **17**, pp. 703-719 (2017)

¹Risk Frontiers, Faculty of Science and Engineering, Macquarie University, Sydney

²Commonwealth Scientific and Industrial Research Organisation (CSIRO), Clayton, Victoria

³Laboratoire Magmas et Volcans, University Blaise Pascal

Stuart Mead created the depth-pressure curves, generated the terrain model, ran simulations, analysed results and wrote the manuscript. Vincent Lemiale implemented the quadratic rheology model in SPH. Christina Magill undertook building surveys, provided input into vulnerability and loss calculations, reviewed and edited the manuscript. Jean-Claude Thouret also helped with building surveys, provided georeferencing data based on additional fieldwork and contributed to manuscript review. Mahesh Prakash assisted with implementation of the rheology model, provided assistance with using SPH and reviewed the manuscript.

Appendix A: Stuart Mead and Paul W. Cleary¹ *Validation of DEM prediction for granular avalanches on irregular terrain*. Journal of Geophysical Research: Earth Surface **120**, pp. 1724-1742 (2015)

¹Commonwealth Scientific and Industrial Research Organisation (CSIRO), Clayton, Victoria

Stuart Mead set-up and ran DEM simulations, analysed experimental and simulated results and wrote most of the manuscript. Paul Cleary was responsible for DEM development, wrote the subsection on DEM method and reviewed the manuscript.

A note on open data and methods

In addition to this thesis and the six publications it contains, significant efforts in programming and data collection also make up the contribution to scientific knowledge. Licensing restrictions limit the release of some work, but source code for all chapters are publicly available wherever possible. This data is available from the Zenodo repository [doi:10.5281/zenodo.155144](https://doi.org/10.5281/zenodo.155144) and can be shared freely with the wider community.

Contents

Acknowledgements	iii
Abstract	v
List of publications and thesis structure	vii
List of publications	viii
A note on open data and methods	ix
Contents	xi
List of Figures	xv
List of Tables	xix
1 Introduction	1
1.1 Consequences of lahars	2
1.2 Quantifying lahar risk	3
1.3 A lahar risk assessment methodology	9
1.4 Thesis aim and objectives	10
1.5 Thesis overview and structure	12
1.5.1 Part I: Lahar hazard	12
1.5.2 Part II: Physical vulnerability	14
I Lahar hazard	17
I.1 Overview of objectives and contribution to thesis aim	19
I.2 Summary and relevance to lahar risk	19
I.2.1 Numerical modelling of lahars	21
2 Determining change points in data completeness for the Holocene eruption record	25
2.1 Introduction	26
2.2 Volcanoes of the World Catalogue	30
2.3 Statistical Model	32
2.4 Metropolis-Hastings approach	35
2.5 Comparisons of data completeness	36
2.5.1 Completeness for all eruptions	39
2.5.2 Completeness for large eruptions	42
2.6 Discussion	43

2.7	Conclusion	46
3	Rain-triggered lahar susceptibility using a shallow landslide and surface erosion model	47
3.1	Introduction	49
3.2	Generation of rain-triggered lahars	52
3.2.1	Overland flow erosion model	53
3.2.2	Shallow landsliding model	55
3.2.3	Calculating lahar susceptibility	57
3.3	Controls on rain-triggered lahar initiation volume	58
3.3.1	Case study: The October 28, 1995 lahar, Mangatoetoe Stream, Ruapehu Volcano, New Zealand	58
3.3.2	Estimation of simulation parameters and initial conditions	59
3.3.3	Effect of hydraulic diffusivity on shallow landsliding mobilised volume	62
3.3.4	Effect of infiltration rate on overland erosion	62
3.3.5	Estimates of total mobilised volume	63
3.3.6	Susceptibility of the Mangatoetoe Stream to rain-triggered lahars	64
3.4	Applicability to probabilistic lahar hazard assessment	65
3.5	Conclusion	67
3.6	Appendix: Shallow-water hydrodynamics model	68
4	Probabilistic hazard modelling of rain-triggered lahars	69
4.1	Background	70
4.2	Methods	71
4.2.1	Rain-triggered lahar susceptibility	71
4.2.2	Lahar flow modelling	71
4.3	Study area and simulation inputs	73
4.4	Generation of probabilistic lahar hazard maps	74
4.5	Discussion and limitations	75
4.6	Conclusion	77
II	Physical vulnerability	79
II.1	Overview of objectives and contribution to thesis aim	81
II.2	Summary and relevance to lahar risk	81
II.2.1	Smoothed particle hydrodynamics for lahar modelling	82
5	Modelling environmental flows in complex terrain	85
5.1	Introduction	86
5.2	Methods	88
5.2.1	Workflow outline and software integration	88
5.2.2	Structure-from-Motion (SfM)	89
5.2.3	Point cloud processing and surface generation	90
5.2.4	Numerical modelling	90
5.3	Case study: Arequipa, Peru	91
5.3.1	Image collection	91
5.3.2	Feature matching, SfM and MVS	91
5.3.3	Mesh generation	93

5.3.4	SPH simulation	93
5.4	Conclusion	94
6	Quantifying lahar damage using numerical modelling	97
6.1	Introduction	98
6.2	Case study: Quebrada Dahlia, Arequipa, Peru	99
6.3	Developing building vulnerability relationships	102
6.3.1	Critical depth-pressure curves	104
6.4	Lahar numerical modelling and results	106
6.4.1	Lahar rheology and implementation in smoothed particle hydrodynamics	106
6.4.2	Lahar simulations	107
6.4.3	Flow behaviour	109
6.5	Application of critical depth-pressure curves	113
6.6	Limitations and discussion	116
6.6.1	Depth-pressure curves	117
6.6.2	Flow scenarios	117
6.6.3	Pressure actions	118
6.6.4	Discussion	118
6.7	Conclusion	119
6.8	Appendix: Calculating ultimate bending moment and shear force	119
7	Summary, limitations and applicability to lahar risk assessment	123
7.1	Summary of publications	123
7.1.1	Part I: Lahar hazard	123
7.1.2	Part II: Physical vulnerability	125
7.2	Limitations	125
7.3	Improvements to lahar risk assessment and conclusion	127
	References	131
	Appendices	157
A	Validation of DEM prediction for granular avalanches on irregular terrain	157
A.1	Introduction	158
A.2	Experimental setup and materials	163
A.3	Dilation of granular material during avalanche	166
A.4	DEM method, particle properties and simulation	167
A.5	Comparison of experimental and DEM avalanches	171
A.6	Sensitivity of avalanche deposit to particle attributes	178
A.7	Conclusions	181
A.8	Acknowledgements	184
B	Supplementary images for Chapter 6	185

List of Figures

1.1	Inundation of Armero, Columbia from lahars generated in the 13 November 1985 eruption of Nevado del Ruiz. Image courtesy of United States Geological Survey.	2
1.2	Natural disaster risk assessment process for a single hazard, from Magill et al. (2006) and Marzocchi et al. (2012).	4
1.3	Example event tree structure for a single volcanic source, from Newhall and Hoblitt (2002) and Marzocchi and Bebbington (2012). Grey trees are identical clones of each subsequent branch.	5
1.4	Solid earth bridge across Quebrada San Lazaro, Arequipa, Peru. Photo taken in September 2013 by Christina Magill.	7
1.5	Schematic representation of lahar risk assessment methodology, from van Westen et al. (2006). Colours highlight components affected by unknown frequency-magnitude relationships, changing terrain and unpredictable lahar behaviour.	9
I.1	Cumulative number of eruptions (black) and lahars (grey) recorded in the Volcanoes of the World 4.0 database (Siebert et al., 2010).	20
I.2	Proportion of eruptions with documented lahars (red) to eruptions without documented lahars (grey) for each VEI category in the complete portion of the Volcanoes of the World 4.0 database.	21
2.1	Cumulative number of eruptions recorded in the Volcanoes of the World 4.0 database (Siebert et al., 2010).	27
2.2	Histogram of recorded Volcanic Explosivity Index (VEI) in the Volcanoes of the World database (Siebert et al., 2010).	31
2.3	(a) Example of the presence function at VEIs of 2, 4 and 6, (b) shape of the presence function at different α and β values, and (c) histogram of a theoretical dataset.	34
2.4	Posterior distributions of the change point year k from the MCMC simulation, and cumulative number of $\text{VEI} \geq 4$ eruptions for (a) the United States of America, and (b) Indonesia.	37
2.5	Cumulative number of eruptions (filled points) and eruption magnitudes (hollow points) recorded for the regions of (a) Canada and Western USA, (b) Iceland and Arctic Ocean, and (c) South America.	40
2.6	Cumulative number of eruptions (filled points) and eruption magnitudes (hollow points) recorded for (a) Indonesia, (b) Japan, and (c) the United States of America.	41

2.7	Cumulative number of $\text{VEI} \geq 4$ eruptions (filled points) and eruption magnitudes (hollow points) recorded for the regions of (a) Alaska, (b) Japan, Taiwan, Marianas and (c) New Zealand to Fiji.	44
3.1	Digital elevation model and streamlines of Ruapehu volcano with upper and lower estimates of deposit depths.	60
3.2	Mobilised deposit volumes for varying rainfall durations at the Mangatoetoenui stream with annual recurrence intervals of 2, 10, 50 and 100 years.	65
4.1	Study area overview showing Ruapehu volcano, Mangatoetoenui Glacier and the Tongariro River and Mangatoetoenui Stream confluence.	73
4.2	Annual exceedance probabilities (AEP) for lahars exceeding (top) 0.5 and (bottom) 0.1 m in height.	76
5.1	Terrain generation and modelling workflow outline.	88
5.2	(a) Case study area in Quebrada San Lazaro and, (b) dense point cloud reconstruction from the SfM-MVS.	92
5.3	Watertight surface reconstruction of the case study area using SSD (looking downstream towards bridge).	94
5.4	SPH simulations of a flash flood in Quebrada San Lazaro with varying flow rates.	95
6.1	Location of Arequipa in relation to El Misti volcano, showing the main quebradas and the location of the Quebrada Dahlia study area.	100
6.2	Overview of Quebrada Dahlia study area, Arequipa.	101
6.3	Range of design compressive stress for building types 1A - 6C.	105
6.4	Critical depth and dynamic pressures for failure of structural classes A0, A and B for brick widths of 0.15 m and 0.25 m.	105
6.5	Evolution of dynamic pressure and velocity magnitudes for a $75 \text{ m}^3\text{s}^{-1}$ flow along Quebrada Dahlia for a Newtonian flow (NF), hyper-concentrated flow (HCF) and debris flow (DF).	110
6.6	Directional components of dynamic pressure for a $75 \text{ m}^3\text{s}^{-1}$ flow along Quebrada Dahlia for a Newtonian flow (NF), hyper-concentrated flow (HCF) and debris flow (DF).	111
6.7	Comparison of mean pressure magnitude (grey lines) and mean normal pressure (black lines) on block 'West 2' in the parallel and perpendicular orientations for a $75 \text{ m}^3\text{s}^{-1}$ flow along Quebrada Dahlia.	112
6.8	Mean normal pressures applied to each city block in the perpendicular and parallel orientations for a $75 \text{ m}^3\text{s}^{-1}$ flow.	113
6.9	Critical depth-pressure curves for building classes A0, A and B subjected to Newtonian flow. Peak normal pressures and corresponding depths applied to each city block are plotted as points for each flow rate.	114
6.10	Critical depth-pressure curves for building classes A0, A and B subjected to a hyper-concentrated flow. Peak normal pressures and corresponding depths applied to each city block are plotted as points for each flow rate.	115
6.11	Critical depth-pressure curves for building classes A0, A and B subjected to a debris flow. Peak normal pressures and corresponding depths applied to each city block are plotted as points for each flow rate.	115

6.12	Building loss fraction for all flow scenarios where buildings are assumed to have a brick width of 0.15 m.	116
6.13	Building loss fraction for all flow scenarios where buildings are assumed to have a brick width of 0.25 m.	116
7.1	Schematic representation of lahar risk assessment methodology, from van Westen et al. (2006), highlighting areas improved by chapters in this thesis.	128
A.1	Flume configuration used in the DEM simulations, based on digitized contours of Iverson et al. (2004). Particles are initially located behind the reservoir at the top of the flume. Reproduced from Mead and Cleary (2011).	164
A.2	Variation with time of the total sand volume (solid line), volume of sand on the flume surface (dotted line) and volume of sand retained in the reservoir (dashed line) for both experiment A (black) and experiment B (grey) of Iverson et al. (2004).	167
A.3	(left) Final deposit of the Iverson et al. (2004) experiment and (right) spherical particle simulations at 13 seconds.	172
A.4	(left) Vertical orthophotographs depicting the avalanche experiment of Iverson et al. (2004), and (right) DEM simulation for case 1. Timestamps show the time elapsed since the opening of the head gate. Particles in the simulation are coloured by speed. Red laser contours are projected at 5 mm intervals in the experiment.	173
A.5	Outline of sand from the avalanche experiment isopachs (black, dashed line), extracted from the experimental images (solid blue line) and DEM simulation for case 1 (red, solid). Timestamps show the time elapsed since the opening of the head gate.	175
A.6	Cross-section along the centreline of the final avalanche deposit for the experiment (dashed blue line) and DEM case 1 (solid red line). The base of the flume is the thick black line.	177
A.7	Variation of the centre of mass position (X_{com}) of the DEM particles in the final deposit in the downhill direction along the flume for three aspect ratio combinations with a friction coefficient of 0.45. Each curve shows a different amount of angularity with rounded particles given by the solid line, mildly angular particles by the dashed line and highly angular particles by the dotted line.	179
A.8	Final avalanche deposit thickness for DEM simulations with mildly angular particles for (a) elongated, (b) intermediate, and (c) low aspect ratios.	180
A.9	Final avalanche deposit thickness for DEM simulations with an intermediate aspect ratio range for: (a) rounded, (b) mildly angular, and (c) highly angular particles.	181
A.10	Final avalanche deposit thickness for DEM simulations for elongated, mildly angular particles with friction coefficients of: (a) 0.45, (b) 0.50, and (c) 0.55.	182
A.11	Centre of mass of DEM particles in the down slope direction for friction coefficients between 0.45 and 0.55, for (a) elongated, (b) intermediate and (c) low aspect ratios at rounded (solid line), mildly angular (dashed line) and highly angular (dotted line) angularities.	183

B.1	Critical depth-pressure curves for building classes A0, A and B with brick widths of 0.25 m subjected to Newtonian flow. Peak normal pressures and corresponding depths applied to each city block are plotted as points for each flow rate.	185
B.2	Critical depth-pressure curves for building classes A0, A and B with brick widths of 0.25 m subjected to a hyper-concentrated flow. Peak normal pressures and corresponding depths applied to each city block are plotted as points for each flow rate.	186
B.3	Critical depth-pressure curves for building classes A0, A and B with brick widths of 0.25 m subjected to a debris flow. Peak normal pressures and corresponding depths applied to each city block are plotted as points for each flow rate.	186

List of Tables

2.1	Data completeness change point dates, number of eruptions after the change point and average recurrence interval for all eruptions using the Markov Chain Monte Carlo method. The change point dates are calculated from the 5 th , 50 th and 95 th percentiles of the change point posterior distribution.	39
2.2	Data completeness change point dates, number of eruptions after the change point and average recurrence interval for large magnitude eruptions (Volcanic Explosivity Index ≥ 4) using the Markov Chain Monte Carlo method. The change point dates are calculated from the 5 th , 50 th and 95 th percentiles of the change point posterior distribution.	42
3.1	Range of hydraulic diffusivities used in lahar susceptibility simulations based on the characteristic timescale H^2/D_0	61
3.2	Failed shallow landslide material volume estimates (in m ³) for 18 and 6 hour rainfall scenarios with varying diffusivities and infiltration rate I_z of 1.0 mm/hr.	62
3.3	Overland erosion material volume estimates (in m ³) for 18 and 6 hour rainfall scenarios at varying infiltration rates.	63
3.4	Combined overland erosion and shallow landslide material volume estimates (in m ³) for 18 and 6 hour rainfall scenarios with an infiltration rate of 1 mm/hr.	64
4.1	Solid volume fractions of mobilised material for each scenario at Mangatoe-toenui Stream.	74
6.1	Individual building type and vulnerability classes for each block in the Quebrada Dahlia study area. Block ID increases from north to south.	102
6.2	Building types and simplified structural classes from Thouret et al. (2014).	103
6.3	Density, particle concentration and rheology coefficients for hyper-concentrated streamflow and debris flow simulations, taken from Govier et al. (1957) and Julien and Lan (1991).	108
A.1	Particle angularity, aspect ratio and internal friction used for DEM simulations of the avalanche.	170

Chapter 1

Introduction

The Javanese term ‘lahar’ refers to gravity driven mass flows containing a mixture of volcanoclastic debris and water, often originating from a volcanic source (Blong, 1984; Lavigne et al., 2000; Vallance, 2000). This definition is broad and represents the range of variability in lahar sediment-water ratios, initiation mechanisms, volume and consequences. The presence of volcanic activity is used to group flows into primary lahars, where initiation is caused by the volcanic activity itself (Blong, 1984; Vallance, 2000), and secondary lahars, where initiation is a result of other environmental conditions such as rainfall.

Regardless of associated volcanic activity, four components required for lahar flows and their genesis are:

- water,
- easily entrained volcanic debris,
- a terrain gradient (slope), and
- a triggering mechanism (Vallance, 2000).

Following the law of conservation of energy, the lahar triggering mechanism, initial location and availability of water and debris combine to determine the gravitational potential energy. The slope and debris-water ratio then controls the dissipation and exchange of this energy into kinetic energy. Flow behaviour will be similar to that of water (i.e. Newtonian) at low debris concentrations and the event can be regarded as a water flood. The effect of water as a pore fluid is diminished at high debris concentrations, and the flow will be more representative of a dry landslide or avalanche. Here, lahars are regarded as flows that encompass the behaviour between these two extremes, but which may also transform from or into water flood flows or almost dry avalanches.

This definition encompasses the spatial and temporal variability in lahar components that cause individual lahar phases to undergo flow transformations through dilution and sediment entrainment (bulking) or deposition (e.g. Pierson and Scott, 1985; Fagents and Baloga, 2006; Manville et al., 2013). These transformations in flow behaviour (e.g. from debris flow to hyper-concentrated flows) enable lahars to travel large distances and affect communities tens to hundreds of kilometres away from their source. The complexity of lahar behaviour, flow transformations and interaction between sediment, water and terrain makes the damaging consequences of lahars on communities and infrastructure difficult to predict.

1.1 Consequences of lahars

Lahar damage is not caused by a subset of specific lahar compositions or sources, but rather through the intersection of lahar flows with exposed and vulnerable populations. The consequences of lahars are often severe, having been responsible for 17% of volcanic fatalities since 1600AD (Auken et al., 2013). Lahars from the 13 November 1985 eruption of Nevado del Ruiz in Columbia, alone, resulted in 8% of global volcanic fatalities since 1600AD. A series of pyroclastic surges melted the glacier on Nevado del Ruiz, forming four lahars that flowed down flanks of the volcano, entraining debris and causing catastrophic damage in the form of 23,000 lives lost and 5,000 homes destroyed (Lowe et al., 1986; Pierson et al., 1990; Voight, 1990). Primary lahars on snow and ice-capped volcanoes, such as the 1985 Nevado del Ruiz lahar, are commonly caused by pyroclastic surges, hot blasts, avalanches, lava flows or ejection of crater lake fluids onto snow or sediment (Newhall and Self, 1982). These lahars can have volumes in excess of $100,000 \text{ m}^3$ and consequences more severe than the eruption magnitude may suggest (Newhall and Self, 1982).



FIGURE 1.1: Inundation of Armero, Columbia from lahars generated in the 13 November 1985 eruption of Nevado del Ruiz. Image courtesy of United States Geological Survey.

Secondary lahars are also destructive, persisting for several years after volcanic activity has ceased (Pierson and Major, 2014; Newhall and Solidum, 2015). Unconsolidated volcanoclastic material deposited on the slopes of volcanoes provides an easily mobilised source of volcanic debris necessary for the genesis of lahars (Pierson and Major, 2014). In tropical climates this sediment is commonly mobilised through rainfall (e.g. Lavigne et al., 2000; Lavigne and Thouret, 2003; Miyabuchi and Daimaru, 2004; van Westen and Daag, 2005;

Barclay et al., 2007; Capra et al., 2010; Dumaisnil et al., 2010; Miyabuchi et al., 2015). Non-tropical regions are also susceptible to secondary lahars provided an adequate water source, such as snow-melt, is present (e.g. Major et al., 2000; Fiorillo and Wilson, 2004; Lecointre et al., 2004; Pierson et al., 2013; Thouret et al., 2013).

Rain-triggered secondary lahars following the 2010 eruption of Merapi volcano, Indonesia, demonstrate the impacts and damaging effects of lahars. The 2010 eruption ejected up to 60 million m³ of pyroclastic material, mantling every catchment on Merapi volcano with a layer of pyroclastic deposits and altering the nature of lahar risk downstream (de B  lizar et al., 2013). Secondary lahars were initially triggered on the western slopes of the volcano where most rainfall fell and prevailing winds deposited more tephra. Several lahar events caused building destruction and 860 houses were damaged by lahars during the 2010-2011 rainy season (de B  lizar et al., 2013). Channels on the slopes and volcanoclastic fan of Merapi were transformed from narrow streams into wide lahar corridors, exposing areas unaffected by lahars for decades (de B  lizar et al., 2013) and placing the city of Yogyakarta at risk, as previously suggested by Lavigne (1999).

1.2 Quantifying lahar risk

A common and simple probabilistic definition of risk, originating in part from Varnes (1984), is that risk is the expected loss within an area caused by the damaging phenomena of interest over a given reference period. In the physical sense, such as when estimating expected building loss, risk is then related to the probability of the hazard occurring, number of exposed elements and the vulnerability of these exposed elements (van Westen et al., 2006). These components of risk are referred to from here on as hazard, exposure and vulnerability. Risk has previously been expressed in a formulaic manner, such as in Varnes (1984) and van Westen et al. (2006), as the product of the hazard and its consequences (defined as *exposure* \times *vulnerability*). However, experience in this thesis has suggested that the components of risk cannot be simplified in such a discrete manner to warrant the definition of a ‘risk formula’. Rather, we adopt a similar approach to Biass et al. (2013) that expresses risk as a general function of the three components:

$$R = f(H, A, V), \quad (1.1)$$

where R is risk, H is the probability of hazard occurrence, A is the number of elements exposed to the hazard and V is the vulnerability of these elements to the hazard.

The need for disaster risk assessment and a greater understanding of all components of risk is emphasised in the Sendai framework for disaster risk reduction which highlights the benefits of risk knowledge, such as in the form of risk maps, for the prevention, mitigation and effective responses to risk (UNISDR, 2015). The increasing economic damage caused

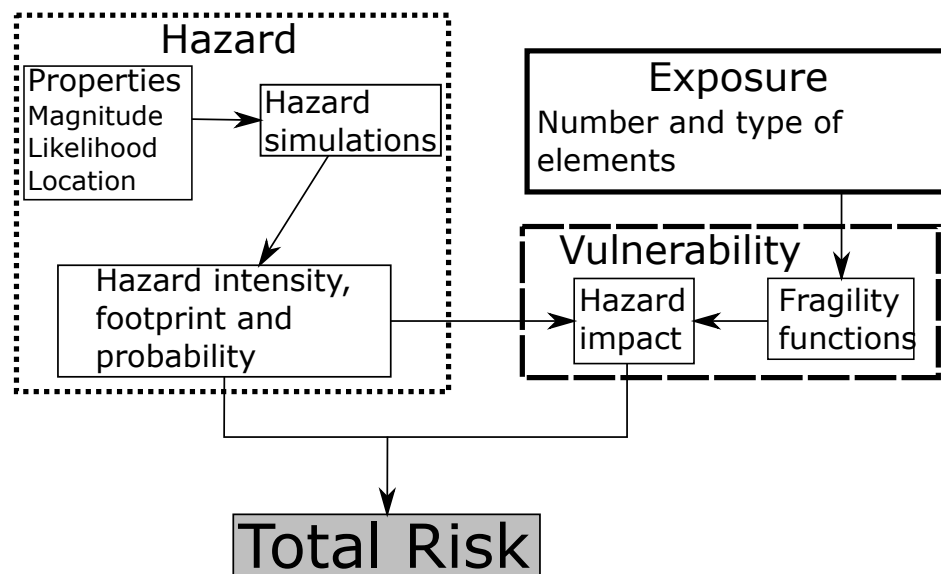


FIGURE 1.2: Natural disaster risk assessment process for a single hazard, from Magill et al. (2006) and Marzocchi et al. (2012).

by volcanic events (Jenkins et al., 2014b) further demonstrates the need for systematically evaluated, quantitative risk assessments which can provide actionable metrics necessary for long term risk planning (Thompson et al., 2017).

There are fewer examples of volcanic risk assessment relative to other natural disaster disciplines such as flooding or cyclones, where hazards occur with a higher frequency (Leonard et al., 2014; Biass et al., 2016). A generic, single hazard process for assessing the risk of natural disasters is shown in Fig. 1.2. Similar approaches are typically applied in volcanic risk assessment for individual volcanoes on a hazard-by-hazard basis due to complexities and interactions in volcanic processes and their hazardous phenomena (Magill and Blong, 2005a), varying hazard footprints and mode of impact. Multi-phenomena volcanic risk assessments are rare, but when applied (e.g. Marzocchi et al., 2004; Neri et al., 2008; Alberico et al., 2011) still assess the risk of each volcanic phenomena separately before combining individual assessments through the use of conditional probabilities.

Quantitatively, the overall risk from individual or multiple volcanic phenomena are calculated through the use of logic tree structures, shown in Fig. 1.3, which link volcanic unrest to sequentially more specific hazard or risk outcomes (Newhall and Hoblitt, 2002). The link to an event tree structure is sometimes explicitly mentioned, such as in Jenkins et al. (2012a) or the *BET_VH*-style approaches of Marzocchi et al. (2004), Neri et al. (2008), and Alberico et al. (2011); but is also implicitly followed by several authors (e.g. Magill and Blong, 2005a; Magill and Blong, 2005c; Magill et al., 2006; Biass and Bonadonna, 2013; Biass et al., 2013; Biass et al., 2014; Scaini et al., 2014; Biass et al., 2016) as a set of logical steps to calculate volcanic risk.

Non-Bayesian probabilistic risk assessment usually begins with an estimate of the frequency-magnitude relationship for the volcanic eruption and generation of the specific hazardous

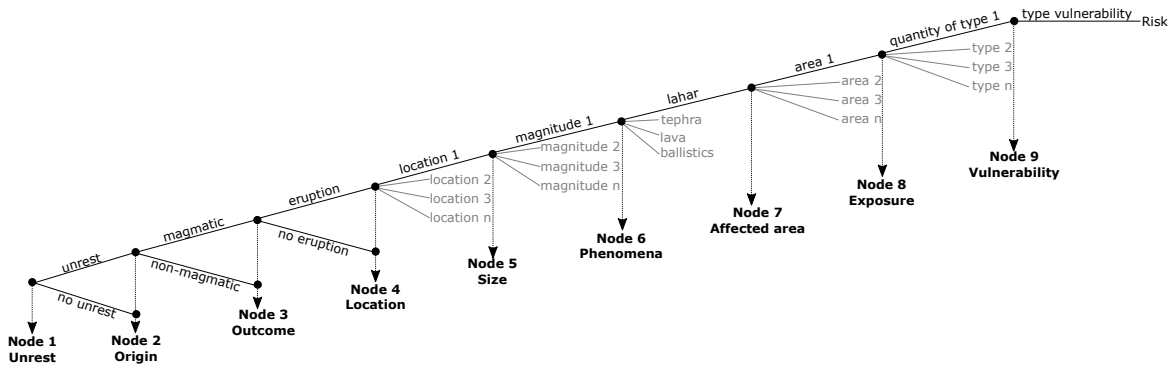


FIGURE 1.3: Example event tree structure for a single volcanic source, from Newhall and Hoblitt (2002) and Marzocchi and Bebbington (2012). Grey trees are identical clones of each subsequent branch.

process (e.g. ashfall Bonadonna, 2006; Magill et al., 2006; Biass et al., 2014). The affected area (*footprint*) and *intensity* of the hazard can then be determined. Modern, quantitative estimates of hazard footprints and intensities rely on models of the physical processes (Magill and Blong, 2005a) run a large number of times, for example through Monte-Carlo simulation, to account for the inherent natural randomness of the system, referred to as the aleatoric uncertainty (Woo, 1999; Biass et al., 2014). Exposure to the hazard is quantified through summing the elements of interest (e.g. buildings) within the hazard footprint. This is achieved with few conceptual problems through the use of readily available census, remotely sensed or geographic information system (GIS) data (van Westen et al., 2006). Finally, damage to exposed elements (*loss*) is quantified through relationships that express the probability of failure as a function of the hazard intensity and characteristics of the exposed element. In a purely physical sense these functions, called vulnerability functions, relate the energy exerted on the element by the volcanic hazard to the structural strength of the element or its affected components (see e.g. Jenkins et al., 2014a).

The relatively straightforward approach to risk assessment described in the previous paragraph is effective and frequently used for volcanic hazards such as ballistics or ashfall. This is because the processes are primarily controlled by well studied and understood physical laws, exposure and vulnerability can be determined with a reasonable degree of certainty, and hazard intensity metric(s) can be identified, physically measured, validated and extracted from hazard models. However, lahar properties (e.g. source area, volume, terrain), processes (e.g. flow, entrainment and deposition), and the effect of these properties and processes on populations, buildings and infrastructure, are difficult to determine as a result of changes in environmental factors brought about by volcanic activity. This directly affects accurate estimation of the components of lahar risk. For example, the 2010 eruption of Merapi volcano altered the spatial and temporal probability of lahar initiation through the deposition of more tephra on the western flank of the volcano. This in turn affected the size, frequency and presumably composition (i.e. sediment concentration and characteristics) of lahars, changing

terrain and altering the exposure (de Bélizal et al., 2013). Lahar induced damage also varied depending on lahar sediment concentration and vulnerability of specific building types (Jenkins et al., 2015). Specifically, the accurate estimation and quantification of lahar risk components is hampered by:

(i) An unknown frequency-magnitude relationship:

The deterministic prediction of volcanic eruption magnitudes, styles and hazardous phenomena are affected by large epistemic uncertainties and complexities in physical volcanic processes (Marzocchi and Bebbington, 2012). Instead, probabilistic approaches that estimate long term recurrence rates and magnitudes are usually used to assess the likelihood of various hazard scenarios (Marzocchi and Bebbington, 2012). The relationship between hazard frequency and magnitude relies on either statistical (e.g. Bebbington, 2009) or semi-empirical (i.e. based on geologic, historic and expert information, e.g. Scott et al. (1997)) approaches. However, the use of both approaches is limited by incompleteness of the historic and geologic records in addition to stationary process assumptions (i.e. that the eruption rate is constant with time).

Catalogues of past eruptions such as LaMEVE (Crosweller et al., 2012) or Smithsonian Institutions Volcanoes of the World (Global Volcanism Program, 2013) are affected by under recording which varies by eruption magnitude and geographical region (Lamb, 1970; Newhall and Self, 1982; Siebert et al., 2010). Furthermore, small volume lahars and eruptions are not likely to be preserved in geologic records due to erosion and remobilisation by landscape processes (Hodgson and Manville, 1999). This incompleteness affects all volcanic hazard analyses and needs to be accounted for before any assessment of hazard frequency.

The assumption of stationarity is common in eruption frequency-magnitude relationships, particularly those described by stochastic models (e.g. Klein, 1982; Mulargia et al., 1987; Connor et al., 2001; Wang and Bebbington, 2012). The assumption of stationarity requires hazard to be a stationary process where the probability of events does not change with time; this has been considered valid for estimating the frequency of eruptions over long time periods (e.g. Klein, 1982; Newhall and Self, 1982; Mulargia et al., 1987; Guttorp and Thompson, 1991; Coles and Sparks, 2006; Marzocchi and Zaccarelli, 2006; Deligne et al., 2010; Furlan, 2010; Jenkins et al., 2012b; Wang and Bebbington, 2012). However, as demonstrated by the 2010 Merapi eruption, the spatial and temporal frequency of lahars is linked to both volcanic eruption and non-static environmental processes that limit the use of stationary process assumptions.

(ii) Changing terrain and dynamic volcanic environments:

Volcanic landscapes are highly dynamic environments as a result of disturbances caused by explosive eruptions (Pierson and Major, 2014). Sediment deposited in catchments by volcanic processes alter terrain shape and drainage characteristics. As a



FIGURE 1.4: Solid earth bridge across Quebrada San Lazaro, Arequipa, Peru. Photo taken in September 2013 by Christina Magill.

self-regulating system, catchments respond to these disruptions through erosion and aggradation processes in an attempt to return the system to equilibrium (Pierson and Major, 2014). Three controlling components of lahar flows (water, volcanic debris and slope) are therefore not only spatially, but temporally varying. In addition to affecting static process assumptions explained previously, the changing lahar components limit the reliability of inputs (e.g. terrain models) needed for deterministic flow models often used in risk assessment.

These dynamic volcanic environments are further complicated by human interaction. Fig. 1.4 displays one example of human interaction that modifies both environment and exposure. A solid earth crossing is built across Quebrada San Lazaro, Arequipa, Peru. This crossing will significantly affect the path of any flows down the quebrada, increasing inundation upstream and potentially destroying the crossing. This interaction has not only affected the lahar hazard, but also added another element of exposure to the risk. Since risk assessments necessarily occur in populated areas, this additional dynamic component is unavoidable.

(iii) Lahar behaviour, and the effect of the behaviour is hard to predict:

The lithology, size and concentration of sediment in a lahar varies with the triggering mechanism, eruption sequence, available sediment, erosional processes and prevailing meteorological conditions. This variability and the lack of universal constitutive laws for lahar-like mass flows (Fagents and Baloga, 2006; McDougall, 2016) makes the prediction of lahar motion and runout difficult.

The entrainment and deposition of sediment typically results in multiple phases and transformations of flow ranging from flood-like surges to dense debris flow pulses (e.g. Pierson and Scott, 1985; Vallance and Scott, 1997; Scott et al., 2005; Fagents and Baloga, 2006; Manville et al., 2013). Lahar triggering also affects the initial composition and erosional behaviour of flows. Initially dilute, clay poor flows triggered through melting of snow, rainfall or crater lake outbursts readily entrain debris (Manville et al., 2000) and typically undergo flow transformations (Manville et al., 2013). Large

scale flank collapses of saturated volcanic material (e.g. Osceola mudflow Vallance and Scott (1997); Casita volcano flank collapse Scott et al. (2005)) often incorporate older or hydrothermally altered material with a higher cohesion that result in a wider area of inundation (i.e. hazard footprint) compared to similarly sized non-cohesive lahars (Vallance and Scott, 1997).

The epistemic uncertainty introduced in quantitative hazard assessments by this varied and unpredictable behaviour limits the applicability and practicality of lahar hazard assessment. This limitation is further compounded when considering the impact of lahars on buildings and infrastructure. Variations in lahar density change the magnitude of hydrostatic and dynamic forces applied to structure (Jenkins et al., 2015), while different flow behaviours affect the velocity of lahars around structures, influencing dynamic forces and other sources of damage such as scour.

The limitations summarised above form practical obstacles to probabilistic lahar risk assessment. Incompleteness in historical and geologic records mean that the true rate of eruptions is unknown. Probabilistic hazard assessments therefore require a judgement on record completeness that may not be fully objective or reproducible (see Chapter 2). The uncertainty in eruption rate propagates to affect frequency-magnitude estimates of lahar occurrence which are further affected by non-stationary processes, changing terrain and dynamic volcanic environments.

Lahars, particularly large lahars, are usually associated with large scale landscape change (Pierson and Major, 2014) which fundamentally alters the balance of energy and lahar risk. For example, the Osceola mudflow formed from the collapse of a 600 m high, 2.0 to 2.5 km³ volume at the peak of Mt. Rainier, Washington USA (Vallance and Scott, 1997). Although the collapse can guide the plausible range of lahar volumes, this previous energy state (i.e. one with higher gravitational potential energy) no longer exists. This means that the frequency-magnitude and initiation location of lahars changed as a result of the event, violating stationary process assumptions. Statistical methods, such as poisson point processes which assume events are independent and identically distributed (iid., see Chapter 2), therefore cannot be used in lahar hazard assessments. This results in approximations of lahar frequency-magnitude relationships that are not fully quantitative (see e.g. van Westen et al., 2006, Chapter 3) as they neglect mechanical processes of lahar initiation.

The dangerous and destructive nature of lahars mean that limiting assumptions and simplifications of lahar processes are made in current lahar hazard and risk assessments to overcome the previously highlighted issues. A survey of 120 hazard maps by Calder et al. (2015) identified lahars as being the most frequently mapped hazard. The effect of uncertainties and limitations on hazard assessment was also highlighted by the fact that 83% of all maps qualitatively expressed the probability of impact (e.g. high-medium-low). For lahar hazard, these qualitative assessments sometimes make use of computational lahar models (e.g. Scott et al., 1997; Scott et al., 2001; Aguilera et al., 2004; Robinson and Clynne,

2012; Amigo, 2013; Darnell et al., 2013; Thouret et al., 2013; Pistolesi et al., 2014), which are themselves a source of epistemic uncertainty.

The need for quantitative risk assessments by stakeholders (e.g. UNISDR, 2015) requires (but is not limited to) simultaneous scientific advancements in numerical modelling, statistical methods and probabilistic analysis techniques (Calder et al., 2015). In order to address this need here, I first identify some necessary advancements by considering the effect of previously discussed limitations on a lahar risk assessment process.

1.3 A lahar risk assessment methodology

Lahars bear many similarities to non-volcanic mass flows and landslides. Given the practical obstacles faced when using volcanic risk assessment methodologies, lahar risk may be better approached using a methodology similar to that shown in van Westen et al. (2006) for landslide risk. A schematic representation of this methodology, modified to suit lahars, is shown in Figure 1.5.

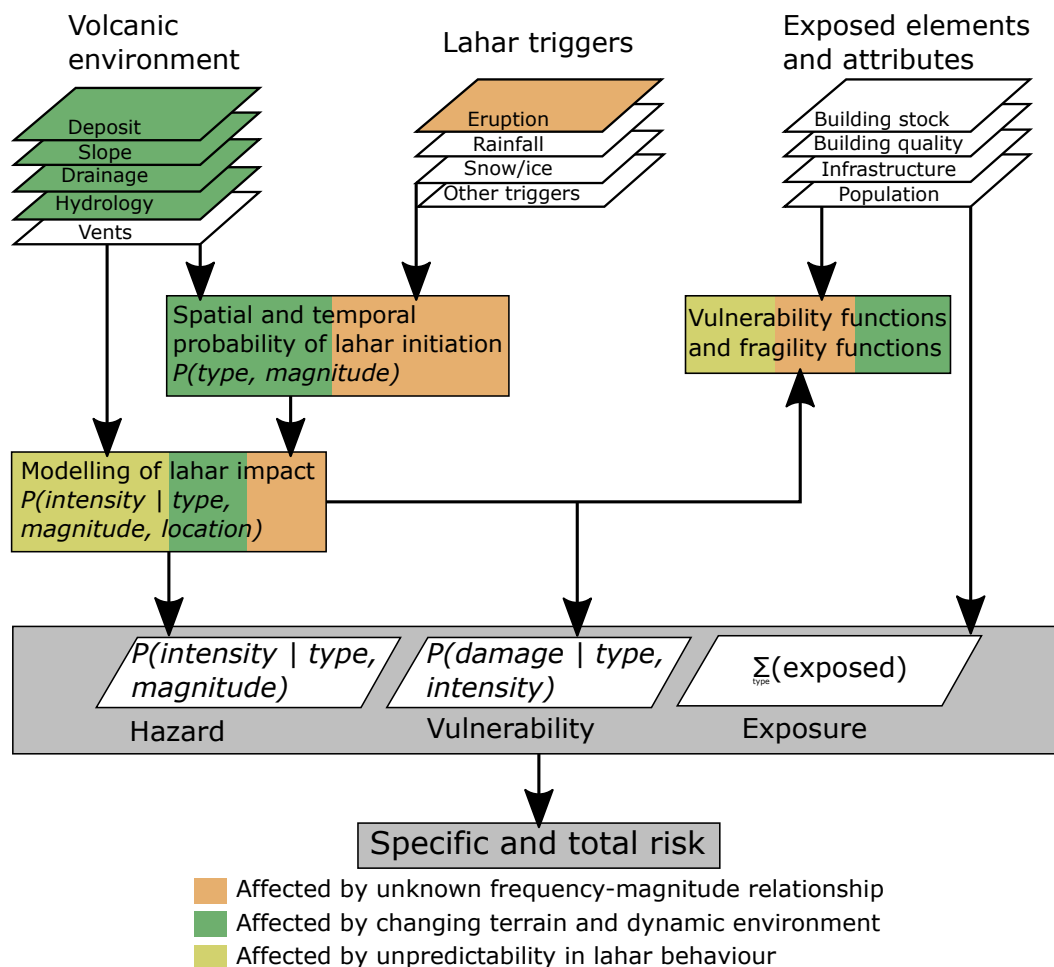


FIGURE 1.5: Schematic representation of lahar risk assessment methodology, from van Westen et al. (2006). Colours highlight components affected by unknown frequency-magnitude relationships, changing terrain and unpredictable lahar behaviour.

In this proposed methodology, the spatial and temporal probability of lahar initiation is separated from numerical modelling of lahar impact metrics (e.g. runout or pressure). In landslide hazard assessment the spatial and temporal probability, defined as *susceptibility*, is calculated as a function of potential landslide triggers (e.g. earthquakes) and environmental conditions that affect slope stability. The use of susceptibility is the critical difference between landslide and traditional volcanic risk assessment processes (e.g. as shown in Fig. 1.2). Quantitative susceptibility models can then be used as inputs into lahar models to determine the specific lahar hazard (i.e. probability of hazard intensity, given a lahar type and size). The specific risk (e.g. for a certain type of lahar trigger) can then be determined in combination with lahar vulnerability and exposed elements.

Components of Fig. 1.5 are colour coded to highlight elements affected by unknown frequency-magnitude relationships, changes in the terrain and the unpredictability of lahar behaviour. These effects can be summarised as:

- Unknown frequency-magnitude relationships affect accurate estimation of eruption frequency and size, limiting both primary and secondary lahar susceptibility estimates.
- Primary environmental inputs such as deposit characteristics, terrain slope, drainage and hydrology are all affected by dynamic volcanic processes which alter the terrain.
- The unpredictability of lahar behaviour affects models of lahar impact in addition to vulnerability functions.

The uncertainty (both epistemic and aleatoric) of key inputs into the lahar risk assessment process has flow-on effects that increase the overall uncertainty of lahar hazard and vulnerability estimates. Ultimately, the flow-on effects highlighted here limit quantitative lahar hazard and vulnerability assessment. This results in mostly qualitative lahar hazard assessments, causing risk estimates to be relative measures that are open to interpretation. Improvements in the quantification of primary inputs, probabilistic analysis techniques and understanding of lahar behaviour is needed to improve the assessment and quantification of lahar risk (Calder et al., 2015). Although epistemic uncertainty has a large impact, particularly in the understanding of lahar behaviour, risk assessment is also affected by the inherent randomness (i.e. aleatoric uncertainty) in lahar processes. The accurate estimation of risk under uncertain and changing environmental conditions is therefore crucial for quantifying lahar risk.

1.4 Thesis aim and objectives

Probabilistic volcano hazard models, developed with strong links to risk assessment, have broad utility for end-users in engineering, planning, insurance and emergency response sectors (Stirling and Wilson, 2002; Stirling et al., 2017). These hazard and risk models need to be quantitative in order to provide actionable, numerical metrics for the end-users

(UNISDR, 2015; Mead et al., 2016; Thompson et al., 2017) and, to facilitate comparisons between hazards, locations and potential mitigation measures (Wilson et al., 2014). However, examples of quantitative lahar hazard and risk assessments are limited (Calder et al., 2015; Mead et al., 2016) due, in part, to the practical obstacles identified in this introduction.

The aim of this thesis is to facilitate practical advancements in the quantification of lahar risk, through focused improvement of specific components outlined in Fig. 1.5. Collectively, these advancements will demonstrate a pathway to the quantification of lahar risk under uncertain and changing environmental conditions. This aim will be achieved by addressing five research objectives, summarised and justified as:

Objective 1. The frequency-magnitude relationship of volcanic eruptions needs to be quantified:

Obstacles to quantitative lahar hazard assessment begin with inadequate quantification of the frequency-magnitude relationship for volcanic eruptions (Stirling et al., 2017). Primary and secondary lahar recurrence rates are conditional on a volcano's eruption sequence, style and magnitude. However, incomplete geological and historical records introduce difficulties and uncertainties in estimating the frequency-magnitude relationship (Mead and Magill, 2014; Stirling et al., 2017). Therefore, the true recurrence rate of volcanic eruptions needs to be quantified before any assessment of lahar occurrence rate.

Objective 2. Predict lahar initiation probabilities in response to weather-driven events:

The size and frequency of lahars are also controlled by local topographic, hydraulic and meteorological conditions (Manville et al., 2000). While numerical models exist to predict the runout and velocity of lahar events (e.g. Pitman and Le, 2005; Kelfoun, 2011; Pudasaini, 2012; Iverson and George, 2014), all rely on an estimate of initial lahar size and location (Mead et al., 2016). This gap presents an opportunity to (i) accurately estimate initial lahar volumes and, (ii) correlate these volumes with conditional probabilities of eruptions and meteorological events.

Objective 3. Develop a probabilistic lahar hazard assessment methodology:

Current lahar hazard assessments are qualitative or semi-quantitative in nature (e.g. Scott et al., 1997; Scott et al., 2001; Aguilera et al., 2004; Robinson and Clynne, 2012; Amigo, 2013; Darnell et al., 2013; Thouret et al., 2013; Pistolesi et al., 2014), mainly due to difficulties in the robust estimation of lahar likelihood. When these issues are resolved (i.e. when objectives 1 and 2 are achieved), a new approach for probabilistic lahar hazard assessment can be developed.

Objective 4. Reduce the uncertainty and improve quality of terrain model inputs for lahar risk assessment:

Of all challenges to lahar risk assessment identified in this introduction, the changing

terrain in response to dynamic volcanic environments has the largest effect on the risk assessment methodology in Fig. 1.5. New, fast and accurate techniques to measure and represent the complex terrain are needed to improve the quantification of lahar hazard and vulnerability.

Objective 5. Quantify the impact of lahars on buildings and infrastructure:

Quantitative (physical) vulnerability assessments are lacking for lahars due to difficulties in determining the cause of damage, a lack of guidelines or methodologies to facilitate vulnerability assessment and the challenges in assessing post-event impacts (Wilson et al., 2014). Improvements to the quantification of vulnerability through development of lahar-specific fragility functions and vulnerability relationships will enhance risk assessment through better understanding of the structure and needs of risk models (Stirling et al., 2017). It will improve assessment of losses and allow better understanding of the importance of lahar hazard, exposure and vulnerability in determining these losses.

Overall, the publications in this thesis serve to demonstrate approaches that make the quantification of lahar risk possible while concentrating on improvements to lahar hazard and vulnerability assessment.

1.5 Thesis overview and structure

This thesis presents a series of five publications that directly contribute to improving the understanding and quantification of lahar hazard and vulnerability. These publications are separated into two parts discussing aspects lahar hazard (Part I) and vulnerability (Part II). Each publication expands the explanation on specific issues identified in this chapter, summarises the current state of research and proposes solutions that, when applied in a framework such as in Fig. 1.5, can lead to improvements in the quantification of lahar risk. As each chapter provides a separate and distinct contribution to the goal, an explanation of linkages between publications, objectives and additional discussion relevant to the aim of this thesis is provided in an overview of each part (I.1, II.1) and is summarised in following sections.

1.5.1 Part I: Lahar hazard

The first part of this thesis focuses on the development of methods to quantify frequency-magnitude relationships which, when coupled with computational models of lahar flow, can be used to produce quantitative probabilistic lahar hazard maps. The overview of this part introduces and summarises numerical modelling approaches relevant to lahars, based in part on complementary research undertaken during candidature. This publication (Mead and Cleary, 2015) is provided in appendix A for reference.

Chapter 2: Determining change points in data completeness for the Holocene eruption record

Chapter 2 (Mead and Magill, 2014) presents a statistical model of volcanic eruption records that accounts for incompleteness. A Markov Chain Monte Carlo (MCMC) method is then used to identify dates, called change points, after which an eruption catalogue is complete. This chapter is applied to the Smithsonian Institutions “Volcanoes of the World” (VOTW) eruption catalogue to identify change point dates and uncertainty in this date at region and country scales. This method can be applied to determine the frequency-magnitude relationship of volcanic eruptions, presenting a viable, reproducible alternative to previous methods while also quantifying uncertainty in eruption rate. The accurate understanding of eruption frequency-magnitude relationships directly contributes to primary lahar susceptibility models as eruption style has a significant role in determining deposit properties that contribute to triggering of secondary lahars.

Chapter 3: Rain-triggered lahar susceptibility using a shallow landslide and surface erosion model

The concept of lahar susceptibility is introduced in chapter 3 (Mead et al., 2016). Most previous studies of lahar hazard rely on the historic record and expert elicitation to define lahar volume inputs used in lahar models. This approach neglects mechanics of lahar initiation and changes in energy states, resulting in qualitative or semi-quantitative estimates of hazard. Focusing on rain-triggered secondary lahars, we propose a new, physically based approach to defining volume inputs into lahar models. A fully quantitative estimate of spatial and temporal initiation probability (i.e. frequency-magnitude relationship) is elicited in combination with rainfall intensity-frequency-duration relationships. This physically based, quantitative approach improves the understanding of lahar initiation processes in addition to enabling fully quantitative lahar hazard assessment in conjunction with lahar flow models.

Chapter 4: Probabilistic hazard modelling of rain-triggered lahars

Chapter 4 acts as a logical, combined conclusion to Mead and Magill (2014) and Mead et al. (2016). Quantitative, probabilistic lahar hazard assessments are made possible by improvements in frequency-magnitude relationships from previous chapters. A methodology to express lahar hazard in the form of an annual exceedance probability (AEP) is developed and demonstrated for a case-study area at Ruapehu Volcano, New Zealand. This method is demonstrated through the use of a shallow-layer lahar model (Pitman and Le, 2005), but can make use of any lahar runout or flow model that takes lahar volumes as an input. This chapter highlights that, through the use of lahar susceptibility approaches such as Mead et al. (2016), the problem of obtaining quantitative and probabilistic lahar hazard assessments is tractable.

1.5.2 Part II: Physical vulnerability

The second part of this thesis presents studies on the development and application of computational modelling techniques to better understand interactions between lahar hazard and exposure, how these interactions affect vulnerability and, the role of all three components in determining overall building loss. Explained in section 1.2, interactions between these components mean they cannot be separated into individual discrete elements of hazard, exposure and vulnerability. The broad aim (and therefore title) of this part is to develop physical vulnerability relationships in order to understand their role in loss from lahar events. This requires the improvement of primary inputs into lahar impact models used to define vulnerability functions and understand loss.

Chapter 5: A distributed computing workflow for modelling environmental flows in complex terrain

Mead et al. (2015) (Chapter 5) approaches the issue of using terrain models in changing volcanic environments. The accuracy of lahar impact models is dependent on an accurate representation of terrain. However, changes in volcanic environments mean terrain models, which are costly to acquire, need to be frequently updated. This chapter presents an alternative approach to acquiring terrain models using a low-cost photogrammetry method. This method focuses on obtaining detailed, fine scale features important for numerical modelling of flow around buildings. This is a crucial requirement for accurate estimation of flow and forces applied to buildings and infrastructure, which is necessary for understanding physical vulnerability and lahar induced losses.

Chapter 6: Examining the impact of lahars on buildings using numerical modelling

The utility of the photogrammetric approach from Mead et al. (2015) is demonstrated in chapter 6 which makes use of high-resolution terrain models to understand the damaging effect of lahars on buildings. Building losses for a range of flow scenarios are estimated using a lahar rheological model implemented in smoothed particle hydrodynamics, newly developed vulnerability relationships and a terrain model generated through the process explained in Mead et al. (2015). The new building vulnerability relationships developed in this chapter directly contribute to improving the quantification of risk through vulnerability functions. In addition, the building losses are used to draw some conclusions on the relative importance of lahar hazard, vulnerability and exposure. While all components play a role in determining loss, exposure was found to have a larger effect on total loss than vulnerability. This may mean that strategies to reduce exposure to lahars can have more of an effect on reducing loss than strategies to decrease vulnerability.

The final chapter (Chapter 7) summarises and critically assesses each publication, discusses the implications and contributions of this work to lahar risk assessment, and highlights key limitations and areas of future research that may improve the quantification of lahar risk.

Part I

Lahar hazard

I.1 Overview of objectives and contribution to thesis aim

This part consists of three chapters aimed at improving lahar hazard assessment with the eventual goal of enabling quantitative, probabilistic lahar hazard assessment. All three chapters improve inputs into lahar risk assessment workflows (see Fig. 1.5) through providing practical approaches to quantify lahar susceptibility and hazard. The research objectives for this part are to

1. quantify the frequency-magnitude relationship of lahars and volcanic eruptions,
2. understand controls on lahar triggering and develop models to estimate lahar susceptibility and,
3. develop a methodology for probabilistic quantification of lahar hazard using numerical models.

Objective 1 is addressed in chapter 2 and 3, objective 2 is addressed in chapter 3 and objective 3 is addressed through chapters 3 and 4. The primary contribution of this part to the thesis aim of improving quantitative lahar risk assessment is in the probabilistic quantification of lahar hazard. This is addressed in chapter 4, but relies on the findings of chapters 2 and 3. These two chapters (Mead and Magill, 2014; Mead et al., 2016) make the application to lahar risk possible through new methods to determine the frequency-magnitude relationship of volcanic eruptions and lahars, which are often affected by uncertainty in historic records and changing volcanic environments.

I.2 Summary and relevance to lahar risk

The first step in any natural hazard assessment is to determine the frequency-magnitude relationship of the hazard. Usually expressed as an annual recurrence interval (ARI) or annual exceedance probability (AEP), these relationships often rely on catalogues of past events for the estimation of frequency. For an accurate estimate, the number of events needs to be high, reducing aleatoric uncertainty, and the database should be unbiased, containing as few systematic errors as possible.

Catalogues of global volcanism, such as the Smithsonian Institutions Volcanoes of the World (VOTW) database (Global Volcanism Program, 2013), are commonly ‘incomplete’, as events are under reported due to a lack of documented observations, insufficient geological evidence or minimal detection technologies. This incompleteness is best demonstrated in Fig. I.1, showing cumulative eruptions and lahar events recorded in the VOTW catalogue (as of May 2013).

Incomplete databases of volcanic eruptions and associated hazards, such as lahars, restrict the ability to perform even cursory analysis of volcanic hazards and their frequency. Therefore,

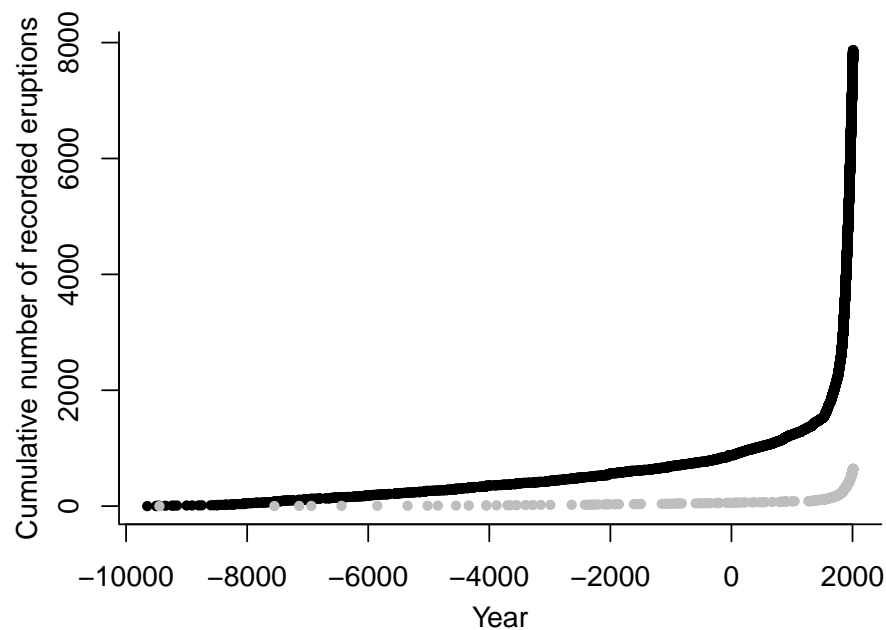


FIGURE I.1: Cumulative number of eruptions (black) and lahars (grey) recorded in the Volcanoes of the World 4.0 database (Siebert et al., 2010).

selection of the date after which the record is considered complete (referred to as the change point) is necessary. In Chapter 2 I reviewed approaches to determining change points and adapted a Markov Chain Monte Carlo (MCMC) method to calculate completeness of the eruption record.

This approach was able to systematically identify change points by region, country and eruption size, along with estimating uncertainty in these dates. Change points for all regions were used to create a ‘complete’ catalogue of eruptions where the effect of under recording is minimal. This catalogue was used to investigate the relationship between eruption size (expressed as the Volcanic Explosivity Index (VEI), see (Newhall and Self, 1982)) and lahar occurrence (Fig. I.2).

While this is only a first order estimate of lahar occurrence, Fig. I.2 shows a trend where the proportion of eruptions with documented lahars increases with eruption size. This suggests, although does not conclusively prove, that lahars may be material limited processes where the mechanics of tephra deposits are important for determining lahar initiation processes and frequency. The mechanics of lahar initiation, focusing on rain-triggered lahars are reviewed in chapter 3. In this chapter I introduce the concept of lahar susceptibility, defined as the occurrence probability of a particular lahar volume at a specific location. A model to predict lahar susceptibility was developed through a combination of shallow landsliding and overland erosion models, with probability of occurrence obtained through integration of rainfall intensity-frequency-duration (IFD) relationships.

Lahar hazard is often quantified through an estimate of probable initial lahar volumes.

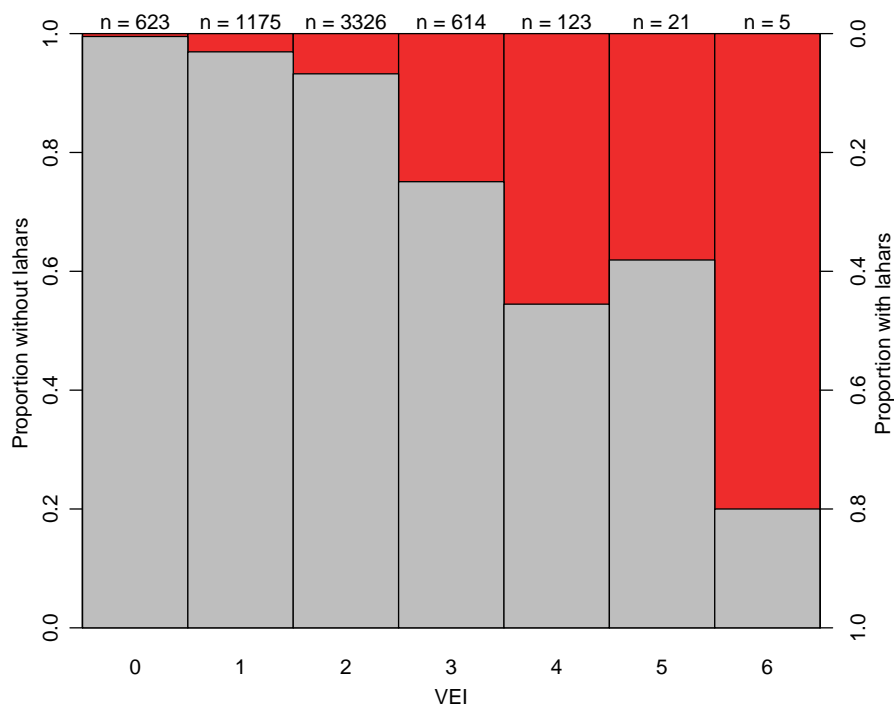


FIGURE I.2: Proportion of eruptions with documented lahars (red) to eruptions without documented lahars (grey) for each VEI category in the complete portion of the Volcanoes of the World 4.0 database.

However, reliance on geologic or historic records may result in biased estimates, as discussed in chapters 2 and 3. Probabilistic initial lahar volumes, an output of the model in chapter 3, provides an avenue for direct probabilistic quantification of lahar hazard, which reduces the effect of bias from previous lahars and eruptions. I demonstrated this in chapter 4, where probabilistic initial volumes from chapter 3 are used to estimate the AEP of lahar hazard through integration with a lahar flow model in Titan2D. This chapter is a demonstration of a new approach to determine frequency-magnitude relationships, reducing the reliance on biased estimates highlighted in chapter 2.

I.2.1 Numerical modelling of lahars

Reliable numerical models are an important requirement for achieving the goal of probabilistic lahar hazard assessment. The tools and methodologies developed in chapters 2 and 3 are focused on the implementation of numerical models into hazard assessment workflows. To provide context to this implementation, a brief overview of numerical modelling, opportunities and limitations is provided here.

Empirical models of lahar flow (e.g. LaharZ Iverson et al., 1998; Pierson, 1998; Schilling, 2014) are commonly used to simulate lahar inundation areas; however, like McDougall (2016), I favour numerical models that provide hazard intensity information (e.g. velocities and pressures) for their usefulness in quantifying lahar damage and physical vulnerability.

These numerical models are typically based on depth averaged equations of motion similar to the shallow water equations. Depth averaged approaches are favoured for the comparable level of detail to field measurements, their ability to capture the flowing free surface and computational efficiency which enables large scale geophysical hazard assessment (Iverson and Ouyang, 2015). Savage and Hutter (1989) and Savage and Hutter (1991) derived one-dimensional depth averaged equations of motion by assuming that granular material flows as an incompressible, shallow, finite volume of Coulomb-like material. The applicability of this approach, known as the Savage-Hutter (SH) method, can be limited by the five key simplifying assumptions explained in (Hutter et al., 2005):

1. incompressibility of the avalanche
2. small avalanche thickness and topographic curvature (the shallowness assumption)
3. Coulomb-like bed friction
4. simplified Mohr-Coulomb internal friction behaviour, causing preferential flow in one direction, and
5. uniformity of the vertical velocity profile.

Hutter et al. (2005) provided discussion and justification of these five assumptions. They noted that SH models can usually provide an accurate description of avalanche dynamics along nominally smooth beds where the assumptions of shallowness and uniform vertical velocity profiles are most valid. The simplification of the Mohr-Coulomb behaviour to cause preferential flow in one direction was identified as the most critical assumption when considering avalanches over irregular, three-dimensional terrain. To address the limitations of classic SH methods, Savage-Hutter and similar depth-averaged approaches have been developed to incorporate a more complete description of granular flow. These depth-averaged approaches have been modified and extended to multidimensional avalanches over more complex terrain (Hutter et al., 1993; Gray et al., 1999; Denlinger and Iverson, 2001; Pitman et al., 2003; Pudasaini and Hutter, 2003; Denlinger and Iverson, 2004), multi-phase flows with intergranular fluid (Iverson and Denlinger, 2001; Savage and Iverson, 2003; Pitman and Le, 2005; Pudasaini, 2012), erosion and deposition processes (Capart and Young, 1998; Bouchut et al., 2008; Tai and Kuo, 2008; Iverson, 2012) and dilatancy (Kowalski and McElwaine, 2013; Iverson and George, 2014). Gray et al. (2003) simplified a hydraulic theory for granular avalanches to develop a shallow-water like model for granular flow. These methods are able to use numerical schemes that capture shocks and model elements of flow around obstacles (e.g. Hákonardóttir and Hogg, 2005; Cui et al., 2007; Gray and Cui, 2007; Cui and Gray, 2013). A recent advance in depth-averaged approaches has been the implementation of the $\mu(I)$ rheology (Jop et al., 2006) by Forterre (2006) and Gray and Edwards (2014). This rheology is well suited to modelling dense granular flows. Despite being able to model the

behaviour of complicated granular flows, these depth-averaged approaches are still limited by the shallowness assumption. While the shallowness assumption is valid for mass flows where the topographic curvature is small, natural landscapes can be steep and irregular with obstacles such as buildings in the flow path that may affect the accuracy of the depth-averaged predictions. In these instances, momentum transfer and forces need to be accounted for in three dimensions to fully capture the transitions between static and dynamic states (Denlinger and Iverson, 2004). To account for these three dimensional stresses, Denlinger and Iverson (2004) developed a quasi-three dimensional computational method and tested it against laboratory scale avalanche experiments in Iverson et al. (2004). While features of the avalanche such as the static stranding of sand behind an obstacle are reproduced, computational grid issues were observed to cause some errors (Iverson et al., 2004).

The lack of universal constitutive laws for granular and granular mixture flows (McDougall, 2016) means numerical modelling of lahars is an ongoing and advancing field of research (e.g. recent publications of Iverson and George, 2014; Iverson and George, 2016; Mergili et al., 2017). In consideration of this fact and the range of currently used lahar numerical models (e.g. O'Brien et al., 1993; Fagents and Baloga, 2005; Pitman and Le, 2005; Kelfoun, 2011; Pudasaini, 2012; Iverson and George, 2014), methods developed here are not reliant on a single modelling software package. Instead, they focus on improving and providing inputs common to all modelling approaches.

Determining change points in data completeness for the Holocene eruption record

Stuart Mead and Christina Magill

Bulletin of Volcanology

Volume 76, Issue 11, November 2014

doi: 10.1007/s00445-014-0874-y

Abstract

Changes in data completeness for the Smithsonian Institutions “Volcanoes of the World” (VOTW) eruption catalogue, by region and for selected countries, is determined and utilised to estimate average eruption recurrence intervals. In the VOTW database the number of documented volcanic eruptions has increased markedly since the middle of the last millennium. This is largely attributed to population expansion, geological investigation and improvements in detection and recording technologies, rather than an increase in volcanic activity. Simple methods, such as break-in-slope or stationarity tests, can be used to determine changes in data completeness, but often require subjective choices, introducing additional uncertainty. A Markov Chain Monte Carlo (MCMC) simulation method for assessing and determining changes in the completeness of natural hazard event catalogues is adapted to determine the completeness of the database. Data completeness is assumed to follow a step-change model, where the probability of documenting an eruption is VEI dependent before the change point date and 100% after. A distribution of candidate change point dates is obtained for each region and country subset which allows uncertainty in the data completeness date to be quantified, and for uncertainty in eruption frequencies to be expressed and propagated through statistical models.

Keywords

data completeness · eruption frequency · recurrence interval · Markov Chain Monte Carlo · change point model · volcanic hazard

2.1 Introduction

Hazard frequency analysis, determination of recurrence intervals and loss estimation for natural hazard events often rely on catalogues or databases describing past occurrences (Kysely et al., 2011; Wirtz et al., 2014). For these purposes, the proportion of recorded events needs to be as high as possible to reduce aleatoric uncertainty and the database should contain no or very few systematic errors. Under reporting of past hazard events may result from a variety of factors including a lack of documented observations, incomplete or insufficient geological evidence and investigation, or minimal detection technology. This leads to datasets that can be considered, at least partly, ‘incomplete’ as they do not contain all events that occurred over the time period in question. The effect of incomplete datasets can be large, especially when data is utilised to estimate the frequency or recurrence interval of events. Issues in data completeness are evident in several catalogues of natural hazard events, including hailstorms (Schuster et al., 2005), cyclones in the Atlantic (Landsea, 2007), earthquakes (Woessner and Wiemer, 2005), avalanches (Dussauge-Peisser et al., 1999), landslides (Kirschbaum et al., 2010) and volcanic eruptions (Hayakawa, 1997; Siebert et al., 2010). In order to use these datasets for hazard frequency calculation, a cut-off date is typically chosen, after which point the dataset is assumed to be adequately complete. This date (referred to here as the change point) is critical, as it needs to be recent enough to eliminate errors due to missing data, while maximising the number of records in the dataset in order to adequately sample both large, lower frequency events and smaller, harder to detect events.

A common approach to deal with under recording in hazard datasets is to assume events occur at a constant rate with respect to time, with any non-stationarity in the rate attributed to under recording and an incomplete dataset. Tests for stationarity are usually based on classical statistics approaches, such as measuring recurrence interval convergence (e.g. Dussauge-Peisser et al., 1999; Schuster et al., 2005; Landsea, 2007), divergence (e.g. Klein, 1982; Mulargia et al., 1987) or regression analysis (e.g. Marzocchi and Zaccarelli, 2006). However, in most instances the choice of date or limits of stationarity are based on subjective assumptions. These classical methods also rely on the asymptotic properties of large datasets to provide confidence in the estimates (Rotondi and Garavaglia, 2002), requiring monitoring of scale dependence and restricting the applicability of these methods to smaller datasets.

Under recording of volcanic eruptions is particularly evident in catalogues of global volcanism, such as the large magnitude explosive eruptions (LaMEVE) database (Crosweller et al., 2012), the Smithsonian Institutions Volcanoes of the World (VOTW) database (Global Volcanism Program, 2013) and in the database of Hayakawa (1997) (Coles and Sparks, 2006; Furlan, 2010). Of these eruption catalogues, the VOTW database is the most comprehensive source of volcanic eruptions of all sizes (Crosweller et al., 2012) and is frequently used in global (e.g. Chester et al., 2000; Small and Naumann, 2001), regional (e.g. Jenkins et al., 2012b; Auker et al., 2013) and volcano specific assessments (e.g. Connor et al., 2001; Mendoza-Rosas and De la Cruz-Reyna, 2008). The under recording of eruptions is

particularly evident in the VOTW database (Siebert et al., 2010), which aims to document all volcanic activity during approximately the previous 10,000 years. Evidence for eruptions comes from historical accounts (directly observed and recorded) and geological observations dated using techniques such as tephrochronology and radiocarbon (Siebert et al., 2010). Figure 2.1 displays the notable increase in the number of eruptions documented in the catalogue within approximately the last 500 years. This increase has been attributed to population spread, colonisation and better recording technologies rather than an increase in the rate of volcanic eruptions (Newhall and Self, 1982; Siebert et al., 2010). This artificial change in

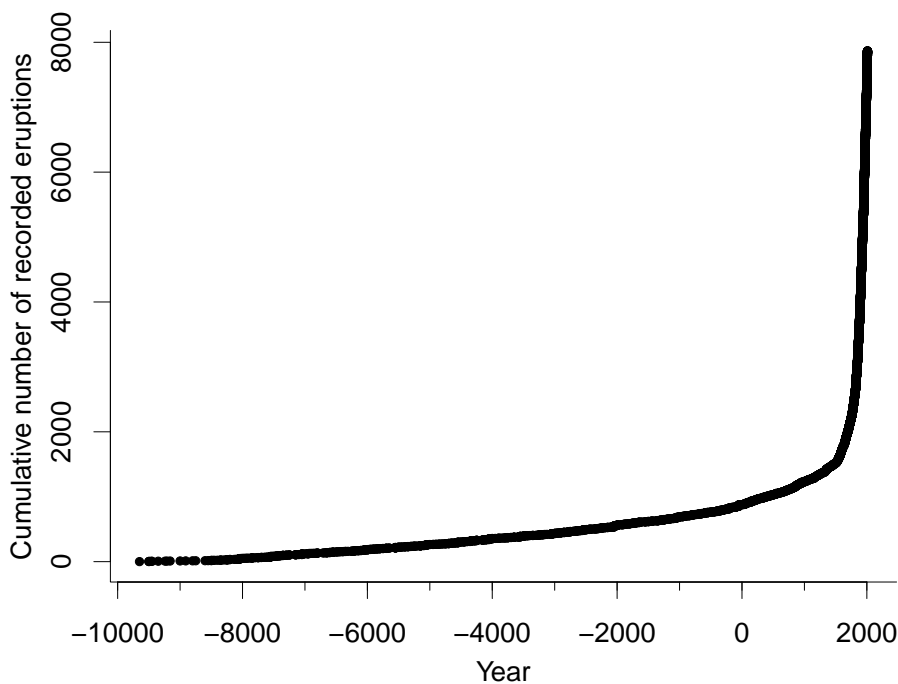


FIGURE 2.1: Cumulative number of eruptions recorded in the Volcanoes of the World 4.0 database (Siebert et al., 2010).

the rate of volcanic eruptions greatly affects estimates of eruption frequency. For example, 291 eruptions are documented in the database from 1000AD to 1500AD; however, 7,417 eruptions are recorded in the period from 1500AD to 2000AD. Completeness of the VOTW database varies by region (Lamb, 1970; Newhall and Self, 1982; Siebert et al., 2010) and therefore necessitates change point selection on a regional or country scale. However, in some regions there is not enough data to undertake stationarity tests with high certainty. This is particularly true when considering larger size eruptions, where for some regions (e.g. Atlantic Ocean, and Philippines and South East Asia), less than 20 eruptions have been documented with a Volcanic Explosivity Index (VEI, a semi-quantitative scale for eruption size used in the VOTW catalogue) greater than or equal to four. As a leading source of information on volcanic eruptions, the VOTW catalogue is frequently relied on to describe eruptive histories and characteristics on global, regional and volcano specific scales. Most analyses of this type require a choice of the point in time after which eruptions were consistently reported. To

support similar studies in the future, we calculate change points in data completeness for the VOTW eruption catalogue to determine data completeness on both regional and country scales, where enough data are available.

Most approaches to deal with under recording of volcanic eruptions also rely on the concepts of stationarity and independence, generally assuming eruption events (e.g. Newhall and Self, 1982; Guttorp and Thompson, 1991; Coles and Sparks, 2006; Deligne et al., 2010; Furlan, 2010; Jenkins et al., 2012b) or periods of repose (e.g. Klein, 1982; Mulargia et al., 1987; Marzocchi and Zaccarelli, 2006; Wang and Bebbington, 2012) fit a Poisson distribution (i.e. the intervals between eruptions are independent and identically distributed exponential random variables). While this assumption is considered valid for the global eruption record, the stationarity assumption may break down when considering eruptions on regional and country scales, as attempted here. For example, Watt et al. (2013) suggest that regional volcanism can increase following the end of glacial cycles, which implies that eruptions on a regional scale are not independent. In a data completeness study, Guttorp and Thompson (1991) identified periodicity in Icelandic eruption catalogue (containing 22 known volcanoes), indicating a lack of independence. However, these same authors found little deviation from the Poisson process in the Japanese eruption record (which contained 77 known volcanoes). Furthermore, De la Cruz-Reyna (1991) explains that aggregation on a global scale is not the sole reason for the Poissonian nature of global volcanism and that even an individual volcano may be represented by a Poisson process. Several studies and hazard assessments (e.g. Klein, 1982; Mulargia et al., 1987; Connor et al., 2001; Wang and Bebbington, 2012) have assumed independent and identically distributed eruptions from individual volcanoes. A visual examination of regional VOTW eruption records confirm the claim of Newhall and Self (1982) that under recording has a much greater effect on the eruption catalogue than any non-stationarity in volcanism. While we make the assumption here that the distribution of eruptions within a region or country is Poisson, changes in the frequency of volcanic activity can occur and should ideally be considered in regional scale analysis.

A simple approach to determine global eruption recording completeness by region and eruption size was demonstrated by Jenkins et al. (2012b), using a ‘break-in-slope’ method (as described by Hakimhashemi and Grünthal, 2012). This method is well suited when determining change points in regions such as South East Asia where easily identifiable changes in recording are evident and coincident with increased colonisation beginning in the 16th century. However, this method is more problematic in regions such as Japan, where data gradually becomes more complete over time, resulting in a more complicated relationship between documented events and time. Regions such as this require more subjective choices for curve fitting, calculation of slope and determination of breakpoints. This need for subjective decisions introduces problems in reliably determining reproducible change points. Simple approaches to determine data completeness, such as the example described above or inferring from recurrence interval divergence (e.g. Klein, 1982; Mulargia et al., 1987) usually come

down to a subjective choice (Mulargia et al., 1987). In contrast, statistical models of recording bias involve developing a formula for the probability of an eruption being documented and are useful for reducing the need for time consuming analysis as well as reliance on unreproducible subjective decisions (Coles and Sparks, 2006; Furlan, 2010). These statistical models usually follow a general form of:

$$\lambda_t(t, x) = \lambda(t, x) \cdot p(t, x) \quad (2.1)$$

In simple terms, the likelihood of an eruption of size x at time t is equal to the underlying eruption rate $\lambda(t, x)$ multiplied by the probability $p(t, x)$ of recording an eruption of that size at that time (e.g. Guttorp and Thompson, 1991; Coles and Sparks, 2006; Deligne et al., 2010; Furlan, 2010). Guttorp and Thompson (1991) developed a recording probability function based on the number of records in each year of the VOTW catalogue. The function was smoothed using a locally linear fit to reduce noise, and scaled to determine an observance probability by assuming the probability of recording an eruption to be 100% in 1980. Guttorp and Thompson (1991) acknowledged that the constraints on probability function shape and assumption of maximum in 1980 were unreasonable, but necessary for analysis. Coles and Sparks (2006) presented a statistical model of the same general form based on a Poisson point process for eruptions of magnitude $(M) \geq 4$, defined as:

$$M = \log_{10}(m) - 7, \quad (2.2)$$

where m is the estimated mass generated by the eruption, and using the 2000 year dataset of Hayakawa (1997). Deligne et al. (2010) used the same approach on a much larger dataset of large magnitude eruptions. This model assumes the probability of an eruption being documented increases with magnitude and time closer to present, with parameters determined using a classical maximum likelihood approach. The fitted models generally suggested a rapid rise in recording during the most recent 300 years and eruption magnitude dependence on under recording. However, as with the prescribed model of Guttorp and Thompson (1991), the applicability of this model is limited by the prescription of shape in the recording probability function and the assumption of an increasing recording probability with time, meaning only present day data can be considered 100% complete.

Furlan (2010) utilised a similar model to Coles and Sparks (2006) but developed an alternative formulation to express recording probability through the use of a step function, bypassing the limitation of shape and recording probability prescription in the Coles and Sparks (2006) approach. The statistical model parameters were fitted using Metropolis-Hastings Markov Chain Monte Carlo (MCMC) simulation (see Gilks et al., 1995). The outcome of MCMC simulation is a distribution of parameter values that accounts for the data and prior knowledge, termed the posterior distribution. This posterior distribution can be used to provide more information than parameter estimates obtained from maximum likelihood estimates (Coles, 2001). In Furlan (2010) the step function was generated by averaging the

chain of posterior values into a single function, with the approach able to estimate data completeness change points in an automated fashion without subjectivity. Change points were determined at two different threshold magnitudes in the eruption dataset of Hayakawa (1997). However, the size of the dataset was relatively small, containing only 221 and 67 events globally at magnitude thresholds of 4.0 and 5.1 respectively. Due to the small number of events, only a global scale change point was obtained; whereas, in reality, different countries or regions will have differing completeness change points (e.g. Lamb, 1970; Newhall and Self, 1982; Jenkins et al., 2012b).

Here, a similar MCMC method is utilised but applied to determine the change points in the Smithsonian VOTW 4.0 catalogue for all defined regions and for specific countries. This work builds on the method demonstrated by Furlan (2010) through using a more comprehensive database of volcanic eruptions, which allows for the application of more informative priors based on analysis of the dataset and estimations of data completeness change points on smaller scales. Estimation of the change points at this finer scale provides more value for regional hazard assessments, where under recording is most likely different to the global average. In addition we use the posterior distribution of the change point to quantify uncertainty in data completeness through examining the modes and broadness of the posterior. This is an improvement on more simple models and allows for uncertainty to be propagated through statistical models when calculating eruption frequency.

2.2 Volcanoes of the World Catalogue

Eruption data was downloaded from the online VOTW Catalogue 4.0 in May 2013 (Global Volcanism Program, 2013). This database was chosen as it contains the most extensive list of volcanic eruptions extending over approximately the past 10,000 years. The major difference between this catalogue and that of Hayakawa (1997) (used in Furlan, 2010) is the quantification of eruption size: Hayakawa (1997) used the magnitude scale (Eq. 2.2), while the VOTW catalogue uses VEI assigned according to the method of Newhall and Self (1982). Eruption magnitude has previously been used to estimate data completeness (e.g. Coles and Sparks, 2006; Deligne et al., 2010; Furlan, 2010) and had the benefit in these applications of being a purely quantitative and continuous measure of eruption size (Crosweller et al., 2012). In contrast the VEI scale is semi-quantitative, as it is sometimes assigned based on qualitative measures (Newhall and Self, 1982); however, in the majority of cases VEI is determined based on the volume of erupted material and has a value consistent with magnitude classification (Crosweller et al., 2012). As the VEI scale and VOTW catalogue are frequently used to describe eruptive histories, we chose to use this scale and catalogue to frame the data completeness issues in terms of the commonly used descriptions and database. The VOTW database also contains information on smaller (VEI or $M \leq 4$) eruptions included in this study, which are generally not the focus of other available datasets (e.g. LaMEVE, Hayakawa

(1997)). Using a VEI rather than magnitude scale meant this study required different and more informative priors than those used by Furlan (2010); these will be discussed in the following section.

For VEIs of 2 and higher, the number of eruptions in the VOTW catalogue follow a decreasing trend, shown in Fig. 2.2 (note, Plinian/Caldera forming eruptions are classified in the VOTW catalogue with a VEI of 4). There are fewer eruptions of $\text{VEI} < 2$ documented in the database; this is generally attributed to the default VEI for explosive eruptions being assigned as 2. While the number of VEI 2 eruptions is possibly over estimated due to its use as a default assignment (Newhall and Self, 1982), plume measurement data from historical eruptions support the relative abundance of VEI 2 eruptions in the entire catalogue (Newhall and Self, 1982; Siebert et al., 2010). Newhall and Self (1982) and De la Cruz-Reyna (1991) also suggest that smaller eruptions (i.e. $< \text{VEI} 2$) are under reported, bringing into question the completeness of VEI 1 records within the database. To alleviate these issues, we accumulate all eruptions with an assigned VEI of 0, 1 and 2 into a single category, designated as $\text{VEI} \leq 2$. Note also that some early VEI 1 to 4 data, originating from Newhall and Self (1982), have had VEI values incremented by 1 VEI unit. With some exceptions, the date of 1700AD was used as the cut-off for this increase. This increase does not have a visible effect on recording in the database and the impact to the calculated change point date is unknown. To resolve ambiguity, we assumed that all recorded VEI entries in the database are correct, and made no further corrections ourselves. Analyses of the VOTW Catalogue were undertaken for every

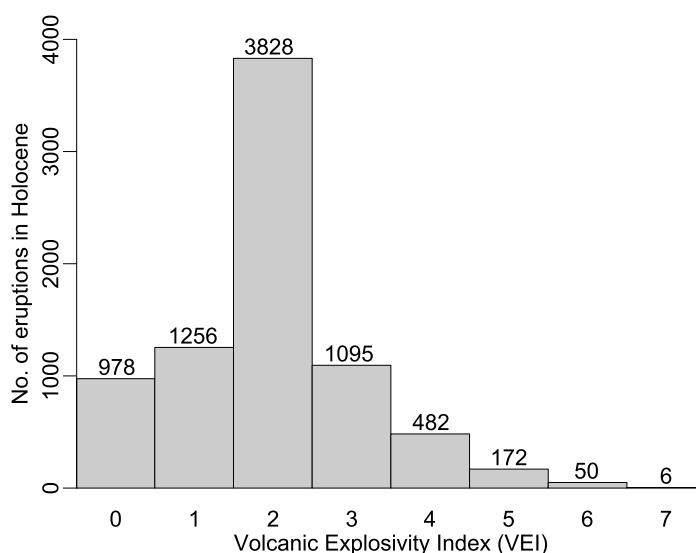


FIGURE 2.2: Histogram of recorded Volcanic Explosivity Index (VEI) in the Volcanoes of the World database (Siebert et al., 2010).

geographical region defined in the database as well as for countries where more than 100 eruptions (of any size) have been recorded. The difference in recorded eruptions between regions (defined geographically) and countries (defined by political boundaries) can be small when the record is dominated by one country. For example, the Indonesian region (includes

Indonesia, Andaman Islands and the entire island of Borneo) has only 12 more eruptions than the country of Indonesia. Similarly, the Japan, Taiwan and Marianas region is dominated by the record of Japan. In other cases, countries such as USA are an aggregation of a number of regions, including Alaska, Western USA and Hawaii, with the record dominated by Alaskan and Hawaiian volcanoes. The selection of regional and country boundaries can affect the model and the effect of this is addressed in the discussion.

The change point dates were calculated considering the entire eruption catalogue (VEIs 0-2 accumulated) and for a threshold VEI of 4. These two different analyses were conducted for a number of reasons: firstly, large VEI (≥ 4 in this context) eruptions are better preserved in the geological record and have a long recording history, although occurring less frequently than smaller eruptions (Siebert et al., 2010). By analysing separately the larger eruptions, more large VEI eruptions may be included in the portion of the catalogue considered complete, improving further hazard analysis by sampling more of the lower frequency, large size eruptions. Secondly, the default assignment of VEI 2 (Newhall and Self, 1982) and possible under recording of VEI 0, 1 and 3 eruptions (Newhall and Self, 1982; De la Cruz-Reyna, 1991) makes the lower VEI record more questionable and Poissonian behaviour is not assured (although suspected by De la Cruz-Reyna, 1991). By doing two analyses per region or country, we obtain completeness dates for all eruptions, which could be less robust due to continuing recording uncertainties (albeit counterbalanced by a larger amount of data), as well as more reliable VEI ≥ 4 dates.

2.3 Statistical Model

In order to assess the presence of under recording, we use the modified Poisson point process model of Coles and Sparks (2006), given as:

$$\lambda_M(t, x) = \lambda(t, x) \cdot p(t, x), \quad (2.3)$$

where $\lambda_M(t, x)$ is the modified intensity function which accounts for under recording, t is the eruption year, x the eruption magnitude, $\lambda(t, x)$ the intensity function denoting eruption rate and $p(t, x)$ a function describing the probability of an eruption being documented.

The intensity function is assumed to be a two dimensional Poisson point process (see Pickands III, 1971; Coles, 2001; Coles and Sparks, 2006) above a threshold magnitude u given by the generalised Pareto distribution (GPD)

$$\lambda(t, x) = \frac{1}{\sigma} \left[1 + \xi \frac{(x - u)}{\sigma} \right]^{-\frac{1}{\xi} - 1}, \quad (2.4)$$

where $\sigma > 0$ and $\left[1 + \xi \frac{(x - u)}{\sigma} \right] > 0$.

In Eq. 2.4, the parameters μ and σ control the location and scale of the distribution, while

ξ controls the shape and endpoint of the tail. In all cases presented here $\xi < 0$, meaning the distribution is bounded by a maximum at $\mu - \sigma/\xi$. The GPD is a power law type relationship commonly used in peaks over threshold (POT) methods (Deligne et al., 2010). In POT methods, the choice of threshold (u) is vital to ensure the validity of the intensity function (Davison and Smith, 1990; Coles and Sparks, 2006). As the GPD is modelling the tail of a processes distribution, threshold selection is a balance between minimising errors through inclusion of as much data as possible, while still sampling the correct region (tail) of the data. This typically results in choosing the lowest threshold value where the data is still adequately represented by the model (Lang et al., 1999; Coles, 2001; Coles and Sparks, 2006). Referring to Fig. 2.2, thresholds of VEI 1 or higher would result in a distribution that could adequately be represented by the GPD model, when VEI 0 – 2 are accumulated into a single category. The GPD approximation was also tested using the mean residual life method (see Coles, 2001) on a subset of the data starting from 1800AD to reduce the effect of under-recording. The mean residual life plot for the data is approximately linear after VEI 1; therefore, threshold VEIs (u) of 1 or higher are likely to be adequately approximated by a GPD, subject to the number of entries being large enough to provide a reasonable approximation.

The presence function expresses the probability of recording an eruption of VEI x at time t (Fig. 2.3a). In this implementation, we use the single change point step function proposed by Furlan (2010) as:

$$p(t, x) = \begin{cases} \frac{1}{1 + \exp^{-\alpha - \beta x}} & \text{for } t \leq k \\ 1 & \text{for } t > k \end{cases}, \quad (2.5)$$

where k is the year of the change in recording, and α and β are parameters controlling the scale and shape of the recording probability function. This observation probability function has two states: in the first state, before year k , eruptions are incompletely observed, with the recording probability assumed to follow the upper function with a shape similar to a logistic function (Fig. 2.3b). The shape of this function represents the recording bias for large size eruptions, where probability increases with x , the VEI of the eruption. In the second state, after year k , eruptions of any VEI greater than the threshold are assumed to have a recording probability of 100% (completely observed).

The recording probability function (Eq. 2.5) shows sensitivity to the choice of α and β values (Fig. 2.3b). Increases to α (black lines) shifts the presence function curve towards higher VEI values, in effect reducing the recording probability of eruptions, particularly for $\text{VEI} \leq 4$. The function displays a larger sensitivity to β values, returning recording probabilities that differ by up to 70% for perturbations of 1.5. The optimal choice of these values is therefore vital to the applicability and versatility of the statistical model. The effect of the presence function on an artificially generated dataset is demonstrated in Fig. 2.3c. At parameter values of $\alpha = 3.5$ and $\beta = 1$, VEI 2 eruptions are predicted to be under recorded by more than 50%; however, there is almost no impact to the probability of eruptions being recorded with assigned VEIs of between 5 and 7.

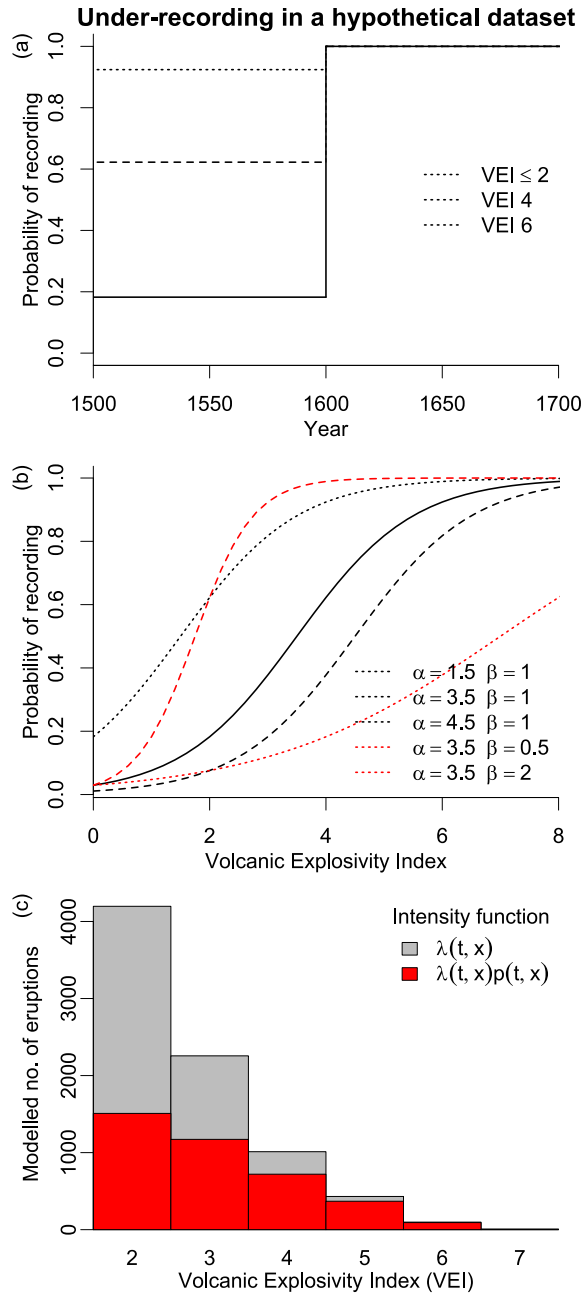


FIGURE 2.3: (a) Example of the presence function at VEIs of 2, 4 and 6. Before year $k = 1600$, eruptions are assumed to be recorded with a probability equal to $\frac{1}{1 + \exp(-\alpha - \beta x)}$, where x is the VEI, $\alpha = 3.5$ and $\beta = 1$, (b) shape of the presence function at different α and β values, and (c) histogram of a theoretical dataset generated using the standard intensity function $\lambda(t, x)$ (in grey) and the modified intensity function $\lambda(t, x)p(t, x)$ (in red). The effect of the presence function is demonstrated by the larger amount of under-recording at lower VEIs. Parameters used in this demonstration were: $\mu = 1.5$, $\sigma = 1.5$, $\xi = -0.25$, $\alpha = 3.5$, $\beta = 1$ and $k = 1567$.

2.4 Metropolis-Hastings approach

The objective of the MCMC simulation is to find the year k after which eruption data are consistent with the unmodified presence function in Eq. 2.4. Using the approach of Furlan (2010), the likelihood function for eruptions larger than VEI u can be given as:

$$L(\mu, \sigma, \alpha, \beta, k; (t, x), \dots, (t_i, x_i)) = \exp \left\{ \int_{x=u}^{+\infty} \int_{t=0}^k \lambda(t, x) \frac{1}{1 + \exp^{-\alpha - \beta x}} dt dx \right\} \times \\ \exp \left\{ \int_{x=u}^{+\infty} \int_{t=k+1}^{2013} \lambda(t, x) dt dx \right\} \times \prod_{i: 0 < t_i \leq k} \lambda(t_i, x_i) \frac{1}{1 + \exp^{-\alpha - \beta x}} \times \prod_{i: k < t_i \leq 2013} \lambda(t_i, x_i) \quad (2.6)$$

The parameters μ , σ , ξ , α , β and k were estimated using a Metropolis-Hastings MCMC method, which samples proposed parameter values from a broad initial distribution (prior) and retains the values that give a high likelihood in a chain of likely parameter values (posterior distribution); for more details on MCMC methods, see Coles (2001) and Gilks et al. (1995).

The Metropolis-Hastings algorithm used here is functionally similar to the algorithm used by Furlan (2010), with parameters σ and α transformed to avoid poor mixing in the posterior. A new parameter, ζ , is added as a replacement for σ with the relationship

$$\sigma = \frac{\xi(u - \mu)}{n_e \log(1 + \exp^{\zeta})^{-\xi-1}} \quad (2.7)$$

and α is transformed into α^* through the relationship

$$\alpha^* = \alpha + \beta \bar{x}, \quad (2.8)$$

where \bar{x} is the mean VEI of the dataset.

The proposal values for μ , ζ , ξ , α^* and β were chosen using a random walk with the formula $v_p = v_c + N(0, \omega_v)$, where v denotes the properties of μ , ζ etc. and ω_v is a tuning parameter that controls the efficiency of the algorithm but has no effect on the model (Coles, 2001). In our model the tuning parameters were adjusted to $\omega_{\mu, \zeta, \xi} = 0.1$ and $\omega_{\alpha, \beta} = 0.25$ through trial and error to ensure proposal values were well mixed (i.e. propose values with steps large enough to sample the entire target distribution, but not too large as to give low chances of acceptance. c.f. Gilks et al. (1995), p. 8). The formula for the proposed change point value, k_p , is shown in Eq. 2.9. The next candidate for the change point is drawn from a uniform distribution centred on the current candidate, and with half-width (k_w) equal to the average return period with limits at the temporal boundaries

$$k_p \sim U [\max(k_c - k_w, Y_0) : \min(k_c + k_w, Y_{max})], \quad (2.9)$$

where Y_0 and Y_{max} are the earliest and latest year with documented eruptions, respectively,

and k_p and k_c are proposed and current values of k (change point year) respectively. This random walk is an efficient means of exploring the support of k between Y_0 and Y_{max} .

The sensitivity of the GPD and presence function to the parameter values suggests that the prior distributions may not need to be as broad as those specified by Furlan (2010). In preliminary simulations, the use of the VEI scale appeared to require more restrictive priors. The GPD parameters of μ , ζ and ξ were given normal prior distributions with a mean of 0 and variances of 10. This gave a sufficiently broad prior that did not constrain the simulation, while still generally restricting the GPD to expected values. Parameters α^* and β control the recording probability function (Fig. 2.3) with the transition from low to high probabilities expected to occur between VEI 2 and 5. This hypothesis appears to be supported by preliminary examination of the eruption database. As the data completeness change point is expected to change between countries and regions and, given the lack of information on location specific recording, the prior distribution of k was chosen to be uniform between Y_0 and Y_{max} . This broad prior ensured that no preference was given to particular values of the change point year, making the posterior primarily determined by the data.

The starting values for the MCMC algorithm were chosen to be $\mu = 1.5$, $\alpha = 1.5$, $\xi = -0.25$, $\alpha = 3.5$ and $\beta = 1.0$ with k chosen as the first quartile (Q_1) of the documented eruption data. Two separate analyses for each region and country were run, one with a threshold value (u) of 1 and the other with the threshold set to 3 (i.e. all VEIs and VEI ≥ 4 , respectively). Geweke's diagnostics (Geweke, 1992) and the autocorrelation function were used to determine the properties of the MCMC chain, the algorithm was run for 200,000 iterations with the first 5,000 discarded (burn in) and one in 10 observations retained (thinning) in order to improve convergence, reduce correlation with initial values and reduce the amount of autocorrelation within the MCMC chain.

2.5 Comparisons of data completeness

As explained earlier, analyses of the VOTW catalogue were undertaken for every geographical region defined in the database as well as for countries with more than 100 eruptions on record. Simulations for two threshold levels provide two different change point dates; one considering the entire eruption catalogue (VEIs 0-2 accumulated) and one considering VEI ≥ 4 eruptions only. As examples, Fig. 2.4 displays the frequency of the change point year k in the posterior distribution and the cumulative number of eruptions for VEI ≥ 4 eruptions in the United States of America and Indonesia (country). The width of the posterior distribution (grey bars in Fig. 2.4) can be used to infer certainty in the change point, with broader distributions suggesting greater uncertainty. The four peaks in the distribution between 1000BC and 1800AD for the United States of America (Fig. 2.4a) can indicate other likely change point dates within the distribution. The posterior distribution of k for the USA is much broader than for Indonesia, this is because a large proportion (77%) of the large VEI eruptions in the USA have been

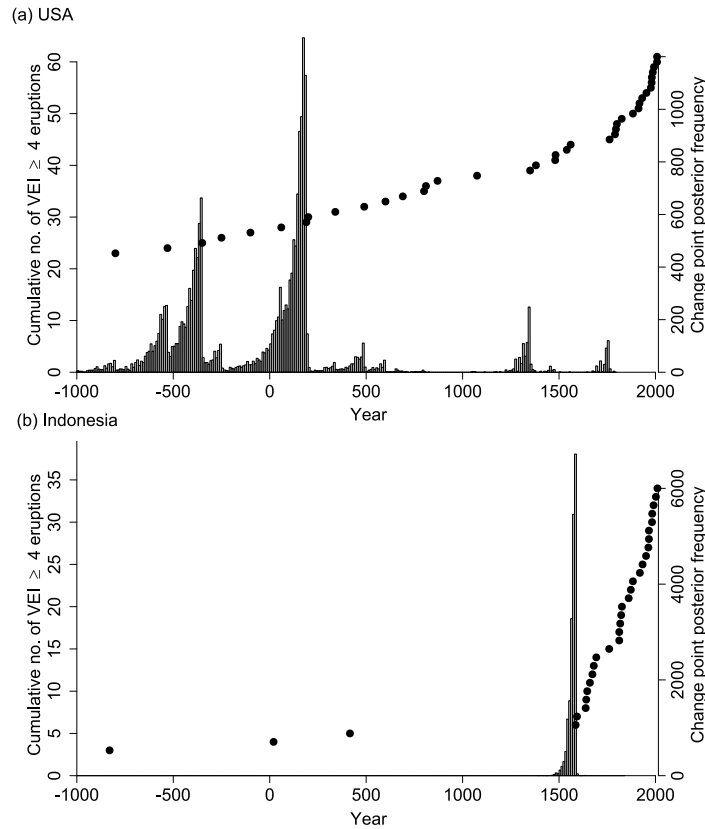


FIGURE 2.4: Posterior distributions of the change point year k from the MCMC simulation, and cumulative number of $\text{VEI} \geq 4$ eruptions for (a) the United States of America, and (b) Indonesia.

documented through geological studies and dating rather than through historical accounts. This results in an eruption catalogue for the USA characterised by a relatively steady increase in the number of eruptions documented throughout time and demonstrates a greater level of uncertainty in the change point date. In contrast, only 13% of Indonesian large $\text{VEI} \geq 4$ eruptions were obtained from non-historical records at 17 volcanoes (Global Volcanism Program, 2013). The dominance of historical accounts post-colonisation results in a sudden increase in the rate of documented eruptions in the late 1500's, causing the posterior distribution of k to be relatively narrow. The variability in derived posterior distributions for different regions and countries suggests that the distributions could be used to estimate uncertainty in the change point date and consequently in the calculation of average eruption recurrence intervals. While Furlan (2010) estimated the step function change point as the average of the posterior, in our approach we quantify the uncertainty by using the 5th, 50th and 95th percentiles of the change point posterior. This allows for estimates of the upper, median and lower bounds of derived average recurrence intervals.

The percentiles of the change point posterior, corresponding number of eruptions, and average recurrence intervals were calculated for each catalogue region and for selected countries and are shown in Tables 2.1 and 2.2 for all eruptions and $\text{VEI} \geq 4$ eruptions respectively. The corresponding recurrence intervals were calculated by dividing the number of years since

the change point date by the number of eruptions since the date. For $VEI \geq 0$ the difference between the 5th and 95th percentile recurrence interval for each region and country is negligible, with only small differences in the number of eruptions occurring since the calculated change point dates. The change point date occurs in the 18th or 19th century for most countries and regions, with some exceptions: for the countries of (and regions that contain) Japan and Guatemala, dates occur in the mid-16th century and, for Italy, in the late 17th century to early 18th century. These countries have longer written records and documented historical observation.

The impact that regional and country boundaries have on the change point is demonstrated in Table 2.1 by the dominance of the Alaskan regional record on the change point for the United States (as a country). The change point date for all eruptions in the Canada and Western USA region occurs 60 years after the Alaskan record is considered complete. However, when the regions of Alaska, Western USA (minus Canada) and Hawaii are grouped, the change point date is dominated by the Alaskan record. This demonstrates the impact that groupings (regional or otherwise) have on calculated change point dates and suggests a possible improvement to this approach could be attained by grouping volcanoes into better defined regions based on their recent activity or recording history, keeping in mind the requirements of independence and stationarity.

Large eruptions (defined here as $VEI \geq 4$) are more likely to be observed and documented, both in historical records and through dating techniques such as tephrochronology. As a result the catalogue will, in general, be considered complete earlier if analysing larger eruptions in isolation. This date is important to determine as the lower frequency of large eruptions usually means there is a lack of data if a shorter time period is considered. The increased probability of eruptions being documented results in broader posterior distributions and larger differences in recurrence intervals (Table 2.2) when compared to $VEI \geq 0$. The change point dates for $VEI \geq 4$ eruptions all occur earlier than the change points for the complete catalogue, but the actual dates vary greatly between regions and countries, and with large differences between the 5th and 95th percentile recurrence intervals. The country scale change point dates proposed by Jenkins et al. (2012b) (who used a change-in-slope method) appear to agree with the results of the MCMC simulations in most cases, although the MCMC analysis tends to suggest earlier dates that reduce the estimated recurrence intervals. Two notable differences between the calculated change points of Jenkins et al. (2012b) and this analysis is for the countries of Mexico and Nicaragua. In both instances, the countries entire catalogue was assumed to be complete by Jenkins et al. (2012b); however, the MCMC simulations suggests that only a subset of the catalogue is complete, resulting in a difference of more than 250 years in the calculated recurrence intervals.

TABLE 2.1: Data completeness change point dates, number of eruptions after the change point and average recurrence interval for all eruptions using the Markov Chain Monte Carlo method. The change point dates are calculated from the 5th, 50th and 95th percentiles of the change point posterior distribution.

	Percentile	Change point year (AD)			Number of eruptions (all) after change point year				Average recurrence interval (years)		
		5%	50%	95%	5%	50%	95%	Total	5%	50%	95%
Region	Africa and Red Sea	1819	1820	1820	136	134	134	163	1.4	1.4	1.4
	Alaska	1782	1784	1784	307	306	306	340	0.7	0.7	0.7
	Antarctica	1891	1893	1899	41	40	39	60	2.9	2.9	2.8
	Atlantic Ocean	1986	1988	1990	5	5	5	82	4.9	4.3	4.1
	Canada and Western USA	1831	1841	1842	33	31	31	134	5.4	5.4	5.4
	Hawaii and Pacific Ocean	1817	1820	1820	156	154	154	306	1.2	1.2	1.2
	Iceland and Arctic Ocean	1693	1702	1706	126	124	122	299	2.5	2.5	2.5
	Indonesia	1768	1770	1770	1142	1140	1140	1260	0.2	0.2	0.2
	Japan, Taiwan, Marianas	1541	1542	1542	1023	1022	1022	1366	0.5	0.5	0.5
	Kamchatka and Mainland Asia	1734	1737	1737	315	313	313	566	0.9	0.9	0.9
	Kuril Islands	1757	1760	1765	139	138	135	148	1.8	1.8	1.8
	Mediterranean and W Asia	1631	1682	1682	205	193	193	326	1.8	1.7	1.7
	Melanesia and Australia	1850	1855	1856	378	377	376	419	0.4	0.4	0.4
	México and Central America	1503	1517	1518	616	613	612	712	0.8	0.8	0.8
	Middle East and Indian Ocean	1731	1750	1751	213	210	209	240	1.3	1.2	1.2
	New Zealand to Fiji	1835	1836	1851	290	289	284	388	0.6	0.6	0.6
	Philippines and SE Asia	1799	1808	1825	156	154	151	186	1.4	1.3	1.2
	South America	1728	1737	1738	631	629	628	805	0.4	0.4	0.4
	West Indies	1952	1965	1965	18	15	15	67	3.2	3	3
Country	Chile	1730	1737	1742	300	299	297	338	0.9	0.9	0.9
	Colombia	1820	1822	1822	67	66	66	103	2.8	2.8	2.8
	Costa Rica	1818	1821	1821	98	97	97	134	2	1.9	1.9
	Ecuador	1723	1725	1738	181	180	177	266	1.6	1.6	1.5
	El Salvador	1760	1766	1769	96	95	94	108	2.6	2.6	2.6
	France	1731	1748	1756	186	183	181	231	1.5	1.4	1.4
	Guatemala	1562	1565	1565	109	107	107	120	4.0	4.2	4.2
	Iceland	1692	1702	1706	119	116	114	290	2.7	2.7	2.7
	Indonesia	1770	1770	1770	1128	1128	1128	1248	0.2	0.2	0.2
	Italy	1678	1682	1682	184	182	182	304	1.8	1.8	1.8
	Japan	1541	1542	1543	959	958	957	1300	0.5	0.5	0.5
	Mexico	1864	1869	1869	52	51	51	159	2.8	2.8	2.8
	New Zealand	1834	1836	1855	221	220	216	277	0.8	0.8	0.7
	Nicaragua	1847	1849	1849	151	150	150	186	1.1	1.1	1.1
	Papua New Guinea	1871	1872	1872	187	186	186	218	0.7	0.7	0.7
	Philippines	1800	1822	1825	152	149	148	183	1.4	1.3	1.3
	Russia	1735	1737	1759	451	449	442	706	0.6	0.6	0.6
	United States	1783	1784	1784	517	515	515	769	0.4	0.4	0.4
	Vanuatu	1854	1856	1861	132	131	130	137	1.2	1.2	1.1

2.5.1 Completeness for all eruptions

As discussed previously, the posterior distributions for $\text{VEI} \geq 0$ were relatively tight and resulted in little difference between the calculated 5th and 95th percentile recurrence intervals. In all instances the change point dates appeared to be strongly correlated with an increase in the recording of eruptions with VEI less than or equal to 2. Examples of this effect can be seen for the regions of Canada and Western USA, Iceland and Arctic Ocean, and South America (Fig. 2.5). In the regions of Canada and Western USA (Fig. 2.5a) and Iceland and Arctic Ocean (Fig. 2.5b), there is a sudden increase in the number of recorded $\text{VEI} \leq 2$ eruptions that appears to constrain the location of the change point to dates just before this time. In South America (Fig. 2.5c), the increase in documented $\text{VEI} \leq 2$ eruptions is not as sudden but still results in a very narrow posterior distribution, giving a high level of certainty in the recurrence interval estimate for the region.

While, in most cases, countries will have less eruptions on record than their respective regions, the change point is generally easier to distinguish as recording of small eruptions is likely correlated with social, population and political changes in the country (Siebert et al., 2010). Sudden increases for countries such as USA (Fig. 2.6c) and Indonesia (Fig. 2.6a) also make it easy to determine the change in data completeness by alternate methods (e.g. Jenkins et al., 2012b). However, countries with longer historical records and more extensive

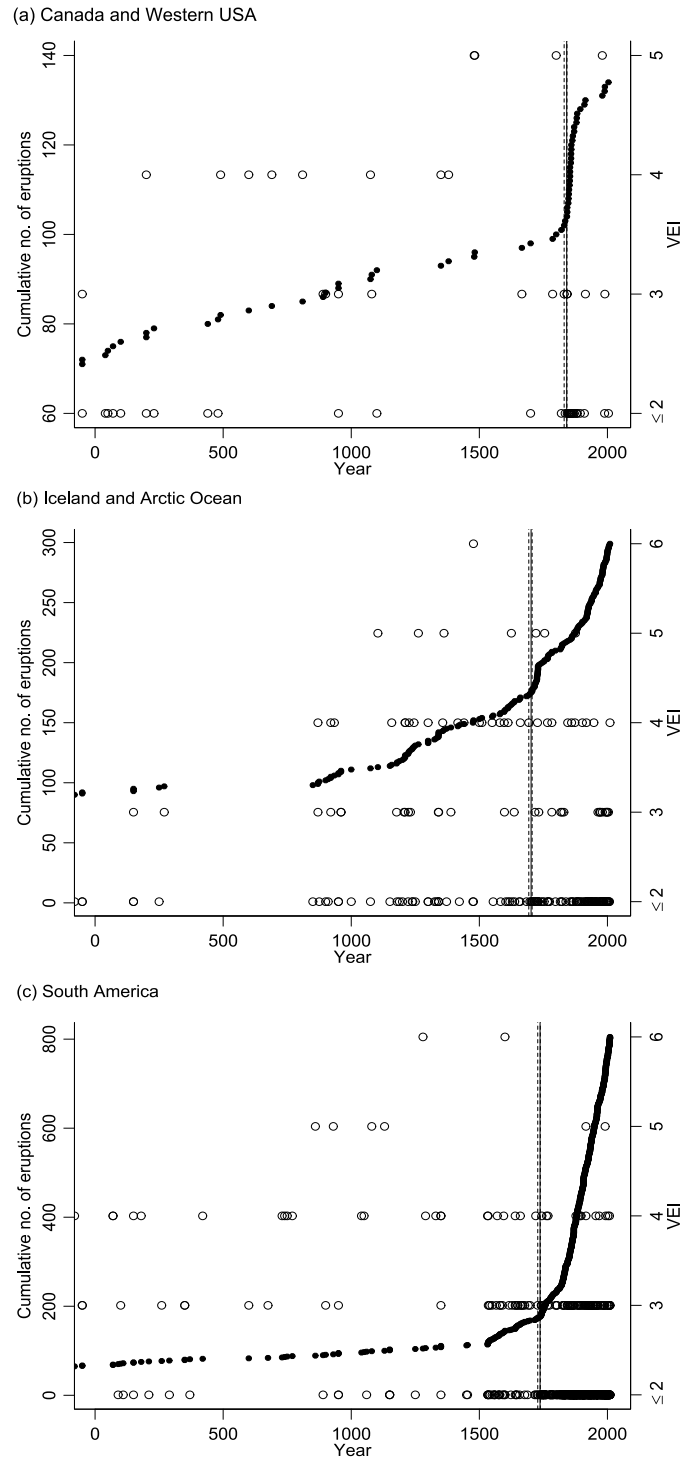


FIGURE 2.5: Cumulative number of eruptions (filled points) and eruption magnitudes (hollow points) recorded for the regions of (a) Canada and Western USA, (b) Iceland and Arctic Ocean, and (c) South America, displaying the 50th percentile (solid line), and the 5th and 95th percentiles (dotted lines) of the change point posterior. The change point appears to be primarily controlled by the amount of VEI < 4 eruptions recorded.

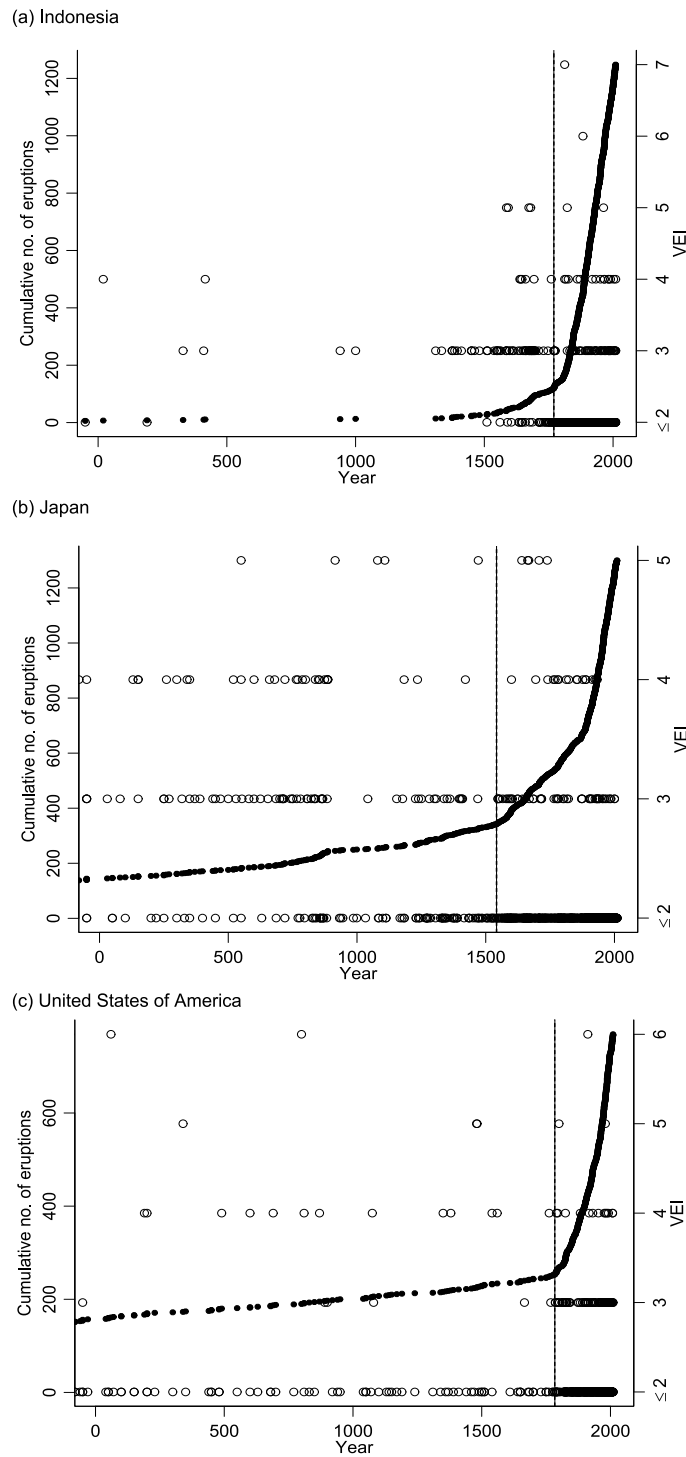


FIGURE 2.6: Cumulative number of eruptions (filled points) and eruption magnitudes (hollow points) recorded for (a) Indonesia, (b) Japan, and (c) the United States of America displaying the 50th percentile (solid line), and the 5th and 95th percentiles (dotted lines) of the change point posterior. The change point appears to be primarily controlled by the amount of VEI < 4 eruptions recorded.

TABLE 2.2: Data completeness change point dates, number of eruptions after the change point and average recurrence interval for large magnitude eruptions (Volcanic Explosivity Index ≥ 4) using the Markov Chain Monte Carlo method. The change point dates are calculated from the 5th, 50th and 95th percentiles of the change point posterior distribution.

Percentile		Change point year (AD, negative values are BC)			Number of eruptions (VEI ≥ 4) after change point year				Average recurrence interval (years)		
		5%	50%	95%	5%	50%	95%	Total	5%	50%	95%
Region	Africa and Red Sea	-8167	-7655	-6075	10	10	9	11	1017.7	966.5	898.3
	Alaska	1461	1724	1762	14	12	11	36	39.2	23.8	22.5
	Atlantic Ocean	-1914	-329	-85	11	10	10	13	356.7	233.9	209.5
	Canada and Western USA	-2403	-653	-446	19	16	15	22	232.3	166.4	163.7
	Iceland and Arctic Ocean	779	855	1073	38	38	35	51	32.4	30.4	26.8
	Indonesia	1535	1575	1586	29	29	28	34	16.4	15	15.1
	Japan, Taiwan, Marianas	-2148	-382	113	84	66	59	117	49.5	36.2	32.2
	Kamchatka and Mainland Asia	1613	1815	1924	14	12	8	107	28.4	16.3	10.8
	Kuril Islands	1561	1662	1688	12	12	12	15	37.4	29	26.8
	Mediterranean and W Asia	-3128	-2638	-2500	24	24	23	27	214.1	193.7	196.1
	Melanesia and Australia	171	1866	1903	24	11	11	30	76.6	13.1	9.7
	México and Central America	-868	-383	391	47	45	36	70	61.2	53.2	45
	New Zealand to Fiji	692	1589	1708	8	6	4	41	164.7	70.2	75.5
	Philippines and SE Asia	1159	1335	1380	11	11	10	16	77.4	61.4	63
	South America	-1488	-1339	-1064	64	64	60	89	54.7	52.3	51.2
	West Indies	1900	1901	1902	2	2	2	28	54.9	54.3	54
	Chile	1490	1633	1888	8	8	6	24	65	47.1	20.3
	Colombia	-4319	-2014	-1053	16	14	12	18	395.6	287.4	255.3
	Costa Rica	1398	1400	1400	1	1	1	22	612.2	610.4	610
	Ecuador	-1355	-739	-444	32	29	27	43	105.2	94.8	90.9
	France	-5025	-694	-103	20	14	11	24	351.8	193.1	192.1
	Guatemala	1581	1659	1714	7	7	7	8	61.3	50.1	42.3
	Iceland	773	856	1073	38	38	35	51	32.6	30.4	26.8
	Indonesia	1533	1575	1586	29	29	28	34	16.4	15	15.1
	Italy	-3185	-2640	-2464	21	21	20	24	247.4	221.4	223.7
Country	Japan	-3064	-997	128	90	70	56	114	56.4	43	33.6
	Mexico	541	772	1575	15	15	10	25	97.9	82.5	43.5
	New Zealand	-4336	1453	1644	26	4	3	39	244.1	139.3	122
	Nicaragua	-3459	-1471	-1061	10	9	9	12	546.9	386.8	341.2
	Papua New Guinea	113	308	1875	23	23	10	28	82.5	74	13.5
	Philippines	1162	1340	1400	11	11	10	16	77.1	60.9	61
	Russia	1620	1689	1810	26	25	20	118	15	12.8	10
	United States	-380	1350	1765	37	22	16	61	64.6	30	15.3

geological studies, such as Japan (Fig. 2.6b), have a more consistent increase in the number of documented eruptions, and several viable change point dates are visible¹. Our single change point model indicates that the most likely change point date for Japan is between 1541 and 1543, with the dominance and consistent recording of VEI 2 eruptions appearing to be the primary driver of the date. This is also a possible weakness in the single change point model, and a multiple change point model proposed by Furlan (2010) might better identify the multiple break points present in these cases.

2.5.2 Completeness for large eruptions

The posterior distributions for large eruptions (VEI ≥ 4) were generally much broader and had more complicated shapes when compared to VEI ≥ 0 . As an example, the percentiles of the change point for the Alaskan region are shown in Fig. 2.7a, however the shape of the change point posterior is bimodal, with peaks in the 16th and 18th centuries. The first peak corresponds to two VEI 4 eruptions being documented through radiocarbon dating and the second peak corresponds to the beginning of written historical records. Other regions, New Zealand to Fiji for example, and countries such as Mexico, also exhibit a strong correlation

¹The change point for USA coincides with the end of the American revolutionary war in 1784. While this may indicate a strong correlation to historical events, the change in recording is unlikely to be caused by this event as western states and Alaska were unmonitored and unexplored at this time. The likely cause of this date is modern geologic assessments ‘backfilling’ eruption histories. Thus, care needs to be taken when correlating eruption recording to historical/organisational/political changes.

between written records and data completeness, indicating that geological studies included in the VOTW catalogue are incomplete in these areas even for large events.

Historical records for the Japan, Taiwan and Marianas region (Fig. 2.7b) start from 680AD, and are supplemented by a large number of eruptions documented through other dating techniques. This results in a gradually increasing eruption record, with steps that could be related to either increases in activity or increases in recording and monitoring. As a result the calculated posterior distribution spans more than 2,000 years, expressing the large uncertainty in assigning a single date for regions such as this, and also suggesting a multiple change point model could be more appropriate in these circumstances. Countries with eruption histories dominated by geological records, such as Ecuador and Nicaragua (figures not shown), also have very broad posteriors causing larger uncertainty in recurrence interval estimates.

2.6 Discussion

Change point posteriors are strongly affected by the recording frequency of smaller eruptions. This was particularly noticeable when considering $\text{VEI} \geq 0$ eruptions where the change point dates in all instances correlated with an increase in the recording of eruptions with $\text{VEI} \leq 2$. The statistical model itself suggests this would be the case, with smaller eruptions having a very low probability of documentation, meaning that most $\text{VEI} \leq 2$ eruptions should occur after the change point (Fig. 2.4). These smaller eruptions are typically heavily related to the start of written historical records, with 78% of small eruptions being classified by the Global Volcanism Program (2013) as historical. These results suggest that the start of the historical eruption record appears to be a good indicator of data completeness, particularly when considering smaller eruptions in isolation. As Table 2.1 shows, the accumulation of VEI 0, 1 & 2 eruptions into a single composite category does not appear to have had an impact on the change point date. This is likely due to the dominance of VEI 2 records in the current catalogue, the large number of eruptions considered and the selection of a single change point model. In areas where VEI 0 or 1 eruptions are more frequent or if future VEI 0 and 1 eruptions are recorded more accurately, this accumulation may be less valid. A more complex presence function that better describes the decreased recording probability of VEI 0 and 1 eruptions or a multiple change point model may be more suitable in these areas, where both the increase in recording of VEI 2 eruptions (i.e. what is generally detected here) and the actual increase in VEI 0 and 1 eruptions needs to be considered.

Due to their higher frequency, smaller eruptions affect the change point more profoundly than large eruptions. This is because the lower frequency of large eruptions and more gradual improvement in the large VEI eruption record with time makes it more difficult to detect a systematic change in reporting. The gradual improvement in recording is likely due to larger eruptions being easier to distinguish in the geological record. Larger VEI eruptions have been

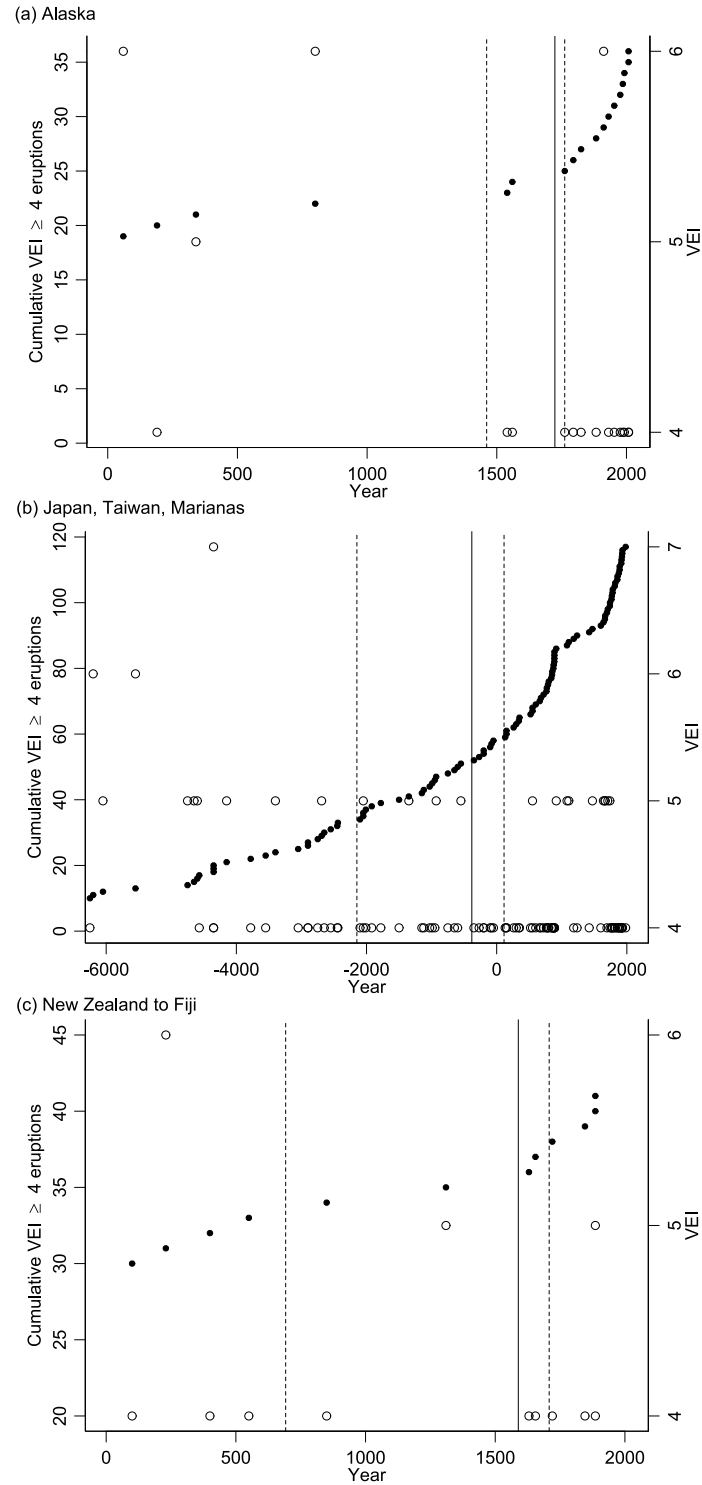


FIGURE 2.7: Cumulative number of $\text{VEI} \geq 4$ eruptions (filled points) and eruption magnitudes (hollow points) recorded for the regions of (a) Alaska, (b) Japan, Taiwan, Marianas and (c) New Zealand to Fiji displaying the 50th percentile (solid line), and the 5th and 95th percentiles (dotted lines) of the change point posterior. Note, x axis values vary for each case.

primarily dated through geological techniques, with only 32% present in historical records, of which most have been documented in the past 300 years. The difficulty in detecting change points in the large VEI eruption record generally results in a very broad posterior distribution, highlighting the uncertainty in estimating return intervals for large eruptions.

A key benefit of the method presented here is the ability to express uncertainty in the date of completeness, particularly for regions and countries with long geological records such as Japan, Ecuador, Nicaragua and Mexico. In these instances, the start of the historical record is not a reliable measure for determining completeness as the data is heavily supplemented by geological studies. This results in posterior distribution being considerably broader and sometimes multi-modal, which increases the uncertainty of recurrence interval estimates. While percentiles of the posterior distribution are used here to efficiently display the median and uncertainty for many regions with simple posterior distributions, this approach may not be suitable when dealing with multi-modal distributions displaying varying peaks (Fig. 2.4a, for example). It may be better in such cases to investigate or sample from the posterior directly, applying additional data analysis and expert inference to determine the ideal date of data completeness within the broad range identified. Multiple change point models such as the one suggested by Furlan (2010) could possibly decrease the uncertainty in these situations, albeit with increased complexity and subjectivity in determining which change point to use.

The presence function utilised here is limited by the assumption that there is a single, dramatic shift in the recording of volcanic eruptions for the subset of data being analysed. While this assumption appears valid for regions such as South East Asia and South America (and countries within), where the increase in recording is strongly correlated with exploration and colonisation, it may be less valid for countries which have extensive historical records augmented by detailed geological studies and dating. For these areas, the eruption record is generally characterised by a steadier improvement in recording throughout time. For countries and regions which exhibit these characteristics, presence functions that account for an increase in recording probability with time and eruption size, such as the 6 parameter model of Coles and Sparks (2006) or the multiple change point models demonstrated by Furlan (2010), may be more suitable. However, the usefulness of these approaches is limited by the choice of a single threshold date that is generally required to separate ‘well recorded’ and under recorded data. It is for this reason that a single change point model was chosen here; however, it could with additional analysis be possible to implement functions that take into account the steady increase in recording with time.

Variations in data completeness, and consequently estimated recurrence intervals, between regions, countries and different eruption sizes indicates that assessments of data completeness need to be undertaken at an appropriate scale, rather than globally. However, the accuracy and level of uncertainty in most statistical analyses (including Bayesian inference) are heavily dependent on the size and accuracy of the dataset. As a result, the change point dates may move as improvements are made to various catalogues, especially in respect to

improved geological records for large eruptions (for example, Table 2.2 suggests the large VEI eruption record for Africa and Red Sea is complete since the early Holocene, which may be proved incorrect with further geologic studies). The nature of the MCMC algorithm means that these change points can be recalculated easily for updated or new datasets or regions without subjectivity.

2.7 Conclusion

Markov Chain Monte Carlo simulation has been used to assess the completeness of the Smithsonian Institutions VOTW catalogue for all eruptions within approximately the past 10,000 years and independently for large eruptions (\geq VEI 4). These analyses were conducted on regional and, where enough data were available, country scales. Complete records of VEI ≥ 0 eruptions generally begin from the middle of the last millennium, but vary considerably between regions and countries due to social, population and political changes. As suggested by Siebert et al. (2010), the presence of volcanic eruptions in media and social discourse could also increase sensitivity to volcanic eruptions, leading to better recording of these events (e.g. the eruption of Krakatau in 1883). Results from the MCMC simulations appear to support this hypothesis, with countries such as Japan and Italy, which are commonly associated with volcanism and with long written histories, having longer complete records. When considering all eruption sizes, the change point is strongly correlated with an increase in recording of VEI eruptions less than or equal to 2. In most cases a sudden increase in documentation results in relatively high certainty in the change point date, causing more reliable estimates of the average recurrence interval.

The completeness of documented large eruptions ($\text{VEI} \geq 4$) occurs earlier than for eruptions of all sizes, which is to be expected given that large eruptions are easier to observe in geological records and more likely to be documented in historical accounts. The relatively low number of documented large events, due largely to long recurrence intervals, results in higher uncertainty in the calculated change point dates, which propagates into large differences in recurrence intervals between 5th and 95th percentiles. In instances such as these the nature and shape of the posterior distribution can be used to increase the certainty in eruption recurrence intervals. The multi-modal nature of some distributions suggests there may be a selection of candidate dates from which the data can be assumed to be complete, as opposed to a continuous distribution. The ability to explore the posterior distribution in order to increase understanding and uncertainty of the eruption record highlights the value of future approaches utilising Bayesian inference. Through using this MCMC approach, consistent, non-subjective change point dates and average recurrence intervals are identified, both with estimates of uncertainty.

Rain-triggered lahar susceptibility using a shallow landslide and surface erosion model

Stuart Mead, Christina Magill and James Hilton

Geomorphology

Volume 273, November 2016

doi: 10.1016/j.geomorph.2016.08.022

Abstract

Lahars are mass flows containing variable concentrations of water and volcanic debris that can cause catastrophic impacts to life, livelihoods and infrastructure downstream from their volcanic origin. Accurate and quantitative information on lahar hazards are essential for reducing the impact of these events. Lahar hazard assessments often focus on the use of numeric or empirical models to describe flow behaviour and inundation areas, which rely on historic lahar events and expert elicitation to define model inputs. This results in qualitative or semi-quantitative estimates of hazard that do not account for the mechanics of lahar initiation or, in the case of rain-triggered lahars, the dependence of rainfall intensity and duration on initiation. Here we develop a method for calculating rain-triggered lahar susceptibility, defined as the occurrence probability of a particular lahar initial volume at a specific location. The model relies on terrain and deposit characteristics and a probabilistic measure of rainfall in the form of rainfall intensity-frequency-duration relationships. Results for a case study of the October 28, 1995 lahar at Mangatoetoenui stream, Ruapehu Volcano, New Zealand, indicate lahar volume is controlled by a characteristic timescale, relating the deposit depth H to the hydraulic diffusivity D_0 in the ratio $\frac{H^2}{D_0}$. The timescale describes the transmission of positive pore pressures within the deposit, leading to shallow failure. As a consequence of this timescale, rainfall duration is the most important factor determining initial lahar sediment volume. Rainfall intensity plays a minor role, controlling the volume of water in the lahar mixture. This observation is consistent with power law relationships used to determine lahar triggering rainfall thresholds. The rain-triggered lahar susceptibility approach developed here

is anticipated to improve probabilistic lahar hazard assessments by providing quantitative, reproducible estimates of initial lahar volumes.

Keywords

lahar initiation · erosion · shallow landslide · susceptibility · hazard

3.1 Introduction

Lahars are a class of volcanic mass flows containing a mixture of water and volcanoclastic debris that form as a consequence of the presence of four controlling factors: (1) water; (2) easily entrained debris; (3) steep slopes and; (4) a triggering mechanism (Vallance, 2000). This definition of lahars encompasses a wide range of flow volumes and behaviours. For example, four categories of lahar (snow-slurry, large dilute lahars, smaller concentrated lahars and lahars generated from remobilised tephra) were observed during and immediately following the 1995 Ruapehu eruptive sequence (Cronin et al., 1997a). Syneruptive lahars are generated from overflow or expulsion of water following eruptions within the Crater Lake, while secondary lahars (i.e. lahars not caused directly from an eruption as defined in Blong (1984) and Vallance (2000)) result from the remobilisation of tephra triggered by snow-melt or heavy rainfall. The sediment concentration, flow behaviour, bulking (incorporation of sediment) and volume of these lahars vary depending on the triggering mechanism, debris availability and lithology, all of which can cause differing hazard outcomes. The interactions between and difficulty in quantifying these quasi-static spatial (e.g. terrain, material properties) and temporal (e.g. rainfall, snow depth, eruption frequency) controlling factors makes lahar hazard complex to determine.

Here we refer to hazard as a probabilistic measure expressing the likelihood of a specific event (e.g. lahar of a certain size and type at a specific location) occurring within a reference period. For hazard assessment, the reference period is typically a single year with hazard metrics (e.g. run-out, arrival time or velocity) expressed using an annual exceedance probability (AEP) (van Westen et al., 2006). This expression of hazard is commonly used in other volcanic hazard assessments (e.g. Bonadonna et al., 2005; Magill and Blong, 2005b; Jenkins et al., 2012b; Calder et al., 2015; Thompson et al., 2015), landslide hazard (e.g. Varnes, 1984; van Westen et al., 2006) and flood hazard (e.g. Merz et al., 2007). The complexity in quantifying mass flow hazards is not unique to lahars, landslide hazard and risk assessment also suffers from difficulties in the quantification and interaction between initiation mechanisms, flow types and environmental parameters. These issues are comprehensively discussed and analysed in the context of landslides by van Westen et al. (2006).

Qualitative, semi-quantitative and purely quantitative estimates of lahar hazard have previously been obtained through the use of three main inputs: environmental factors (e.g. terrain, material properties), triggering factors (e.g. rainfall, snow-melt, eruption) and historic records (Calder et al., 2015). Qualitative estimates of lahar hazard (e.g. Waitt et al., 1995; Wolfe and Pierson, 1995; Bacon et al., 1997; Sherrod et al., 1997; Hoblitt et al., 1998) are often conducted where limited information is available. These commonly utilise expert opinion to identify the origin and likely paths of lahar inundation based on historical and geological information. Inundation paths are typically assumed to follow drainage channels with lahar magnitude based on estimates of probable maximum volume. Since these estimates are subject to broad assumptions and rely on sparse historical data, there is considerable uncertainty in

the resulting hazard footprints. As a consequence of this uncertainty, the resultant qualitative hazard maps are most often used for communication or initial estimates of hazard.

Semi-quantitative methods that display a relative or indicative hazard are common as they strike a balance between accounting for uncertainty due to limited information and the need to provide some indication of probability. Carranza and Castro (2006) developed a method to determine distal lahar hazard given limited baseline information. A weight of evidence approach was used to determine distal lahar inundation zones at Pinatubo volcano prior to the 1991 eruption. The lahar source zone was estimated by an energy cone (H/L ratio) (Sheridan, 1979) and the distal lahar inundation zone was determined based on four factors: (1) proximity to the source zone, (2) proximity to a drainage line, (3) elevation, and (4) terrain gradient. Although these purely statistical methods are useful for predicting hazard zones with little historical or geological information, they have several drawbacks. For example, the mechanics of initiation are neglected, changes in environmental conditions are usually not accounted for, and an assumption that all events occur under the same conditions is made (van Westen et al., 2006), which is not entirely valid for lahars, as highlighted in Cronin et al. (1997a). Furthermore, causal relationships such as those outlined in Carranza and Castro (2006) are generalised and simplified to only consider metrics that are easily calculated on digital elevation models (van Westen et al., 2006; Frattini et al., 2009).

Non-statistical, semi-quantitative estimates are often elicited from outputs of computational lahar models (e.g. Scott et al., 1997; Scott et al., 2001; Aguilera et al., 2004; Robinson and Clynne, 2012; Amigo, 2013; Darnell et al., 2013; Thouret et al., 2013; Pistolesi et al., 2014). These lahar models range in complexity, from empirical solutions (e.g. Iverson et al., 1998; Pierson, 1998) and simplified numerical models (e.g. Fagents and Baloga, 2005), to more complex single-phase (e.g. O'Brien et al., 1993) or two fluid (e.g. Pitman and Le, 2005; Pudasaini, 2012; Iverson and George, 2014) two-dimensional models with the possibility to incorporate downstream sediment entrainment and deposition (e.g. Fagents and Baloga, 2006). As deterministic models, these methods have been used to describe the behaviour and outcomes of specific lahar events (e.g. Carrivick et al., 2010; Procter et al., 2010; Córdoba et al., 2015); however, probabilistic hazard assessment requires that these outcomes are attached to a recurrence probability. Several authors (Scott et al., 1997; Scott et al., 2001; Aguilera et al., 2004; Robinson and Clynne, 2012; Amigo, 2013; Thouret et al., 2013) determine this recurrence probability through providing probabilistic initial conditions of lahar volume and source location to the computational model. In all these cases, volumes were determined from geological and geomorphological evidence, previous historical events, observations of lahars at similar volcanoes and expert opinion. A qualitative estimate of probability (e.g. high to low or most likely to least likely) was then used when determining and mapping the hazard footprints from lahar models. However, these qualitative and semi-quantitative measures of hazard are relative indications only and can be open to interpretation by end users (Calder et al., 2015).

Typically, the previously discussed qualitative and semi-quantitative hazard estimates rely on geologic and historic records to prescribe lahar volume, type and frequency. This is an important limitation on hazard estimates as historic data is often incomplete (Coles and Sparks, 2006; Deligne et al., 2010; Mead and Magill, 2014) and can be irrelevant under different environmental conditions (e.g. land usage) or when topography changes (Volentik et al., 2009), which is often the case in volcanic settings. In order to provide a fully quantitative measure of lahar hazard, such as in the form of an AEP, the spatial and temporal probability of lahar initiation by size, type and location needs to be directly quantified in terms of the antecedent conditions. This spatial and temporal probability of initiation is termed susceptibility (van Westen et al., 2006). Here we define lahar susceptibility as the probability of a lahar with a specific initial volume of water and sediment occurring over a certain duration (annually) and area given a triggering mechanism. This definition encompasses both spatial and temporal probabilities, which can then be combined with lahar inundation models to determine the specific hazard.

Lahar susceptibility, or its contributing products of lahar initiation regions, types and volumes have previously been identified using deterministic methods. Frattini et al. (2004) used an infinite slope stability model to identify areas of instability in pyroclastic soils during the May 1998 landslide events in Sarno, Italy. Areas of instability identified by the model correlated well with landslide triggering times and areas. Volentik et al. (2009) identified potential rain-triggered lahar source regions through coupling a tephra fallout model to an infinite slope stability model and applying a tephra runoff relationship. Using the infinite slope stability approach, the total volume of tephra within the failure zone ($1.7 \times 10^7 \text{ m}^3$) was used to estimate run-out distance using the empirical relationship between volume and planimetric area of Iverson et al. (1998). A correlation between tephra thickness and decreased infiltration was used to estimate the volume of hyper-concentrated lahars based on the increased runoff. A similar infinite slope stability approach was used by Galderisi et al. (2013) to identify zones of instability following tephra fall at Vulcano Island. These zones of instability were used to guide the selection of potential initiation locations and volumes for subsequent lahar simulation. However, these approaches only identified the spatial component of lahar susceptibility by specifying initial lahar volumes and did not provide information on the temporal aspect of lahar susceptibility by specifying a likelihood or recurrence interval.

The temporal aspect of lahar susceptibility has been more extensively studied, particularly for rain-triggered lahars. Rainfall intensity and duration (I-D) thresholds for lahar initiation have been developed for various volcanoes through coupling lahar acoustic flow monitor (AFM) observations with rain gauge data (e.g. Tuñgol and Regalado, 1996; Lavigne et al., 2000; Lavigne and Thouret, 2003; Barclay et al., 2006; Capra et al., 2010; Jones et al., 2015). While rainfall intensity is a good indicator of rain-triggered lahar initiation, AFM data can only provide a semi-quantitative estimate of the magnitude and type of lahar if combined with direct observation (Jones et al., 2015). As these methods are based on recent

occurrences of lahars, they become less valid as environmental and terrain conditions change, as was the case at Pinatubo volcano where intensity-duration thresholds varied constantly as sediment was transported downstream (van Westen and Daag, 2005; Gran et al., 2011). Frattini et al. (2009) compared rainfall triggering thresholds calculated using physically based (deterministic) and statistical approaches. Statistical models were found to be effective on large datasets, requiring minimal inputs in comparison to the physically based approaches. Although the physically based approaches are sensitive to uncertainties in input data, Frattini et al. (2009) suggested these methods can be adapted to determine the degree of severity (i.e. susceptibility) through calculation of unstable area. The utility of identifying susceptible areas was demonstrated in Gomes et al. (2008), who determined debris flow hazard through a combination of a susceptibility model and an empirical model to determine subsequent inundation areas. Susceptible areas were identified using a shallow landslide model and were used as initiation points for the empirical flow model.

In this paper, we present a physically based approach for determining lahar susceptibility. Since the triggering mechanism is a key input into estimating lahar occurrence, size and type (Lecointre et al., 2004; Pistolesi et al., 2014), we have limited the triggering mechanism to rainfall to reduce complexity. A combined model of lahar initiation related to rainfall intensity and duration is developed from models of shallow landsliding and overland erosion. The occurrence probability of a particular rain-triggered lahar initial volume at a specific location is obtained by combining model outputs with rainfall intensity-frequency-duration (IFD) relationships. This measure of lahar susceptibility can later be applied to determine lahar hazard in combination with computational lahar models.

3.2 Generation of rain-triggered lahars

Rain-triggered secondary lahars (i.e. post-eruption or not occurring as a direct result of an eruption) are generated as a result of modified hydrology and rainfall in the proximal zone of a volcano. Explosive eruptions deposit large volumes of unconsolidated and easily remobilised material that can alter topography and hydrology of the catchment by smoothing topography, damaging vegetation, altering infiltration rates and changing hydraulic properties of streams (Pierson and Major, 2014). The magnitude and frequency of rain-triggered lahars in response to rainfall is controlled by this modified hydrology. The dependence of lahar initiation on rainfall intensity and duration is well established and this relationship has previously been used to define lahar initiation thresholds for specific volcanoes or catchments (e.g. Rodolfo and Arguden, 1991; Tuñgol and Regalado, 1996; Lavigne et al., 2000; Lavigne and Thouret, 2003; van Westen and Daag, 2005; Barclay et al., 2007; Jones et al., 2015). However, lahar initiation thresholds defined in terms of rainfall intensity/duration (I/D) do not provide guidance on lahar magnitude or type and do not consider additional factors such as deposit thickness, material properties (grain-size distribution, porosity, permeability), slope

or vegetation (Jones et al., 2015).

The model presented here estimates the initial volume of debris in a lahar in general terms based on rainfall, terrain and material properties. Since field measurements of material properties are often inexact and difficult to obtain, the model requires a compromise between simplicity, providing a complete description of the physics and data input requirements. This limits our approach to simplified models that describe the most important, but not all, physical processes that occur during lahar initiation. Two models of lahar initiation are used to describe the relationship between rainfall and lahar initial volume. These models describe erosion from overland flow and shallow landsliding, which are the most common lahar-triggering mechanisms (Pierson and Major, 2014). Less common phenomena than can increase runoff efficiency, such as surface crusting of tephra and increased hydrophobicity (e.g. Capra et al., 2010), are not explicitly simulated but can be accounted for in the form of decreased infiltration. We also do not consider the occurrence of deep rainfall induced landslides and flank collapse that usually form large, clay-rich, cohesive debris flows or lahars (Vallance and Scott, 1997; Scott et al., 2005; Fagents and Baloga, 2006). These events are usually not directly triggered by single rainfall episodes, rather resulting from long-term elevated rainfall (e.g. over a season), which increases the volume of pore-water in the material (Scott et al., 2005) and have more in common with traditional deep-seated slope stability processes.

3.2.1 Overland flow erosion model

Explosive eruptions alter vegetation, drainage networks and rainfall runoff relationships on volcanic slopes (Swanson and Major, 2005), often increasing the runoff efficiency, erosion rates and sediment yields (Yamakoshi et al., 2005; Manville et al., 2009; Pierson and Major, 2014). Erosion and sediment delivery from erosion is controlled by the complex interaction of several factors including tephra thickness (controls the time to expose substrate), slope (controls the erosive forces acting on the deposit), rainfall intensity (controls crust formation, rainfall detachment and depth of overland flow), antecedent conditions (controls level of saturation), and grain size and composition (controls permeability). The permeability of the tephra deposit controls the runoff response and development of overland flow. Coarse grained deposits often have a high permeability (Yamakoshi et al., 2005; Manville et al., 2009), while finer deposits have lower permeability that can significantly increase the efficiency of runoff processes (Collins and Dunne, 1986; Yamakoshi et al., 2005; Pierson and Major, 2014). Infiltration capacity can also be reduced by the development of a thin surface crust through raindrop compaction, wetting and drying cycles or blocking of pore spaces through ‘washing in’ of fine particles (Pierson and Major, 2014). The combination of easily eroded sediment and low permeability of fine tephra leads to rapid formation of rills and gullies which increase the efficiency of sediment transport (Collins and Dunne, 1986; Barclay et al., 2007; Pierson et al., 2013; Pierson and Major, 2014). Overland flow, sediment yield and

erosion rates also tend to reduce significantly over time as the fine ash layer is eroded to expose a higher permeability or erosion resistant substrate (Collins and Dunne, 1986; Major and Yamakoshi, 2005; Yamakoshi et al., 2005). Relationships between erosion and rainfall runoff or flow depth can be determined through experimental measurements, such as using ‘rainfall simulators’ (e.g. Leavesley et al., 1989; Daag, 2003), or plot specific measurements (e.g. Collins and Dunne, 1986). However, these relationships rely on site-specific data and measurements, which may not be available pre-eruption. Instead, here we use a simplified, physically based model to describe bedload transport that requires relatively few inputs, most of which can be obtained from current literature and refined to suit site-specific volcano and material properties.

Bedload sediment transport by overland flow is frequently modelled as a function of excess shear stress (e.g. Gilley et al., 1993; Montgomery et al., 1999; Hayes et al., 2002; Julian and Torres, 2006; Castro Díaz et al., 2008; Kean et al., 2013), given in the general form as:

$$q_b = k(\tau_* - \tau_{*c})^\lambda, \quad (3.1)$$

where q_b is the rate of bedload transport per unit width (m^2s^{-1}), k and λ can be constants or scalar functions of the flow, derived experimentally or empirically by several authors (see Castro Díaz et al. (2008) and Castro Díaz et al. (2009) for examples). The excess shear stress $(\tau_* - \tau_{*c})$ is expressed as the difference between the non-dimensional basal shear stress, τ_* and the non-dimensional critical shear stress required to initiate transport, τ_{*c} . Values of τ_{*c} can be obtained through observations, experimental measurements or experimentally derived relationships. The erosion of the sediment bed (h_s) is then governed by the conservation law, given by the Exner equation (Castro Díaz et al., 2008; Liu et al., 2008; Castro Díaz et al., 2009):

$$\frac{\partial h_s}{\partial t} + \frac{1}{1 - \phi} \left(\frac{\partial q_{bx}}{\partial x} + \frac{\partial q_{by}}{\partial y} \right) = 0, \quad (3.2)$$

where ϕ is the porosity of the bed, q_{bx} and q_{by} are the x and y components of bedload transport.

Using this general formulation, multiple bedload transport and critical shear relationships can be chosen as appropriate for the antecedent conditions. Three bedload transport relationships have been implemented; the relationship of Rickenmann (2001) used by Kean et al. (2013) in studies of runoff generated debris flows, the Grass model described in Castro Díaz et al. (2009) and the Meyer-Peter and Müller (MPM) model, also described in Castro Díaz et al. (2009) and used in Carrivick et al. (2010) for lahar simulations at Mt. Ruapehu Volcano, New Zealand. To demonstrate the applicability of the lahar calculation method we use the MPM bedload transport model, shown in Eq. 3.3 (Castro Díaz et al., 2009):

$$\frac{q_{bx,y}}{\sqrt{(\rho_s/\rho_f - 1)gD^3}} = 8 \frac{u}{\sqrt{u^2 + v^2}} \max(\tau_* - 0.047, 0)^{3/2}, \quad (3.3)$$

where D is the median grain diameter, g is gravity, ρ_s and ρ_f are the sediment and fluid

densities and u , v are velocities in the x and y directions. This relationship can easily be substituted with different bedload transport relationships if appropriate for the antecedent conditions. The equations for overland erosion are valid under the following assumptions:

- *Bedload transport only.* This erosion model considers bedload transport only and ignores the contribution of suspended particles to the total sediment load. Suspended sediment transport occurs when the fluid flux is high enough for bed particles to rise above the bed and remain in suspension through lift forces (Castro Díaz et al., 2008). These forces are unlikely to be present in the shallow overland flows that lead to lahar initiation in the upper reaches of a catchment.
- *Sediment does not affect lahar initiation flow.* Bedload transport is calculated from the shear exerted on the sediment bed by the overland flow. We choose to ignore the effects of bed transport and sediment concentration on the dynamics of the flow. High concentrations of sediment are likely to cause non-Newtonian aspects of the flow, typical in lahars, to become important. This model is therefore only suitable for modelling the pre-lahar sediment delivery by Newtonian flow. Lahar initiation points (described in the following section) must therefore be chosen with care to ensure that non-Newtonian effects of sediment load are insignificant.

3.2.2 Shallow landsliding model

Shallow, rain-induced sliding of material on steep slopes can often fluidise into mobile debris flows (Campbell, 1975; Rodolfo and Arguden, 1991; Hungr et al., 2001). These shallow landslides, also called soil slips or translational sliding, have been observed or proposed as a lahar initiation mechanism in many volcanic regions (e.g. Pierson et al., 1996; Hodgson and Manville, 1999; Pareschi et al., 2000; Capra et al., 2003; Miyabuchi and Daimaru, 2004; Swanson and Major, 2005). Shallow landsliding typically requires saturation of the deposit causing positive pore-water pressures that initiate Coulomb failure (Reid et al., 1988; Johnson and Sitar, 1990; Reid, 1994; Iverson et al., 1997). Unsaturated shallow failure can also occur due to increased soil weight or reductions in soil failure, however this phenomena is less common (Iverson et al., 1997). Saturation and positive pore-water pressures usually develop when water concentrates above discontinuities in permeability (Campbell, 1975; Reid et al., 1988; Iverson et al., 1997). These discontinuities are often present in volcanic settings where layers of relatively porous pyroclastic material sit above impervious or nearly impervious layers of fine ash, colluvial material or bedrock (e.g. Hodgson and Manville, 1999; Pareschi et al., 2000; Crosta and Dal Negro, 2003; Frattini et al., 2004; Zanchetta et al., 2004; Ferrucci et al., 2005). Failures often originate on steep slopes at the head of drainage basins (Pareschi et al., 2000; Crosta and Dal Negro, 2003; Frattini et al., 2004) where a small increase in pore-water pressure can overcome the deposit shear strength and trigger widespread failure (Hodgson and Manville, 1999; Manville et al., 2000). Predictions

of shallow failure and pore pressure response to rainfall infiltration often simplify the data requirements and non-linearity of the process into one-dimensional infinite slope stability models (Johnson and Sitar, 1990; Reid, 1994; Iverson et al., 1997; Iverson, 2000). These models simplify the topographic conditions to an infinitely long slope with the slip surface assumed to form parallel to the ground surface (Johnson and Sitar, 1990). This assumption is generally valid for shallow landslides where failure depth is minimal compared to the failure width (Frattoni et al., 2009). Here we use a model developed by Iverson (2000) to predict the depth of rain-triggered shallow landslides using an infinite-slope failure criterion and reduced form of the Richards equation. Several simplifications and approximations were made to reduce data requirements and complexity of the Richards equation; for complete details and justification, refer to Iverson et al. (1997) and Iverson (2000). Shallow failure is assumed to occur when the gravitational forces balance with the resisting Coulomb stresses. This criterion is represented by the dimensionless factor of safety (FS):

$$FS = F_f + F_w + F_c, \quad (3.4)$$

where F_f , F_w and F_c are the frictional, groundwater and cohesive factors of safety which are expressed as:

$$F_f = \frac{\tan \varphi}{\tan \alpha}, \quad (3.5)$$

$$F_w = -\frac{\psi(Z, t)\gamma_w \tan \varphi}{\gamma_s Z \sin \alpha \cos \alpha}, \quad (3.6)$$

$$F_c = \frac{c}{\gamma_s Z \sin \alpha \cos \alpha}, \quad (3.7)$$

where φ is the friction angle, α slope angle, ψ pore-pressure, c cohesion, t time and γ_s and γ_w the unit weights of soil and groundwater respectively. Failure occurs at time t when the factor of safety is equal to or less than 1 and a vertical depth Z . Groundwater pressure effects (F_w) vary as a function of depth and time, which can be split into steady (F_{w0}) and unsteady (F'_w) components:

$$F_{w0}(Z) = \frac{\phi_0(Z)\gamma_w \tan \varphi}{\gamma_s Z \sin \alpha \cos \alpha}, \quad (3.8)$$

$$F'_w(Z, t) = -\frac{\frac{\gamma_w}{\gamma_s} \tan \varphi}{\sin \alpha \cos \alpha} \frac{I_z}{K_z} \cdot \begin{cases} R(t^*) & t^* \leq T^* \\ R(t^*) - R(t^* - T^*) & t^* > T^* \end{cases}, \quad (3.9)$$

where I_z is the rainfall intensity (m/s), t^* and T^* are the rainfall duration and elapsed times, which are normalised values of the rainfall duration, T , and elapsed time, t calculated as:

$$t^* = \frac{t}{Z^2/\hat{D}}, \quad (3.10)$$

$$T^* = \frac{T}{Z^2/\hat{D}}, \quad (3.11)$$

where the effective hydraulic diffusivity \hat{D} is related to the characteristic hydraulic diffusivity D_0 by $\hat{D} = 4D_0 \cos^2 \alpha$. The response function:

$$R(t^*) = \sqrt{\left(\frac{t^*}{\pi}\right)} \exp\left(-\frac{1}{t^*}\right) - \operatorname{erfc}\left(\frac{1}{\sqrt{t^*}}\right) \quad (3.12)$$

describes the downwards propagation of pore-pressure, which is a primary control on the timing and depth of shallow failures in response to rainfall (Iverson, 2000).

This simplified model is valid under the following assumptions:

- *No lateral transmission of groundwater and pore pressure.* The groundwater pressure term (F_w) only considers vertical rainfall infiltration (Iz/Kz) and transmission of pore pressure through the response function. Therefore, vertical diffusion and infiltration timescales must be much shorter and more significant than lateral transmission timescales. This limits study areas to those with much smaller landslide thickness relative to area (Z/\sqrt{A}) and a triggering-rainfall duration shorter than the time required for lateral pore pressure transmission (Tsai and Yang, 2006).
- *Constant rates of infiltration and diffusion.* The model assumes that infiltration and pressure diffusion rates do not change over time. This requires the soil to be saturated or near saturation, which can limit the application to scenarios where prolonged rainfall (e.g. over a rainy season) ensures soil saturation and intense storms trigger the shallow failure (Fiorillo and Wilson, 2004). More advanced models (e.g. Tsai and Yang, 2006; Baum et al., 2010) are able to predict the response to transient infiltration and diffusion rates; However, here we favour the Iverson (2000) model for its simplicity and lower data requirements

3.2.3 Calculating lahar susceptibility

The shallow landslide and erosion models are able to estimate the spatial component of lahar susceptibility (location and volume of mobilised volcanic sediment) in response to rainfall of a certain intensity and duration. The temporal component of susceptibility, which prescribes the probability of a lahar-triggering event, is derived from rainfall intensity-frequency-duration (IFD) relationships.

The relationship between rainfall intensity, duration and frequency is generally expressed in the form of a rainfall intensity-frequency-duration (IFD) relationship. This is a mathematical relationship that provides the probability of rain with a specific intensity (mm/hr) falling over a continuous duration of time. As rainfall in the IFD relationship is assumed to be constant throughout the duration, the normalised infiltration rate (Iz/Kz) and volume of rainfall runoff over a catchment area can be provided to the model expressed in the form of an AEP.

The height and motion of infiltration excess overland flow is calculated using a depth-averaged shallow water (SW) approximation. The two-dimensional shallow water equations are solved using a ‘well-balanced’ finite volume SW method given by Kurganov and Petrova (2007). Our specific implementation is detailed in section 3.6, taken from Cohen et al. (2015), and utilises graphics processing units (GPUs) to increase the speed of the simulations. The bed sediment transport and mass balance is calculated using a bedload transport module attached to the shallow water solution. The height and depth-averaged velocities of the shallow water solution after each timestep are used to calculate the shear stress and bedload transport rate (Eq. 3.3). Erosion of the sediment bed is calculated from the Exner conservation equation (Eq. 3.2) using a central finite difference method. The depth of failure due to shallow landsliding (if any occurs) is then calculated at the end of the rainfall duration through Eqs. 3.5 to 3.12.

The total upstream volume of mobilised volcanic sediment from overland erosion and shallow landsliding can be calculated at specific points. The choice of these points is critical to ensure physics of lahar initiation and flow are adequately captured, and should be sufficiently close to the source material areas to ensure that non-Newtonian fluid effects are negligible. Inherent to this calculation is the assumption that the two initiation models are compatible. In this application the models are applied sequentially, ensuring that timescale similarity is less of an issue as the models are run independently of each other. We presume that each models processes are independent of the other as surface flow conditions do not greatly affect subsurface infiltration (and vice versa). This assumption is adequate for reasonable deposit depths, however it may make the model unsuitable for determining mobilisation of very thin tephra layers.

3.3 Controls on rain-triggered lahar initiation volume

3.3.1 Case study: The October 28, 1995 lahar, Mangatoetoe Stream, Ruapehu Volcano, New Zealand

To demonstrate the applicability of the lahar susceptibility model and investigate the effect of model parameters on mobilised volume estimates, we present a case study similar to the October 28, 1995 lahar that occurred in Mangatoetoe Stream, Ruapehu Volcano. This lahar was chosen due to the relative availability of data and observations of initiation and lahar behaviour. The October 28 Mangatoetoe Stream lahar and volcanic activity of Ruapehu volcano are described in Hodgson and Manville (1999) and Manville et al. (2000), the details relevant for this study are summarised as:

- Eruptions in September 1995 deposited a thin layer of fine-grained, cohesive ash on the eastern side of the volcano.
- Subsequent eruptions on October 11, 12 and 14 deposited up to 0.8 m of coarse ash and lapilli on the slopes above the September deposits. The September deposits were

largely frozen and impermeable.

- Lahars were triggered by heavy rainfall on October 28 in several catchments, including Mangatoetoenui. The nearest rainfall station indicated 23 mm of rain fell in 24 hours, with 9 mm falling in one 6 hour interval. Rainfall data presented in Manville et al. (2000) indicates that all 23 mm of rain fell within 18 hours. The rainfall is expected to have been heavier closer to the volcano.
- The source material for the Mangatoetoenui lahar came from the Mangatoetoenui glacier. The coarse October deposits were removed, while the fine September ashfall deposits remained frozen. This suggests that mobilisation was initiated by shallow landsliding on the frozen ash layer.
- Mobilised material travelled down the north and south branches of the Mangatoetoenui stream, converged at the junction and continued downstream as a debris flow.
- The volume of material mobilised from the Mangatoetoenui glacier was approximately $3.3 \times 10^5 \text{ m}^3$.

While the October 28 lahar is relatively well documented; terrain, material and rainfall properties prior to the event are unknown or too uncertain to comprehensively validate the susceptibility model. Instead, we present two scenarios with initial conditions similar to those reported for the lahar. The results of these scenarios yield similar estimates for the volume of material mobilised and determine the feasibility of the lahar susceptibility model.

3.3.2 Estimation of simulation parameters and initial conditions

A high resolution, accurate digital elevation model (DEM) is critical to the accurate estimation of lahar susceptibility, as terrain slope controls both the overland erosion and shallow landsliding models. A DEM of Ruapehu volcano with a cell resolution of 8 metres was obtained from the Geographx New Zealand Digital Elevation Model version 2.1 (Geographx, 2012). The model was primarily derived from January 2012 Land Information New Zealand (LINZ) 1:50,000 topographic contours with a vertical accuracy of $\pm 10 \text{ m}$ and horizontal accuracy of $\pm 20 \text{ m}$. This DEM (shown in Fig. 3.1a) was chosen for its high spatial resolution; however, it is likely that volcanic and glacial processes have changed the terrain since 1995. We assume the 2012 DEM is not significantly different for the purposes of this study from the conditions before the October 28 1995 lahar, although the data cannot be directly compared due to the lack of high resolution data from 1995. Hodgson and Manville (1999) reported that 23 mm of rain fell within a 24 hour period on October 28, with 9 mm falling in one 6 hour period. This rainfall was recorded at a gauge 26 km west of Ruapehu and was expected to be heavier on the volcano. Additional rainfall data in Manville et al. (2000) suggests that 23 mm fell within an 18 hour period. For simplicity, we assume the recorded rainfall represents the rainfall over the Mangatoetoenui catchment and simulate two rainfall scenarios: a lower intensity event with 1.3 mm/hr of rainfall over 18 hours and a higher intensity event with 1.5

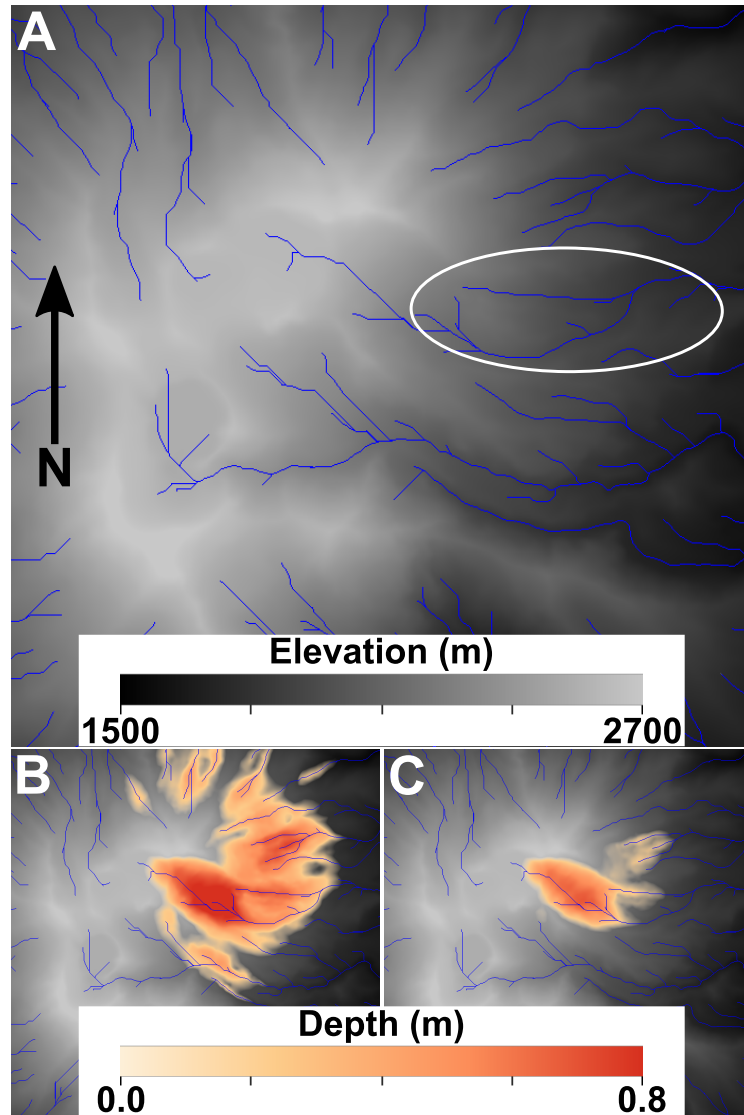


FIGURE 3.1: (a) Digital elevation model and streamlines of Ruapehu volcano. The North and South branches of Mangatoetoenui Stream are circled. Upper and lower estimates of deposit depths are shown in (b) and (c).

mm/hr of rainfall over 6 hours.

The hydraulic properties and depth of the ash deposits from the October 11-14 eruptions are unknown. We assume the deposit sits above a completely impermeable layer of frozen fine ash, consistent with observations. The distribution of deposit depth was estimated by creating two representative deposits with depth proportional to an energy cone centred above the Mangatoetoenui glacier and scaled so that the maximum depth was 0.8 m, which is the maximum depth reported in Hodgson and Manville (1999). The deposit depth estimates are shown in Fig. 3.1b and 3.1c. Both deposits have a maximum depth of 0.8 m on the Mangatoetoenui glacier, with the depth of material in the North and South branches of Mangatoetoenui stream having differing deposit depths. The total volume of material upstream of the North and South Mangatoetoenui confluence is $8.42 \times 10^5 \text{ m}^3$ for the larger estimate (Fig. 3.1b) and

TABLE 3.1: Range of hydraulic diffusivities used in lahar susceptibility simulations based on the characteristic timescale H^2/D_0 .

H^2/D_0	D_0 (m^2s^{-1})
30 minutes	3.55×10^{-4}
1 hour	1.78×10^{-4}
6 hours	2.96×10^{-5}
18 hours	9.88×10^{-6}

$5.26 \times 10^5 \text{ m}^3$ for the lower estimate (Fig. 3.1c). All lahar initiation volumes were calculated at the confluence, therefore materials outside of the Mangatoetoenui catchment are not considered in this study. As artificially created depth estimates, these deposits do not consider the material loss and rilling from the 19-21 October lahars; rather they represent a plausible range of ash volumes on the Mangatoetoenui glacier in order to create a scenario similar to the one just prior to the October 28 lahar.

Hydraulic diffusivity is the ratio between permeability (K) and specific storage (S_s) which controls the transmission of pore pressure through the material. Measurements of hydraulic diffusivity or the specific storage component are rare, vary according to the size and shape of pores within the ash deposit and therefore cannot be applied easily from different study areas. Here, hydraulic diffusivity was estimated from the characteristic timescale H^2/D_0 , which describes the approximate time necessary for pore pressure transmission from the surface to the depth H (Iverson, 2000). Given there was little rainfall in the preceding 5 days before the October 28 lahar (Manville et al., 2000), we presume failure was triggered by relatively rapid transmissions of pore pressure rather than gradual increases of pore pressure from accumulation above the water table. The latter style of landsliding relies on an accumulation of rainfall over a period of time and favours deeper landslides (cf. Iverson, 2000). The transient pore pressure response time is therefore between 0 and 18 hours, which we use to estimate a range of hydraulic diffusivities (Table 3.1). Hydraulic conductivity (permeability) for the lahar source area is similarly difficult to establish. Infiltration rates vary with grain size of tephra deposits, and can be as low as 1 mm/hr ($2.77 \times 10^{-7} \text{ m/s}$) for fine ash and up to 100 mm/hr ($2.77 \times 10^{-5} \text{ m/s}$) for coarse ash deposits (Pierson and Major, 2014). Given the relative coarseness of the ash ($\sim 1 \text{ mm}$ in diameter) (Hodgson and Manville, 1999), rainfall excess overland flow should be minimal in source areas. This is reinforced by observations of Hodgson and Manville (1999) who identified shallow landsliding as the primary lahar initiation mechanism. We therefore set the hydraulic conductivity to 1.0 mm/hr, resulting in a rainfall excess of between 0.3 and 0.5 mm/hr.

The Meyer-Peter and Müller model (Eq. 3.3) was used to calculate bedload erosion and transport. This model has been previously used to study bedload transport processes on Ruapehu (Carrivick et al., 2010). Median grain diameter was assumed to be 1 mm based on the measurements of Hodgson and Manville (1999), and the tephra density was set to $2,400 \text{ kg}\cdot\text{m}^{-3}$ (Carrivick et al., 2010). The Mannings friction factor for the shallow water simulations

TABLE 3.2: Failed shallow landslide material volume estimates (in m^3) for 18 and 6 hour rainfall scenarios with varying diffusivities and infiltration rate I_z of 1.0 mm/hr.

H^2/D_0	D_0	18 hr (1.3 mm/hr)		6 hr (1.5 mm/hr)	
		Upper	Lower	Upper	Lower
30 min	3.55×10^{-4}	4.55×10^5	2.84×10^5	4.55×10^5	2.84×10^5
1 hour	1.78×10^{-4}	4.55×10^5	2.84×10^5	4.55×10^5	2.84×10^5
6 hours	2.96×10^{-5}	4.55×10^5	2.84×10^5	3.38×10^5	2.58×10^5
18 hours	9.88×10^{-6}	3.38×10^5	2.58×10^5	0.96×10^5	0.72×10^5

was 0.025, which is expected in un-vegetated streams and channels (Chow, 1959). Porosity of the tephra was undefined in Hodgson and Manville (1999), therefore we assume a porosity of 0.4 which is within the range of porosity estimates for debris flow source deposits in Zanchetta et al. (2004).

3.3.3 Effect of hydraulic diffusivity on shallow landsliding mobilised volume

Shallow landslides in the thin and sandy (more permeable) deposits typically found on post-eruption volcanic slopes are initiated from the development of positive pore pressures in response to rainfall (Iverson, 2000). This means that, provided rainfall is falling at an intensity close to the hydraulic conductivity of the soil, the pore pressure transmission timescale H^2/D_0 is the most important control on the volume of mobilised material. Failure volume estimates for the Mangatoetoe catchment calculated using the shallow landsliding model (Table 3.2) demonstrate the importance of hydraulic diffusivity and the characteristic transmission timescale. For both the 18 and 6 hour rainfall scenarios, mobilised volume estimates for pore pressure transmission timescales less than the rainfall duration are $4.55 \times 10^5 \text{ m}^3$ for the larger deposit and $2.84 \times 10^5 \text{ m}^3$ for the smaller deposit. The hydraulic diffusivity in these cases is high enough to allow positive pore pressures to transmit through the entire deposit depth (up to 0.8 m) and initiate failure. The volume estimates only differ when the transmission timescale is equal or greater than the rainfall period (i.e. 18 hours for the 18 hour rainfall scenario and 6 to 18 hours for the 6 hour rainfall scenario), as positive pore pressures are not sufficiently developed in the deepest areas of the deposit to trigger failure.

3.3.4 Effect of infiltration rate on overland erosion

The infiltration rate controls the volume of excess overland flow, which in turn controls the rate of erosion of the deposit. Table 3.3 shows estimates of the volume of material eroded for both rainfall scenarios at infiltration rates varying from 0 mm/hr (impermeable) to 1 mm/hr. The eroded volume increases as the infiltration rate approaches 0, which is expected as the volume of rainfall runoff is larger. More material is also eroded for the larger volume deposit

TABLE 3.3: Overland erosion material volume estimates (in m^3) for 18 and 6 hour rainfall scenarios at varying infiltration rates.

Infiltration rate (mm/hr)	18 hr (1.3 mm/hr)		6 hr (1.5 mm/hr)	
	Upper	Lower	Upper	Lower
0.00	6.45×10^4	4.54×10^4	5.46×10^4	3.80×10^4
0.25	6.03×10^4	4.24×10^4	5.00×10^4	3.49×10^4
0.50	5.35×10^4	3.76×10^4	4.58×10^4	3.18×10^4
0.75	4.65×10^4	3.24×10^4	4.01×10^4	2.80×10^4
1.00	3.93×10^4	2.70×10^4	3.42×10^4	2.35×10^4

as the availability of erodible material is higher. For all scenarios and deposit estimates the eroded volume is between $2.35 \times 10^4 \text{ m}^3$ and $6.45 \times 10^4 \text{ m}^3$, which is an order of magnitude less than the estimate of mobilised material ($\sim 3.3 \times 10^5 \text{ m}^3$) from Hodgson and Manville (1999). Although there is considerable uncertainty in the initial conditions provided to the lahar initiation model, these results indicate that overland erosion alone cannot have mobilised enough material to create a lahar with the volume of the October 28 event, even in the most extreme case of an impermeable deposit. This is consistent with the observations that the primary initiation mechanism of the October 28 lahar was shallow landsliding (Hodgson and Manville, 1999).

3.3.5 Estimates of total mobilised volume

As described earlier, the total mobilised volume is the sum of material eroded through overland erosion and material mobilised through shallow landsliding of the post-erosion deposit. The combined material volume estimates, shown in Table 3.4, range from $0.86 \times 10^5 \text{ m}^3$ to $4.59 \times 10^5 \text{ m}^3$. These estimates are different from the sum of shallow landslide and eroded volume estimates (Tables 3.2, 3.3) as overland erosion also alters the depth and slope of the deposit, which affects stability of the deposit. The characteristic pore pressure transmission timescale (H^2/D_0) is still the primary control on mobilised volume and reflects the dominance of shallow landsliding in the October 28 Mangatoetenui lahar. A similar volume of material to the Mangatoetenui lahar was mobilised in the larger deposit for 18 and 6 hour rainfall scenarios with a characteristic timescale equal to the rainfall period. For the smaller deposit, the estimated volume is within 15% of the Mangatoetenui lahar volumes for characteristic timescales between 30 minutes and 6 hours for the 18 hour rainfall scenario, and characteristic timescales of 30 minutes and 1 hour for the 6 hour rainfall scenario. While there are considerable uncertainties in model inputs as well as field estimates of the Mangatoetenui lahar source volume, the similarity between the model results and estimates of Hodgson and Manville (1999) suggests that the model proposed here captures the primary physical mechanisms of rain-triggered lahar initiation. The dominance of shallow landsliding and mobilisation of the deposit at the frozen ash layer, which forms a permeability barrier,

TABLE 3.4: Combined overland erosion and shallow landslide material volume estimates (in m^3) for 18 and 6 hour rainfall scenarios with an infiltration rate of 1 mm/hr.

H^2/D_0	D_0	18 hr (1.3 mm/hr)		6 hr (1.5 mm/hr)	
		Upper	Lower	Upper	Lower
30 min	3.55×10^{-4}	4.59×10^5	2.87×10^5	4.58×10^5	2.86×10^5
1 hour	1.78×10^{-4}	4.59×10^5	2.87×10^5	4.58×10^5	2.86×10^5
6 hours	2.96×10^{-5}	4.59×10^5	2.87×10^5	3.30×10^5	2.50×10^5
18 hours	9.88×10^{-6}	3.33×10^5	2.51×10^5	1.16×10^5	0.86×10^5

also agrees with the observations of the lahar source areas. Disparity in volume estimates between the model and literature indicate that initial deposit depth in the Mangatoetoeui catchment is likely to be between the upper and lower deposit depths used in the model, with a hydraulic diffusivity of less than $2.96 \times 10^5 \text{ m}^2\text{s}^{-1}$ (corresponding to a characteristic timescale of less than 6 hours).

3.3.6 Susceptibility of the Mangatoetoeui Stream to rain-triggered lahars

The lahar initiation model described and demonstrated in the previous sections can be used to calculate the rain-triggered lahar susceptibility. A probability can be assigned to mobilised lahar volumes through the use of probabilistic rainfall intensities obtained from rainfall IFD tables. Figure 3.2 displays the annual recurrence intervals (ARI) of mobilised sediment volumes for Mangatoetoeui stream. Volumes were calculated at rainfall intensities with a recurrence interval of 2, 10, 50 and 100 years and for rainfall durations of 30 minutes, 2 hours, 6 hours, 12 hours and 24 hours. The smaller deposit depth estimation (Fig. 3.1c) was used and hydraulic diffusivity was set at $2.96 \times 10^5 \text{ m}^2\text{s}^{-1}$ ($H^2/D_0 = 6$ hours). Rainfall IFD tables were obtained from version 3 of the New Zealand National Institute of Water and Atmospheric Research (NIWA) high intensity rainfall design system (NIWA, 2016). Mobilised volume estimates (Fig. 3.2) show rainfall duration has a large effect on sediment volume and demonstrate the effect of the pore pressure transmission timescale H^2/D_0 . Erosion is the primary mechanism of lahar initiation when rainfall duration is less than H^2/D_0 , this is reflected in the relatively low mobilised volumes and increase in eroded volume as rainfall intensity increases for rainfall durations of 30 minutes and 2 hours. At longer rainfall durations, positive pore pressures are able to develop in deeper areas of the deposit, resulting in more material being mobilised through shallow landsliding. The mobilised volume converges at rainfall durations much greater than H^2/D_0 (e.g. 12 and 24 hours in Fig. 3.2) since most of the deposit is unstable and the effect of erosion is negligible in comparison to failure depths.

While mobilised volumes are similar across all ARIs, there is a large difference in the relative proportion of sediment. For example, in a 12 hour rainfall event, rainfall intensity

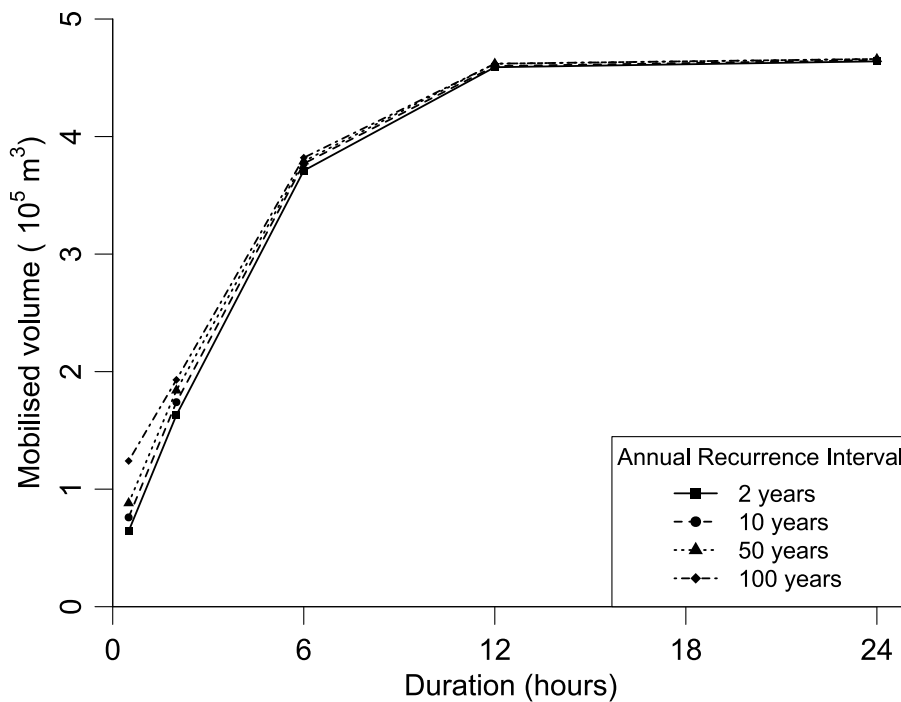


FIGURE 3.2: Mobilised deposit volumes for varying rainfall durations at the Mangatoetoenui stream with annual recurrence intervals of 2, 10, 50 and 100 years.

with an ARI of 2 years mobilises 3,451 m³ of sediment per mm of rainfall, but only 1,624 m³ of sediment per mm of rainfall is mobilised for a 100-year rainfall intensity. Larger rainfall intensity ARIs result in greater volumes of rainfall and effectively decreases the initial sediment concentration of the lahar. This is likely to result in different flow behaviours for the lahar and indicates that rainfall intensity, for a given duration, will control the initial size (i.e. volume of sediment and water) and type of lahar (e.g. hyper-concentrated flow or debris flow) generated during the rain event in the system considered here.

3.4 Applicability to probabilistic lahar hazard assessment

Lahars are a hazard of widespread concern as they pose a significant threat to life, infrastructure and livelihoods (Pierson et al., 2014; Calder et al., 2015). However, determining the probability of lahar hazards is complicated by the uniqueness in environmental and triggering factors for lahar events, resulting in quantitative lahar hazard analyses that are often lacking in comparison to other volcanic hazards such as tephra fall (Calder et al., 2015). The method presented here is able to elicit lahar susceptibility in a quantitative and reproducible manner and could be used to provide inputs to computational lahar models (e.g. those of Iverson et al., 1998; Pitman and Le, 2005) to create probabilistic hazard footprints. This combination of lahar susceptibility and lahar run-out models would be able to provide purely quantitative probabilistic lahar hazard estimates and has the potential to improve probabilistic lahar hazard

assessment.

However, while data requirements of the lahar susceptibility model have been minimised as much as possible, a considerable amount of data is still required for a given study area. As with most models of lahar processes, this susceptibility model requires an accurate, current and high-resolution digital elevation model to reduce uncertainty and increase the accuracy of terrain slope estimation. Advances in remote sensing technology (e.g. satellite altimetry) is expected to increase the availability of such terrain models in the future. In the event of a volcanic eruption, a second, post-eruption digital elevation model would ideally be required to determine the depth of volcanic deposits that may erode or landslide away. While isopach maps generated in the aftermath of an eruption can provide an estimation of thickness on the ground, these are often unsuitable for detailed modelling of lahar triggering areas close to the vent. These thickness measurements, which can be obtained either through ash dispersion modelling or physical measurements, do not consider the effect of topography of the ash sedimentation process and assume an equal thickness deposition across all slopes. This neglects the smoothing of topography that occurs following explosive eruptions (Pierson and Major, 2014), where thicker deposits rest in topographic lows (Engwell et al., 2013). Provided topographic effects are accounted for, isopach map estimates could be substituted for post-eruption elevation models. This would be useful in forecasting lahar hazards and understanding the cascading and multi-hazard effects of explosive eruptions. Rainfall intensity-frequency-duration thresholds are also required to attach a probability to lahar initiation volumes. While this data is readily available in developed countries and at well-monitored volcanoes, rainfall IFD relationships may be difficult to obtain for more remote volcanoes or in less developed regions.

Deposit material properties, such as friction angle, grain size, cohesion, density and permeability are also required to calculate the factor of safety in the shallow landslide model and rainfall runoff and erosion rates in the erosion model. These properties are easily measured, well reported in the literature, and tend to have a minimal effect on the volume of mobilised material. Where these parameters are unknown, such as permeability in the Mangatoetoenui case study, the uncertainty can be incorporated into susceptibility estimates through stochastic modelling.

Hydraulic diffusivity can be more difficult to measure and, as a consequence, is reported less in the literature. However, results here have demonstrated the importance of hydraulic diffusivity is in the effect it has on the pore pressure diffusion timescale H^2/D_0 , which relates depth to diffusivity. It may be possible to broadly determine the diffusivity through estimating the specific storage of a deposit, or through observations of lahar triggering rainfall intensity and duration. As rainfall duration, and not intensity, is the primary control of shallow landsliding, the pore pressure diffusion time is likely to be at the point in intensity-duration thresholds (e.g. Jones et al., 2015), where rainfall intensity plays a negligible role in comparison to duration. The hydraulic diffusivity can then be determined from the pore

pressure diffusion time and median deposit depth.

3.5 Conclusion

Lahar hazard assessments often rely on qualitative or semi-quantitative estimates of lahar initial volumes that are based on the historic record, which is often unreliable, or expert judgement and elicitation, which is unreproducible. As an alternative, the lahar susceptibility model presented here is able to quantitatively express the location, volume and probability of rain-triggered lahar initial volumes through an approach based on the mechanics of initiation. Although data requirements are relatively high, the susceptibility model can provide insight into lahar initiation processes, even with crude estimations of input parameters as demonstrated by the October 28 Mangatoetoeenui lahar case study.

In the Mangatoetoeenui case study the relative importance of the primary initiation mechanisms appears to be controlled by the time it takes for positive pore pressures to develop in the deposit following rainfall. This is expressed as the characteristic pore pressure transmission time H^2/D_0 , relating deposit depth (H) to the hydraulic diffusivity (D_0). If the rainfall duration is less than H^2/D_0 , erosion dominates the lahar sediment delivery mechanism and rainfall intensity controls the initial volume of volcanic material. Shallow landsliding plays an increasing role in the mobilisation of sediment as the rainfall duration increases, which is a consequence of positive pore pressures being developed at deeper depths in the deposit. Lahar susceptibility estimations for the Mangatoetoeenui stream on Ruapehu Volcano, New Zealand, indicate that mobilised volumes of sediment do not change to a large degree as the annual exceedance probability decreases. However, the total volume of the lahar (i.e. including water) will increase, and the difference in sediment concentration is likely to result in different lahar behaviours. Overall, the case study indicates that rainfall intensity has a rapidly diminishing effect on initial lahar volumes as the rainfall duration increases, with the rainfall probability playing a role in determining the relative concentration of sediment, and consequently type, of lahar. This conclusion is consistent with the power-law relationships used in intensity-duration analysis of lahar triggering.

Results of the rain-triggered lahar susceptibility model are consistent with general observations of lahar initiation as well as the specific observations and volume estimates provided in the Mangatoetoeenui case study. However, validation of the susceptibility model is limited by scarcity of input data and information on the lahar source zones. Further research and measurement of processes within the lahar source zone is needed in order to completely characterise lahar hazard. The need for accountable, defensible and quantitative probabilistic lahar hazard assessments is clear, with the lack of reliable, probabilistic inputs forming an important barrier to this goal (Calder et al., 2015). The lahar susceptibility model presented here, while needing deeper investigation, is capable of alleviating some of these issues and, with further research, can be used to develop a greater understanding on lahar initiation

processes.

3.6 Appendix: Shallow-water hydrodynamics model

The depth-averaged equations of motion used in the shallow-water hydrodynamics application here is taken from Kurganov and Petrova (2007). The specific implementation is detailed Cohen et al. (2015), but reproduced here for completeness. The Kurganov and Petrova (2007) is ideally suited to this application as it is well-balanced (i.e. can simulate ‘lake at rest’ steady states), positivity preserving (i.e. can predict very low fluid depths) and can handle discontinuities in terrain. In vector form, the (Kurganov and Petrova, 2007) shallow water system can be written as:

$$\mathbf{U}_t + \mathbf{F}(\mathbf{U}, B)_x + \mathbf{G}(\mathbf{U}, B)_y = \mathbf{S}(\mathbf{U}, B) \quad (3.13)$$

with the unknown height and discharge vector $\mathbf{U} = (w, hu, hv)^T$. The water surface w is denoted by $w = h + B$ where h is the fluid depth above the bottom topography B . The x- and y-direction velocities are u, v respectively. The fluxes and source terms are then:

$$\mathbf{F}(\mathbf{U}, B) = \begin{bmatrix} hu \\ \frac{(hu)^2}{w-B} + \frac{1}{2}g(w-B)^2 \\ \frac{(hu)(hv)}{w-B} \end{bmatrix}, \quad (3.14)$$

$$\mathbf{G}(\mathbf{U}, B) = \begin{bmatrix} hv \\ \frac{(hu)(hv)}{w-B} \\ \frac{(hv)^2}{w-B} + \frac{1}{2}g(w-B)^2 \end{bmatrix}, \quad (3.15)$$

$$\mathbf{S}(\mathbf{U}, B) = \begin{bmatrix} 0 \\ -(w-B)B_x \\ -(w-B)B_y \end{bmatrix} \quad (3.16)$$

These shallow water equations are solved on a fixed grid using a central-upwind scheme. Critically, this scheme is modified in Kurganov and Petrova (2007) to ensure the method is well-balanced and preserves low fluid heights through a piecewise bilinear approximation of the base topography function B and modified reconstructions of w, u, v . For these details the reader is referred to sections 3.1 and 3.2 of Kurganov and Petrova (2007) as our implementation is exactly the same. The bed sediment transport and mass balance is calculated using a bedload transport module attached to this solution. The height (h) and depth-averaged velocities (u, v) of the shallow water solution after each timestep are used to calculate the shear stress and corresponding bedload transport rate. Height of the bed is then updated using the Exner equation (Eq. 3.2).

Probabilistic hazard modelling of rain-triggered lahars

Stuart R. Mead and Christina Magill

Journal of Applied Volcanology

Volume 6, Issue 8, 2017

doi: 10.1186/s13617-017-0060-y

Abstract

Probabilistic quantification of lahar hazard is an important component of lahar risk assessment and mitigation. Here we propose a new approach to probabilistic lahar hazard assessment through coupling a lahar susceptibility model with a shallow-layer lahar flow model. Initial lahar volumes and their probabilities are quantified using the lahar susceptibility model which establishes a relationship between the volume of mobilised sediment and exceedance probabilities from rainfall intensity-frequency-duration curves. Rainfall-triggered lahar hazard zones can then be delineated probabilistically by using the mobilised volumes as an input into lahar flow models. While the applicability of this model is limited to rain-triggered lahars, this approach is able to reduce the reliance on historic and empirical estimates of lahar hazard and creates an opportunity for the generation of purely quantitative probabilistic lahar hazard maps. The new approach is demonstrated through the generation of probabilistic hazard maps for lahars originating from the Mangatoetoenui Glacier, Ruapehu volcano, New Zealand.

Keywords

probabilistic lahar hazard · susceptibility · rain-triggered lahar · numerical modelling

4.1 Background

Lahars are among the most hazardous volcanic processes and are responsible for a large proportion of volcanic fatalities (Auker et al., 2013). Reliable information on the likelihood of lahar occurrence and the resulting inundation area is critical for the mitigation of risks posed by lahars (Pierson et al., 2014). Lahar hazard assessments typically provide this information in the form of hazard maps quantifying the probability and extent of potential lahars to varying degrees (Calder et al., 2015). In these assessments, models that approximate lahar behaviour and/or run-out are frequently used (e.g. Aguilera et al., 2004; Carranza and Castro, 2006; Darnell et al., 2013; Thouret et al., 2013; Pistolesi et al., 2014; Córdoba et al., 2015). Commonly used models include Laharz (Iverson et al., 1998; Schilling, 2014), an empirical model relating lahar volume to cross-sectional and planimetric inundation area; the two-phase shallow layer model of Pitman and Le (2005) implemented in the Titan2D toolkit (Pitman et al., 2003; Patra et al., 2005); and single phase rheology approaches such as Kelfoun (2011), Flo-2D and Delft3D, used in Caballero et al. (2006) and Carrivick et al. (2009) and Carrivick et al. (2010). Regardless of methodology, the accuracy and output of these methods is dependent on the value and accuracy of model inputs. The initial lahar volume or volumetric flux is one such input that determines initial lahar size and gravitational potential energy. Since lahar size and energy transfer are important factors controlling lahar behaviour and runout (Lube et al., 2012), an accurate estimate of initial volume is therefore crucial for accurate and reliable hazard footprint estimates. Commonly, initial lahar volumes are estimated from volumes of previous lahar events or rely on expert judgement. However, historic data is often incomplete or can be irrelevant under different environmental conditions which limits probabilistic lahar hazard estimates.

Recently, Mead et al. (2016) presented a physically based model for determining initial volumes of rain-triggered lahars. Lahar susceptibility, defined as the probability of an initial lahar volume at a specific location, was determined through assigning annual probabilities to lahar volumes using rainfall intensity-frequency-duration (IFD) curves. The potential of coupling lahar susceptibility model outputs to lahar flow model inputs in order to quantify lahar hazard probabilistically was discussed, but not demonstrated. Here, the work of Mead et al. (2016) is extended by coupling lahar susceptibility outputs to the two-phase shallow layer model of Pitman and Le (2005). Outputs of the combined model in the form of probabilistic hazard maps are demonstrated for lahar scenarios originating from Mangatoetoenui Glacier, Mt. Ruapehu, New Zealand. This work is intended to demonstrate an approach for probabilistic estimates of lahar hazard and highlight areas of research needed to enhance the reliability of these hazard estimates.

4.2 Methods

The probabilistic lahar hazard approach proposed here relies on the combination of two modelling methods. Lahar flow is simulated as a two-phase flow using Titan2D with initial volumes determined using the lahar susceptibility model of Mead et al. (2016). Details of each method are summarised below; for full details readers are referred to Patra et al. (2005) and Pitman and Le (2005) for the Titan2D toolkit and Mead et al. (2016) for the rain-triggered lahar susceptibility model.

4.2.1 Rain-triggered lahar susceptibility

In the rain-triggered lahar susceptibility approach described in Mead et al. (2016), lahar volumes are estimated from deposit properties, rainfall intensity and rainfall duration using a combined shallow landslide and overland erosion model. The total initial volume of the lahar is calculated in the combined model as the sum of the material mobilised through overland erosion and shallow landsliding for a given rainfall intensity and duration. In the overland erosion model, the height and motion of infiltration excess rainfall (i.e. net rainfall after infiltration into the deposit) is simulated using a depth averaged shallow water (SW) approximation. The entrainment of volcanic sediment is calculated from the height and velocity of the overland flow using the Meyer-Peter and Müller (MPM) bedload transport model (see Castro Díaz et al. (2008)), and the total volume of mobilised volcanic sediment is calculated at the end of the rainfall duration. The volume of volcanic material mobilised through shallow landsliding is calculated using the approach developed by Iverson (2000) where shallow slope failures are assumed to occur when gravitational forces are greater or equal to the resisting Coulomb stresses. In the Iverson (2000) model, resisting stresses are reduced in proportion to the rainfall infiltration rate (i.e. deposit permeability) and hydraulic diffusivity, which controls the transmission of pore pressure through the deposit. The depth, and consequently volume, of the shallow failure is calculated at the end of the rainfall duration. The probability of specific lahar volumes can be estimated using this method through the use of rainfall intensity-frequency-duration (IFD) tables. These tables express the probability of rainfall intensities occurring over a given duration and can be used to estimate the occurrence probability of specific lahar volumes being triggered by rainfall. These lahar volumes, when used as an input in Titan2D, can then be used to express lahar inundation in a probabilistic manner. Here, the mobilised volume estimates and recurrence intervals calculated in Mead et al. (2016) are used as the probabilistic input for the lahar flow model.

4.2.2 Lahar flow modelling

The choice of lahar flow model can have a large effect on the quality and reliability of probabilistic hazard estimates and therefore needs to be considered in conjunction with the needs

of the hazard assessment. The prediction of lahar flow is difficult due to complex physical processes such as entrainment and deposition of sediment, changing solid concentrations and flow transformations (e.g. Doyle et al., 2009). While empirical models such as Laharz can be used to estimate lahar inundation areas (Schilling, 2014), numerical models are able to provide more information (e.g. velocities and pressures) useful for estimating the intensity of the hazard (McDougall, 2016). A range of numerical models have been used or proposed (e.g. Pudasaini, 2012) for lahar flow modelling; however, the selection of numerical models and their parameters is complicated by the lack of universal constitutive laws governing lahar flow behaviour (McDougall, 2016).

While input parameters for simple models that rely on bulk measures of the lahar (e.g. internal and basal friction, solid concentration) can be calibrated to previous lahar flows, in practice, the complexity of lahar events mean the calibration can only be optimised on one characteristic of the lahar to the detriment of others. For example, a reduction of friction values to match long runout lahars will result in excessively mobile lahars with high momentum in proximal (near source) zones. Recent, more advanced models of two-phase flow (e.g. Pudasaini, 2012; Iverson and George, 2014; Iverson and George, 2016; Mergili et al., 2017) may improve predictions of lahar flow. However, these models rely on a large array of input parameters that are often not known or measurable *a priori* and, as yet, do not demonstrate the ability to model transformations in flow behaviour.

Probabilistic lahar hazard estimates are obtained through the use of volume and location outputs from the lahar susceptibility method as the input for lahar flow models. Consequently, the flow modelling approach can be chosen according to an assessment of modelling capabilities needed to accurately simulate the lahar hazard. To demonstrate this approach, we chose to use the two-phase material model of Pitman and Le (2005) to model lahar runout and dynamics. This model, implemented in the Titan2D toolkit (Pitman et al., 2003; Patra et al., 2005), simulates the flow of mixtures of soil, rock and interstitial fluid (water) over natural terrains. The main inputs required for this method is a digital elevation model (DEM), initial height and area of the mixture (pile height) and basal and internal friction values. The Pitman and Le (2005) model has previously been applied to simulate lahars (e.g. Williams et al., 2008; Procter et al., 2010; Córdoba et al., 2015). Crucially, this model does not consider the effects of erosion, deposition or transformation of the lahar and therefore will not reproduce all features of a lahar. Consequently, simulations using this method will not exactly match the outcomes of actual lahars, but will provide a probabilistic guide to the lahar hazard. In order to couple the susceptibility model material volumes to the inputs in the Titan2D toolkit, the Titan2D code was modified to add support for user defined pile heights in the form of a geographical information system (GIS) raster file. The modified source code is provided in the Zenodo repository <https://doi.org/10.5281/zenodo.153993>.

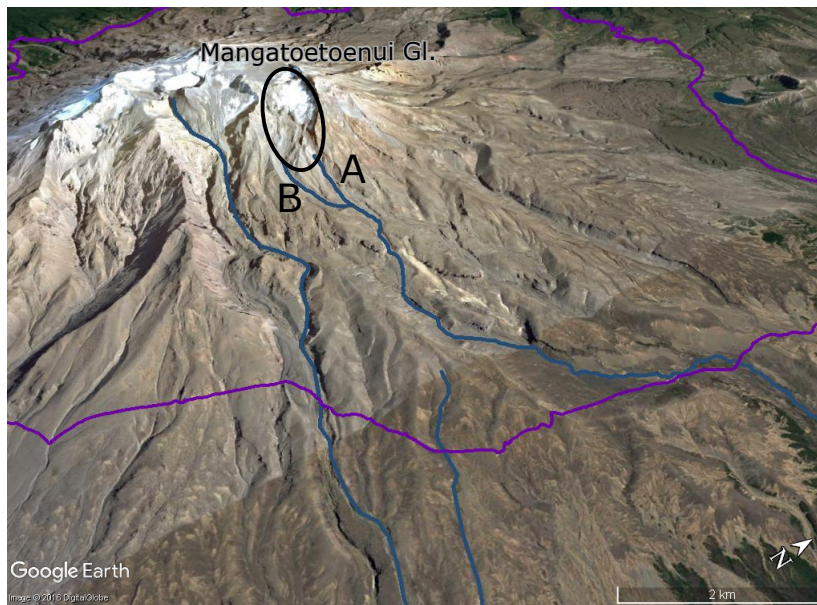


FIGURE 4.1: Study area overview showing Ruapehu volcano (left), round the mountain track (purple), Mangatoetoenui Glacier (circled) and the North and South branches of Mangatoetoenui Stream (‘A’ and ‘B’ respectively).

4.3 Study area and simulation inputs

The process outlined in the previous section is demonstrated through the generation of probabilistic hazard maps for lahars originating from the Mangatoetoenui Glacier, Ruapehu volcano, New Zealand. The Mangatoetoenui Glacier and Stream are located on the north-eastern flank of Ruapehu volcano, draining eastwards into Tongariro River (Fig. 1). A hydro-electric dam, trout fisheries and several towns located along Tongariro River are at risk from lahars originating on the north-eastern flanks of the volcano (Cronin et al., 1997b). In this study, deposit characteristics are chosen to create a scenario with similar conditions to those in Mangatoetoenui Stream prior to the October 28, 1995 lahar described in Hodgson and Manville (1999) and used in lahar susceptibility estimations by Mead et al. (2016). The initial conditions in this study only consider a limited range of initial volumes and solid volume fractions, with all other inputs fixed, which means the generated hazard maps only represent a subset of the possible parameter space. A complete hazard assessment would consider the range of other inputs (such as basal and internal friction), their uncertainty and model suitability (Calder et al., 2015).

Titan2D simulations for all volumes were run for 30 minutes of simulation time using a 25 metre resolution digital elevation model (DEM) sourced from Landcare Research NZ Ltd. (2010). The DEM spanned the region from Mangatoetoenui Glacier (see Fig. 4.1) in the west to the confluence of Mangatoetoenui Stream and Tongariro River in the east, and was chosen because it best represented hydrological features of the terrain, despite the lower resolution compared to the contour-derived Land Information New Zealand DEM (c.f. Stevens et al., 2003).

Mobilised material volumes in the source study area were calculated for rainfall durations of 30 minutes, 2 hours, 6 hours, 12 hours and 24 hours at annual exceedance probabilities (AEP) of 0.5 (2 years annual recurrence interval (ARI)), 0.1 (10 years ARI), 0.02 (50 years ARI) and 0.01 (100 years ARI), using the susceptibility simulations first presented in Mead et al. (2016). We assumed most material is mobilised in a single event to match the observations of Hodgson and Manville (1999). GIS raster files of mobilised material depths from the susceptibility simulations were used as the pile height input in Titan2D. The internal friction angle of the material was given as 32° , which is between the minimum and maximum material angles of repose (Procter et al., 2010), basal friction was set to 20° to represent a reasonably fluid granular material.

In our simulations, the solids volume fraction of each modelled lahar was computed from the volumes of mobilised material and rainfall. The solid volume fraction was estimated as the volume fraction of solids in the total volume of mobilised material and water. Volume fractions, shown for each scenario in Table 4.1, decrease as ARI increases since higher rainfall intensities result in proportionally greater volumes of rainfall relative to the amount of mobilised material. The volume fractions in this table indicate the range of lahar compositions a lahar numerical model is expected to simulate. Higher concentration scenarios (e.g. 6 hour ARI 2 scenario) are near limits at which particle interactions may dominate flow behaviour. The Pitman and Le (2005) model is well suited to modelling mixtures at these concentrations. However, lower solid concentrations (e.g. below 30%) could be expected for similar initial conditions. This could limit the applicability of the Pitman and Le (2005) model which makes the simplifying assumption that pressure is the only fluid stress acting on the solids, whereas this may not be the case at low concentrations.

TABLE 4.1: Solid volume fractions of mobilised material for each scenario at Mangatoetoenui Stream.

ARI (y)	AEP	Duration				
		30 min	2 h	6 h	12 h	24 h
2	0.5	0.67	0.67	0.70	0.64	0.53
10	0.1	0.61	0.60	0.62	0.56	0.46
50	0.02	0.55	0.52	0.54	0.49	0.39
100	0.01	0.60	0.50	0.51	0.46	0.36

4.4 Generation of probabilistic lahar hazard maps

Lahar hazard maps derived from overall annual exceedance probabilities are shown in Fig. 4.2 for lahar height thresholds of 0.5 and 0.1 m. While lahar properties such as velocity and sediment concentration are also important to consider when evaluating overall lahar hazard, height is used here to express the hazard due to its ease in interpretation and use in delineation of hazard zones. Overall exceedance probabilities were calculated from simulated maximum

lahar height at each grid cell using the complementary function:

$$1 - p_{(h \geq x)}, \quad (4.1)$$

where $p_{(h \geq x)}$ is the probability of observing no lahar heights (h) greater than the threshold height x , defined using the formula of Tonini et al. (2016) as:

$$p_{(h \geq x)} = \prod_i [1 - p^i(h > x)], \quad (4.2)$$

where $p^i(h > x)$ is the probability of lahar heights exceeding the threshold for each AEP value i :

$$p^i(h > x) = i \cdot p(h > x), \quad (4.3)$$

in this instance $i = 0.5, 0.1, 0.02, 0.01$ and $p(h > x)$ is determined from the cumulative distribution of simulated lahar heights for each AEP.

4.5 Discussion and limitations

The deposit characteristics for this demonstration were chosen to create a scenario similar to the tephra deposit in the Mangatoetoe Catchment prior to the October 28, 1995 lahars. A rainfall event (23 mm total in 24 hours, 9 mm in one 6-hour interval) triggered lahars in multiple catchments of Ruapehu (Manville et al., 2000), including the Mangatoetoe catchment. The Mangatoetoe lahar, described in Hodgson and Manville (1999), travelled downstream as a debris flow for the first 5 km (the proximal zone) and then progressively transformed into a hyper-concentrated flow between 5 and 9 km from the source due to the entrainment of streamflow and deposition of sediment. The lahar continued to dilute downstream, eventually reaching the Tongariro River. The lahar was confined to the Mangatoetoe catchment, although a small deposit was observed in a distributary valley of the Whangaehu catchment (Hodgson and Manville, 1999).

The similarities in initial conditions between the October 28 lahar and simulations mean that the hazard maps in Fig. 4.2 should show a reasonable degree of similarity between the hazard outlines and observations of the lahar. However; these hazard maps indicate that a large proportion of the lahar source material enters the Whangaehu catchment (shown in Fig. 4.2). Lahar heights also appear to fall below 0.1 m downstream of the walking track encircling Ruapehu (8 km from source, purple line in Fig. 4.2). This differs from the extent of lahar deposits identified in Hodgson and Manville (1999), but is close to the distance (9 km) where flow fully transformed from a debris flow to hyper-concentrated flow. Differences in the DEM representation and initial deposit characteristics contribute to these observed errors, but the main source of error is the lack of representation of dilution, entrainment and flow transformation processes in current numerical models. The friction parameters used

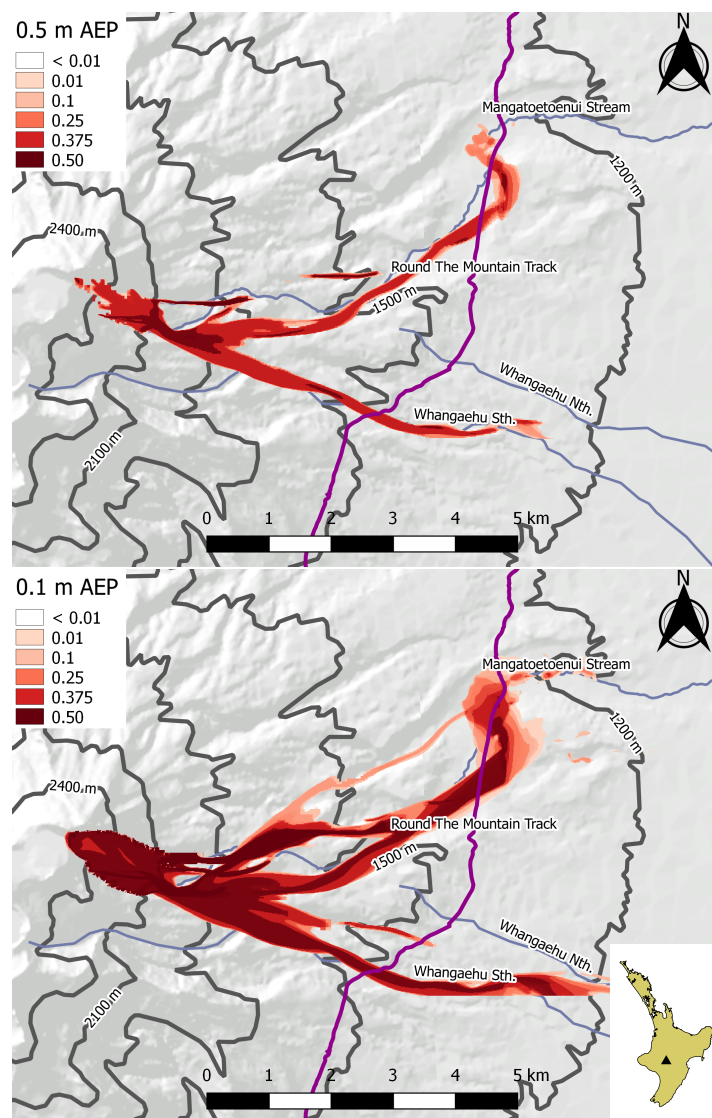


FIGURE 4.2: Annual exceedance probabilities (AEP) for lahars exceeding (top) 0.5 and (bottom) 0.1 m in height.

here provide a runout prediction near to the transition to hyper-concentrated flow, but also represent a highly mobile initial mass of material that causes a large proportion of the lahar volume to enter the Whangaehu catchment. This highlights the current state of lahar models as a key limitation of the proposed methodology and shows that operational hazard maps generated using this approach would still require expert guidance.

While differences in AEPs are visible in the vicinity of the walking track, there is little difference in lahar extent between AEPs in upstream portions of the Mangatoetoeenui catchment (Fig. 4.2). This lack of difference can be attributed to the deeply incised channel walls present in upper reaches of Mangatoetoeenui stream, but can also be caused by similar initial volumes of material being mobilised for all rainfall ARIs (see Mead et al. (2016) for explanation). However, the level of detail is limited in this demonstration as only 5 rainfall duration scenarios are simulated for each rainfall ARI, affecting the validity and resolution

of the cumulative distribution used to determine event AEP. A complete hazard mapping exercise would need to sample the entire spectrum of rainfall durations in order to increase the resolution of the cumulative distribution.

4.6 Conclusion

The probabilistic lahar hazard maps generated here by combining numerical modelling with initial volumes determined through the susceptibility approach of Mead et al. (2016) have demonstrated a potential methodology for probabilistic hazard mapping of lahars. However, through this demonstration, some key limitations and simplifications have been identified that could affect the feasibility of this technique. Importantly, lahar numerical modelling approaches require further research to develop advanced methods capable of representing entrainment, deposition and flow transformations typical of lahars. Recent and ongoing research in this area (e.g. Pudasaini, 2012; Pudasaini and Krautblatter, 2014; Iverson and George, 2016) may, in the future, provide alternative modelling approaches capable of accurately predicting additional features of lahar flows. Another limitation seen in this demonstration is the reduced parameter space used to generate the hazard maps. A complete lahar hazard assessment would need to quantify the range and uncertainty of all inputs into the model (e.g. basal and internal frictions) in addition to simulating a larger number of rainfall durations. However, simulations spanning the entire range of input parameters increases the computational requirements of this approach, which could impact on the feasibility of the method for lahar hazard assessment.

Part II

Physical vulnerability

II.1 Overview of objectives and contribution to thesis aim

This part contains two chapters focusing on quantifying physical vulnerability and the effect of lahars on buildings and infrastructure. The city of Arequipa, Peru, is used as a case study area for this work. Several suburbs of Arequipa are located on volcanoclastic fans southwest of El Misti Volcano, a stratovolcano with a history of explosive eruptions. This area is characterised by large amount of anthropogenic and environment-induced terrain change. This change and the exposure of populations, buildings and infrastructure to lahars make Arequipa an ideal location to test and explore improved approaches to lahar risk assessment. The objectives of this part are

1. to understand the role of hazard, exposure and vulnerability in determining building losses, and
2. to reduce uncertainty and improve quality of terrain inputs into lahar risk assessment.

Objective 2 is a necessary prerequisite for objective 1. A low-cost photogrammetry method is developed in chapter 5 (Mead et al., 2015) to improve accuracy of numerical models in the vicinity of buildings. The improvements in terrain model quality can contribute to all aspects of the lahar risk assessment process (see Fig. 1.5). Objective 1 is addressed in chapter 6, where new building vulnerability functions and a lahar rheology model is developed to assess and understand damage caused by lahars. Specific contributions of this chapter to lahar risk assessment includes new building fragility functions for varying flow rheologies and an improved understanding of lahar damage mechanisms in complex environments.

II.2 Summary and relevance to lahar risk

The broad aim of this part is to use numerical modelling to investigate the relative importance of lahar hazard intensity, exposure and vulnerability on overall building loss. The numerical modelling aspect of these two chapters uses smoothed particle hydrodynamics (SPH), which is relatively well established for modelling of environmental flows (e.g. Cleary and Prakash, 2004; Cleary et al., 2012; Cleary et al., 2015). However, a key issue in accurate modelling of lahar flow is the dependence, to the first order, on an accurate representation of terrain. Accurate (generally implying high resolution) digital elevation models (DEMs) are costly to acquire and require frequent updating in an area such as Arequipa due to terrain changes brought about by volcanic, environmental and human actions. To overcome these issues, a low cost photogrammetry method was developed to create high resolution three dimensional terrain models. Described in chapter 5, terrain models generated using this approach are suitable for estimating the impact of lahars on building loss.

The focus of chapter 6 is on the physical vulnerability of buildings. While other aspects of vulnerability (e.g. human, social, lifeline) are equally as important, this restriction is

necessary for practical reasons. I chose to focus on building vulnerability due to the strong links to loss of life (Wilson et al., 2014) and significant gaps in the literature (discussed in the chapter 6 introduction). Building losses under a range of hypothetical lahar flow rates and compositions are estimated using terrain models generated through the process outlined in chapter 5. Loss estimation required the development of vulnerability functions in the form of depth-pressure curves for building typologies present in Arequipa and enabled an assessment of the interaction between hazard, exposure and vulnerability. Building loss results were analysed, and suggest that building strength plays a minor role in determining overall losses in comparison to the effects of exposure and lahar properties such as rheology.

II.2.1 Smoothed particle hydrodynamics for lahar modelling

The following two chapters make use of three-dimensional smoothed particle hydrodynamics (SPH); a meshless, Lagrangian computational fluid dynamics method well suited to modelling free surface flows in complex environments. SPH is a continuum method that tracks the motion of interpolation points (often called 'particles') that represent the fluid and its properties in a Lagrangian reference frame. An interpolation kernel is used to interpolate these discrete point values into a smooth continuum. For full details the reader is referred to Monaghan (1994) and Cleary and Prakash (2004). Here, only important components of the SPH method relevant to implementation of lahar rheology models are summarised.

The continuity equation is expressed in SPH as (Monaghan, 1994):

$$\frac{d\rho_a}{dt} = \sum_b m_b (\mathbf{v}_a - \mathbf{v}_b) \cdot \nabla W_{ab}, \quad (\text{II.1})$$

where ρ_a is the density of particle a , t is time, \sum_b is the sum of all particles (b for convenience) within the interpolation radius, and $\mathbf{v}_{a,b}$ denote the velocity vectors of particles a and b respectively. The interpolation kernel, denoted W_{ab} is evaluated over the distance between particles a and b . The momentum equation used here is (Monaghan, 1994):

$$\frac{d\mathbf{v}_a}{dt} = \sum_b m_b \left[\left(\frac{P_a}{\rho_a^2} + \frac{P_b}{\rho_b^2} \right) - \frac{\xi}{\rho_a \rho_b (\mu_a + \mu_b)} \frac{\mathbf{v}_{ab} \cdot \mathbf{r}_{ab}}{\mathbf{r}_{ab} + \zeta^2} \right] \nabla_b W_{ab} + g, \quad (\text{II.2})$$

where $P_{a,b}$, $\rho_{a,b}$ and $\mu_{a,b}$ are pressures, densities and viscosities of particles a and b , gravity is g and \mathbf{r}_{ab} is the location vector from particle a to b . Singularities when $\mathbf{r}_{ab} = 0$ are smoothed with small values of ζ and $\xi = 4.9633$ to calibrate for fluid viscosity (e.g. Prakash et al., 2014). In all simulations described here, SPH flows are initialised from an inflow boundary specified in the simulation. These inflow boundaries generate SPH particles at the specified mass flow rate (i.e. with a constant size and density, particles are generated with a prescribed initial velocity), allowing flows to develop according to the SPH continuity and momentum equations.

For completeness, we duplicate part of chapter 6 here explaining how rheology models are implemented into SPH. Non-Newtonian lahar rheology was implemented in SPH using an apparent Newtonian viscosity (η). Assuming the fluid is isotropic, constitutive equations for rheology can be written as a generalised Newtonian fluid in terms of the apparent viscosity:

$$\tau = \eta \dot{\gamma} \quad (\text{II.3})$$

where τ is the shear stress, $\dot{\gamma}$ the shear rate, and η is the apparent viscosity. When the apparent viscosity is constant the fluid is Newtonian with a viscosity of η . Non-Newtonian fluids can be modelled using Eq. II.3 by developing relationships for η based on constitutive equations (Mitsoulis, 2007). Using this approach, the apparent viscosity for the quadratic rheology is:

$$\eta = \frac{\tau_y}{\dot{\gamma}} + \mu + \alpha \dot{\gamma} \quad (\text{II.4})$$

where τ_y the yield strength, μ the viscosity and α is the turbulent-dispersive parameter, a coefficient that combines the effects of turbulence and dispersive stresses caused by sediment collisions. Here, we also use the viscosity regularisation approach of Papanastasiou (1987), described in Mitsoulis (2007) and Minatti and Paris (2015). Regularisation is required as the apparent viscosity approaches infinity at low strain rates when using Eq. II.4. At these high viscosities, the simulation time step approaches zero, significantly increasing computational time. Using the Papanastasiou (1987) approach, the regularised viscosity used in simulations is:

$$\hat{\eta} = \frac{\tau_y}{\dot{\gamma}} (1 - \exp^{-c\dot{\gamma}}) + \mu + \alpha \dot{\gamma}, \quad (\text{II.5})$$

where c is the viscosity scaling parameter, larger values of c result in a better approximation of the constitutive equation (Eq. II.4), while smaller values result in smaller apparent viscosities and larger simulation time steps. Here we set $c = 200$, a value which yielded the best balance between simulation speed and accuracy from validation simulations.

Lahar rheology model for SPH

The bulk flow behaviour of lahar sediment-water mixtures is controlled by the relative concentration of sediment within the flow (Dumaisnil et al., 2010). In particular, the clay content and proportion of fine sediment in suspension will greatly influence the transition from a Newtonian (i.e. constant viscosity and zero shear strength) to non-Newtonian fluid (Pierson, 2005). This transition and lahar flow behaviour is affected by inter-particle interactions (collisions and electrochemical attractions), particle-bed interactions and particle-fluid interactions, the combination of which is complex and likely exists as a continuous process (Pierson, 2005). Flows can be predominantly Newtonian with sediment volume concentrations of up to 35%, provided there are few clay or fine particles present. The inter-particle interactions between larger proportions of fines or coarse sediment in the fluid will result

in a small but measurable yield strength. Flows with a non-zero yield strength are often termed hyper-concentrated (Pierson, 2005; Manville et al., 2013) and can also be characterised by a marked dampening of turbulence (Pierson and Costa, 1987). At higher sediment concentrations, particle-particle collisions and the internal friction between particles begin to dominate, causing the yield strength to increase significantly. These flows tend to exhibit commonly observed lahar behaviours such as suspension of large boulders, unsorted particle deposits and rapid consolidation of the deposit as the pore fluid drains. Viscosity of the pore fluid also plays an important role in moderating the effect of inter-particle interactions (Doyle et al., 2010). At low viscosities (e.g. water), inertial forces and particle collisions dominate energy transfer within the fluid, while at higher viscosities (e.g. with a significant proportion of clay) the energy is mostly dissipated through fluid-particle interactions.

Several single-phase rheological models have been proposed to describe non-Newtonian lahar behaviour; most of these models follow the general form of the Herschel-Bulkley equation (Manville et al., 2013)

$$\tau = \tau_y + \mu \dot{\gamma}^m, \quad (\text{II.6})$$

where m is the shear power, which describes the response to shear (i.e. shear-thickening or shear-thinning). A simple rheological description for lahar flows assumes they behave as a viscoplastic material, commonly called a Bingham fluid. Bingham fluids have a non-zero shear strength and shear power, m , of 1. Flows of Bingham fluids typically have two components consisting of a basal shearing layer (shear layer) topped with a non-shearing plug layer (Rodriguez-Paz and Bonet, 2004). In more general terms, O'Brien et al. (1993) and Jan and Shen (1997) describe the total shear stress of generic sediment-water flows as being controlled by the summation of all the debris flow strength components: cohesive yield strength, Mohr-Coulomb shear stress, viscous shear stress, turbulent shear stress and the dispersive (particle collision) shear stress. At high viscosities and relatively low velocities, the turbulent stresses can be assumed negligible (Pierson and Costa, 1987; O'Brien et al., 1993; Jan and Shen, 1997). By combining all the relevant stresses, a generalised quadratic rheology model (Julien and Lan, 1991; O'Brien et al., 1993; Jan and Shen, 1997) can be expressed as:

$$\tau = \tau_y + \mu \dot{\gamma} + \alpha \dot{\gamma}^2, \quad (\text{II.7})$$

Rheological parameters for τ_y , μ and α were studied for debris flows by Phillips and Davies (1991) and O'Brien and Julien (1988). We chose to implement and use this quadratic rheology model for lahars as it summarises the principal components of non-Newtonian lahar behaviour, namely a yield strength, viscous effects and a dilatant (shear-thickening) effect from particle collisions.

A distributed computing workflow for modelling environmental flows in complex terrain

Stuart R. Mead, Mahesh Prakash, Christina Magill, Matt Bolger and Jean-Claude Thouret

Environmental Software Systems. Infrastructures, Services and Applications

IFIP Advances in Information and Communication Technology, Volume 448, 2015

doi: 10.1007/978-3-319-15994-2_32

Abstract

Numerical modelling of extreme environmental flows such as flash floods, avalanches and mudflows can be used to understand fundamental processes, predict outcomes and assess the loss potential of future events. These extreme flows can produce complicated and dynamic free surfaces as a result of interactions with the terrain and built environment. In order to resolve these features that may affect flows, high resolution, accurate terrain models are required. However, terrain models can be difficult and costly to acquire, and often lack detail of important flow steering structures such as bridges or debris. To overcome these issues we have developed a photogrammetry workflow for reconstructing high spatial resolution three dimensional terrain models. The workflow utilises parallel and distributed computing to provide inexpensive terrain models that can then be used in numerical simulations of environmental flows. A section of Quebrada San Lazaro within the city of Arequipa, Peru is used as a case study to demonstrate the construction and usage of the terrain models and applicability of the workflow for a flash flood scenario.

Keywords

Structure-from-Motion · photogrammetry · numerical modelling · rapid mass flow · natural hazards

5.1 Introduction

Extreme environmental flows and mass movements such as floods, landslides, avalanches and debris flows pose significant risk to exposed populations and can cause substantial damage to buildings, infrastructure and the environment. Due to safety concerns and difficulty in predicting the occurrence of these events, field measurements are rare and, when available, are generally limited to depth and point velocity measurements (e.g. Manville and Cronin, 2007). As a consequence, computational flow models are commonly employed in an attempt to predict the outcomes of specific events, understand fundamental processes and to provide a greater understanding and delineation of the hazard. Two-dimensional (2D) depth-averaged numerical models such as the shallow-water (SW) method for fluids or Savage-Hutter method for granular mass movements are widely used to simulate environmental flows. These depth-averaged approaches are suitable for predicting large scale flow features and inundation; however the shallowness assumption can be limiting within complex environments (such as urban areas) where there are large and sudden changes in the terrain gradient. Complex and varying topography causes the flow to have three dimensional features and varying vertical velocity profiles which cannot be captured by depth-averaged approaches. For these circumstances, three dimensional (3D) particle based flow modelling methods, such as smoothed particle hydrodynamics (SPH), may be more suitable as they have the ability to predict and track the motion of objects or debris within the flow, model complex flooding scenarios including interaction with buildings, and predict forces on structures (Cleary and Prakash, 2004). Use of SPH and other 3D methods has traditionally been limited due to their high computational requirements. However, advances in processing power and parallel computing solutions such as OpenMP and Message Passing Interface (MPI) have created opportunities to simulate larger areas at higher resolutions.

In both depth-averaged 2D and fully 3D flow modelling approaches, topographic information (in the form of terrain models) is required as a primary input and modelled outcomes are highly sensitive to the accuracy of this topographic data (Williams et al., 2013). For example, Legleiter et al. (2011) examined the effects of uncertain topographic data on a typical 2D depth-integrated (i.e. Shallow Water) method, finding that the method was sensitive to morphological features such as point bars. Small scale bed features were also found to affect results, albeit at a reduced level as flow depth increased. The applicability and accuracy of simulation predictions is therefore reliant on accurate reproduction of small scale flow steering features and topographic obstacles in the terrain model.

While advances in computational power and remote sensing methods have generally increased the dimensionality and resolution of terrain models (Javernick et al., 2014), quality and accuracy has not necessarily increased at the same pace. Measurements of the terrain are commonly acquired from satellite or aerial platforms using techniques such as LiDAR, stereo photogrammetry or radar interferometry. This information is then used to create gridded digital terrain models (DTM), a representation of the topography at a single point in time.

Frequent data acquisition is critical to ensuring currency of the DTM, as sediment transport processes and human interaction continually modify the terrain and create small scale features that may affect the behaviour of flows. The frequency of data acquisition is, however, limited by high computational requirements, costly equipment and lengthy data processing times (Javernick et al., 2014), resulting in an inaccurate representation of the current shape and features of the terrain. In addition, terrain models can be limited by the acquisition platform. High altitude aerial platform methods are not suitable when the area of interest has large amounts of cloud cover, which is often the case before and after weather based flow events. Tall trees, buildings and bridges may also cause occlusion, leading to inadequate representations of key terrain features.

For high resolution modelling, accurate reproduction of small-scale terrain features and the 3D terrain structure is particularly important, although grid based terrain models are limited in their ability to reproduce these 3D features. Reasons for this have been described by Kreylos et al. (2013) and include:

- Constraints of a rectangular grid system limits the gradient of the slope, and therefore flow direction, to eight cardinal directions.
- Re-projection of steep topographic features, such as dips, overhangs or bridges, onto a horizontal plane degrades the level of detail captured, implicitly reducing the resolution.
- Gridding can have a directional dependence, and features such as channels that do not align with the primary grid direction can be degraded.

Three dimensional terrain representations, such as triangulated irregular networks (TIN) or point based methods (Kreylos et al., 2013) present a feasible alternative to reduce the limitations of grid-based terrain models as well as more accurately reproducing terrain features.

Here, we demonstrate a workflow to acquire and process detailed 3D terrain models for use in 3D flow modelling and visualisation. The process utilises and integrates several core technologies to provide a fast, reliable and inexpensive method for terrain generation and numerical modelling that eliminates or reduces many of the common limitations of traditional terrain models. Open source libraries and data structures are used to enhance the flexibility of the process and allow users to extend this methodology. The workflow utilises parallel and distributed computing to allow for rapid turnaround time from terrain acquisition to output of numerical simulation results. The key components of the workflow are (1) acquisition of ground images and low altitude aerial images from a light remote control quadcopter, (2) image feature detection, matching and 3D scene reproduction using Structure-from-Motion (SfM) photogrammetry, (3) point cloud processing, including re-projection and meshing; and (4) numerical modelling using SPH. The low cost and high speed of this method allows for faster acquisition of terrain models, increasing their currency, while the point based approach enables features to be more accurately represented. The application of this workflow is

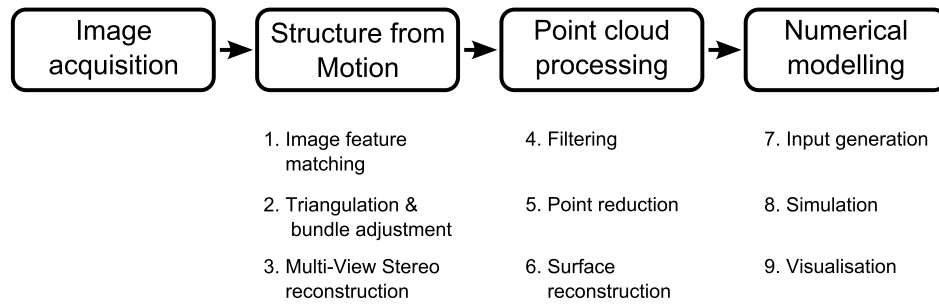


FIGURE 5.1: Terrain generation and modelling workflow outline.

demonstrated as a case study by simulating flash flood scenarios in complex terrain for the city of Arequipa, Peru.

5.2 Methods

5.2.1 Workflow outline and software integration

The four stages of the terrain generation and modelling process are shown in Fig. 5.1. The first stage, image acquisition, involves capturing images of the terrain from multiple angles, taken either aerially and from ground level. The main objective of this stage is to collect as many images of the area of interest as possible. The Structure-from-Motion (SfM) stage uses these images to generate a point cloud representation of the area using photogrammetry and computer vision methods including feature identification and matching, camera pose estimation and point cloud reconstruction using multi-view stereo (MVS). The dense point cloud produced by the SfM stage is then processed using algorithms to filter out erroneous points, reduce the size of the point cloud and reconstruct a manifold, watertight surface mesh representing the terrain. In the final numerical modelling stage, the terrain mesh model is converted into an input for simulation and subsequent visualisation.

The modelling and terrain generation process, shown in Fig. 5.1, is sequential with each step relying on inputs from the previous. Aside from the requirements for inputs, each component of the process is independent from each other. This makes the process well suited for implementation into a workflow tool, where each software component can be developed and modified independently. This is particularly important for image feature detection (step 1 in Fig. 5.1), surface reconstruction (step 6) and numerical modelling (steps 7-9), as these are all active areas of research where a range of approaches (e.g. fully 3D or 2D depth-averaged numerical models) could be employed and may be more appropriate depending on user requirements.

We chose to implement this process (referred to hereafter as the modelling workflow) into Workspace, a cross-platform workflow framework with a plug-in architecture (Workspace, 2014). The plug-in architecture exposes data types and operations, enabling the development

of new workflows and operations. Other advantages of Workspace for this application are:

- 3D visualisation capabilities allows for integrated model checking, without the need for additional software packages,
- the distributed/parallel execution engine, which allows components of the workflow to be processed on multiple CPUs, both locally and distributed through TCP and cluster based systems, and,
- the engine is built upon permissive free software licenses, allowing for extensions and applications to be developed without third party licensing requirements.

Currently image feature matching, point cloud processing (steps 4-6), input generation (step 7) and visualisation (step 9) are implemented within Workspace. The triangulation, bundle adjustment and multi-view stereo processes are run separately, but are executed within the workspace from a command line operation. The SPH simulations (step 8) are run externally using the terrain model generated within the workflow.

5.2.2 Structure-from-Motion (SfM)

Structure-from-Motion (SfM) is a photogrammetry method that reconstructs sparse 3D points and camera viewpoints from image collections of a scene. Dense 3D point clouds can be reconstructed by coupling with MVS methods, which construct dense 3D point clouds from overlapping images and camera viewpoints (Furukawa et al., 2010). The accuracy of SfM-MVS approaches is said to be nearly on par with laser scanners (Seitz et al., 2006).

To obtain camera viewpoints, the SfM process is as follows: (1) within each image, find and compute descriptors for unique features such as building corners (keypoints); (2) find matching keypoints in images taken from different angles; (3) obtain an estimate of camera parameters and location through triangulation of the image matches; and, (4) optimise the matrix of camera parameters and locations (bundle adjustment). For a detailed description of the SfM process, see Snavely et al. (2006).

In the workflow, our approach differs slightly from the commonly used methods presented by Snavely et al. (2006) in that we utilise the open source library OpenCV (www.opencv.org) to compute and match features. OpenCV is a BSD-licensed computer vision and machine learning software library with a feature detection and matching framework that allows for a variety of different keypoint extraction and descriptor methods. Currently implemented matching methods are SIFT (Lowe, 1999), SURF (Bay et al., 2006) and BRISK (Leutenegger et al., 2011). These provide a range of keypoint descriptors that can be utilised depending on requirements for speed, robustness or commercial purposes (SIFT and SURF are patented methods, freely available for non-commercial use only).

Following the triangulation and bundle adjustment stage of the workflow, the camera pose and sparse point cloud are used to create a dense reconstruction of the scene using MVS. The MVS method used here implements view-clustering to group images in order to

reduce memory requirements and reconstruction speed. For details on the view-clustering MVS method used here refer to (Furukawa and Ponce, 2010).

5.2.3 Point cloud processing and surface generation

Following dense reconstruction, the point cloud is converted into a structure that can be used in the Point Cloud Library (PCL), a large scale open project for point cloud processing (Rusu and Cousins, 2011). The PCL libraries contains algorithms for filtering, feature and object detection, processing and smoothing, model fitting and surface reconstruction. Currently, the following PCL operations are implemented in Workspace: (1) normal and curvature estimation using OpenMP; (2) statistical processing and filtering; (3) moving least squares smoothing and up-sampling (useful for DTM generation); and, (4) iterative closest point registration. These operations, and others within the libraries can be used interchangeably in the workflow to filter, smooth and transform the point clouds depending on output requirements. As a result, the workflow can be easily modified or extended to have uses beyond the creation of surfaces for numerical modelling.

For simulation of environmental flows, a watertight reconstruction of the surface is required, with minimal artificial perturbations or mesh artefacts such as non-manifold geometry. The main challenge with creating surfaces from the SfM-MVS process is handling non-uniform point density, noise and misaligned points; while being scalable to large point clouds. There are several surface reconstruction methods currently available and research in this area is active. In this workflow, the Smoothed Signed Distance Coloured (SSD-C) surface reconstruction method of Calakli and Taubin (2012) is used. This method was chosen for its speed and durability, however additional methods may be easily substituted if required.

5.2.4 Numerical modelling

The reconstructed surface created from the previous steps has a number of potential applications, including visualisation and as an input for numerical modelling. Here, we demonstrate an application for high-resolution numerical modelling within a complicated urban environment using 3D smoothed particle hydrodynamics (SPH). SPH is a versatile, meshless, Lagrangian particle method that has been used to model environmental phenomena such as tsunamis, dam breaks, landslide initiation, lava flows and mudflows (Cleary and Prakash, 2004). SPH is particularly advantageous for modelling complicated flows within complex environments due to the natural handling of complex topography and free surface flows, and the ability to include additional physics such as non-Newtonian rheology and entrainment of dynamic objects.

In the workflow, the reconstructed surface is converted into a data structure that can be read by the SPH software, which is run externally to the workflow due to the long computational time (in the order of weeks to months) required for high resolution simulations.

Once completed, the data can be analysed and visualised within Workspace using separate data analysis workflows.

5.3 Case study: Arequipa, Peru

To demonstrate the applicability of this method, we present a case study of the workflow for Arequipa City, Peru. Arequipa's central business district is located approximately 17 km south-west of El Misti, a steep potentially active volcano. The city is exposed to flash floods and lahars (volcanic debris flows) due to climatic conditions and the city's proximity to El Misti. Areas along the main quebradas (ravines) of San Lazaro and Huarangal are at risk from flash floods and lahars during the rainy season or after eruptions (Thouret et al., 2013). For example, flash floods in February 2011 destroyed 20 houses and caused damage to another 400, mostly along the quebradas and steep slopes. Much of this damage was attributed to heavy rainfall or breakout floods caused by infill obstacles such as makeshift crossings (Thouret et al., 2013). High resolution terrain models are required to represent the small scale of these features, while the rapidly changing environment requires frequent updating to accurately represent the topography for hazard simulations. This area was therefore chosen as a case study to demonstrate the value of the modelling workflow.

5.3.1 Image collection

An approximately 200 m long and 200 m wide area of Quebrada San Lazaro was studied and is shown in Fig. 5.2a, looking upstream from a road bridge. The area in question contained the bridge and an upstream bend in the channel, which are thought to create over-bank flow and strong 3D flow features that are ideal to test the use of SPH. In total, 2,000 images of the area were acquired in September 2013; 600 images were taken from the ground and 1,400 aerially. The aerial images were obtained from a DJI Phantom, a small ($35 \times 35 \times 19$ cm), lightweight (take off mass < 1 kg) quadcopter with an attached camera.

The objective of the image collection stage was to acquire as many images as possible from multiple angles to ensure all features were reproduced correctly and that there was minimal occlusion. A quadcopter is ideal in these circumstances, as its light weight and manoeuvrability means that it can be flown in close proximity to buildings to acquire images from multiple angles. In other areas (e.g. larger regions with less changes to terrain) a higher, more stable, but less manoeuvrable, aerial platform such as a helium balloon may be more suitable.

5.3.2 Feature matching, SfM and MVS

Image features for the case study were detected and matched using SIFT feature descriptors. In an unordered image set, such as the one used in this case study, each image can potentially match each other image, meaning that image matching has $O(n^2)$ complexity. To reduce the

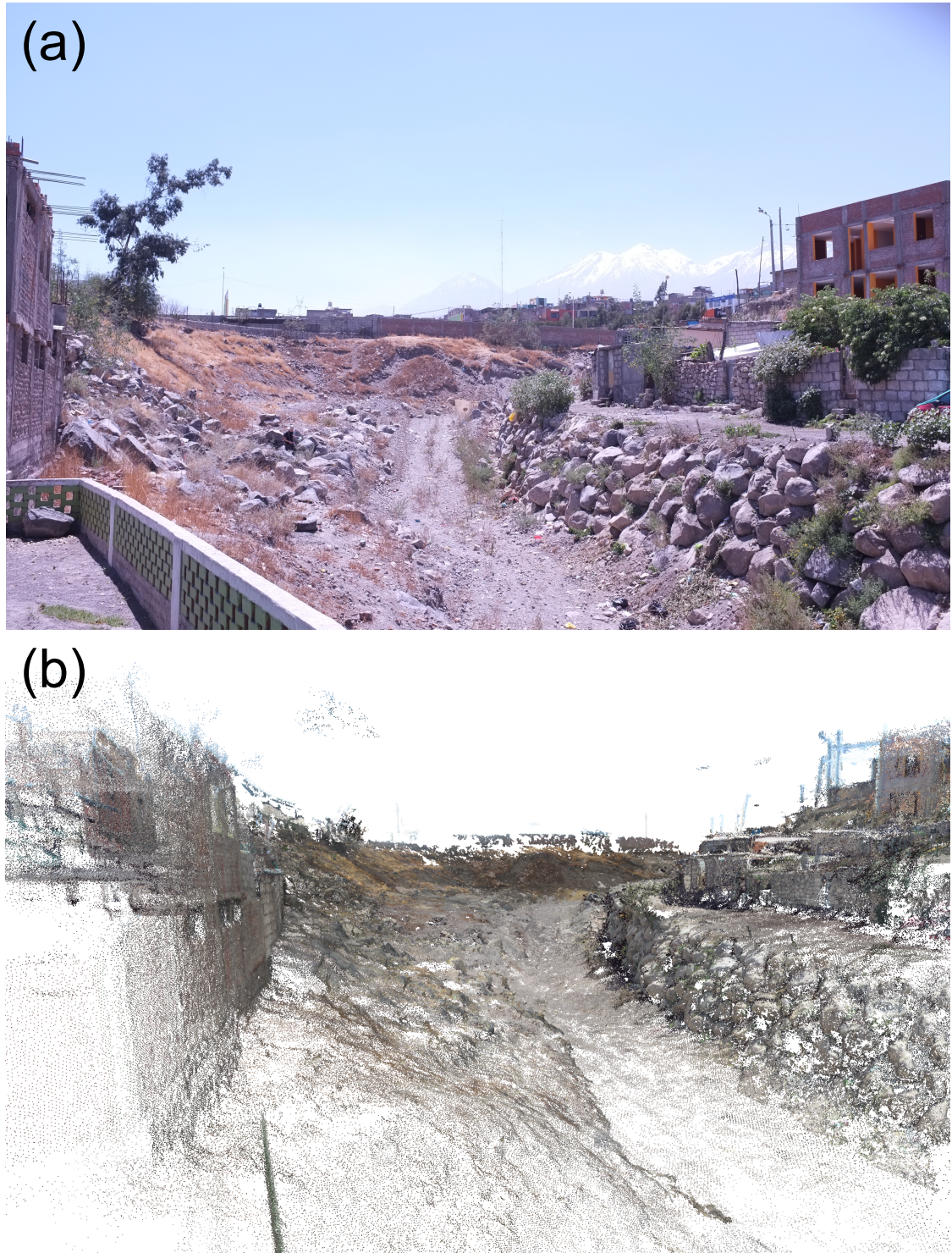


FIGURE 5.2: (a) Case study area in Quebrada San Lazaro and, (b) dense point cloud reconstruction from the SfM-MVS.

time taken to match images, we parallelised this portion of the workflow, enabling matches to be determined on local and external CPU cores using the Workspace parallel execution engine. A speed-up of 600% was achieved using parallel processing on 12 CPU cores (at 2.93 GHz), the speed-up of the parallel implementation in this case is limited by the file I/O. Following image matching, the triangulation, bundle adjustment and multi-view stereo processes are run separately using VisualSFM (Wu, 2013), which utilises the CMVS-PMVS method of Furukawa and Ponce (2010).

5.3.3 Mesh generation

The SfM-MVS process created a dense point cloud containing ~ 8.5 million nodes. This point cloud was transformed using a Helmert transformation. This transformed the point cloud coordinates to match measured distances between features, ensuring the model was ‘to scale’. Geo-referencing was not needed for this application, but the Helmert transformation can be used in conjunction with ground control points to reproject the point cloud into geographic coordinates if needed. An image of the point cloud taken from a similar view angle to Fig. 5.2a is shown in Fig. 5.2b, where the point cloud model appears to correspond well with the real topography. The density of the raw point cloud varied due to occlusion and the number of images taken of a particular area. The maximum point cloud density was approximately 250 points in a 0.25 m^2 area. However, for this application, point densities of this magnitude are much higher than required and the point cloud was reduced by 10% to have a maximum of 1 point within a 1 cm radius (7.6 million points over the entire case study area). The filtered point cloud was then reconstructed into a watertight, manifold mesh using SSD reconstruction, shown in Fig. 5.3. For this example, the entire point cloud processing workflow took 10 minutes; however the amount of required memory ($\sim 10 \text{ Gb}$) may limit the scalability of SSD reconstruction to much larger areas.

5.3.4 SPH simulation

Multiple SPH simulations examining the effect of flash flood flow rates on inundation, flow structures and velocities were run, using the terrain model generated from the previous steps. Computational time for the simulations increases by the cube of particle resolution and can therefore be reduced significantly through increasing particle spacing and simplification of the terrain. Terrain resolution and particle spacing was chosen here to be the largest resolution size of the smallest features that might affect the flow. Input flow rates of 25, 50 and $150 \text{ m}^3\text{s}^{-1}$ were considered, with a particle spacing of 12.5 cm. In the highest flow rate scenario, this required 2.8 million fluid particles to be simulated, which took 2 weeks of runtime to simulate 150 seconds of inundation on a 12 core, 2.93 GHz processor.

Figure 5.4 displays the velocities and inundation patterns 40 seconds after the flash flood was initiated for each flow rate. The fluid is shaded by velocity, with red being 10 ms^{-1}

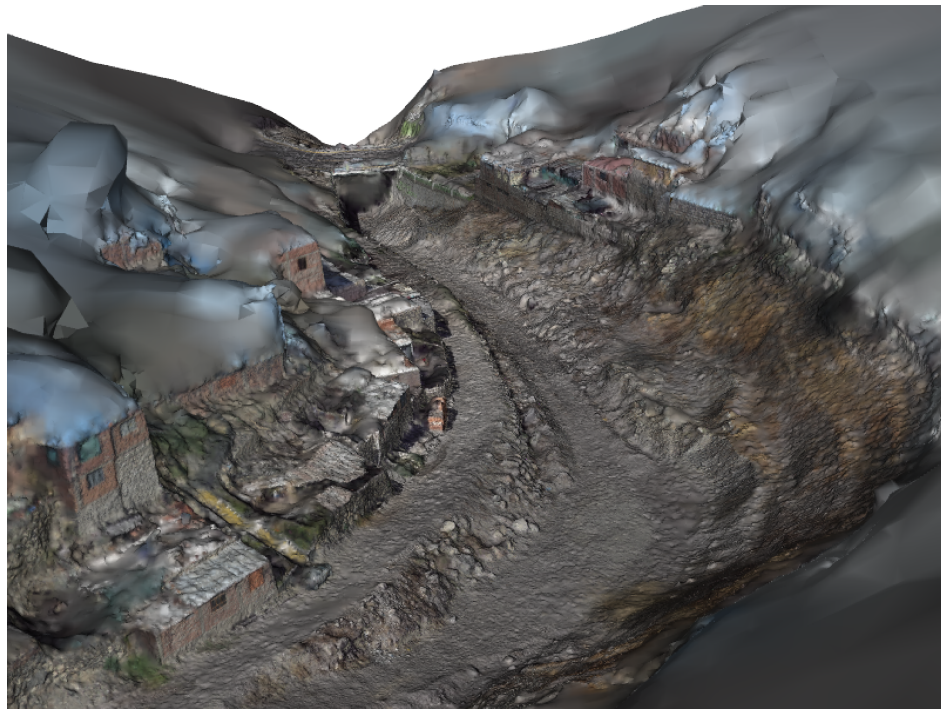


FIGURE 5.3: Watertight surface reconstruction of the case study area using SSD (looking downstream towards bridge).

and blue being 0 ms^{-1} . The inundated area and velocities increase with flow rate, which is expected given the larger volume of water in the flow. The shape and magnitude of some flow structures are also different for the three flow rates. The effect of small features in the terrain is largely invisible in the highest flow rate scenario, with the flow mainly being guided by the bend in the channel. The effects of smaller features on the flow are noticeable for the 50 and $25 \text{ m}^3\text{s}^{-1}$ scenarios. For example, the small access road into the channel (circled in Fig. 5.4) causes hydraulic jumps to form in the lower flow rate scenarios, but the high flow rate scenario is largely unaffected by this feature. This demonstrates the necessity of detailed 3D representations of terrain and modelling, particularly when considering smaller, high frequency flooding scenarios.

5.4 Conclusion

The workflow presented here describes a process for generating 3D terrain models by utilising advances in structure-from-motion, multi-view stereo, point cloud processing and surface generation. The process is inexpensive, rapid, captures fine scale features and accurately represents 3D structures within complex environments. The parallel processing of image matching ensures the workflow is scalable to a large number of images. By reducing the cost and acquisition time, terrain models can be generated at a higher frequency, better capturing transient small-scale features such as flow blockages and obstacles that can affect flow behaviour. Data processing is achieved through the use of a modular workflow engine,

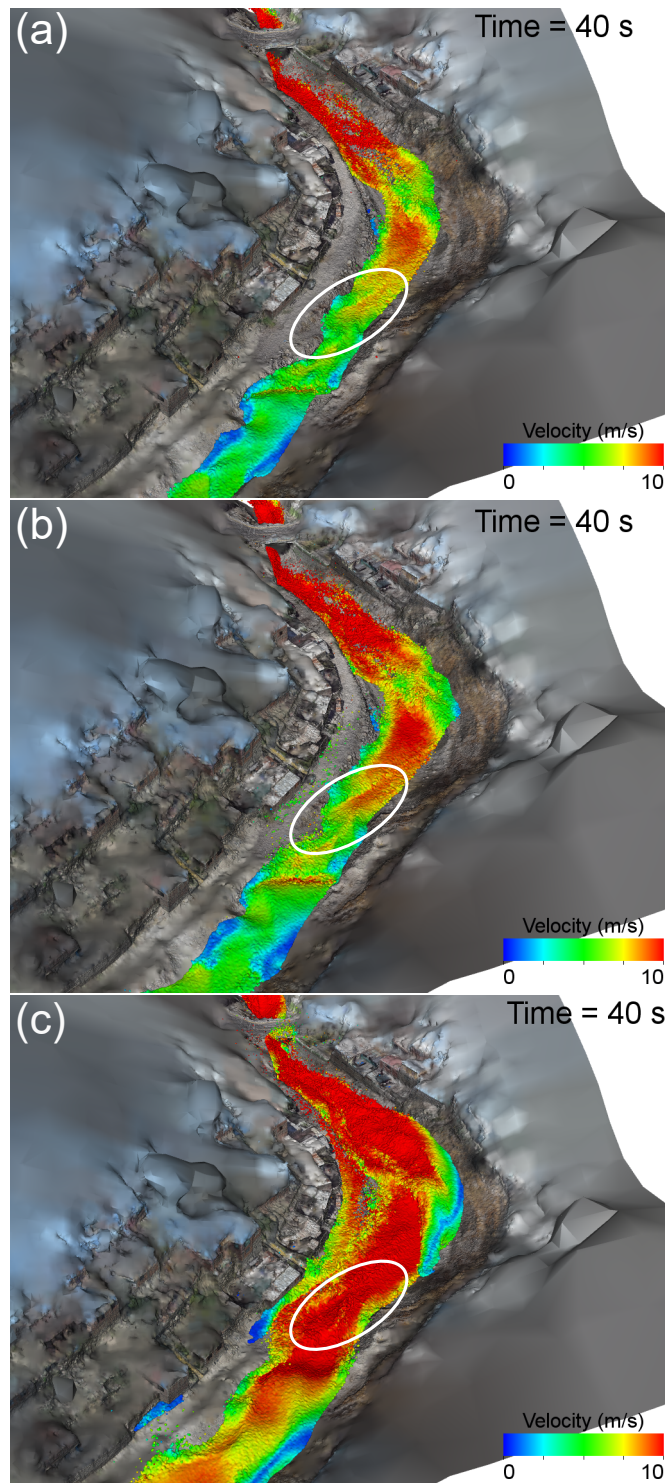


FIGURE 5.4: SPH simulations of a flash flood in Quebrada San Lazaro with flow rates of (a) 25, (b) 50 and, (c) 150 m³s⁻¹. Fluid is shaded by velocity magnitude of the free surface. White circle highlights small road seen to affect flow structures in lower flow rate simulations.

which allows for new methods to be implemented as research into particular areas progresses. The flexibility of the workflow engine, in addition to the usage of open source libraries and data structures provides opportunities beyond the use case demonstrated here, as the process and data generated may be used in various visualisation, terrain analysis and risk assessment fields of study.

The use and an application of this workflow was demonstrated using the case study area of Arequipa, Peru, where the resulting terrain model was used to predict the impacts of flash flood events using smoothed particle hydrodynamics. In addition to the presented numerical modelling application, the resulting terrain models can be used in a variety of applications such as visualisation, building classification and vulnerability estimation.

Quantifying lahar damage using numerical modelling

Stuart R. Mead, Christina Magill, Vincent Lemiale, Jean-Claude Thouret and Mahesh Prakash

Natural Hazards and Earth System Sciences

Volume 17, 2017

doi: 10.5194/nhess-17-703-2017

Abstract

Lahars are volcanic flows containing a mixture of fluid and sediment which have the potential to cause significant damage to buildings, critical infrastructure and human life. The extent of this damage is controlled by properties of the lahar, location of elements at risk and susceptibility of these elements to the lahar. Here we focus on understanding lahar-induced building damage. Quantification of building damage can be difficult due to the complexity of lahar behaviour (*hazard*), varying number and type of buildings exposed to the lahar (*exposure*) and the uncertain susceptibility of buildings to lahar impacts (*vulnerability*). In this paper, we quantify and examine the importance of lahar hazard, exposure and vulnerability in determining building damage with reference to a case study in the city of Arequipa, Peru. Numerical modelling is used to investigate lahar properties that are important in determining the inundation area and forces applied to buildings. Building vulnerability is quantified through the development of critical depth–pressure curves based on the ultimate bending moment of masonry structures. In the case study area, results suggest that building strength plays a minor role in determining overall building losses in comparison to the effects of building exposure and hydraulic characteristics of the lahar.

Keywords

lahar · hazard · building vulnerability · rheology · simulation

6.1 Introduction

Lahars, defined as gravity driven flows containing a mixture of volcanic sediment and water (Vallance and Iverson, 2015), have caused severe damage to infrastructure and buildings (e.g. de Bélizal et al., 2013; Pierson et al., 2013; Ettinger et al., 2015; Jenkins et al., 2015) in addition to being responsible for a large proportion of volcanic fatalities (Auker et al., 2013). Assessing the extent of potential lahar damage can be difficult due to the complexity of flow behaviour, varying number of elements (e.g. buildings and bridges) exposed to lahars and a lack of knowledge in the structural capacity of these elements to withstand damage causing components of the lahar flow. Using the common definitions of Varnes (1984), we define the damaging components of lahar flow (e.g. velocity, depth and pressure) as the hazard; environmental characteristics of exposed elements (e.g. building locations and orientations) as the exposure; and the ability of exposed elements to withstand the hazard (e.g. building strength) as vulnerability. Lahar induced damage is controlled by the interactions of these factors; however, the importance of each component can vary. Here we focus on quantifying and examining the role of hazard, exposure and vulnerability in determining lahar induced building damage.

Post-event field assessments of building damage can elicit information relating lahar hazard to structural damage. However, these assessments tend to only record information on substantial damage, are affected by terrain changes during the event which alter exposure, and often rely on a-priori assumptions of building strength and vulnerability (Wilson et al., 2014; Ettinger et al., 2015). Pre-event assessments are affected by the lack of reliable hazard intensity measures (van Westen et al., 2006; Ettinger et al., 2015), differences in spatial and temporal scales, uncertainty surrounding site-specific lahar triggers (Di Baldassarre and Montanari, 2009), and a lack of structural information on building stock (Ettinger et al., 2015). These issues are reflected in the relative lack of studies on hazard impact in urban areas (Wilson et al., 2014; Jenkins et al., 2015) and often results in a reliance on expert judgement to develop vulnerability models for lahars and flash floods (Ettinger et al., 2015).

The physical vulnerability of buildings, defined as the susceptibility of a building to damage with respect to the hazard (Künzler et al., 2012), is a function of building characteristics such as size, shape, age, construction materials, structural integrity, maintenance and build quality (Martelli, 2011; Künzler et al., 2012; Ettinger et al., 2015). Information on these building properties is often lacking and hard to collect on a large scale. This commonly leads to the simplification of vulnerability into a measure that can provide a relative indication of vulnerability and consequent damage (Künzler et al., 2012). Studies simplifying vulnerability into a relative index use a combination of qualitative and quantitative metrics obtained through building surveys, interpretation of remote sensing data and GIS techniques to map and analyse vulnerability on a large scale (e.g. Lavigne, 1999; Künzler et al., 2012; Galderisi et al., 2013; Thouret et al., 2013; Thouret et al., 2014; Ettinger et al., 2015). These methods can be applied to understand and highlight spatial patterns in vulnerability; however, as a

relative measure, they cannot provide guidance on absolute damage for any specific event.

A direct estimation of damage caused by specific events requires quantified relationships describing a buildings response to the hazard. Buildings can be damaged through a number of mechanisms including: (i) direct damage resulting from static and dynamic forces imposed by the flow; (ii) damage to foundations through erosion and scour; (iii) buoyancy effects of the flow causing structures to float; (iv) direct damage from larger debris (missiles) within the flow; and (v) indirect damage caused by chemical and biological actions such as seeping induced weakness of mortar (Kelman and Spence, 2004). All these actions, apart from chemical and biological effects, are related directly to lahar depth, velocity or a combination of depth and velocity. Thus, a common approach in determining building damage thresholds for a particular building type is to relate damage to hazard intensity measures of depth and/or velocity (e.g. Zanchetta et al., 2004; Custer and Nishijima, 2015; Jenkins et al., 2015). However, building typologies are affected by socio-economic, cultural and institutional conditions (Künzler et al., 2012) and hazard intensities (flow depth and velocity) are affected by building environmental factors such as local elevation, distance from main channels and orientation (Thouret et al., 2014). This results in complex interactions between hazard, exposure and vulnerability. These issues cause direct vulnerability relationships to be site-specific and requires detailed investigation of the regions at risk to examine the relative effects and role of hazard, exposure and vulnerability on building loss.

We attempt to quantify and examine the components that determine building damage in a small area within the city of Arequipa, Peru. A relative index of vulnerability on a city-block scale was developed for Arequipa in Thouret et al. (2013) and Thouret et al. (2014). The studies by Thouret et al. highlighted two groups of vulnerability indicators (building characteristics and the physical setting) that play an important role in determining vulnerability within Arequipa. In this study, we separate the building characteristics (i.e. vulnerability) from physical setting (i.e. exposure) to examine the effect of hazard (flow rate and rheology), exposure (building orientation and location) and vulnerability (building type) components on building loss within Arequipa. Physical vulnerability of buildings is explicitly separated from exposure through the development of a building damage model dependent on flow velocity, depth and sediment concentration. Simulations of lahar flow using smoothed particle hydrodynamics are used to examine how flow characteristics and the physical setting of city blocks affects forces on buildings and the consequent damage. While, for reasons explained earlier, damage functions presented here are necessarily specific to Arequipa, the hazard modelling approach and vulnerability model development are described in detail to support risk assessment in other regions affected by lahars.

6.2 Case study: Quebrada Dahlia, Arequipa, Peru

The central business district of Arequipa, the second largest city in Peru, is situated 17 km south-west of the summit of El Misti (Fig. 6.1), a steep stratovolcano with a history of

explosive eruptions. Rapid population growth since 1960 has resulted in an expansion of the city towards the ring plain and steep slopes of El Misti (Thouret et al., 2013). Arequipa is drained by several ravines (locally called quebradas or torrenteras), shown in Fig. 6.1, that have been shaped by lahars and floods originating from the volcano on volcanoclastic fans north-east of the city. These quebradas are normally dry but carry water sporadically during the December to March rainy season (Vargas Franco et al., 2010; Martelli, 2011; Thouret et al., 2013; Sandri et al., 2014). Flash floods and hyper-concentrated flows occur relatively frequently in the quebradas, with return periods between 2 and 10 years (Vargas Franco et al., 2010; Thouret et al., 2013). Previous studies of lahar hazard and vulnerability for Arequipa identified seven alluvial terraces (T0, T1, T1', T2, T2', T3 and T4) based on stratigraphy and local elevation above the quebrada and the Rio Chili valley (Martelli, 2011; Thouret et al., 2013; Thouret et al., 2014). The likelihood of inundation by a lahar or flash flood decreases with each terrace. Terrace levels T0 and T1 (up to 3 m above the quebrada) are frequently flooded (approx. every 2 to 10 years). The higher terraces (T1' to T2', 3 to 10 m above the quebrada) are rarely flooded (estimated 20 to 100 years) and the highest terraces (T3 and T4) are only likely to be inundated by lahars linked to large eruptions (Thouret et al., 2013; Thouret et al., 2014). A city wide vulnerability study by Thouret et al. (2014) identified that the city blocks most vulnerable to flash floods and lahars were on lower terraces and typically within 100 metres of a quebrada. To build on this study and investigate the vulnerability

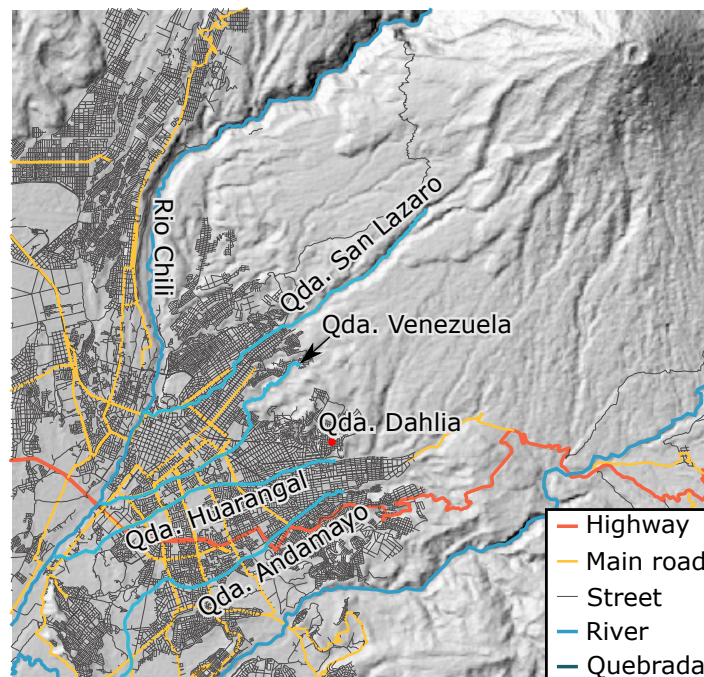


FIGURE 6.1: Location of Arequipa in relation to El Misti volcano, showing the main quebradas and the location of the Quebrada Dahlia study area.

of the quebrada channel and banks in detail, simultaneous photogrammetry and building surveys were undertaken along short sections (approximately 200 m) of several quebradas

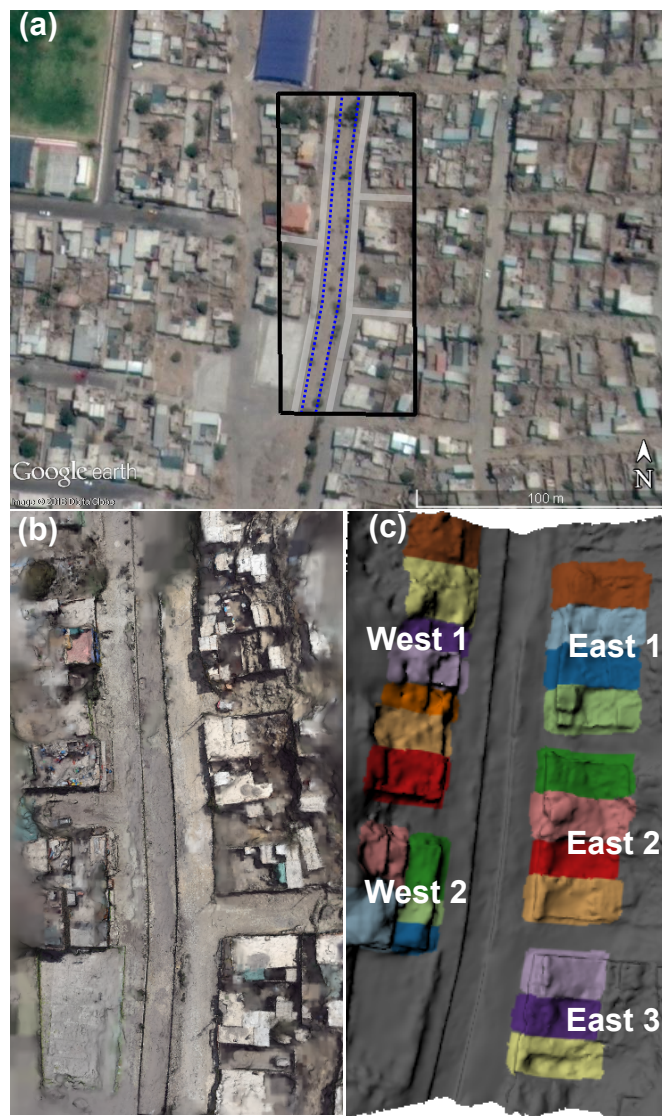


FIGURE 6.2: Overview of Quebrada Dahlia study area, Arequipa, (a) aerial image with black outline showing study area, dashed outline showing channel banks and transparent lines showing streets in the area, (b) photogrammetric reconstruction of the surface and (c) individual buildings and building blocks identified from building surveys.

during September 2013. Here we focus on one 150 m long section of Quebrada Dahlia to examine lahar hazard and building damage. Quebrada Dahlia is a small tributary of Quebrada Mariano Melgar-Huarangal (Fig. 6.1), which is situated in the Mariano Melgar District on the north-easternmost fan of Arequipa, shown in detail in Fig. 6.2. The case study area was chosen for the following reasons:

- The quebrada channel is relatively straight, reducing the effect of bends in the water-course on lahar dynamics.
- Building quality varies from well built reinforced masonry buildings to makeshift structures with little to no mortar. This allows for an investigation of the effects of building quality on damage caused by lahars.
- All buildings are situated on the lowest terraces (T0 – T1', 1 – 5 m above the channel), meaning they may be affected by even the smallest events identified in Vargas Franco

et al. (2010) and Thouret et al. (2013).

A three-dimensional reconstruction of the terrain and buildings along Quebrada Dahlia was created using the photogrammetry method described in Mead et al. (2015). The surface reconstruction, shown in Fig. 6.2b, contained 1.4 million points with a surface density of between 150 and 750 points per m². A GNSS-D survey undertaken in October 2014 enabled geo-referencing of the terrain reconstruction for possible inclusion in future GIS applications. The surface reconstruction was smoothed and reduced to create a lower-resolution terrain model shown in Fig. 6.2c, to be used in the lahar simulations. The terrain model in Fig. 6.2c contains 22 buildings identified during building surveys in 2013. Streets and the quebrada (shown in Fig. 6.2a) separate these buildings into five city blocks (labelled in Fig. 6.2c), referred to hereafter as ‘blocks’. Typology of each building was characterised through surveys undertaken in 2013 following the approach of Thouret et al. (2014). In this approach, buildings are classified as one of 8 structural types (1A – 8C) based on a visual inspection to determine construction material, roof type and structural support (see Table 6.1). These types were then grouped into larger simplified structural classes. Using this building classification system, the study area contains 8 class A0 buildings, 7 class A buildings and 7 class B buildings (see Table 6.2 for a description of building types and structural classes).

TABLE 6.1: Individual building type and vulnerability classes for each block in the Quebrada Dahlia study area. Block ID increases from north to south.

Block	ID	Type	Vulnerability Class	Vulnerability Class	Type	ID	Block
West 1	1	1A	A	A0	2A	1	East 1
	2	1A	A0	A0	2A	2	
	3	4	B	A	3	3	
	4	4	A0	A0	1B	1	East 2
	5	2B	A0	A	3	2	
	6	3	A	A0	1B	3	
	7	4	B	A0	1A	4	
West 2	1	4	B	B	4	1	East 3
	2	4	B	A	3	2	
	3	4	B	A	3	3	
	4	4	B				
	5	3	A				

6.3 Developing building vulnerability relationships

Buildings and infrastructure can be damaged through a variety of mechanisms brought upon by actions of a lahar. Here, as in most other studies of lahar damage (Zanchetta et al., 2004; Toyos et al., 2008; Ettinger et al., 2015; Jenkins et al., 2015), we focus on the direct damage resulting from hydrostatic and hydrodynamic forces applied to buildings. We regard

TABLE 6.2: Building types and simplified structural classes from Thouret et al. (2014).

Typology	Building description	Simplified structural class
1A 1B 2A 2B	Unreinforced masonry of lapilli, ignimbrite or terracotta with no roof support structure (i.e. metal sheet roof).	A0
3	Terracotta masonry with reinforced concrete roof.	A
4	Terracotta masonry with reinforced concrete frame and roof.	B
5	Historical ignimbrite building with mortar.	A
6A 6B 6C	Ignimbrite masonry with reinforced concrete elements or modifications.	B

these actions as the most important, although scour and large debris missiles within the flow can also cause significant damage (Jenkins et al., 2015). Scour and debris actions are neglected here as they are currently too difficult to predict and incorporate into large scale loss analyses (Kelman and Spence, 2004), particularly in regions with limited hazard and exposure information.

The building stock within Arequipa is characterised mostly by masonry structures of varying quality, with some reinforced concrete structures (Thouret et al., 2014). Therefore, we develop vulnerability relationships that are primarily focused on masonry buildings. A structural failure model similar to those employed by Roos (2003), Custer and Nishijima (2015) and Zeng et al. (2015) is implemented. In these models, masonry walls are presumed to fail when the lateral pressure imposed on the wall results in a bending moment or shear force greater than the walls calculated ultimate bending moment or ultimate shear force. The ultimate bending moment (M_u) is calculated using the following equation (Roos, 2003):

$$M_u = (f_t + f_d) \frac{wb^2}{6}, \quad (6.1)$$

where f_t is the tensile strength of the masonry wall, f_d is the design compressive stress acting on the wall, w is the width of the wall facing the flow and b is the thickness of the wall, which is assumed equal to the brick width. Tensile strength and design compressive stresses for buildings in Arequipa are calculated using the approach specified in Australian Standard (AS) 3700-2011 and summarised in section 6.8 in addition to an approach to calculating ultimate shear force. Preliminary investigations using these two approaches suggested the force required to overcome the ultimate moment was consistently lower than the force required to overcome the ultimate shear force. Therefore, we chose to focus the remainder of this study on the ultimate bending moment only.

The use of a foreign standard to calculate the ultimate moment should still be valid for the

study area if construction material properties from Arequipa are used as inputs. However, some specifications and assumptions of the standard may not be relevant. Notably, observations during the building survey suggests that construction methods and conformity to specifications within the standard differs substantially to those specified in AS3700-2011. This difference will influence ultimate bending moments, particularly those for low-quality unreinforced building types (i.e. building types 1A-2B) due to the makeshift nature of construction. For these classes, calculated bending moments will represent a ‘best case’ scenario where masonry unit strength and quality has not been compromised by construction methods.

6.3.1 Critical depth-pressure curves

The range of design compressive stress for each building typology is shown in Fig. 6.3. The range was obtained by calculating the design compressive stress for every configuration of masonry compressive strength (f_c), brick width and thickness coefficient (k_t) in section 6.8. Buildings with reinforced frames (types 3, 4 and 6) are able to withstand much greater compressive stresses than non-reinforced buildings (types 1, 2, 5). Buildings with reinforced frames (types 3, 4 and 6) can withstand much greater compressive stresses than non-reinforced buildings (types 1, 2, 5). The wall thickness has a large effect on building strength, which is consistent with observations of Jenkins et al. (2015). Notably, the design compressive stresses are similar for building types that share the same simplified structural class identified in Thouret et al. (2014), based on the structural classes of Zuccaro et al. (2008). Given these similarities, we also use the simplified structural classes (A0, types 1A-2B; A, types 3 and 5; and B, types 4 and 6A-6C, see Table 2) from Thouret et al. (2014). The critical depth (i.e. hydrostatic pressure) and dynamic pressure required to overcome the ultimate bending moment (Eq. 6.1) for each structural class is shown in Fig. 6.4. These curves assume that both hydrostatic and dynamic pressure acts on walls. Other studies (e.g. Jenkins et al., 2015) assume only dynamic pressure acts on walls due to an equalisation of lahar depths on the inside and outside of buildings. This equalisation can take a reasonable amount of time, which is likely to be much longer than the simulation duration studied here (see following sections).

The curves in Fig. 6.4 indicate the structural limit of each class; combinations of depth and pressure that fall above the curves indicate an applied moment greater than the building can withstand. Conversely, combinations of depth and pressure that fall below the curves indicate an applied moment less than the maximum the building can withstand. Figure 6.4 shows that the critical depth decreases with the density of flows as the hydrostatic pressure gradient is much larger for sediment-rich lahars. The critical depths and pressures are also affected by the structural class, with A0 structures being much less resilient than A and B structures. However, wall thickness has the most dominant effect on determining the strength of buildings. Wider walls increase the section modulus ($wb^2/6$ in Eq. 6.1), resulting in stiffer walls that also have a higher compressive stress capacity.

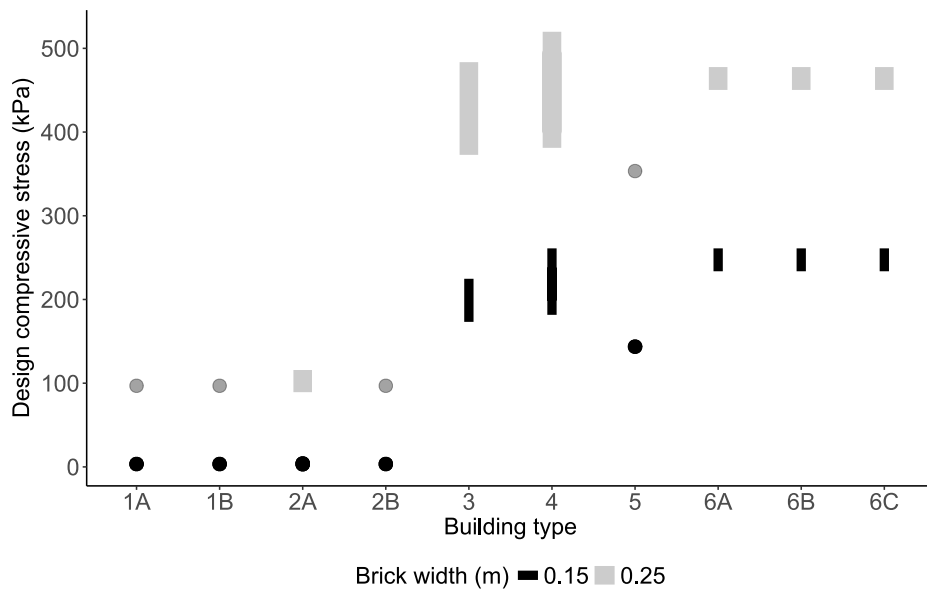


FIGURE 6.3: Range of design compressive stress for building types 1A - 6C defined in Thouret et al. (2014). Compressive stress capacity was calculated for every configuration of compressive strength (f_c), bedded area (A_b), thickness coefficient (k_t) at brick widths (b) of 150 mm and 250 mm.

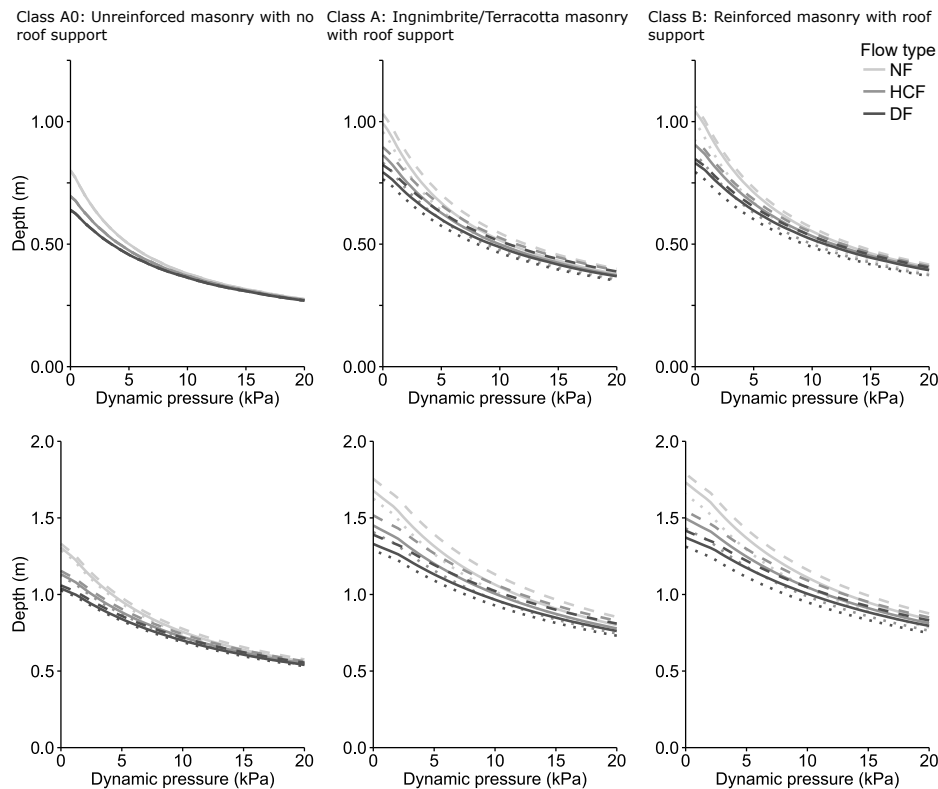


FIGURE 6.4: Critical depth and dynamic pressures for failure of building classes A0, A and B for brick widths of 0.15 m (top) and 0.25 m (bottom). Shading of the lines indicate flow type and density, dotted lines and dashed lines represent the minimum and maximum forces required. Densities are for a Newtonian flow (NF, $\rho = 1000 \text{ kg}\cdot\text{m}^{-3}$), hyper-concentrated flow (HCF, $\rho = 1500 \text{ kg}\cdot\text{m}^{-3}$) and debris flow (DF, $\rho = 1915 \text{ kg}\cdot\text{m}^{-3}$).

6.4 Lahar numerical modelling and results

6.4.1 Lahar rheology and implementation in smoothed particle hydrodynamics

Lahar flow behaviour varies depending on the sediment concentration and composition of the flow. At very low concentrations of sediment, lahars will flow in a similar manner to water. At higher concentrations, interactions between the sediment and water cause a non-linear response to stresses applied to the flow. This non-linearity in the stress-strain relationship requires the use of rheology models that capture both the linear (i.e. water-like, called *Newtonian*) and non-linear (called *non-Newtonian*) shear response. Here we implement a generalised quadratic rheology model to simulate lahar flows along the case study area. The quadratic rheology model can be expressed as (Julien and Lan, 1991; O'Brien et al., 1993; Jan and Shen, 1997):

$$\tau = \tau_y + \mu\dot{\gamma} + \alpha\dot{\gamma}^2, \quad (6.2)$$

where τ is the shear stress, τ_y is the yield strength, μ is the viscosity, $\dot{\gamma}$ the shear rate and α is the turbulent-dispersive parameter, a coefficient that combines the effects of turbulence and dispersive stresses caused by sediment collisions. This model follows the general form of the Herschel-Bulkley equation commonly used to describe non-Newtonian lahar behaviour (Manville et al., 2013).

Commonly used lahar models such as the Pitman and Le (2005) model in Titan2D (Patra et al., 2005) or laharz (Iverson et al., 1998) are able to delineate hazard zones or lahar inundation areas on a large scale. However, the reduced dimensions of these models (e.g. through depth-averaging in Titan2D) means they are unsuitable for the detailed modelling of lahar flow in urban environments required for this study. Instead, we implement the quadratic rheology model using three-dimensional smoothed particle hydrodynamics (SPH) to simulate lahar flows along the case study area. SPH is a Lagrangian method that tracks the physical motion of interpolation points (commonly referred to as particles) through space. It is well suited to modelling free surface fluid flows, predicting and tracking the motion of dynamic objects within the flow (e.g. Cleary et al., 2012; Prakash et al., 2014; Cleary et al., 2015), and modelling complex flooding scenarios involving interactions with buildings (e.g. Mead et al., 2015). The SPH method used here is described in Cleary and Prakash (2004) and Prakash et al. (2014). Non-Newtonian lahar rheology was implemented in SPH using an apparent Newtonian viscosity (η). Assuming the fluid is isotropic, constitutive equations for rheology can be written as a generalised Newtonian fluid in terms of the apparent viscosity:

$$\tau = \eta\dot{\gamma} \quad (6.3)$$

When the apparent viscosity is constant the fluid is Newtonian with a viscosity of η . Non-Newtonian fluids can be modelled using Eq. 6.3 by developing relationships for η based on constitutive equations (Mitsoulis, 2007). Using this approach, the apparent viscosity for the quadratic rheology is:

$$\eta = \frac{\tau_y}{\dot{\gamma}} + \mu + \alpha\dot{\gamma}, \quad (6.4)$$

To reduce computational time we use the viscosity regularisation approach of Papanastasiou (1987), described in Mitsoulis (2007) and Minatti and Paris (2015). Regularisation is required as the apparent viscosity approaches infinity at low strain rates when using Eq. 6.4, reducing the simulation time step and significantly increasing computational cost. Using the Papanastasiou (1987) approach, the regularised viscosity used in simulations is:

$$\hat{\eta} = \frac{\tau_y}{\dot{\gamma}} (1 - \exp^{-c\dot{\gamma}}) + \mu + \alpha\dot{\gamma}, \quad (6.5)$$

where c is the viscosity scaling parameter, larger values of c result in a better approximation of the constitutive equation (Eq. 6.4), while smaller values result in smaller apparent viscosities and larger simulation time steps. Here we set $c = 200$, a value which yielded the best balance between simulation speed and accuracy in validation simulations that compared flow down an inclined plane with analytical solutions.

6.4.2 Lahar simulations

Static and dynamic pressures acting on the buildings in the Quebrada Dahlia study area were determined for twelve different inundation scenarios. Dynamic pressure was calculated as $\frac{\rho v^2}{2}$. Dynamic pressure is used extensively in literature examining the forces applied to buildings by fluids (see e.g. Roos, 2003; Zuccaro et al., 2008; Jenkins et al., 2015; Zeng et al., 2015). The theoretical basis for using dynamic pressure is, based on Bernoulli's theorem: when a fluid interacts with a fixed solid surface, the velocity normal to the surface is zero and the total pressure (i.e. force per unit area) is given as the stagnation pressure

$$P = P_{static} + 0.5\rho v^2 \quad (6.6)$$

where P and P_{static} are the total and static pressure, respectively and v is the velocity normal to the wall.

We use the same SPH particle spacing (12.5 cm) of previous simulations by Mead et al. (2015). This resolution provided the best balance between computational time and resolution of fine scale features that can affect the flows. Inundation scenarios were designed to explore a wide range of flow types and velocities in order to investigate the effect of rheology and velocities on flow dynamics and forces exerted on buildings. Simulations were run for three different flow types (Newtonian, hyper-concentrated streamflow and debris flow) at constant flow rates of 25, 50, 75 and 100 m³s⁻¹.

TABLE 6.3: Density, particle concentration and rheology coefficients for hyper-concentrated streamflow and debris flow simulations, taken from Govier et al. (1957) and Julien and Lan (1991).

Flow type	Density ($\text{kg}\cdot\text{m}^{-3}$)	Particle concentration by volume (%)	Yield strength (τ_y , Pa)	Viscosity (μ , Pa·s)	Dispersive stress coefficient (α)
Hyper-concentrated streamflow	1500	30.3	0.94	0.0137	1.28×10^{-5}
Fine-grained, matrix supported debris flow	1915	55.5	0.672	0.0485	0.00224

The flow rates were chosen to produce scenarios ranging from minimal ($25 \text{ m}^3\text{s}^{-1}$) to extreme ($100 \text{ m}^3\text{s}^{-1}$) overbank flooding. The ratio between inertial and gravitational forces, expressed through the Froude number, was kept below 1 (subcritical flow) for each flow rate by varying the inflow area. Froude number consistency was used here as inertial and gravitational forces are dominant controls on environmental flows such as these. Flow types were selected to represent the characteristics of the most commonly occurring flows in Arequipa – flash flood, hyper-concentrated streamflow and fine-grained, matrix-supported debris flow (Thouret et al., 2013). Rheology of flash flood flows was considered to be completely Newtonian with a viscosity of water (i.e. $\tau_y, \alpha = 0, \mu = 0.001$ and density (ρ) = 1000), rheological parameters for hyper-concentrated and debris flows (Table 6.3) were chosen using the dimensionless ratio between dispersive and viscous stresses explained in Julien and Lan (1991). Values for yield strength (τ_y), viscosity (μ) and the turbulent-dispersive coefficient (α) were taken from the experiments of Govier et al. (1957) and Bagnold (1954), reported in Julien and Lan (1991). For a hyper-concentrated streamflow, we presumed a particle concentration by volume (C_v) of approximately 30% consisting mostly of finer particles, meaning viscous stresses are still relatively important. Debris flow scenarios were assumed to contain larger particles at a higher value C_v of approximately 55%. The particle concentration acts to increase density, viscosity and the dispersive stress coefficient in hyper-concentrated and debris flow rheologies compared to a fully Newtonian water flow. The higher particle concentration of the debris flow (compared to a hyper-concentrated flow) also results in a much higher dispersive stress coefficient, meaning that dispersive stresses will have more importance in determining flow behaviour.

Computational cost limits the length of simulations to the first 45 seconds of lahar flow for each scenario. The flow was not established and constant by 45 seconds, so these simulations do not represent the forces exerted on buildings by a steady flow rate. Instead, the scenarios considered here are more representative of the higher velocity and depth surges or waves in a lahar.

6.4.3 Flow behaviour

Figure 6.5 displays snapshots of velocity and dynamic pressure magnitudes for each flow type at a flow rate of $75 \text{ m}^3\text{s}^{-1}$. Snapshots were taken at 15-second intervals. Lahars mostly followed the developed channel of Quebrada Dahlia for the first 15 seconds before overtopping the bank and spreading outwards. Channel and overbank pressures and velocity profiles are similar for Newtonian and hyper-concentrated flows, but the velocity of overbank flow is much lower for the debris flow rheology. This lower velocity is presumably caused by increased friction in the debris flow due to the higher viscosity and dispersive coefficients. The dynamic pressure differs between each rheology as a result of the varied densities (and lower velocity for debris flows); however, the maximum pressure is still similar between rheologies as maximum velocities are mostly confined to the channel.

The highest dynamic pressure magnitudes in Fig. 6.5 are present along the centre of the channel, with much lower pressures near the buildings. The velocity magnitude may therefore not accurately represent the pressure forces acting perpendicular to the walls of each building. The critical strength of a wall is determined from the forces acting normal (perpendicular) to the structure, therefore it is important to calculate dynamic pressure from velocity normal to the wall. The section of Quebrada Dahlia studied here runs in a North-South direction and the buildings have walls that are oriented either parallel or perpendicular to the channel, so an initial understanding of the perpendicular forces acting on walls can be interpreted from the North-South (N-S) and East-West (E-W) velocity components. Figure 6.6 shows the directional components of dynamic pressure at 40 seconds for a flow rate of $75 \text{ m}^3\text{s}^{-1}$. The section of Quebrada Dahlia studied here runs in a North-South direction and the buildings are oriented parallel to the channel, so a broad understanding of normal pressure acting on buildings can be interpreted from the NS and EW components of pressure. Figure 6.6 shows a consistent pattern for all rheologies where the pressure is dominated by the streamwise (N-S) velocity. The pressure applied to walls facing the stream (\sim E-W direction, 3rd column of Fig. 6.6) is much lower than the pressure applied to walls perpendicular to the stream. Higher pressures for EW velocities are observed along cross streets splitting each city block; however, the pressure that acts perpendicular (NS) to these walls is minimal. These observations indicate that pressure calculated from the magnitude of velocity, which is often assumed to be acting perpendicular to walls (e.g. Zanchetta et al., 2004; Jenkins et al., 2015), can be much higher than actual pressure acting on walls and the use of velocity magnitudes could therefore lead to an over-estimation of building damage.

In order to accurately estimate normal forces on walls, we calculate pressures from the velocity normal to each block. The normal velocity of fluid near each block face (e.g. North and West faces of ‘East 3’ block) is calculated using the dot product of simulated velocity vectors and the direction vector of the block face. This normal velocity (v_n) is averaged across the face and used to calculate a ‘normal’ pressure using $\frac{\rho v_n^2}{2}$. Figure 6.7 compares the mean pressure magnitude and the mean normal pressure acting on the ‘West 2’ block

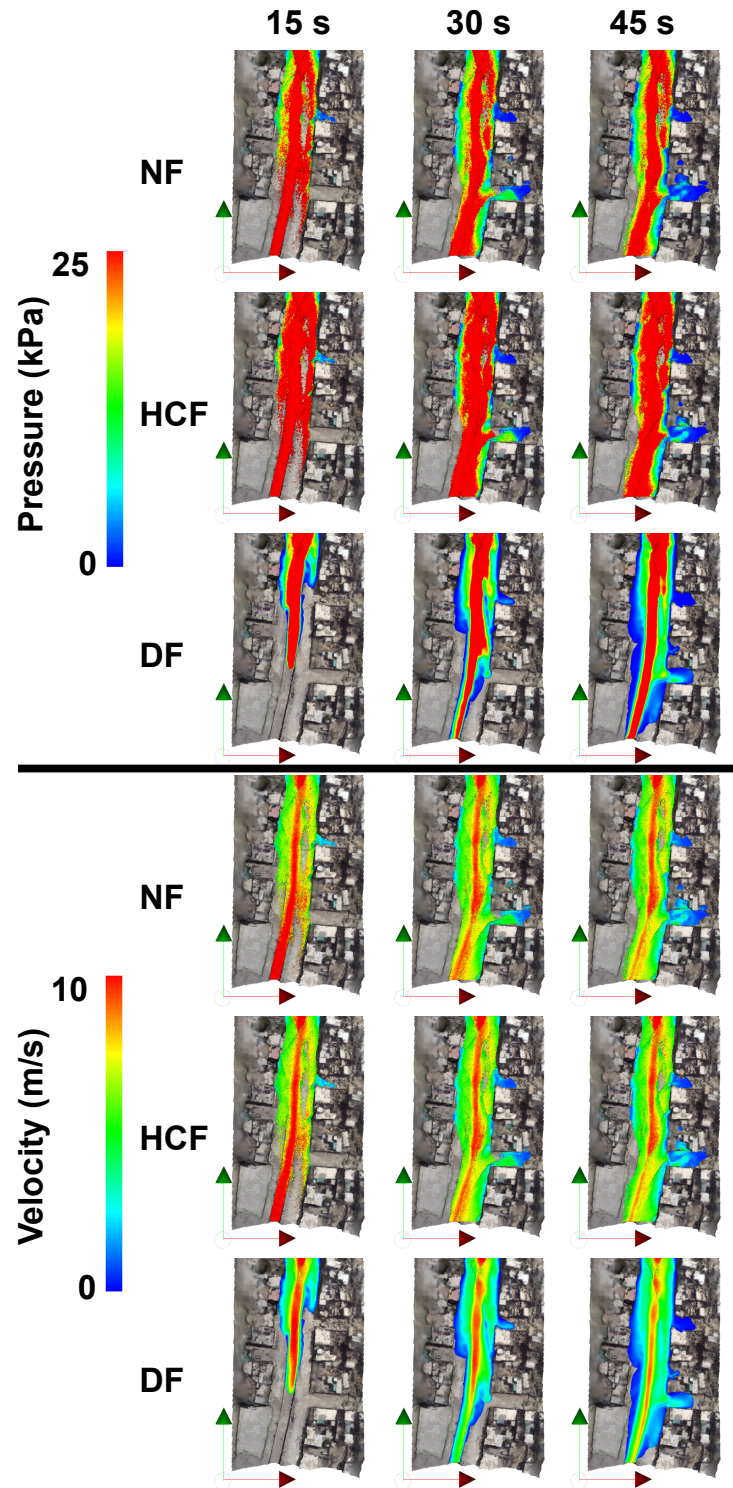


FIGURE 6.5: Evolution of dynamic pressure and velocity magnitudes for a $75 \text{ m}^3\text{s}^{-1}$ flow along Quebrada Dahlia for a Newtonian flow (NF), hyper-concentrated flow (HCF) and debris flow (DF).

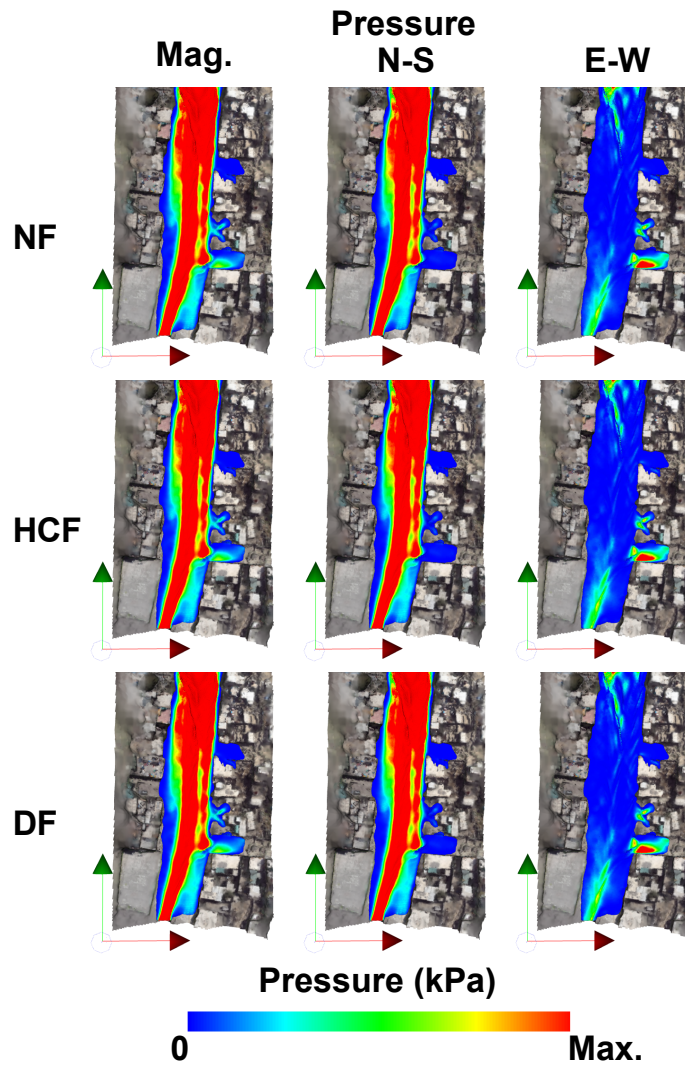


FIGURE 6.6: Directional components of dynamic pressure for a $75 \text{ m}^3\text{s}^{-1}$ flow along Quebrada Dahlia for a Newtonian flow (NF), hyper-concentrated flow (HCF) and debris flow (DF).

(see Fig. 6.2c) for Newtonian, hyper-concentrated and debris flow types. The pressures are measured for walls oriented approximately parallel to the quebrada (labelled ‘Parallel’) and north facing walls that are oriented approximately perpendicular to the quebrada (labelled ‘Perpendicular’). The pressures exerted on parallel walls by the normal velocity are up to five times lower than velocity magnitude pressures. The pressure applied to perpendicular walls also differs between normal velocity and magnitude, with the timing of peak pressure also affected. This further demonstrates the importance of considering normal velocity rather than velocity magnitude when estimating dynamic pressures (and consequently damage).

Pressures acting on each block in the study area, calculated using the technique explained in the previous paragraph, are shown in Fig. 6.8 for a flow rate of $75 \text{ m}^3\text{s}^{-1}$. Blocks ‘East 1’ and ‘West 1’ do not have walls facing perpendicular to the flow and therefore have no pressures recorded in that orientation. The pressure for each block generally follows a similar pattern through time with a well-defined peak pressure and a lower, steady background pressure. The rise of pressure to its peak value and reduction to its background value occurs over the

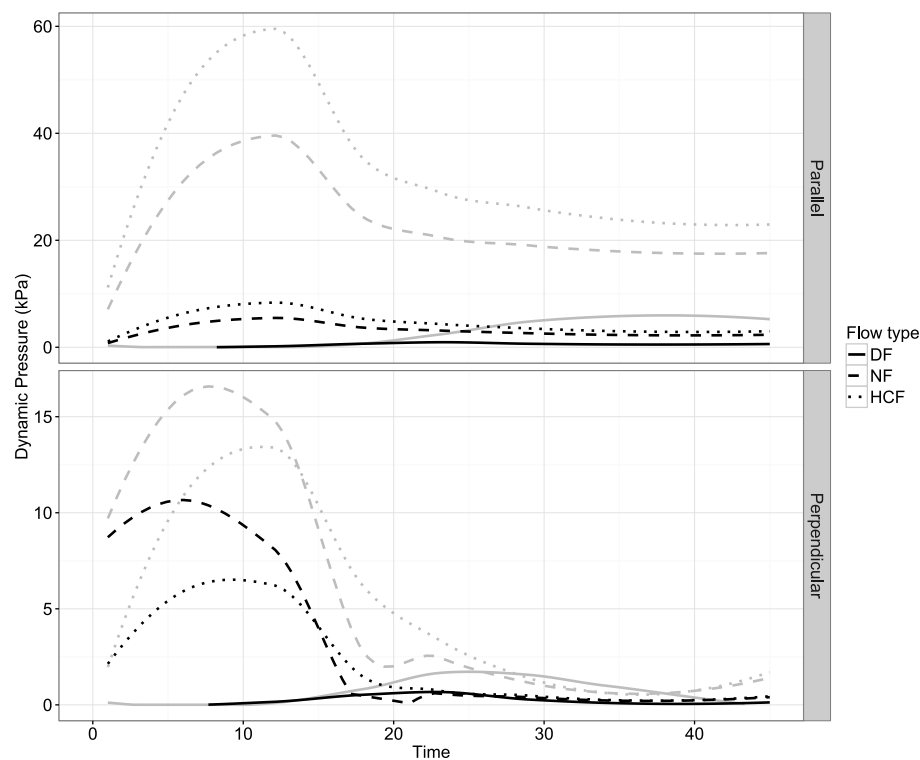


FIGURE 6.7: Comparison of mean pressure magnitude (grey lines) and mean normal pressure (black lines) on block ‘West 2’ in the parallel and perpendicular orientations for a $75 \text{ m}^3\text{s}^{-1}$ flow along Quebrada Dahlia.

space of approximately 20 seconds for each block. This timeframe is too short to allow for an equalisation of hydrostatic pressure between the inside and outside of buildings, confirming that both hydrostatic and dynamic pressures are acting on walls during lahar surges. The timing of the peak is delayed for downstream blocks and the magnitude of the peak for each block varies. The differences in peak pressure are caused by exposure effects such as orientation and elevation of each block relative to the quebrada. Walls facing perpendicular to the stream are generally exposed to higher dynamic pressures than parallel walls, but this effect appears to vary and could be dependent on cross-street elevations (cross-streets leading away from Qda. Dahlia increase in elevation at different rates).

In terms of rheology, hyper-concentrated flows mostly displayed the highest dynamic pressures acting on parallel walls. The higher density (compared to Newtonian flows) is responsible for the larger dynamic pressures (see Jenkins et al., 2015). This effect is moderated by the yield strength of the hyper-concentrated flows which cause the velocity to be lower than Newtonian flows near perpendicular walls. Debris flow pressures are much lower than both Newtonian and hyper-concentrated flows as the yield strength and dilatant rheology components limit overbank flow velocities.

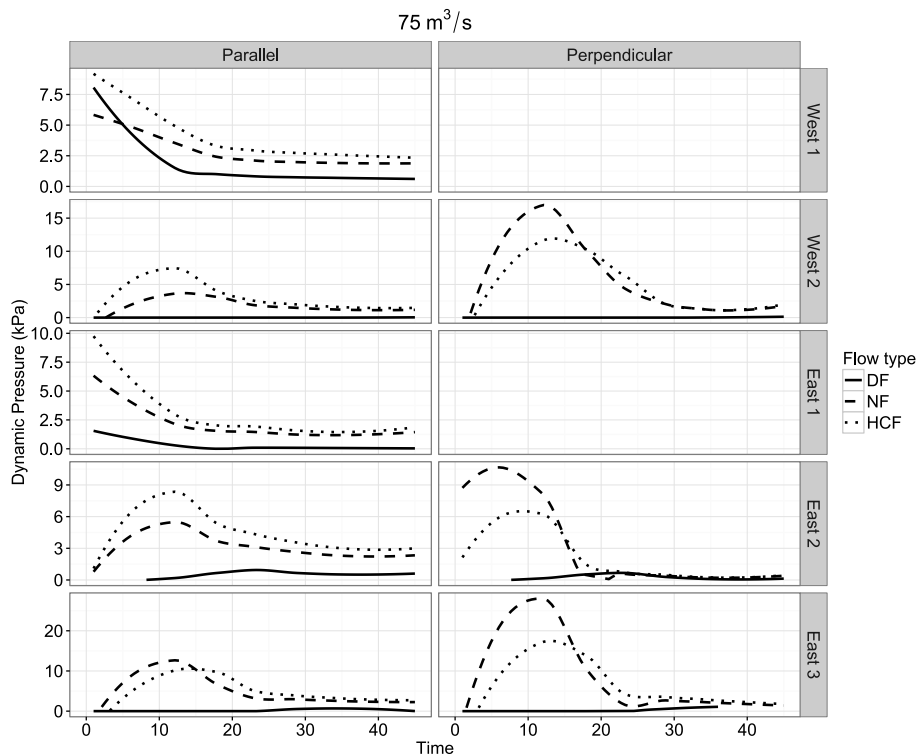


FIGURE 6.8: Mean normal pressures applied to each city block in the perpendicular and parallel orientations for a $75 \text{ m}^3\text{s}^{-1}$ flow.

6.5 Application of critical depth-pressure curves

Depth at the maximum value of pressure acting on block walls for each scenario is used to determine if individual buildings in the study area can withstand the bending moment applied by hydrostatic and dynamic pressure. Figures 6.9 to 6.11 plot the peak pressure and ‘surge depth’ (depth at the time of peak pressure) for Newtonian, hyper-concentrated and debris flows alongside critical depth-pressure curves for structural classes A0, A and B with a brick width of 150 mm (results for 250 mm brick widths are provided in appendix B). The hazard variables of flow rate and lahar rheology appear to influence building damage, although the size of the effect is difficult to determine since most scenarios place depth and pressure combinations well above the critical curves for each block. The flow depth, which affects hydrostatic pressure and bending moment location, generally increases with the flow rate while the dynamic pressure appears to be mostly controlled by the rheology in combination with flow rate. The forces applied to the ‘West 2’ block, containing one class A and 4 class B buildings, are lower than the other blocks. This is possibly due to the relative elevation and orientation of each block to the quebrada (i.e. exposure) affecting dynamic pressure and lahar depth. Debris flow scenarios at flow rates of 25, 50 and $75 \text{ m}^3\text{s}^{-1}$ indicate depths and pressures below the critical limit for this blocks building classes.

The orientation of walls to the flow direction is another element of exposure that affects the normal pressure exerted on walls. In several scenarios, perpendicular walls are subjected to higher dynamic pressures and lower depths than parallel walls. However, this effect appears

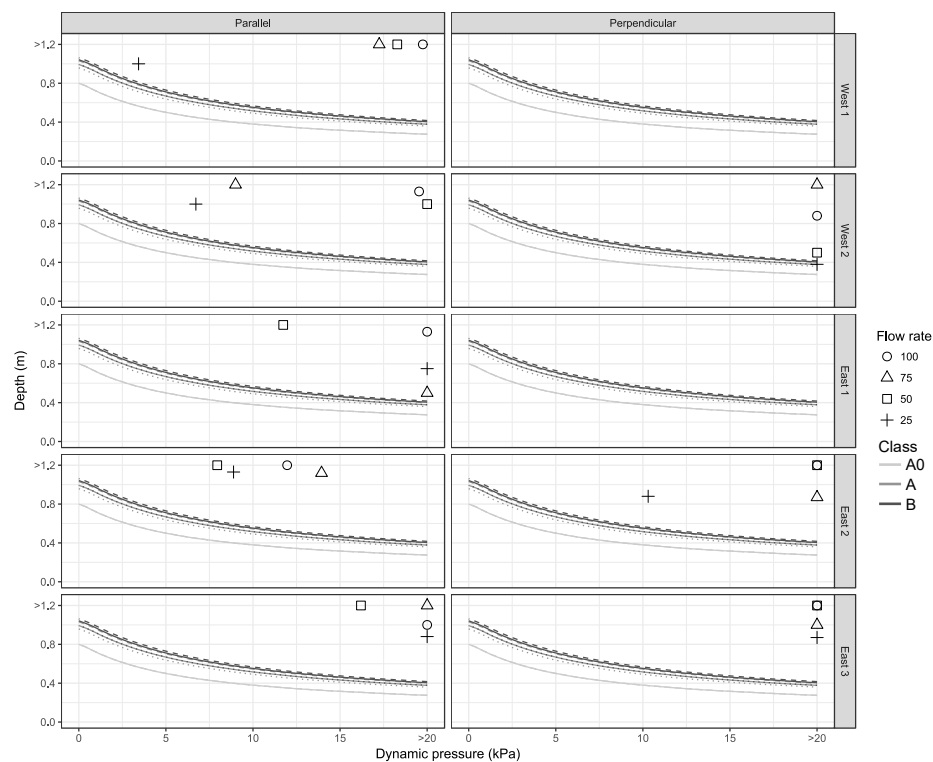


FIGURE 6.9: Critical depth-pressure curves for building classes A0, A and B subjected to Newtonian flow. Peak normal pressures and corresponding depths applied to each city block are plotted as points for each flow rate.

to be conditional to the rheology of the flow as the opposite is true for debris flow scenarios. These two effects demonstrate the importance of considering exposure elements separately to vulnerability.

The proportion of buildings with depths and pressures above the critical curve for each scenario is shown in Fig. 6.12 for 0.15 m brick widths and Fig. 6.13 for 0.25 m brick widths. Assuming a binary damage state model where damage is complete for depth-pressure combinations above the curve, these proportions can be used to directly represent building loss. For the thinner walls, all class A0 buildings are above the curve for all scenarios apart from the $25 \text{ m}^3\text{s}^{-1}$ debris flow. The ‘East 1’ block is not inundated in this scenario, resulting in two undamaged class A0 buildings. Class A and B buildings are also mostly destroyed, with the exception of lower flow rate hyper-concentrated and debris flow scenarios where some blocks are on the edge of inundation and therefore subjected to much lower depth–pressure combinations. Slightly fewer building losses occur with larger brick widths (Fig. 6.13) as the larger section modulus results in a greater resistance to bending moments. However, most buildings are still destroyed in Newtonian and hyper-concentrated flow scenarios. An exception to this is the $75 \text{ m}^3\text{s}^{-1}$ Newtonian flow where the highest pressure on the ‘East 1’ block occurs early in the simulation when the surge depth is low, reducing the magnitude of hydrostatic pressure and lowering the size of the applied moment.

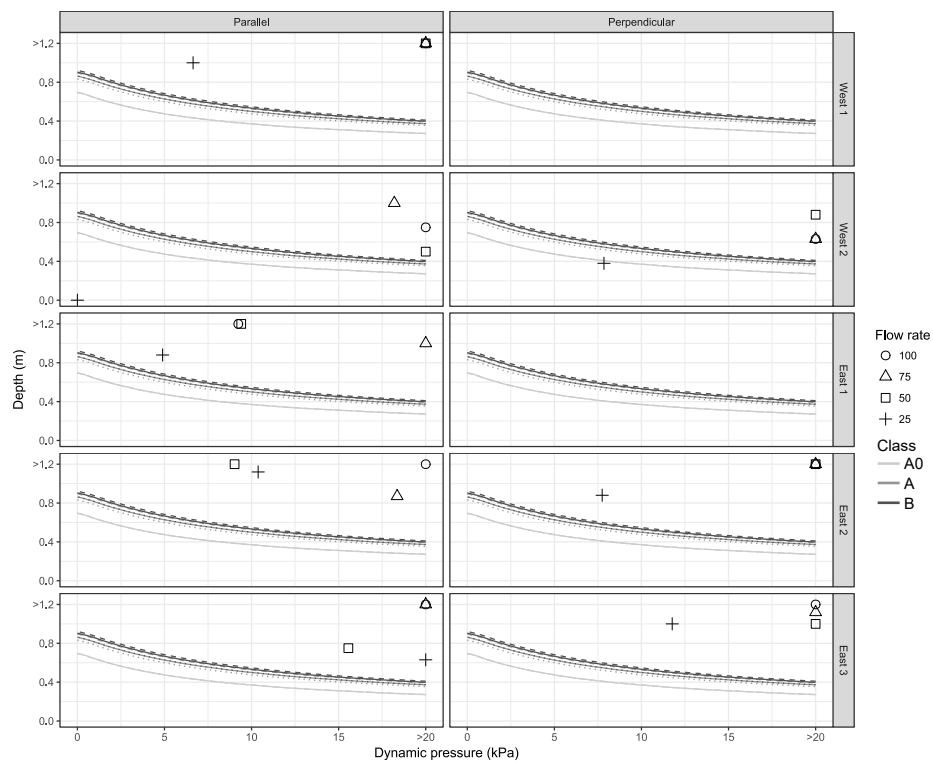


FIGURE 6.10: Critical depth-pressure curves for building classes A0, A and B subjected to a hyper-concentrated flow. Peak normal pressures and corresponding depths applied to each city block are plotted as points for each flow rate.

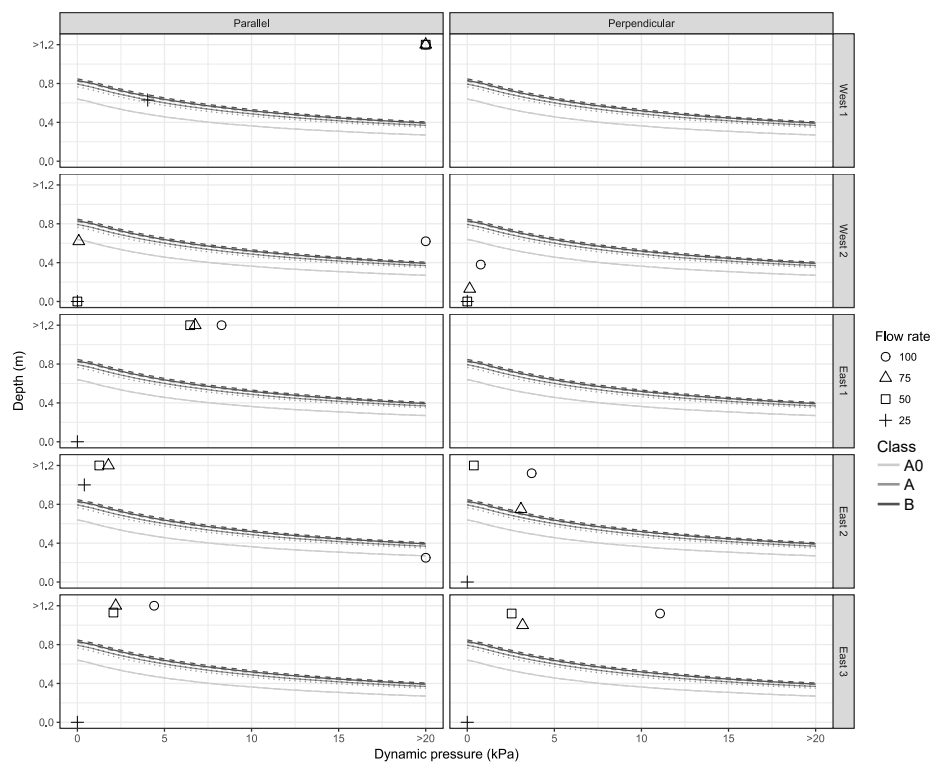


FIGURE 6.11: Critical depth-pressure curves for building classes A0, A and B subjected to a debris flow. Peak normal pressures and corresponding depths applied to each city block are plotted as points for each flow rate.

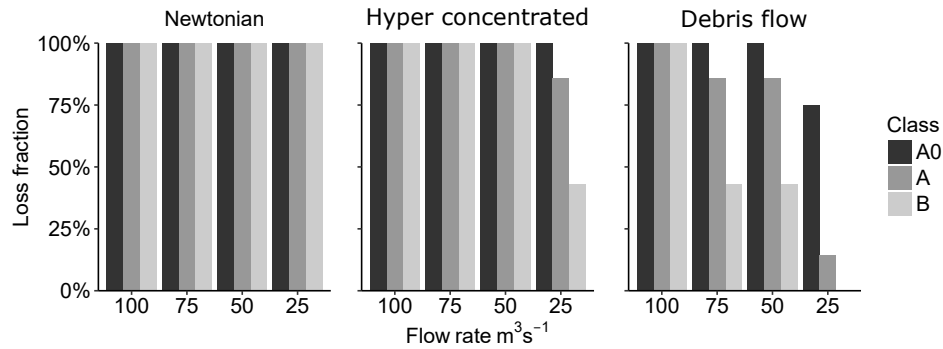


FIGURE 6.12: Building loss fraction for all flow scenarios where buildings are assumed to have a brick width of 0.15 m.

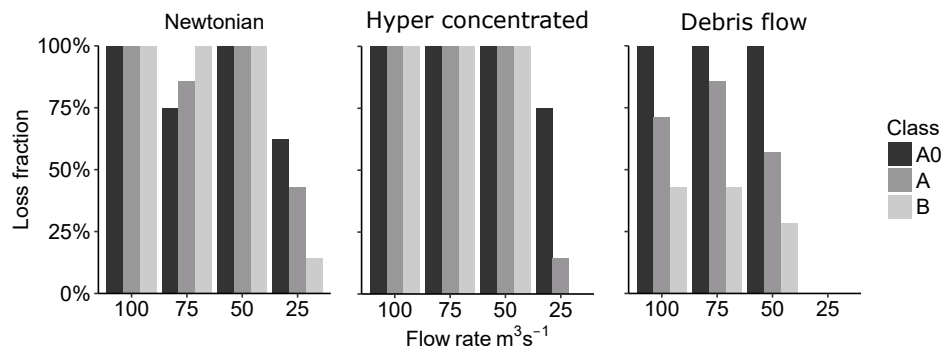


FIGURE 6.13: Building loss fraction for all flow scenarios where buildings are assumed to have a brick width of 0.25 m.

The building loss results indicate that class A0 buildings are most vulnerable, with class A buildings marginally stronger due to the roof support. Losses for type B buildings in this area are much lower; however, this appears to be more related to building exposure than structural strength as most type B buildings are in two blocks subjected to lower depth-pressure combinations for all scenarios. Overall, similar to the observations in Jenkins et al. (2015), the data presented here suggests that building strength (i.e. the vulnerability component) has a minimal effect on losses, and building location (i.e. exposure) relative to flow rate and type (i.e. hazard) plays a much greater role.

6.6 Limitations and discussion

Losses in Figs. 6.12 and 6.13 are estimates based on several assumptions that, while necessary for the estimation of building loss, could limit the accuracy of results. Firstly, the depth-pressure curves are created using ultimate bending moments derived from a foreign standard and do not consider proportional losses, only assuming damage is complete for depths and pressures above the critical curve. Second, the flow scenarios modelled here are a subset of likely scenarios and do not replicate all damage causing actions of lahar flow. Finally, the maximum total pressure was assumed to be the sum of hydrostatic and dynamic pressure and to occur when dynamic pressure was at its peak. These limitations are discussed and justified

in this section to highlight areas of improvement necessary for robust, quantitative estimation of lahar damage and vulnerability.

6.6.1 Depth-pressure curves

The critical depth-pressure curve is the contour where the ratio of applied (pressure) moment equals the ultimate (failure) moment of a given masonry wall. The calculation of ultimate bending moments followed an Australian standard (AS3700-2011). Although bending moment calculations are similar for all national standards and material properties from Arequipa were used as inputs, the standard inherently assumes conformance to construction and design standards. This is demonstrated through the assumption of a minimum mortar strength of 0.2 MPa. Page (1996) suggests this strength can be achieved with correct mortar composition and laying; however, lower strengths are possible if there is low conformance to design standards. The makeshift structures that characterise class A0 buildings are likely to have mortar bond strengths much lower than the implied minimum of 0.2 MPa. This mischaracterisation of mortar strengths for makeshift structures will result in an over-estimation of building strength and critical-depth pressure curves. Additionally, the depth-pressure curves assume a binary damage state, where failure is total when the applied (pressure) moment equals the ultimate (failure) moment. This neglects incremental damage states that require building repair (e.g. to doors or windows) and can cause a reduction in the overall building strength.

Both of these assumptions will result in an under-estimation of loss if violated. Most of the flow scenarios caused depths and pressures that exceeded critical curves by a large margin and resulted in an almost total loss; conversely, flow scenarios that did not result in total or near-total losses usually had depths and pressure values that were well below the critical curves. This suggests that these assumptions are not critical to the results shown here, but may be important to consider in other case study areas.

6.6.2 Flow scenarios

The twelve flow scenarios were chosen to understand the effect of hazard properties (flow rate and rheology) on total loss. These scenarios may not represent any specific lahar event for Qda. Dahlia. Rather, scenarios were chosen to be representative of the range of lahar rheologies and flow rates that can cause building damage in Arequipa. The chosen flows have similar characteristics to observed lahars and lahar deposits (Thouret et al., 2013) and are therefore reasonably representative of the lahar hazards expected in Arequipa.

However, damage caused by these hazards may not be representative as only the direct actions of hydrostatic and dynamic pressure were considered in this study. While direct actions are regarded as the most important source of damage, they are also favoured in risk assessment due to the large scale predictability of hydrostatic and dynamic forces (Kelman and Spence, 2004). Damage is likely to also be caused by scour and large debris missiles

within the flow (Jenkins et al., 2015). In particular, boulders are often carried by lahars at the flow front (Iverson, 1997; Doyle et al., 2011) and can lead to significant damage (e.g. Zeng et al., 2015). However; these actions are harder to predict and incorporate into large scale loss analyses (Kelman and Spence, 2004). These unstudied actions are generally proportional to depth, pressure or velocity, indicating that there may be a relationship between the ratio of applied to ultimate moment and damage through other actions. Given that only direct actions are considered in this study, the curves likely form an upper bound to complete damage, and depth–pressure combinations below the curve may still result in complete building damage through other mechanisms.

6.6.3 Pressure actions

Both hydrostatic and dynamic pressures were considered in bending moment calculations. Slower increases in depth, buildings with many openings and the location of buildings relative to the channel can also affect the equalisation of lahar depths and reduce the effect of hydrostatic pressure. However, lahar depth would still be an important factor to consider in building damage estimation as it controls location of the bending moment and can cause damage through other actions (e.g. inundation damage, buoyancy, corrosion).

The applied depth at the time of maximum pressure was used here to create the depth–pressure combinations to determine building loss. This ‘surge depth’ was not necessarily the maximum depth of the lahar during the simulation. Maximum depths generally occurred at later times in the simulations when hydrostatic pressure may have equalised inside and outside buildings. This assumption of ‘surge depth’ was valid for most cases, although the losses for the $75 \text{ m}^3\text{s}^{-1}$ Newtonian flows indicate that this approach can be too simplistic at times. The complexity of lahar flows within urban environments with intricate geometry and obstacles similar to the case study area means that broad generalisations and assumptions about flow dynamics, such as the assumption of a ‘surge depth’, are often limited in their validity.

6.6.4 Discussion

The combination of pressures applied to each block in the study area created bending moments that, with few exceptions, were much higher than the maximum moment buildings could withstand. The limitations identified in previous sections generally over-estimate building strength and resilience to lahars which would result in greater damage than predicted here. The estimated building losses (Figs. 6.12 and 6.13) therefore represent the minimum expected losses for each flow scenario with damage likely to be more severe due to additional damage actions (e.g. boulders impacting structures) and the over-estimation of building quality, particularly for class A0 buildings.

When inundated, blocks in this study area are subjected to depths and pressures higher

than the strongest structural class buildings can withstand. Specific improvements to reduce vulnerability, such as adding roof support and utilising reinforced frames comprised of equally spaced RC columns will increase the overall strength of buildings by reducing the slenderness ratio (equation A6). Wider masonry units (wall thickness) and stronger mortar joints will also increase the overall building strength by increasing wall stiffness and therefore resistance to bending moments. However, this increased structural strength appears to only reduce losses in very low flow rate scenarios where there is proportionally less inundation. This suggests that while each component of risk has a role in determining overall building losses, the variability in individual losses appears to be predominantly caused by flow dynamics (i.e. lahar hazard) and building exposure (e.g. proportion of building types and orientation within blocks).

6.7 Conclusion

Development of fragility functions in the form of critical depth-pressure curves for building classes within Arequipa have helped to provide insight into possible building losses and their cause. Building vulnerability is largely controlled by social, cultural and institutional factors (Künzler et al., 2012), so the depth-pressure curves are necessarily specific to Arequipa building typologies. However, given sufficient data on building strength, depth-pressure curves can be generated through the same approach as in Appendix A and used to quantify masonry building loss in terms of flow depth and pressure in other regions.

Estimated building losses (Figs. 6.12 and 6.13) are caused by the intersection of lahar hazard (flow rate, flow type) with building exposure (location, proportion of building types and orientation within blocks) and vulnerability (building type and strength). The almost total simulated building loss for all scenarios indicates that substantial losses can be expected in the event of inundation. Furthermore, lahar depths and pressures obtained from simulations were much greater than those most buildings in the study area could withstand, even if retrofitting to improve structural strength was undertaken. This suggests that, in this study area at least, exposure and lahar hazard have a larger role in determining building loss compared to vulnerability.

6.8 Appendix: Calculating ultimate bending moment and shear force

The ultimate bending moment (M_u) and ultimate shear force (V_u) is calculated using the following equation (Roos, 2003):

$$M_u = (f_t + f_d) \frac{wb^2}{6}, \quad (6.7)$$

$$V_u = f_v w b, \quad (6.8)$$

where f_t is the the tensile strength of the masonry wall, f_d is the design compressive stress acting on the wall, w is the width of the wall facing the flow and b is the thickness of the wall. The shear strength of the masonry wall (f_v) is related to the tensile and compressive stress through (Roos, 2003):

$$f_v = 0.5f_t + 0.5f_d \quad (6.9)$$

The tensile strength is assumed to be 0.2 MPa as, according to AS3700-2011, the tensile strength should be no greater than this value. The brick thickness, b , is between 150 and 250 mm for terracotta bricks (Martelli, 2011) and is assumed to be similar for ignimbrite bricks observed in the study area. The design compressive stress, f_d , can be determined by calculating the vertical forces (i.e. building weight) acting on the walls. This can be estimated from building properties such as number and weight of floors, weight of the masonry and building design (e.g. Roos, 2003). However, such detailed building data is lacking and carries considerable uncertainty for a heterogeneous urban area with varied construction materials, building ages and designs such as Arequipa. Instead we use the design compressive capacity (f_o), specified in AS3700-2011, to determine the design compressive stress:

$$f_d = k f_o, \quad (6.10)$$

$$f_o = \phi f_c A_b, \quad (6.11)$$

where f_c is the characteristic compressive strength of the masonry, ϕ is the capacity reduction factor, A_b is the bedded area of the masonry (wall width \times length) and k is a reduction factor based on the wall design. The characteristic compressive strength is determined using the unconfined compressive strength tests of Martelli (2011) on building materials sourced from Arequipa. Presuming the mortar is of relatively low quality (M2), the characteristic compressive strengths (according to AS3700-2011) are 3.8 MPa for ignimbrite masonry and between 3.5 and 4.54 MPa for terracotta masonry. The slenderness reduction factor, k , describes the susceptibility to buckling. Following AS3700-2011, this factor is calculated as

$$k = 0.67 - 0.02 (S_{rs} - 14) \quad (6.12)$$

for buildings with a reinforced concrete roof or floor (i.e. typologies 3-6C), and

$$k = 0.67 - 0.025 (S_{rs} - 10) \quad (6.13)$$

for buildings with other roof or floor supports (typologies 1-2). This factor requires a calculation of the slenderness ratio, S_{rs} :

$$S_{rs} = \frac{a_v H}{k_t b}, \quad (6.14)$$

where H is the height between floors or supports, taken as 2.8 metres for reinforced concrete type buildings and 3 metres for non-reinforced buildings (Martelli, 2011). The vertical slenderness coefficient, a_v , is determined from the lateral support along the top edge of the wall. Walls with roof support (types 3-6C) have a coefficient of 1, while unsupported walls (types 1A-2B) act as a cantilever and have a coefficient of 2.5. Considering the thinnest bricks, the slenderness coefficient is negative for building types 1A-2B as the design is out of the range of those considered in AS3700-2011. Acknowledging the low strength of these frequently makeshift structures, the slenderness coefficient is therefore set to 0.01. The thickness coefficient, k_t , takes into account the strength of supporting columns. This coefficient is set to 1 for non-reinforced frame buildings and is dependent on the spacing and thickness of reinforced beams within the masonry for reinforced buildings. Estimates of the spacing and thickness suggest that the coefficient will be between 1.4 and 2 for type 6A-6C buildings and between 1 and 1.2 for type 4 buildings. The large spacing between reinforced columns and their relative width, pictured in Thouret et al. (2014), are responsible for the much lower coefficients assigned to type 4 buildings.

Summary, limitations and applicability to lahar risk assessment

The objective of this thesis was to enable the quantification of lahar risk through focused improvement of lahar hazard assessment and understanding of lahar behaviour. These improvements were undertaken in reference to a lahar risk assessment methodology adapted from van Westen et al. (2006). An annotated version of the methodology, shown in Fig. 7.1, highlights improvements to the process made by each publication. This chapter first summarises and evaluates the individual contribution of each study and contributions towards the thesis aim. Common limitations between chapters is discussed in section 7.2 and a full discussion of the progress in quantitative lahar risk assessment made possible through this thesis is provided in section 7.3.

7.1 Summary of publications

The publications contained within this thesis are linked by the common goal of improving the quantification of lahar hazard and vulnerability. Each publication focuses on the development or application of specific tools and methodologies to achieve the broader thesis aim. Therefore, each chapter provides an individual contribution to its topic area in addition to the improvement of quantitative lahar risk assessment. The important aspects, relevance, future work and conclusions of the individual studies are highlighted in this section with respect to the separate parts on lahar hazard (Part I) and vulnerability (Part II) assessment.

7.1.1 Part I: Lahar hazard

In chapter 2 (Mead and Magill, 2014) the issue of estimating eruption frequency from an incomplete eruption record is addressed using Markov Chain Monte Carlo simulations to identify change points in data completeness. The accurate estimation of eruption frequency is important for all forms of volcanic hazard assessment; however, under recording of eruptions is evident in catalogues of global volcanism (e.g. LaMEVE (Crosweller et al., 2012), Smithsonian Institution Volcanoes of the World (Global Volcanism Program, 2013), and

Hayakawa's 2000 year eruption database (Hayakawa, 1997)). Change points identified in the Volcanoes of the World database enable the estimation of eruption recurrence intervals for all eruptions, and separately large ($\text{VEI} \geq 4$) eruptions, at a regional and country scale. These unbiased, reproducible estimates enable decisions on eruption frequency to be made despite the uncertainty in record completeness. In addition to the change point date, a broad estimate of uncertainty was provided through percentiles of the change point posterior distribution. While some posterior distributions were multi-modal, indicating several candidate dates as opposed to a continuous distribution of dates, the potential for propagation of uncertainties through hazard models highlights the value of this approach.

A trend was observed in analysis of the complete portion of the catalogue where larger VEI eruptions were found to produce proportionally more lahars than small eruptions. This indicated that lahar initiation may be a material limited process and focused the study of lahar hazard assessment in this direction. Rain-triggered lahar initiation processes were investigated in chapter 3 (Mead et al., 2016). The range of initiation processes observed in the literature were reviewed and a model describing rain-triggered lahar susceptibility was developed. Presuming that lahar initiation is the result of overland erosion and shallow landsliding, the model identified several aspects of rainfall generated lahars important for further study. A key outcome in relation to the aim of quantifying lahar hazard was estimation of the probability of an initial lahar volume occurring from a specific source area, defined as lahar susceptibility. Additionally, the hydraulic response time (H^2/D_0), which describes the transmission of pore-water pressure through a deposit, was identified as an important control in determining the mode of lahar initiation. This suggests that rainfall duration, moderated slightly by rainfall intensity, is an important factor in determining the likelihood of rain-triggered lahar initiation. This has implications for lahar warning systems as it suggests that an estimation of response times could be used to empirically estimate lahar triggering thresholds based on rainfall intensity and duration. However, these conclusions are limited somewhat by the scarcity of input data and future validation studies on lahar initiation processes are necessary to comprehensively understand the likelihood of initiation.

Chapter 4, the final chapter in part I, demonstrates an approach to probabilistic quantification of lahar hazard. Lahar hazard maps expressing the annual exceedance probability (AEP) of rain-triggered lahar heights for a given volcanic deposit were generated through coupling susceptibility outputs (chapter 3) with Titan2D. These hazard maps are purely quantitative, using the definition of van Westen et al. (2006), and are an improvement on most lahar hazard assessments, which often express hazard in terms of an indicative (i.e. semi-quantitative) or qualitative probability. By relying on the mechanics of lahar initiation, this approach is less reliant on the historic record of lahar occurrence, which often limits hazard assessment due to landscape change in volcanic environments. The approach proposed in this chapter opens several avenues of future work required to fully evaluate feasibility of the model. Two key areas of investigation are the assessment of computational requirements for hazard

assessments spanning all possible parameters and, secondly, the integration of all damaging components of lahar flow (i.e. not only lahar height) in order to better estimate damage to exposed elements.

7.1.2 Part II: Physical vulnerability

The complex intersection of lahar hazard, exposure and vulnerability in an urban area was the focus of part II. Chapter 5 (Mead et al., 2015) highlighted issues relating to the acquisition and usage of terrain models in volcanic environments affected by human interaction. Models to predict the flow of lahars, such as those discussed in chapter 4, are sensitive to changes and inaccuracies in terrain reconstructions, which can result in an inadequate estimation of exposed elements and lahar induced damage. Fully three dimensional terrain models obtained using rapid and inexpensive photogrammetric methods such as the one developed in chapter 5 are able to capture fine scale features important for flow simulations. The field of photogrammetry and its application to geosciences in general is a rapidly advancing field, increasing in the scale and detail of terrain reconstructions (e.g. Dietrich, 2016; Javernick et al., 2016). This work presents a subset of this field, focusing on the importance of acquiring building scale details vital to an assessment of lahar induced damage.

The photogrammetric technique in chapter 5 was used to generate terrain for the study in chapter 6. This chapter focuses on the relative importance of lahar hazard, exposure and vulnerability in determining building damage. A lahar rheological model, implemented in smoothed particle hydrodynamics, was used to investigate the effect of lahar composition on building damage. Building vulnerability was quantified through critical depth-pressure curves developed for buildings in Arequipa, Peru. As vulnerability is largely controlled by socio-economic, cultural and institutional factors, the curves are specific to this region. However, the process of developing depth-pressure curves can be applied to support vulnerability assessments in other regions. Simulated total losses in the study area were substantial, limiting the ability to characterise effects of hazard variables such as flow rate on loss. Results of this study did suggest, however, that individual building losses are predominantly controlled by exposure to the hazard rather than building characteristics that determine vulnerability. The hazard intensity, expressed through dynamic pressure, varied with rheology and in response to building orientation (a measure of exposure), demonstrating the complex interactions between components of risk.

7.2 Limitations

The relationship between building orientation, lahar rheology and dynamic pressures exerted on buildings, explained in chapter 6, suggests that lahar risk cannot be simplified into a basic formula comprised of the product and/or sum of discrete separations of hazard, exposure and

vulnerability. The limited investigation of exposure in this thesis, demonstrated to be important in the interaction with hazard, can restrict the validity of conclusions drawn for risk assessment and mitigation. Exposure and its affects are critical areas of study in order to completely understand and mitigate lahar risk. This is particularly important when considering social and cultural aspects of exposure and damage. However, the measurement of physical exposure suffers from few conceptual issues and, although time consuming, accurate classification of exposure is possible (van Westen et al., 2006).

The relative unavailability of input data was a general limitation to accurate quantification of hazard and vulnerability, and also formed the motivation for chapters 2 and 5. Satellite and remote sensing technologies can help to alleviate these issues in modern day risk assessments. However, the dynamic nature of environmental conditions that affect lahars require frequent updating of input data. The cost of this data may not be feasible in many instances, particularly in developing countries at risk from lahars. Cheaper alternatives, such as those developed in chapter 5, may provide a solution but lack of input data is still an important limitation to quantification of hazard and vulnerability. Predictive models, such as those in this thesis, should aim to strike a balance between complete descriptions of physical processes and the availability of data.

The practical application of lahar risk assessment requires decisions that balance computational tractability, complete descriptions of physical processes and parametrisations under uncertain and changing environmental conditions. While most decisions and assumptions have been justified in the context of each publication, several decisions warrant broader discussion in the context of the overall thesis aim. These decisions include:

Chapter 2: A single, dramatic shift in recording of eruptions

The change point model of Mead and Magill (2014) assumes there is a single shift in the recording of eruptions. Practically, this assumption implies that recording of eruptions was inconsistent a single year before the change point, but that 100% of eruptions were recorded after the change point date. The increase in eruption recording is more subtle in reality and wide ranges of uncertainty in the change point date for some regions (e.g. Japan) highlight this fact. Statistical models that assume a more gradual increase in recording may more accurately represent reality. However, the implementation of gradual increases in recording rates into the hazard assessment process poses many, as yet unsolved, conceptual problems. This practical limitation formed the basis of the decision to use a single change point model.

Chapter 3 and 4: Instantaneous mobilisation of material

The rain-triggered lahar susceptibility model (Mead et al., 2016), when coupled with lahar flow models in Chapter 4 implicitly assume a total, instantaneous mobilisation of the deposit and rainfall. This greatly simplifies the complex transition between static and dynamic states observed, for example, by van Asch et al. (2007). The advantage of this simplification is less reliance on complex models (which often require more

parametrisation of uncertain properties) and decreased computational cost. Additionally, this simplification makes the use of lahar susceptibility (see Fig. 7.1) as an input into the hazard modelling process possible. This reduces over-reliance on the historical record that results in semi-quantitative estimates of lahar hazard.

Chapter 6: Direct actions are the sole contributor to building damage

Building loss estimates in Chapter 6 only consider the effect of hydrostatic and dynamic pressure on building damage. Again, this simplifies reality where damage can be caused by a number of possible actions. The most important neglected actions for lahars are impact forces from large debris 'missiles' in the flow and erosion or scour of building foundations. As explained in the chapter, these actions are proportional to depth and velocity, meaning damage functions could be derived if sufficient data are available. Crucially, building damage was almost total despite the restriction in damage actions as vulnerability was observed to have a lesser effect on losses compared to building exposure. This demonstrates that valuable insights for lahar risk assessment can still be derived from approaches with limiting assumptions.

Overall, while acknowledging the impact of these limitations, the assumptions are made to favour enabling the *process* of lahar risk assessment over solutions that restrict practical assessments of risk. Results in this thesis show that, despite limitations, valuable information on the nature of lahar risk can be provided to stakeholders in conditions subject to considerable change and uncertainty.

7.3 Improvements to lahar risk assessment and conclusion

Variability and change is a defining feature of lahars. Initiation, flow and exposure are all dynamic processes, changing in response to volcanic activity and lahars themselves. This variability introduces difficulties in the lahar risk assessment process, shown in Fig. 7.1, related to unknown frequency-magnitude relationships, changing terrain and dynamic environments and unpredictability in lahar behaviour. When undertaken, lahar hazard and vulnerability assessments also require frequent updating to best represent current states; thereby placing practical limits on the monetary and time costs of risk assessment. This thesis has made specific improvements to components of lahar risk assessment, annotated by chapters in Fig. 7.1.

Overall, the key findings and methods of part I provide an opportunity for new, purely quantitative probabilistic lahar hazard assessment pipelines. As lahars are conditional on a volcanoes eruption sequence, style and magnitude, the first step in the probabilistic lahar hazard assessment process is to estimate the recurrence rates of an eruption. This can now be estimated, at a regional and country scale, from incomplete datasets using the method in chapter 2. In addition to being conditional on volcanic activity, lahar initiation is also

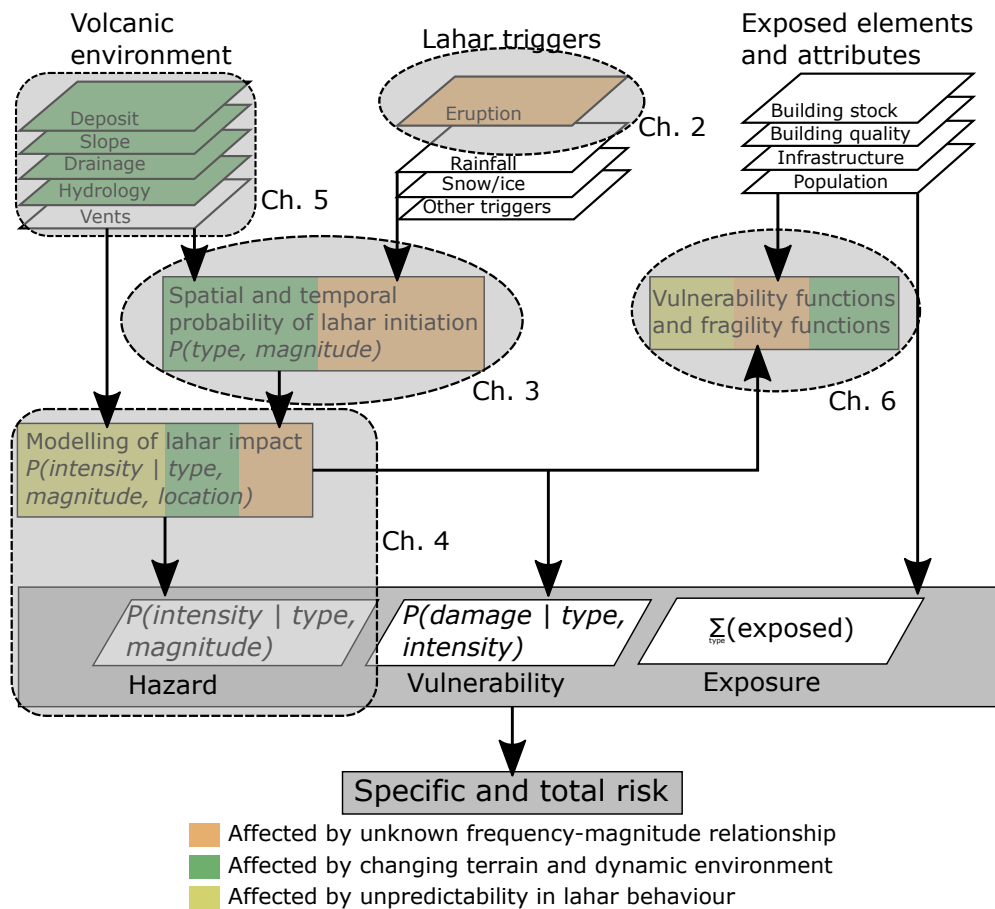


FIGURE 7.1: Schematic representation of lahar risk assessment methodology, from van Westen et al. (2006), highlighting areas improved by chapters in this thesis.

controlled by environmental factors such as rainfall intensity and duration. The concept of susceptibility in lahar hazards is introduced through a method to determine the susceptibility of eruption deposits to rain-triggered lahars (i.e. the lahar frequency-magnitude relationship) described in chapter 3. This method provides an estimate of the initial size and conditional likelihood of potential lahars. Chapter 4 demonstrates how this information can be integrated into lahar numerical models to determine hazard footprints and exceedance probabilities. Finally, the probability of an eruption and of a lahar, given the eruption, can be combined to fully quantify the (non-conditional) lahar hazard.

Part II investigates the effect of lahars on building and infrastructure in urban environments. The impact of terrain changes, caused by volcanic and human activity, on numerical models is reduced through the photogrammetry approach in chapter 5. As this method improves the quantification of primary inputs, it can also be applied to reducing terrain-change based uncertainty of lahar susceptibility and modelling components. Building loss, which is caused by the intersection of hazard, exposure and vulnerability, is investigated in chapter 6. New vulnerability relationships were used in conjunction with lahar numerical models to investigate the relative importance and interactions between lahar hazard, exposure and vulnerability. This study directly contributes to improving the quantification of risk through

the vulnerability functions in addition to, enabling risk management strategies to be targeted at components that deliver the greatest reduction in overall risk.

The methods in each part are generalised approaches to the quantification of hazard and vulnerability. These methods also consider or reduce the scarcity and uncertainties in input data that can limit risk assessments. This reduces overhead costs and enables the transfer of methods to all areas at risk from lahars. Considered as a whole unit, the improvements made to lahar hazard and vulnerability assessment through the course of this research demonstrate that quantification of lahar risk under uncertain and changing environmental conditions is possible. When applied within a framework to mitigate risk, the methods in this thesis have the potential to manage and reduce the severe consequences of lahars.

References

- Aguilera, E., M. T. Pareschi, M. Rosi, and G. Zanchetta (2004). “Risk from Lahars in the Northern Valleys of Cotopaxi Volcano (Ecuador)”. *Natural Hazards* 33 (2), pp. 161–189. doi: 10.1023/B:NHAZ.0000037037.03155.23.
- Akima, H. (1978). “A Method of Bivariate Interpolation and Smooth Surface Fitting for Irregularly Distributed Data Points”. *ACM Trans. Math. Softw.* 4 (2), pp. 148–159. doi: 10.1145/355780.355786.
- Alberico, I., P. Petrosino, and L. Lirer (2011). “Volcanic hazard and risk assessment in a multi-source volcanic area: the example of Napoli city (Southern Italy)”. *Natural Hazards and Earth System Sciences* 11 (4), pp. 1057–1070. doi: 10.5194/nhess-11-1057-2011.
- Amigo, À. (2013). “Estimation of tephra-fall and lahar hazards at Hudson Volcano, southern Chile: Insights from numerical models”. *Geological Society of America Special Papers* 498, pp. 177–199. doi: 10.1130/2013.2498(11).
- Auker, M. R., R. S. J. Sparks, L. Siebert, H. S. Crosweller, and J. Ewert (2013). “A statistical analysis of the global historical volcanic fatalities record”. *Journal of Applied Volcanology* 2 (1), pp. 1–24. doi: 10.1186/2191-5040-2-2.
- Bacon, C. R., L. G. Mastin, K. M. Scott, and M. Nathenson (1997). *Volcano and earthquake hazards in the Crater Lake region, Oregon*. U.S. Geological Survey Open-File Report 97-487. 32 pp.
- Bagnold, R. A. (1954). “Experiments on a Gravity-Free Dispersion of Large Solid Spheres in a Newtonian Fluid under Shear”. *Proceedings of the Royal Society of London A: Mathematical, Physical and Engineering Sciences* 225 (1160), pp. 49–63. doi: 10.1098/rspa.1954.0186.
- Banton, J., P. Villard, D. Jongmans, and C. Scavia (2009). “Two-dimensional discrete element models of debris avalanches: Parameterization and the reproducibility of experimental results”. *Journal of Geophysical Research: Earth Surface* 114, F04013. doi: 10.1029/2008JF001161.
- Barclay, J., J. Alexander, and J. Sušnik (2007). “Rainfall-induced lahars in the Belham Valley, Montserrat, West Indies”. *Journal of the Geological Society* 164 (4), pp. 815–827. doi: 10.1144/0016-76492006-078.

- Barclay, J., J. E. Johnstone, and A. J. Matthews (2006). "Meteorological monitoring of an active volcano: Implications for eruption prediction". *Journal of Volcanology and Geothermal Research* 150 (4), pp. 339–358. doi: 10.1016/j.jvolgeores.2005.07.020.
- Baum, R. L., J. W. Godt, and W. Z. Savage (2010). "Estimating the timing and location of shallow rainfall-induced landslides using a model for transient, unsaturated infiltration". *Journal of Geophysical Research: Earth Surface* 115 (F3), F03013. doi: 10.1029/2009JF001321.
- Bay, H., T. Tuytelaars, and L. Van Gool (2006). "SURF: Speeded Up Robust Features". *Computer Vision – ECCV 2006*. Ed. by A. Leonardis, H. Bischof, and A. Pinz. Vol. 3951. Lecture Notes in Computer Science. Springer Berlin Heidelberg. Chap. 32, pp. 404–417. doi: 10.1007/11744023_32.
- Bebbington, M. S. (2009). "Volcanic Eruptions: Stochastic Models of Occurrence Patterns". *Encyclopedia of Complexity and Systems Science*. Ed. by R. A. Meyers. Vol. 9. New York, NY: Springer New York, pp. 9831–9861. doi: 10.1007/978-0-387-30440-3_580.
- Biass, S., C. Scaini, C. Bonadonna, A. Folch, K. Smith, and A. Höskuldsson (2014). "A multi-scale risk assessment for tephra fallout and airborne concentration from multiple Icelandic volcanoes – Part 1: Hazard assessment". *Natural Hazards and Earth System Sciences* 14 (8), pp. 2265–2287. doi: 10.5194/nhess-14-2265-2014.
- Biass, S. and C. Bonadonna (2013). "A fast GIS-based risk assessment for tephra fallout: the example of Cotopaxi volcano, Ecuador". *Natural Hazards* 65 (1), pp. 477–495. doi: 10.1007/s11069-012-0378-z.
- Biass, S., C. Bonadonna, F. di Traglia, M. Pistolesi, M. Rosi, and P. Lestuzzi (2016). "Probabilistic evaluation of the physical impact of future tephra fallout events for the Island of Vulcano, Italy". *Bulletin of Volcanology* 78 (5), p. 37. doi: 10.1007/s00445-016-1028-1.
- Biass, S., C. Frischknecht, and C. Bonadonna (2013). "A fast GIS-based risk assessment for tephra fallout: the example of Cotopaxi volcano, Ecuador". *Natural Hazards* 65 (1), pp. 497–521. doi: 10.1007/s11069-012-0457-1.
- Blong, R. J. (1984). *Volcanic hazards : A sourcebook on the effects of eruptions*. Sydney: Academic Press. 425 pp.
- Bonadonna, C. (2006). "Probabilistic modelling of tephra dispersal". Ed. by H. Mader, S. Cole, and C. B. Connor. Vol. 1. Special Publications of IAVCEI. Geological Society of London. Chap. 19, pp. 243–259. doi: 10.1144/IAVCEI001.19.
- Bonadonna, C., C. B. Connor, B. F. Houghton, L. Connor, M. Byrne, A. Laing, and T. K. Hincks (2005). "Probabilistic modeling of tephra dispersal: Hazard assessment of a multiphase rhyolitic eruption at Tarawera, New Zealand". *Journal of Geophysical Research: Solid Earth* 110 (B3). doi: 10.1029/2003JB002896.
- Bouchut, F., E. D. Fernandez-Nieto, A. Mangeney, and P. .-. Y. Lagree (2008). "On new erosion models of Savage-Hutter type for avalanches". *Acta Mechanica* 199 (1-4), pp. 181–208. doi: 10.1007/s00707-007-0534-9.

- Caballero, L., J. L. Macías, A. García-Palomo, G. R. Saucedo, L. Borselli, D. Sarocchi, and J. M. Sánchez (2006). “The September 8–9, 1998 Rain-Triggered Flood Events at Motozintla, Chiapas, Mexico”. *Natural Hazards* 39 (1), pp. 103–126. doi: 10.1007/s11069-005-4987-7.
- Calakli, F. and G. Taubin (2012). “SSD-C: Smooth Signed Distance Colored Surface Reconstruction”. *Expanding the Frontiers of Visual Analytics and Visualization*. Ed. by J. Dill, R. Earnshaw, D. Kasik, J. Vince, and P. C. Wong. Springer London. Chap. 18, pp. 323–338. doi: 10.1007/978-1-4471-2804-5_18.
- Calder, E., K. Wagner, and S. Ogburn (2015). “Volcanic hazard maps”. *Global Volcanic Hazards and Risk*. Ed. by S. C. Loughlin, R. S. J. Sparks, S. K. Brown, S. F. Jenkins, and C. Vye-Brown. Cambridge University Press. Chap. 20, pp. 335–342. doi: 10.1017/CBO9781316276273.022.
- Campbell, C. S., P. W. Cleary, and M. Hopkins (1995). “Large-scale Landslide Simulations - Global Deformation, Velocities and Basal Friction”. *Journal of Geophysical Research: Solid Earth* 100 (B5), pp. 8267–8283. doi: 10.1029/94JB00937.
- Campbell, R. H. (1975). *Soil slips, debris flows, and rainstorms in the Santa Monica Mountains and vicinity, southern California*. U.S. Geological Survey Professional Paper 851. 51 pp.
- Capart, H. and D. L. Young (1998). “Formation of a jump by the dam-break wave over a granular bed”. *Journal of Fluid Mechanics* 372, pp. 165–187. doi: 10.1017/S0022112098002250.
- Capra, L., L. Borselli, N. Varley, J. C. Gavilanes-Ruiz, G. Norini, D. Sarocchi, L. Caballero, and A. Cortes (2010). “Rainfall-triggered lahars at Volcán de Colima, Mexico: Surface hydro-repellency as initiation process”. *Journal of Volcanology and Geothermal Research* 189 (1–2), pp. 105–117. doi: 10.1016/j.jvolgeores.2009.10.014.
- Capra, L., J. Lugo-Hubp, and L. Borselli (2003). “Mass movements in tropical volcanic terrains: the case of Teziutlán (México)”. *Engineering Geology* 69 (3–4), pp. 359–379. doi: 10.1016/S0013-7952(03)00071-1.
- Carranza, E. and O. Castro (2006). “Predicting Lahar-Inundation Zones: Case Study in West Mount Pinatubo, Philippines”. *Natural Hazards* 37 (3), pp. 331–372. doi: 10.1007/s11069-005-6141-y.
- Carrivick, J. L., V. Manville, and S. J. Cronin (2009). “A fluid dynamics approach to modelling the 18th March 2007 lahar at Mt. Ruapehu, New Zealand”. *Bulletin of Volcanology* 71 (2), pp. 153–169. doi: 10.1007/s00445-008-0213-2.
- Carrivick, J. L., V. Manville, A. Graettinger, and S. J. Cronin (2010). “Coupled fluid dynamics-sediment transport modelling of a Crater Lake break-out lahar: Mt. Ruapehu, New Zealand”. *Journal of Hydrology* 388 (3–4), pp. 399–413. doi: 10.1016/j.jhydrol.2010.05.023.
- Castro Díaz, M. J., E. D. Fernández-Nieto, and A. M. Ferreira (2008). “Sediment transport models in Shallow Water equations and numerical approach by high order finite volume

- methods". *Computers & Fluids* 37 (3), pp. 299–316. doi: 10.1016/j.compfluid.2007.07.017.
- Castro Díaz, M. J., E. D. Fernández-Nieto, A. M. Ferreiro, and C. Parés (2009). "Two-dimensional sediment transport models in shallow water equations. A second order finite volume approach on unstructured meshes". *Computer Methods in Applied Mechanics and Engineering* 198 (33–36), pp. 2520–2538. doi: 10.1016/j.cma.2009.03.001.
- Chan, L. C. Y. and N. W. Page (1997). "Particle fractal and load effects on internal friction in powders". *Powder Technology* 90 (3), pp. 259–266. doi: 10.1016/S0032-5910(96)03228-7.
- Chen, H. and C. F. Lee (2000). "Numerical simulation of debris flows". *Canadian Geotechnical Journal* 37 (1), pp. 146–160. doi: 10.1139/cgj-37-1-146.
- Chester, D. K., M. Degg, A. M. Duncan, and J. Guest (2000). "The increasing exposure of cities to the effects of volcanic eruptions: a global survey". *Global Environmental Change Part B: Environmental Hazards* 2 (3), pp. 89–103. doi: 10.1016/S1464-2867(01)00004-3.
- Cho, G. C., J. Dodds, and J. C. Santamarina (2006). "Particle shape effects on packing density, stiffness, and strength: Natural and crushed sands". *Journal of Geotechnical and Geoenvironmental Engineering* 132 (5), pp. 591–602. doi: 10.1061/(ASCE)1090-0241(2006)132:5(591).
- Chow, V. T. (1959). *Open-channel hydraulics*. International student edition. McGraw-Hill civil engineering series. New York: McGraw-Hill. 680 pp.
- Cleary, P. W. (2000). "DEM simulation of industrial particle flows: case studies of dragline excavators, mixing in tumblers and centrifugal mills". *Powder Technology* 109 (1-3), pp. 83–104. doi: 10.1016/S0032-5910(99)00229-6.
- (2004). "Large scale industrial DEM modelling". *Engineering Computations* 21 (2-4), pp. 169–204.
- Cleary, P. W. and C. S. Campbell (1993). "Self-lubrication for Long Runout Landslides - Examination by Computer-simulation". *Journal of Geophysical Research: Solid Earth* 98 (B12), pp. 21911–21924. doi: 10.1029/93JB02380.
- Cleary, P. W. (2002). "Landslide Modelling on Real Topography". *Discrete Element Methods: Numerical Modelling of Discontinua*. Ed. by B. Cook and R. Jensen. ASCE, pp. 355–360. doi: 10.1061/40647(259)62.
- (2007). "Granular flows: fundamentals and applications". *Granular and Complex Materials* 8, pp. 141–168.
- (2008). "The effect of particle shape on simple shear flows". *Powder Technology* 179 (3), pp. 144–163.
- (2009). "Industrial particle flow modelling using discrete element method". *Engineering Computations* 26 (6), pp. 698–743. doi: 10.1108/02644400910975487.
- (2010). "DEM prediction of industrial and geophysical particle flows". *Particuology* 8 (2), pp. 106–118.

- Cleary, P. W. and M. Prakash (2004). “Discrete–element modelling and smoothed particle hydrodynamics: potential in the environmental sciences”. *Philosophical Transactions of the Royal Society of London. Series A: Mathematical, Physical and Engineering Sciences* 362 (1822), pp. 2003–2030. doi: 10.1098/rsta.2004.1428.
- Cleary, P. W., M. Prakash, S. Mead, X. Tang, H. Wang, and S. Ouyang (2012). “Dynamic simulation of dam-break scenarios for risk analysis and disaster management”. *International Journal of Image and Data Fusion* 3 (4), pp. 333–363. doi: 10.1080/19479832.2012.716084.
- Cleary, P., M. Prakash, S. Mead, V. Lemiale, G. Robinson, F. Ye, S. Ouyang, and X. Tang (2015). “A scenario-based risk framework for determining consequences of different failure modes of earth dams”. *Natural Hazards* 75 (2), pp. 1489–1530. doi: 10.1007/s11069-014-1379-x.
- Cleary, P. (1998). “Discrete element modelling of industrial granular flow applications”. *TASK. Quarterly-Scientific Bulletin* 2, pp. 385–416.
- Cohen, R. C. Z., J. E. Hilton, S. Hasan Khan, Y. Wang, and M. Prakash (2015). “SWIFT: A GPU based coupled hydrodynamic/hydraulic framework for urban flood prediction”. *The 11th International Conference on CFD in the Minerals and Process Industries*. Ed. by C. Solnordal, P. Liovic, G. Delaney, S. Cummins, M. Schwarz, and P. Witt. CSIRO, pp. 1–6.
- Coles, S. and R. Sparks (2006). “Extreme value methods for modelling historical series of large volcanic magnitudes”. *Statistics in volcanology*. Ed. by H. Mader, S. Coles, C. Connor, and L. Connor. Vol. 1. Geological Society of London, pp. 47–56.
- Coles, S. (2001). *An Introduction to Statistical Modeling of Extreme Values*. Springer London. 209 pp. doi: 10.1007/978-1-4471-3675-0.
- Collins, B. D. and T. Dunne (1986). “Erosion of tephra from the 1980 eruption of Mount St. Helens”. *Geological Society of America Bulletin* 97 (7), pp. 896–905. doi: 10.1130/0016-7606(1986)97<896:eotfte>2.0.co;2.
- Connor, C., B. Hill, B. Winfrey, N. Franklin, and P. Femina (2001). “Estimation of Volcanic Hazards from Tephra Fallout”. *Natural Hazards Review* 2 (1), pp. 33–42. doi: 10.1061/(ASCE)1527-6988(2001)2:1(33).
- Córdoba, G., G. Villarosa, M. F. Sheridan, J. G. Viramonte, D. Beigt, and G. Salmuni (2015). “Secondary lahar hazard assessment for Villa la Angostura, Argentina, using Two-Phase-Titan modelling code during 2011 Cordón Caulle eruption”. *Natural Hazards and Earth System Sciences* 15 (4), pp. 757–766. doi: 10.5194/nhess-15-757-2015.
- Cronin, S. J., V. E. Neall, J. A. Lecointre, and A. S. Palmer (1997a). “Changes in Whangaehu river lahar characteristics during the 1995 eruption sequence, Ruapehu volcano, New Zealand”. *Journal of Volcanology and Geothermal Research* 76 (1–2), pp. 47–61. doi: 10.1016/S0377-0273(96)00064-9.

- Cronin, S. J., V. E. Neall, and A. S. Palmer (1997b). "Lahar history and hazard of the Tongariro River, northeastern Tongariro Volcanic Centre, New Zealand". *New Zealand Journal of Geology and Geophysics* 40 (3), pp. 383–393. doi: 10.1080/00288306.1997.9514769.
- Crosta, G. B., H. Chen, and P. Frattini (2006). "Forecasting hazard scenarios and implications for the evaluation of countermeasure efficiency for large debris avalanches". *Engineering Geology* 83 (1-3), pp. 236–253. doi: 10.1016/j.enggeo.2005.06.039.
- Crosta, G. B. and P. Dal Negro (2003). "Observations and modelling of soil slip-debris flow initiation processes in pyroclastic deposits: the Sarno 1998 event". *Natural Hazards and Earth System Sciences* 3 (1/2), pp. 53–69. doi: 10.5194/nhess-3-53-2003.
- Crosweller, H. S., B. Arora, S. K. Brown, E. Cottrell, N. I. Deligne, N. O. Guerrero, L. Hobbs, K. Kiyosugi, S. C. Loughlin, J. Lowndes, M. Nayembil, L. Siebert, R. S. J. Sparks, S. Takarada, and E. Venzke (2012). "Global database on large magnitude explosive volcanic eruptions (LaMEVE)". *Journal of Applied Volcanology* 1 (1), pp. 1–13. doi: 10.1186/2191-5040-1-4.
- Cui, X. and J. M. N. T. Gray (2013). "Gravity-driven granular free-surface flow around a circular cylinder". *Journal of Fluid Mechanics* 720, pp. 314–337. doi: 10.1017/jfm.2013.42.
- Cui, X., J. M. N. T. Gray, and T. Johannesson (2007). "Deflecting dams and the formation of oblique shocks in snow avalanches at Flateyri, Iceland". *Journal of Geophysical Research: Earth Surface* 112 (F4), F04012. doi: 10.1029/2006JF000712.
- Cundall, P. A. and O. D. L. Strack (1979). "Discrete Numerical-model for Granular Assemblies". *Geotechnique* 29 (1), pp. 47–65.
- Custer, R. and K. Nishijima (2015). "Flood vulnerability assessment of residential buildings by explicit damage process modelling". *Natural Hazards* 78 (1), pp. 461–496. doi: 10.1007/s11069-015-1725-7.
- Daag, A. S. (2003). *Modelling the erosion of pyroclastic flow deposits and the occurrences of lahars at Mt. Pinatubo, Philippines*. International Institute for Geoinformation Science and Earth Observation.
- Darnell, A. R., J. C. Phillips, J. Barclay, R. A. Herd, A. A. Lovett, and P. D. Cole (2013). "Developing a simplified geographical information system approach to dilute lahar modelling for rapid hazard assessment". *Bulletin of Volcanology* 75 (4), pp. 1–16. doi: 10.1007/s00445-013-0713-6.
- Davison, A. C. and R. L. Smith (1990). "Models for Exceedances over High Thresholds". *Journal of the Royal Statistical Society. Series B (Methodological)* 52 (3), pp. 393–442. doi: 10.2307/2345667.
- de Bélizal, E., F. Lavigne, D. S. Hadmoko, J.-P. Degeai, G. A. Dipayana, B. W. Mutaqin, M. A. Marfai, M. Coquet, B. L. Mauff, A.-K. Robin, C. Vidal, N. Cholik, and N. Aisyah (2013). "Rain-triggered lahars following the 2010 eruption of Merapi volcano, Indonesia:

- A major risk". *Journal of Volcanology and Geothermal Research* 261, pp. 330–347. doi: 10.1016/j.jvolgeores.2013.01.010.
- De la Cruz-Reyna, S. (1991). "Poisson-distributed patterns of explosive eruptive activity". *Bulletin of Volcanology* 54 (1), pp. 57–67. doi: 10.1007/BF00278206.
- Debroux, F. and P. W. Cleary (2001). "Characterising the angles of failure and repose of avalanching granular material using the DEM method." *6th World Congress of Chemical Engineering*. 1537. Institute of Chemical Engineers.
- Delaney, G. W. and P. W. Cleary (2010). "The packing properties of superellipsoids". *Epl* 89 (3), p. 34002. doi: 10.1209/0295-5075/89/34002.
- Deligne, N. I., S. G. Coles, and R. S. J. Sparks (2010). "Recurrence rates of large explosive volcanic eruptions". *Journal of Geophysical Research: Solid Earth* 115 (B6), B06203. doi: 10.1029/2009JB006554.
- Denlinger, R. P. and R. M. Iverson (2001). "Flow of variably fluidized granular masses across three-dimensional terrain 2. Numerical predictions and experimental tests". *Journal of Geophysical Research: Solid Earth* 106 (B1), pp. 553–566. doi: 10.1029/2000JB900330.
- (2004). "Granular avalanches across irregular three-dimensional terrain 1. Theory and computation". *Journal of Geophysical Research: Earth Surface* 109 (F1), F01014. doi: 10.1029/2003JF000085.
- Di Baldassarre, G. and A. Montanari (2009). "Uncertainty in river discharge observations: a quantitative analysis". *Hydrology and Earth System Sciences* 13 (6), pp. 913–921. doi: 10.5194/hess-13-913-2009.
- Dietrich, J. T. (2016). "Riverscape mapping with helicopter-based Structure-from-Motion photogrammetry". *Geomorphology* 252, pp. 144–157. doi: 10.1016/j.geomorph.2015.05.008.
- Doyle, E. E., S. J. Cronin, S. E. Cole, and J.-C. Thouret (2010). "The coalescence and organization of lahars at Semeru volcano, Indonesia". *Bulletin of Volcanology* 72 (8), pp. 961–970. doi: 10.1007/s00445-010-0381-8.
- Doyle, E. E., S. J. Cronin, and J.-C. Thouret (2011). "Defining conditions for bulking and debulking in lahars". *Geological Society of America Bulletin* 123 (7-8), pp. 1234–1246. doi: 10.1130/B30227.1.
- Doyle, E., S. Cronin, S. Cole, and J.-C. Thouret (2009). "The challenges of incorporating temporal and spatial changes into numerical models of lahars". *Proceedings of the 18th world international congress on modelling and simulation, modelling and simulation society of Australia and New Zealand*, pp. 13–17.
- Dumaisnil, C., J.-C. Thouret, G. Chambon, E. E. Doyle, S. J. Cronin, and Surono (2010). "Hydraulic, physical and rheological characteristics of rain-triggered lahars at Semeru volcano, Indonesia". *Earth Surface Processes and Landforms* 35 (13), pp. 1573–1590. doi: 10.1002/esp.2003.

- Duman, T. Y., T. Can, O. Emre, M. Kecer, A. Dogan, S. Ates, and S. Durmaz (2005). "Landslide inventory of northwestern Anatolia, turkey". *Engineering Geology* 77 (1-2), pp. 99–114. doi: 10.1016/j.enggeo.2004.08.005.
- Dussauge-Peisser, C., A. Helmstetter, J. R. Grasso, D. Hantz, P. Desvarreux, M. Jeannin, and A. Giraud (1999). "Probabilistic approach to rock fall hazard assessment: potential of historical data analysis". *Natural Hazards and Earth System Sciences* 2 (1-2), pp. 15–26. doi: 10.5194/nhess-2-15-2002.
- Engwell, S., R. Sparks, and W. Aspinall (2013). "Quantifying uncertainties in the measurement of tephra fall thickness". *Journal of Applied Volcanology* 2 (1), pp. 1–12. doi: 10.1186/2191-5040-2-5.
- Ettinger, S., L. Mounaud, C. Magill, A.-F. Yao-Lafourcade, J.-C. Thouret, V. Manville, C. Negulescu, G. Zuccaro, D. De Gregorio, S. Nardone, J. A. L. Uchuchoque, A. Arguedas, L. Macedo, and N. Manrique Llerena (2015). "Building vulnerability to hydro-geomorphic hazards: Estimating damage probability from qualitative vulnerability assessment using logistic regression". *Journal of Hydrology*. doi: 10.1016/j.jhydrol.2015.04.017.
- Fagents, S. A. and S. M. Baloga (2005). "Calculation of lahar transit times using digital elevation data". *Journal of Volcanology and Geothermal Research* 139 (1–2), pp. 135–146. doi: 10.1016/j.jvolgeores.2004.06.013.
- (2006). "Toward a model for the bulking and debulking of lahars". *Journal of Geophysical Research: Solid Earth* 111 (B10), B10201. doi: 10.1029/2005JB003986.
- Ferrucci, M., S. Pertusati, R. Sulpizio, G. Zanchetta, M. T. Pareschi, and R. Santacroce (2005). "Volcaniclastic debris flows at La Fossa Volcano (Vulcano Island, southern Italy): Insights for erosion behaviour of loose pyroclastic material on steep slopes". *Journal of Volcanology and Geothermal Research* 145 (3–4), pp. 173–191. doi: 10.1016/j.jvolgeores.2005.01.013.
- Fiorillo, F. and R. C. Wilson (2004). "Rainfall induced debris flows in pyroclastic deposits, Campania (southern Italy)". *Engineering Geology* 75 (3–4), pp. 263–289. doi: 10.1016/j.enggeo.2004.06.014.
- Forterre, Y. (2006). "Kapiza waves as a test for three-dimensional granular flow rheology". *Journal of Fluid Mechanics* 563, pp. 123–132. doi: 10.1017/S0022112006001509.
- Frattoni, P., G. B. Crosta, N. Fusi, and P. Dal Negro (2004). "Shallow landslides in pyroclastic soils: a distributed modelling approach for hazard assessment". *Engineering Geology* 73 (3–4), pp. 277–295. doi: 10.1016/j.enggeo.2004.01.009.
- Frattoni, P., G. Crosta, and R. Sosio (2009). "Approaches for defining thresholds and return periods for rainfall-triggered shallow landslides". *Hydrological Processes* 23 (10), pp. 1444–1460. doi: 10.1002/hyp.7269.
- Furlan, C. (2010). "Extreme value methods for modelling historical series of large volcanic magnitudes". *Statistical Modelling* 10 (2), pp. 113–132. doi: 10.1177/1471082x0801000201.

- Furukawa, Y., B. Curless, S. M. Seitz, and R. Szeliski (2010). “Towards Internet-scale multi-view stereo”. *2010 IEEE Conference on Computer Vision and Pattern Recognition (CVPR)*, pp. 1434–1441. DOI: 10.1109/CVPR.2010.5539802.
- Furukawa, Y. and J. Ponce (2010). “Accurate, Dense, and Robust Multiview Stereopsis”. *Pattern Analysis and Machine Intelligence, IEEE Transactions on* 32 (8), pp. 1362–1376. DOI: 10.1109/TPAMI.2009.161.
- Galderisi, A., C. Bonadonna, G. Delmonaco, F. Ferrara, S. Menoni, A. Ceudech, S. Biass, C. Frischknecht, I. Manzella, G. Minucci, and C. Gregg (2013). “Vulnerability Assessment and Risk Mitigation: The Case of Vulcano Island, Italy”. *Landslide Science and Practice*. Ed. by C. Margottini, P. Canuti, and K. Sassa. Springer Berlin Heidelberg. Chap. 8, pp. 55–64. DOI: 10.1007/978-3-642-31313-4_8.
- Geographx (2012). *Geographx New Zealand Digital Elevation Model*. Dataset.
- Geweke, J. (1992). “Evaluating the accuracy of sampling-based approaches to the calculation of posterior moments”. *Bayesian statistics 4: proceedings of the Fourth Valencia International Meeting, April 15-20, 1991*. Ed. by J. Bernardo, J. Berger, and M. DeGroot. Clarendon Press, pp. 169–193.
- Gilks, W. R., S. Richardson, and D. J. Spiegelhalter (1995). *Markov chain Monte Carlo in Practice*. Chapman & Hall. 486 pp.
- Gilley, J. E., W. J. Elliot, J. M. Laflen, and J. R. Simanton (1993). “Critical shear stress and critical flow rates for initiation of rilling”. *Journal of Hydrology* 142 (1–4), pp. 251–271. DOI: 10.1016/0022-1694(93)90013-Y.
- Global Volcanism Program (2013). *Volcanoes of the world, v. 4.0*. Ed. by E. Venzke. Online Database. DOI: 10.5479/si.GVP.VOTW4-2013.
- Gomes, R. A. T., R. F. Guimarães, O. A. Carvalho, N. F. Fernandes, E. A. Vargas, and É. S. Martins (2008). “Identification of the affected areas by mass movement through a physically based model of landslide hazard combined with an empirical model of debris flow”. *Natural Hazards* 45 (2), pp. 197–209. DOI: 10.1007/s11069-007-9160-z.
- Govier, G., C. Shook, and E. Lilge (1957). “The rheological properties of water suspensions of finely subdivided magnetite, galena and ferrosilicon”. *Transactions of the Canadian Institute of Mining, Metallurgy and Petroleum* 60, pp. 147–154.
- Gran, K. B., D. R. Montgomery, and J. C. Halbur (2011). “Long-term elevated post-eruption sedimentation at Mount Pinatubo, Philippines”. *Geology* 39 (4), pp. 367–370. DOI: 10.1130/g31682.1.
- Gray, J. M. N. T. and X. Cui (2007). “Weak, strong and detached oblique shocks in gravity-driven granular free-surface flows”. *Journal of Fluid Mechanics* 579, pp. 113–136. DOI: 10.1017/S0022112007004843.
- Gray, J. M. N. T. and A. N. Edwards (2014). “A depth-averaged $\mu(I)$ -rheology for shallow granular free-surface flows”. *Journal of Fluid Mechanics* 755, pp. 503–534. DOI: 10.1017/jfm.2014.450.

- Gray, J. M. N. T. and B. P. Kokelaar (2010). "Large particle segregation, transport and accumulation in granular free-surface flows". *Journal of Fluid Mechanics* 652, pp. 105–137. DOI: 10.1017/S002211201000011X.
- Gray, J. M. N. T., Y. C. Tai, and S. Noelle (2003). "Shock waves, dead zones and particle-free regions in rapid granular free-surface flows". *Journal of Fluid Mechanics* 491, pp. 161–181. DOI: 10.1017/S0022112003005317.
- Gray, J. M. N. T., M. Wieland, and K. Hutter (1999). "Gravity-driven free surface flow of granular avalanches over complex basal topography". *Proceedings of the Royal Society A: Mathematical Physical and Engineering Sciences* 455 (1985), pp. 1841–1874. DOI: 10.1098/rspa.1999.0383.
- Guttorp, P. and M. L. Thompson (1991). "Estimating Second-Order Parameters of Volcanicity from Historical Data". *Journal of the American Statistical Association* 86 (415), pp. 578–583. DOI: 10.1080/01621459.1991.10475082.
- Guzzetti, F., A. C. Mondini, M. Cardinali, F. Fiorucci, M. Santangelo, and K.-T. Chang (2012). "Landslide inventory maps: New tools for an old problem". *Earth-science Reviews* 112 (1-2), pp. 42–66. DOI: 10.1016/j.earscirev.2012.02.001.
- Hakimhashemi, A. H. and G. Grünthal (2012). "A Statistical Method for Estimating Catalog Completeness Applicable to Long-Term Nonstationary Seismicity Data". *Bulletin of the Seismological Society of America* 102 (6), pp. 2530–2546. DOI: 10.1785/0120110309.
- Hákonardóttir, K. M. and A. J. Hogg (2005). "Oblique shocks in rapid granular flows". *Physics of Fluids* 17 (7), p. 077101. DOI: 10.1063/1.1950688.
- Hayakawa, Y. (1997). *Hayakawa's 2000-year eruption catalog*. Web Page.
- Hayes, S. K., D. R. Montgomery, and C. G. Newhall (2002). "Fluvial sediment transport and deposition following the 1991 eruption of Mount Pinatubo". *Geomorphology* 45 (3–4), pp. 211–224. DOI: 10.1016/S0169-555X(01)00155-6.
- Hoblitt, R. P., J. S. Wilder, C. L. Driedger, K. M. Scott, P. T. Pringle, and J. W. Vallance (1998). *Volcano hazards from Mount Rainier, Washington, revised 1998*. U.S. Geological Survey Open-File Report 98-428. 11 pp.
- Hodgson, K. A. and V. R. Manville (1999). "Sedimentology and flow behavior of a rain-triggered lahar, Mangatoetoenui Stream, Ruapehu volcano, New Zealand". *Geological Society of America Bulletin* 111 (5), pp. 743–754. DOI: 10.1130/0016-7606(1999)111<0743:safboa>2.3.co;2.
- Hungr, O. (1995). "A Model for the Runout Analysis of Rapid Flow Slides, Debris Flows, and Avalanches". *Canadian Geotechnical Journal* 32 (4), pp. 610–623. DOI: 10.1139/t95-063.
- Hungr, O., S. G. Evans, M. J. Bovis, and J. N. Hutchinson (2001). "A review of the classification of landslides of the flow type". *Environmental & Engineering Geoscience* 7 (3), pp. 221–238. DOI: 10.2113/gsegeosci.7.3.221.

- Hutter, K., M. Siegel, S. B. Savage, and Y. Nohguchi (1993). “2-dimensional Spreading of a Granular Avalanche down an Inclined Plane .1. Theory”. *Acta Mechanica* 100 (1-2), pp. 37–68. doi: 10.1007/BF01176861.
- Hutter, K., Y. Q. Wang, and S. P. Pudasaini (2005). “The Savage-Hutter avalanche model: how far can it be pushed?” *Philosophical Transactions of the Royal Society A: Mathematical Physical and Engineering Sciences* 363 (1832), pp. 1507–1528.
- Iverson, R. M. and R. P. Denlinger (2001). “Flow of variably fluidized granular masses across three-dimensional terrain 1. Coulomb mixture theory”. *Journal of Geophysical Research: Solid Earth* 106 (B1), pp. 537–552. doi: 10.1029/2000JB900329.
- Iverson, R. M. and D. L. George (2016). “Modelling landslide liquefaction, mobility bifurcation and the dynamics of the 2014 Oso disaster”. *Géotechnique* 66 (3), pp. 175–187. doi: 10.1680/jgeot.15.LM.004.
- Iverson, R. M., M. Logan, and R. P. Denlinger (2004). “Granular avalanches across irregular three-dimensional terrain: 2. Experimental tests”. *Journal of Geophysical Research: Earth Surface* 109 (F1), F01015. doi: 10.1029/2003JF000084.
- Iverson, R. M. (1997). “The physics of debris flows”. *Reviews of Geophysics* 35 (3), pp. 245–296. doi: 10.1029/97RG00426.
- (2000). “Landslide triggering by rain infiltration”. *Water Resources Research* 36 (7), pp. 1897–1910. doi: 10.1029/2000WR900090.
- (2012). “Elementary theory of bed-sediment entrainment by debris flows and avalanches”. *Journal of Geophysical Research: Earth Surface* 117, F03006. doi: 10.1029/2011JF002189.
- Iverson, R. M. and D. L. George (2014). “A depth-averaged debris-flow model that includes the effects of evolving dilatancy. I. Physical basis”. *Proceedings of the Royal Society of London A: Mathematical, Physical and Engineering Sciences* 470 (2170). doi: 10.1098/rspa.2013.0819.
- Iverson, R. M. and C. Ouyang (2015). “Entrainment of bed material by Earth-surface mass flows: Review and reformulation of depth-integrated theory”. *Reviews of Geophysics* 53 (1), pp. 27–58. doi: 10.1002/2013RG000447.
- Iverson, R. M., M. E. Reid, and R. G. LaHusen (1997). “Debris-flow mobilization from landslides”. *Annual Review of Earth and Planetary Sciences* 25 (1), pp. 85–138. doi: 10.1146/annurev.earth.25.1.85.
- Iverson, R. M., S. P. Schilling, and J. W. Vallance (1998). “Objective delineation of lahar-inundation hazard zones”. *Geological Society of America Bulletin* 110 (8), pp. 972–984. doi: 10.1130/0016-7606(1998)110<0972:odolih>2.3.co;2.
- Jan, C.-D. and H. Shen (1997). “Review dynamic modeling of debris flows”. *Recent Developments on Debris Flows*. Ed. by A. Armanini and M. Michiue. Vol. 64. Lecture Notes in Earth Sciences. Springer Berlin Heidelberg. Chap. 7, pp. 93–116. doi: 10.1007/BFb0117764.

- Javernick, L., J. Brasington, and B. Caruso (2014). "Modeling the topography of shallow braided rivers using Structure-from-Motion photogrammetry". *Geomorphology* 213, pp. 166–182. doi: 10.1016/j.geomorph.2014.01.006.
- Javernick, L., D. M. Hicks, R. Measures, B. Caruso, and J. Brasington (2016). "Numerical Modelling of Braided Rivers with Structure-from-Motion-Derived Terrain Models". *River Research and Applications* 32 (5), pp. 1071–1081. doi: 10.1002/rra.2918.
- Jenkins, S., R. Spence, J. Fonseca, R. Solidum, and T. Wilson (2014a). "Volcanic risk assessment: Quantifying physical vulnerability in the built environment". *Journal of Volcanology and Geothermal Research* 276, pp. 105–120. doi: 10.1016/j.jvolgeores.2014.03.002.
- Jenkins, S., T. Wilson, C. Magill, V. Miller, C. Stewart, W. Marzocchi, and M. Boulton (2014b). *Volcanic ash fall hazard and risk: Technical Background Paper for the UN-ISDR 2015 Global Assessment Report on Disaster Risk Reduction*. Tech. rep. United Nations Office for Disaster Risk Reduction. 43 pp.
- Jenkins, S., C. Magill, J. McAneney, and R. Blong (2012a). "Regional ash fall hazard I: a probabilistic assessment methodology". *Bulletin of Volcanology* 74 (7), pp. 1699–1712. doi: 10.1007/s00445-012-0627-8.
- (2012b). "Regional ash fall hazard I: a probabilistic assessment methodology". *Bulletin of Volcanology* 74 (7), pp. 1699–1712. doi: 10.1007/s00445-012-0627-8.
- Jenkins, S., J. Phillips, R. Price, K. Feloy, P. Baxter, D. Hadmoko, and E. de Bélizal (2015). "Developing building-damage scales for lahars: application to Merapi volcano, Indonesia". *Bulletin of Volcanology* 77 (9), pp. 1–17. doi: 10.1007/s00445-015-0961-8.
- Johnson, C. G., B. P. Kokelaar, R. M. Iverson, M. Logan, R. G. LaHusen, and J. M. N. T. Gray (2012). "Grain-size segregation and levee formation in geophysical mass flows". *Journal of Geophysical Research: Earth Surface* 117, F01032. doi: 10.1029/2011JF002185.
- Johnson, K. A. and N. Sitar (1990). "Hydrologic conditions leading to debris-flow initiation". *Canadian Geotechnical Journal* 27 (6), pp. 789–801. doi: 10.1139/t90-092.
- Jones, R., V. Manville, and D. Andrade (2015). "Probabilistic analysis of rain-triggered lahar initiation at Tungurahua volcano". *Bulletin of Volcanology* 77 (8), pp. 1–19. doi: 10.1007/s00445-015-0946-7.
- Jop, P., Y. Forterre, and O. Pouliquen (2006). "A constitutive law for dense granular flows". *Nature* 441 (7094), pp. 727–730. doi: 10.1038/nature04801.
- Julian, J. P. and R. Torres (2006). "Hydraulic erosion of cohesive riverbanks". *Geomorphology* 76 (1–2), pp. 193–206. doi: 10.1016/j.geomorph.2005.11.003.
- Julien, P. and Y. Lan (1991). "Rheology of Hyperconcentrations". *Journal of Hydraulic Engineering* 117 (3), pp. 346–353. doi: 10.1061/(ASCE)0733-9429(1991)117:3(346).
- Kean, J. W., S. W. McCoy, G. E. Tucker, D. M. Staley, and J. A. Coe (2013). "Runoff-generated debris flows: Observations and modeling of surge initiation, magnitude, and

- frequency". *Journal of Geophysical Research: Earth Surface* 118 (4), pp. 2190–2207. doi: 10.1002/jgrf.20148.
- Kelfoun, K. (2011). "Suitability of simple rheological laws for the numerical simulation of dense pyroclastic flows and long-runout volcanic avalanches". *Journal of Geophysical Research: Solid Earth* 116 (B8). B08209, p. 14. doi: 10.1029/2010JB007622.
- Kelman, I. and R. Spence (2004). "An overview of flood actions on buildings". *Engineering Geology* 73 (3–4), pp. 297–309. doi: 10.1016/j.enggeo.2004.01.010.
- Kirschbaum, D., R. Adler, Y. Hong, S. Hill, and A. Lerner-Lam (2010). "A global landslide catalog for hazard applications: method, results, and limitations". *Natural Hazards* 52 (3), pp. 561–575. doi: 10.1007/s11069-009-9401-4.
- Klein, F. W. (1982). "Patterns of historical eruptions at Hawaiian volcanoes". *Journal of Volcanology and Geothermal Research* 12 (1–2), pp. 1–35. doi: 10.1016/0377-0273(82)90002-6.
- Konishi, J., M. Oda, and S. Nemat-Nasser (1983). "Induced anisotropy in assemblies of oval cross-sectional rods in biaxial compression". Ed. by J. T. Jenkins and M. Satake. Elsevier, pp. 31–39.
- Kowalski, J. and J. N. McElwaine (2013). "Shallow two-component gravity-driven flows with vertical variation". *Journal of Fluid Mechanics* 714, pp. 434–462. doi: 10.1017/jfm.2012.489.
- Kreylos, O., M. Oskin, E. Cowgill, P. Gold, A. Elliott, and L. Kellogg (2013). "Point-based computing on scanned terrain with LidarViewer". *Geosphere* 9 (3), pp. 546–556. doi: 10.1130/ges00705.1.
- Künzler, M., C. Huggel, and J. M. Ramírez (2012). "A risk analysis for floods and lahars: case study in the Cordillera Central of Colombia". *Natural Hazards* 64 (1), pp. 767–796. doi: 10.1007/s11069-012-0271-9.
- Kurganov, A. and G. Petrova (2007). "A Second-Order Well-Balanced Positivity Preserving Central-Upwind Scheme for the Saint-Venant System". *Communications in Mathematical Sciences* 5 (1), pp. 133–160.
- Kysely, J., L. Gaál, and J. Pícek (2011). "Comparison of regional and at-site approaches to modelling probabilities of heavy precipitation". *International Journal of Climatology* 31 (10), pp. 1457–1472. doi: 10.1002/joc.2182.
- Lamb, H. H. (1970). "Volcanic Dust in the Atmosphere; with a Chronology and Assessment of Its Meteorological Significance". *Philosophical Transactions of the Royal Society of London Series A: Mathematical and Physical Sciences* 266 (1178), pp. 425–533. doi: 10.2307/73764.
- Landcare Research NZ Ltd. (2010). *NZDEM North Island 25 metre*. Dataset.
- Landsea, C. (2007). "Counting Atlantic tropical cyclones back to 1900". *Eos, Transactions American Geophysical Union* 88 (18), pp. 197–202. doi: 10.1029/2007EO180001.

- Lang, M., T. B. M. J. Ouarda, and B. Bobée (1999). “Towards operational guidelines for over-threshold modeling”. *Journal of Hydrology* 225 (3–4), pp. 103–117. doi: 10.1016/S0022-1694(99)00167-5.
- Lavigne, F., J.-C. Thouret, B. Voight, K. Young, R. LaHusen, J. Marso, H. Suwa, A. Sumaryono, D. S. Sayudi, and M. Dejean (2000). “Instrumental lahar monitoring at Merapi Volcano, Central Java, Indonesia”. *Journal of Volcanology and Geothermal Research* 100 (1–4), pp. 457–478. doi: 10.1016/S0377-0273(00)00151-7.
- Lavigne, F. (1999). “Lahar hazard micro-zonation and risk assessment in Yogyakarta city, Indonesia”. *GeoJournal* 49 (2), pp. 173–183. doi: 10.1023/A:1007035612681.
- Lavigne, F. and J.-C. Thouret (2003). “Sediment transportation and deposition by rain-triggered lahars at Merapi Volcano, Central Java, Indonesia”. *Geomorphology* 49 (1–2), pp. 45–69. doi: 10.1016/S0169-555X(02)00160-5.
- Leavesley, G. H., G. C. Lusby, and R. W. Lichty (1989). “Infiltration and erosion characteristics of selected tephra deposits from the 1980 eruption of Mount St. Helens, Washington, USA”. *Hydrological Sciences Journal* 34 (3), pp. 339–353. doi: 10.1080/02626668909491338.
- Lecointre, J., K. Hodgson, V. Neall, and S. Cronin (2004). “Lahar-Triggering Mechanisms and Hazard at Ruapehu Volcano, New Zealand”. *Natural Hazards* 31 (1), pp. 85–109. doi: 10.1023/B:NHAZ.0000020256.16645.eb.
- Legleiter, C. J., P. C. Kyriakidis, R. R. McDonald, and J. M. Nelson (2011). “Effects of uncertain topographic input data on two-dimensional flow modeling in a gravel-bed river”. *Water Resources Research* 47 (3), W03518. doi: 10.1029/2010WR009618.
- Leonard, G. S., C. Stewart, T. M. Wilson, J. N. Procter, B. J. Scott, H. J. Keys, G. E. Jolly, J. B. Wardman, S. J. Cronin, and S. K. McBride (2014). “Integrating multidisciplinary science, modelling and impact data into evolving, syn-event volcanic hazard mapping and communication: A case study from the 2012 Tongariro eruption crisis, New Zealand”. *Journal of Volcanology and Geothermal Research* 286, pp. 208–232. doi: <http://dx.doi.org/10.1016/j.jvolgeores.2014.08.018>.
- Leutenegger, S., M. Chli, and R. Y. Siegwart (2011). “BRISK: Binary Robust invariant scalable keypoints”. *2011 IEEE International Conference on Computer Vision (ICCV)*, pp. 2548–2555. doi: 10.1109/ICCV.2011.6126542.
- Li, W. C., H. J. Li, F. C. Dai, and L. M. Lee (2012). “Discrete element modeling of a rainfall-induced flowslide”. *Engineering Geology* 149, pp. 22–34. doi: 10.1016/j.enggeo.2012.08.006.
- Liu, X., B. J. Landry, and M. H. García (2008). “Two-dimensional scour simulations based on coupled model of shallow water equations and sediment transport on unstructured meshes”. *Coastal Engineering* 55 (10), pp. 800–810. doi: 10.1016/j.coastaleng.2008.02.012.

- Liu, Z. and H. A. Koyi (2013). “Kinematics and internal deformation of granular slopes: insights from discrete element modeling”. *Landslides* 10 (2), pp. 139–160. doi: 10.1007/s10346-012-0318-8.
- Lo, C.-M., M.-L. Lin, C.-L. Tang, and J.-C. Hu (2011). “A kinematic model of the Hsiaolin landslide calibrated to the morphology of the landslide deposit”. *Engineering Geology* 123 (1-2), pp. 22–39. doi: 10.1016/j.enggeo.2011.07.002.
- Lowe, D. G. (1999). “Object recognition from local scale-invariant features”. *The Proceedings of the Seventh IEEE International Conference on Computer Vision*. Vol. 2, pp. 1150–1157. doi: 10.1109/ICCV.1999.790410.
- Lowe, D. R., S. N. Williams, H. Leigh, C. B. Connort, J. B. Gemmell, and R. E. Stoiber (1986). “Lahars initiated by the 13 November 1985 eruption of Nevado del Ruiz, Colombia”. *Nature* 324 (6092), pp. 51–53. doi: 10.1038/324051a0.
- Lu, M. and G. R. McDowell (2007). “The importance of modelling ballast particle shape in the discrete element method”. *Granular Matter* 9 (1-2), pp. 69–80. doi: 10.1007/s10035-006-0021-3.
- Lube, G., S. J. Cronin, V. Manville, J. N. Procter, S. E. Cole, and A. Freundt (2012). “Energy growth in laharc mass flows”. *Geology* 40 (5), pp. 475–478. doi: 10.1130/G32818.1.
- Magill, C. and R. Blong (2005a). “Volcanic risk ranking for Auckland, New Zealand. I: Methodology and hazard investigation”. *Bulletin of Volcanology* 67 (4), pp. 331–339. doi: 10.1007/s00445-004-0374-6.
- (2005b). “Volcanic risk ranking for Auckland, New Zealand. I: Methodology and hazard investigation”. *Bulletin of Volcanology* 67 (4), pp. 331–339. doi: 10.1007/s00445-004-0374-6.
- (2005c). “Volcanic risk ranking for Auckland, New Zealand. II: Hazard consequences and risk calculation”. *Bulletin of Volcanology* 67 (4), pp. 340–349. doi: 10.1007/s00445-004-0375-5.
- Magill, C., R. Blong, and J. McAneney (2006). “VolcaNZ—A volcanic loss model for Auckland, New Zealand”. *Journal of Volcanology and Geothermal Research* 149 (3–4), pp. 329–345. doi: 10.1016/j.jvolgeores.2005.09.004.
- Major, J., T. Pierson, R. Dinehart, and J. Costa (2000). “Sediment yield following severe volcanic disturbance—A two-decade perspective from Mount St. Helens”. *Geology* 28 (9), pp. 819–822. doi: 10.1130/0091-7613(2000)28<819:syfsvd>2.0.co;2.
- Major, J. J. and T. Yamakoshi (2005). “Decadal-scale change of infiltration characteristics of a tephra-mantled hillslope at Mount St Helens, Washington”. *Hydrological Processes* 19 (18), pp. 3621–3630. doi: 10.1002/hyp.5863.
- Manville, V., K. A. Hodgson, B. F. Houghton, J. R. Keys, and J. D. L. White (2000). “Tephra, snow and water: complex sedimentary responses at an active snow-capped stratovolcano, Ruapehu, New Zealand”. *Bulletin of Volcanology* 62 (4-5), pp. 278–293. doi: 10.1007/s004450000096.

- Manville, V., J. J. Major, and S. A. Fagents (2013). “Modeling lahar behaviour and hazards”. *Modeling volcanic processes : the physics and mathematics of volcanism*. Ed. by S. A. Fagents, T. K. P. Gregg, and R. M. C. Lopes. Cambridge: Cambridge University Press, pp. 300–330. DOI: 10.1017/CBO9781139021562.014.
- Manville, V., K. Németh, and K. Kano (2009). “Source to sink: a review of three decades of progress in the understanding of volcanoclastic processes, deposits, and hazards”. *Sedimentary Geology* 220 (3-4), pp. 136–161. DOI: 10.1016/j.sedgeo.2009.04.022.
- Manville, V. and S. J. Cronin (2007). “Breakout Lahar from New Zealand’s Crater Lake”. *Eos, Transactions American Geophysical Union* 88 (43), pp. 441–442. DOI: 10.1029/2007EO430001.
- Martelli, K. (2011). “The physical vulnerability of urban areas facing the threat of inundation from lahars and flash floods: application to the case study of Arequipa, Peru”. Thesis. Université Blaise Pascal - Clermont-Ferrand II. 337 pp.
- Marzocchi, W. and M. S. Bebbington (2012). “Probabilistic eruption forecasting at short and long time scales”. *Bulletin of Volcanology* 74 (8), pp. 1777–1805. DOI: 10.1007/s00445-012-0633-x.
- Marzocchi, W., A. Garcia-Aristizabal, P. Gasparini, M. L. Mastellone, and A. Di Ruocco (2012). “Basic principles of multi-risk assessment: a case study in Italy”. *Natural Hazards* 62 (2), pp. 551–573. DOI: 10.1007/s11069-012-0092-x.
- Marzocchi, W., L. Sandri, P. Gasparini, C. Newhall, and E. Boschi (2004). “Quantifying probabilities of volcanic events: The example of volcanic hazard at Mount Vesuvius”. *Journal of Geophysical Research: Solid Earth* 109 (B11), B11201. DOI: 10.1029/2004JB003155.
- Marzocchi, W. and L. Zaccarelli (2006). “A quantitative model for the time-size distribution of eruptions”. *Journal of Geophysical Research: Solid Earth* 111 (B4), B04204. DOI: 10.1029/2005JB003709.
- McDougall, S. (2016). “Landslide Runout Analysis - Current Practice and Challenges”. *Canadian Geotechnical Journal* In Press, pp. 1–59. DOI: 10.1139/cgj-2016-0104.
- Mead, S. and P. W. Cleary (2011). “Three dimensional avalanche modelling across irregular terrain using DEM: Comparison with experiment”. *19th International Congress on Modelling and Simulation (MODSIM2011)*.
- Mead, S. R. and P. W. Cleary (2015). “Validation of DEM prediction for granular avalanches on irregular terrain”. *Journal of Geophysical Research: Earth Surface* 120 (9). 2014JF003331, pp. 1724–1742. DOI: 10.1002/2014JF003331.
- Mead, S. R., P. W. Cleary, and G. K. Robinson (2012). “Characterising the failure and repose angles of irregularly shaped three-dimensional particles using DEM”. *Proceedings of the Ninth International Conference on CFD in the Minerals and Process Industries, CSIRO, Melbourne, Australia*, pp. 10–12.

- Mead, S. R., M. Prakash, C. Magill, M. Bolger, and J.-C. Thouret (2015). “A Distributed Computing Workflow for Modelling Environmental Flows in Complex Terrain”. *Environmental Software Systems. Infrastructures, Services and Applications*. Ed. by R. Denzer, R. Argent, G. Schimak, and J. Hřebíček. Vol. 448. IFIP Advances in Information and Communication Technology. Springer International Publishing. Chap. 32, pp. 321–332. doi: 10.1007/978-3-319-15994-2_32.
- Mead, S. and C. Magill (2014). “Determining change points in data completeness for the Holocene eruption record”. *Bulletin of Volcanology* 76 (11), pp. 1–14. doi: 10.1007/s00445-014-0874-y.
- Mead, S., C. Magill, and J. Hilton (2016). “Rain-triggered lahar susceptibility using a shallow landslide and surface erosion model”. *Geomorphology* 273, pp. 168–177. doi: 10.1016/j.geomorph.2016.08.022.
- Mendoza-Rosas, A. T. and S. De la Cruz-Reyna (2008). “A statistical method linking geological and historical eruption time series for volcanic hazard estimations: applications to active polygenetic volcanoes”. *Journal of Volcanology and Geothermal Research* 176 (2), pp. 277–290. doi: 10.1016/j.jvolgeores.2008.04.005.
- Mergili, M., J.-T. Fischer, J. Krenn, and S. P. Pudasaini (2017). “r.avaflow v1, an advanced open-source computational framework for the propagation and interaction of two-phase mass flows”. *Geoscientific Model Development* 10 (2), pp. 553–569. doi: 10.5194/gmd-10-553-2017.
- Merz, B., A. H. Thielen, and M. Gocht (2007). “Flood Risk Mapping At The Local Scale: Concepts and Challenges”. *Flood Risk Management in Europe*. Ed. by S. Begum, M. F. Stive, and J. Hall. Vol. 25. Advances in Natural and Technological Hazards Research. Springer Netherlands. Chap. 13, pp. 231–251. doi: 10.1007/978-1-4020-4200-3_13.
- Minatti, L. and E. Paris (2015). “A SPH model for the simulation of free surface granular flows in a dense regime”. *Applied Mathematical Modelling* 39 (1), pp. 363–382. doi: 10.1016/j.apm.2014.05.034.
- Mitsoulis, E. (2007). “Flows of viscoplastic materials: models and computations”. *Rheology Reviews*, pp. 135–178.
- Miyabuchi, Y. and H. Daimaru (2004). “The June 2001 rainfall-induced landslides and associated lahars at Aso volcano (southwestern Japan): implications for hazard assessment”. *Acta Vulcanologica* 16 (1-2), p. 21.
- Miyabuchi, Y., F. Maeno, and S. Nakada (2015). “The October 16, 2013 rainfall-induced landslides and associated lahars at Izu Oshima Volcano, Japan”. *Journal of Volcanology and Geothermal Research* 302, pp. 242–256. doi: 10.1016/j.jvolgeores.2015.07.012.
- Monaghan, J. (1994). “Simulating Free Surface Flows with SPH”. *Journal of Computational Physics* 110 (2), pp. 399–406. doi: 10.1006/jcph.1994.1034.

- Montgomery, D. R., M. S. Panfil, and S. K. Hayes (1999). "Channel-bed mobility response to extreme sediment loading at Mount Pinatubo". *Geology* 27 (3), pp. 271–274. doi: 10.1130/0091-7613(1999)027<0271:cbmrte>2.3.co;2.
- Mulargia, F., P. Gasperini, and S. Tinti (1987). "Identifying different regimes in eruptive activity: An application to Etna volcano". *Journal of Volcanology and Geothermal Research* 34 (1–2), pp. 89–106. doi: 10.1016/0377-0273(87)90095-3.
- Nadim, F., O. Kjekstad, P. Peduzzi, C. Herold, and C. Jaedicke (2006). "Global landslide and avalanche hotspots". *Landslides* 3 (2), pp. 159–173. doi: 10.1007/s10346-006-0036-1.
- Neri, A., W. Aspinall, R. Cioni, A. Bertagnini, P. Baxter, G. Zuccaro, D. Andronico, S. Barsotti, P. Cole, T. E. Ongaro, T. Hincks, G. Macedonio, P. Papale, M. Rosi, R. Santacroce, and G. Woo (2008). "Developing an Event Tree for probabilistic hazard and risk assessment at Vesuvius". *Journal of Volcanology and Geothermal Research* 178 (3), pp. 397–415. doi: 10.1016/j.jvolgeores.2008.05.014.
- Newhall, C. G. and R. U. Solidum (2015). "Eruptions and lahars of Mount Pinatubo, 1991–2000". *Global Volcanic Hazards and Risk*. Ed. by S. C. Loughlin, S. Sparks, S. K. Brown, S. F. Jenkins, and C. Vye-Brown. Cambridge University Press, pp. 249–254. doi: 10.1017/CBO9781316276273.009.
- Newhall, C. and R. Hoblitt (2002). "Constructing event trees for volcanic crises". *Bulletin of Volcanology* 64 (1), pp. 3–20. doi: 10.1007/s004450100173.
- Newhall, C. G. and S. Self (1982). "The volcanic explosivity index (VEI) an estimate of explosive magnitude for historical volcanism". *Journal of Geophysical Research: Oceans* 87 (C2), pp. 1231–1238. doi: 10.1029/JC087iC02p01231.
- NIWA (2016). *High Intensity Rainfall Design System v3*. Online Database.
- O'Brien, J. and P. Julien (1988). "Laboratory Analysis of Mudflow Properties". *Journal of Hydraulic Engineering* 114 (8), pp. 877–887. doi: 10.1061/(ASCE)0733-9429(1988)114:8(877).
- O'Brien, J., P. Julien, and W. Fullerton (1993). "Two-Dimensional Water Flood and Mudflow Simulation". *Journal of Hydraulic Engineering* 119 (2), pp. 244–261. doi: 10.1061/(ASCE)0733-9429(1993)119:2(244).
- Oda, M., S. Nemat-Nasser, and J. Konishi (1985). "Stress-induced anisotropy in granular masses". *Soils and foundations* 25 (3), pp. 85–97. doi: 10.3208/sandf1972.25.3_85.
- Okura, Y., H. Kitahara, and T. Sammori (2000). "Fluidization in dry landslides". *Engineering Geology* 56 (3–4), pp. 347–360. doi: 10.1016/S0013-7952(99)00118-0.
- Owen, P. J., P. W. Cleary, and C. Mériaux (2009). "Quasi-static fall of planar granular columns: comparison of 2D and 3D discrete element modelling with laboratory experiments". *Geomechanics and Geoengineering* 4 (1), pp. 55–77. doi: 10.1080/17486020902767388.
- Page, A. W. (1996). "Unreinforced masonry structures-an Australian overview". *Bulletin of the New Zealand national society for earthquake engineering* 29 (4), pp. 242–255.

- Papanastasiou, T. C. (1987). “Flows of Materials with Yield”. *Journal of Rheology* 31 (5), pp. 385–404. doi: 10.1122/1.549926.
- Pareschi, M., M. Favalli, F. Giannini, R. Sulpizio, G. Zanchetta, and R. Santacroce (2000). “May 5, 1998, debris flows in circum-Vesuvian areas (southern Italy): Insights for hazard assessment”. *Geology* 28 (7), pp. 639–642. doi: 10.1130/0091-7613(2000)28<639:mdfica>2.0.co;2.
- Patra, A. K., A. C. Bauer, C. C. Nichita, E. B. Pitman, M. F. Sheridan, M. Bursik, B. Rupp, A. Webber, A. J. Stinton, L. M. Namikawa, and C. S. Renschler (2005). “Parallel adaptive numerical simulation of dry avalanches over natural terrain”. *Journal of Volcanology and Geothermal Research* 139 (1-2), pp. 1–21. doi: 10.1016/j.jvolgeores.2004.06.014.
- Phillips, C. J. and T. R. H. Davies (1991). “Determining rheological parameters of debris flow material”. *Geomorphology* 4 (2), pp. 101–110. doi: 10.1016/0169-555X(91)90022-3.
- Pickands III, J. (1971). “The two-dimensional Poisson process and extremal processes”. *Journal of Applied Probability* 8 (4), pp. 745–756. doi: 10.2307/3212238.
- Pierson, T. C. (1998). “An empirical method for estimating travel times for wet volcanic mass flows”. *Bulletin of Volcanology* 60 (2), pp. 98–109. doi: 10.1007/s004450050219.
- (2005). “Hyperconcentrated flow — transitional process between water flow and debris flow”. *Debris-flow Hazards and Related Phenomena*. Berlin, Heidelberg: Springer Berlin Heidelberg, pp. 159–202. doi: 10.1007/3-540-27129-5_8.
- Pierson, T. C. and J. E. Costa (1987). “A rheologic classification of subaerial sediment-water flows”. *Reviews in Engineering Geology* 7, pp. 1–12. doi: 10.1130/REG7-p1.
- Pierson, T. C., A. S. Daag, P. Delos Reyes, M. T. M. Regalado, R. U. Solidum, and B. S. Tubianosa (1996). “Flow and deposition of posteruption hot lahars on the east side of Mount Pinatubo, July–October 1991”. *Fire and Mud: eruptions and lahars of Mount Pinatubo, Philippines*, pp. 921–950.
- Pierson, T. C., R. J. Janda, J.-C. Thouret, and C. A. Borrero (1990). “Perturbation and melting of snow and ice by the 13 November 1985 eruption of Nevado del Ruiz, Colombia, and consequent mobilization, flow and deposition of lahars”. *Journal of Volcanology and Geothermal Research* 41 (1), pp. 17–66. doi: 10.1016/0377-0273(90)90082-Q.
- Pierson, T. C. and J. J. Major (2014). “Hydrogeomorphic Effects of Explosive Volcanic Eruptions on Drainage Basins”. *Annual Review of Earth and Planetary Sciences* 42 (1), pp. 469–507. doi: 10.1146/annurev-earth-060313-054913.
- Pierson, T. C., J. J. Major, À. Amigo, and H. Moreno (2013). “Acute sedimentation response to rainfall following the explosive phase of the 2008–2009 eruption of Chaitén volcano, Chile”. *Bulletin of Volcanology* 75 (5), pp. 1–17. doi: 10.1007/s00445-013-0723-4.
- Pierson, T. C. and K. M. Scott (1985). “Downstream Dilution of a Lahar: Transition From Debris Flow to Hyperconcentrated Streamflow”. *Water Resources Research* 21 (10), pp. 1511–1524. doi: 10.1029/WR021i010p01511.

- Pierson, T. C., N. J. Wood, and C. L. Driedger (2014). "Reducing risk from lahar hazards: concepts, case studies, and roles for scientists". *Journal of Applied Volcanology* 3 (1), pp. 1–25. DOI: 10.1186/s13617-014-0016-4.
- Pistolesi, M., R. Cioni, M. Rosi, and E. Aguilera (2014). "Lahar hazard assessment in the southern drainage system of Cotopaxi volcano, Ecuador: Results from multiscale lahar simulations". *Geomorphology* 207, pp. 51–63. DOI: 10.1016/j.geomorph.2013.10.026.
- Pitman, E. B. and L. Le (2005). "A two-fluid model for avalanche and debris flows". *Philosophical Transactions of the Royal Society of London A: Mathematical, Physical and Engineering Sciences* 363 (1832), pp. 1573–1601. DOI: 10.1098/rsta.2005.1596.
- Pitman, E. B., C. C. Nichita, A. Patra, A. Bauer, M. Sheridan, and M. Bursik (2003). "Computing granular avalanches and landslides". *Physics of Fluids* 15 (12), pp. 3638–3646. DOI: 10.1063/1.1614253.
- Pouliquen, O., J. Delour, and S. B. Savage (1997). "Fingering in granular flow". *Nature* 386 (6627), pp. 816–817. DOI: 10.1038/386816a0.
- Prakash, M., K. Rothauge, and P. W. Cleary (2014). "Modelling the impact of dam failure scenarios on flood inundation using {SPH}". *Applied Mathematical Modelling* 38 (23), pp. 5515–5534. DOI: 10.1016/j.apm.2014.03.011.
- Procter, J. N., S. J. Cronin, I. C. Fuller, M. Sheridan, V. E. Neall, and H. Keys (2010). "Lahar hazard assessment using Titan2D for an alluvial fan with rapidly changing geomorphology: Whangaehu River, Mt. Ruapehu". *Geomorphology* 116 (1–2), pp. 162–174. DOI: 10.1016/j.geomorph.2009.10.016.
- Pudasaini, S. P. and K. Hutter (2003). "Rapid shear flows of dry granular masses down curved and twisted channels". *Journal of Fluid Mechanics* 495, pp. 193–208. DOI: 10.1017/S0022112003006141.
- Pudasaini, S. P. (2012). "A general two-phase debris flow model". *Journal of Geophysical Research: Earth Surface* 117 (F3). DOI: 10.1029/2011JF002186.
- Pudasaini, S. P. and M. Krautblatter (2014). "A two-phase mechanical model for rock-ice avalanches". *Journal of Geophysical Research: Earth Surface* 119 (10), pp. 2272–2290. DOI: 10.1002/2014JF003183.
- Reid, M. E. (1994). "A Pore-Pressure Diffusion Model for Estimating Landslide-Inducing Rainfall". *The Journal of Geology* 102 (6), pp. 709–717. DOI: 10.2307/30065645.
- Reid, M. E., H. P. Nielsen, and S. J. Dreiss (1988). "Hydrologic Factors Triggering a Shallow Hillslope Failure". *Bulletin of the Association of Engineering Geologists* xxv (3), pp. 349–361. DOI: 10.2113/gseegeosci.xxv.3.349.
- Rickenmann, D. (2001). "Comparison of bed load transport in torrents and gravel bed streams". *Water Resources Research* 37 (12), pp. 3295–3305. DOI: 10.1029/2001WR000319.
- Robinson, J. E. and M. A. Clynne (2012). *Lahar hazard zones for eruption-generated lahars in the Lassen Volcanic Center, California*. U.S. Geological Survey Scientific Investigations Report 2328-0328. 13 pp.

- Rodolfo, K. S. and A. T. Arguden (1991). "Rain-Lahar Generation and Sediment-Delivery Systems at Mayon Volcano, Philippines". *Sedimentation in Volcanic Settings*. Vol. 45. SEPM Society for Sedimentary Geology, pp. 71–87. doi: 10.2110/pec.91.45.0071.
- Rodriguez-Paz, M. X. and J. Bonet (2004). "A corrected smooth particle hydrodynamics method for the simulation of debris flows". *Numerical Methods for Partial Differential Equations* 20 (1), pp. 140–163. doi: 10.1002/num.10083.
- Roos, W. (2003). *Damage to buildings*. Report. Delft Cluster.
- Rothenburg, L. and R. J. Bathurst (1992). "Micromechanical Features of Granular Assemblies with Planar Elliptic Particles". *Geotechnique* 42 (1), pp. 79–95.
- Rotondi, R. and E. Garavaglia (2002). "Statistical Analysis of the Completeness of a Seismic Catalogue". *Natural Hazards* 25 (3), pp. 245–258. doi: 10.1023/A:1014855822358.
- Rusu, R. B. and S. Cousins (2011). "3D is here: Point Cloud Library (PCL)". *2011 IEEE International Conference on Robotics and Automation (ICRA)*, pp. 1–4. doi: 10.1109/ICRA.2011.5980567.
- Salciarini, D., C. Tamagnini, and P. Conversini (2010). "Discrete element modeling of debris-avalanche impact on earthfill barriers". *Physics and Chemistry of the Earth* 35 (3-5), pp. 172–181. doi: 10.1016/j.pce.2009.05.002.
- Sandri, L., J.-C. Thouret, R. Constantinescu, S. Biass, and R. Tonini (2014). "Long-term multi-hazard assessment for El Misti volcano (Peru)". *Bulletin of Volcanology* 76 (2), pp. 1–26. doi: 10.1007/s00445-013-0771-9.
- Santamarina, C. and G. Cascante (1998). "Effect of surface roughness on wave propagation parameters". *Geotechnique* 48 (1), pp. 129–136.
- Savage, S. B. and K. Hutter (1989). "The Motion of a Finite Mass of Granular Material down a Rough Incline". *Journal of Fluid Mechanics* 199, pp. 177–215. doi: 10.1017/S0022112089000340.
- (1991). "The dynamics of avalanches of granular materials from initiation to runout. Part I: Analysis". *Acta Mechanica* 86 (1-4), pp. 201–223. doi: 10.1007/BF01175958.
- Savage, S. and R. Iverson (2003). "Surge dynamics coupled to pore-pressure evolution in debris flows". *3rd International Conference on Debris-Flow Hazards Mitigation: Mechanics, Prediction, and Assessment*. Ed. by R. D. and C. C.L, pp. 503–504.
- Scaini, C., S. Biass, A. Galderisi, C. Bonadonna, A. Folch, K. Smith, and A. Höskuldsson (2014). "A multi-scale risk assessment for tephra fallout and airborne concentration from multiple Icelandic volcanoes — Part 2: Vulnerability and impact". *Natural Hazards and Earth System Sciences* 14 (8), pp. 2289–2312. doi: 10.5194/nhess-14-2289-2014.
- Schilling, S. P. (2014). *Laharz_py: GIS tools for automated mapping of lahar inundation hazard zones*. U.S. Geological Survey Open-File Report 2331-1258. 78 pp. doi: 10.3133/ofr20141073.

- Schuster, S. S., R. J. Blong, and M. S. Speer (2005). "A hail climatology of the greater Sydney area and New South Wales, Australia". *International Journal of Climatology* 25 (12), pp. 1633–1650. doi: 10.1002/joc.1199.
- Scott, K. M., J. W. Vallance, N. Kerle, J. Luis Macías, W. Strauch, and G. Devoli (2005). "Catastrophic precipitation-triggered lahar at Casita volcano, Nicaragua: occurrence, bulking and transformation". *Earth Surface Processes and Landforms* 30 (1), pp. 59–79. doi: 10.1002/esp.1127.
- Scott, W. E., T. C. Pierson, S. P. Schilling, J. E. Costa, C. A. Gardner, J. W. Vallance, and J. J. Major (1997). *Volcano hazards in the Mount Hood region, Oregon*. U.S. Geological Survey Open-File Report 97-89. 14 pp.
- Scott, W. E., R. M. Iverson, S. P. Schilling, and B. J. Fisher (2001). *Volcano hazards in the Three Sisters region, Oregon*. U.S. Geological Survey Open-File Report 99-437. 14 pp.
- Seitz, S. M., B. Curless, J. Diebel, D. Scharstein, and R. Szeliski (2006). "A Comparison and Evaluation of Multi-View Stereo Reconstruction Algorithms". *2006 IEEE Computer Society Conference on Computer Vision and Pattern Recognition (CVPR)*. Vol. 1, pp. 519–528. doi: 10.1109/CVPR.2006.19.
- Sheridan, M. F. (1979). "Emplacement of pyroclastic flows: A review". *Geological Society of America Special Papers* 180, pp. 125–136. doi: 10.1130/SPE180-p125.
- Sherrod, D. R., L. G. Mastin, W. E. Scott, and S. P. Schilling (1997). *Volcano hazards at Newberry Volcano, Oregon*. U.S. Geological Survey Open-File Report 97-513. 14 pp.
- Siebert, L., T. Simkin, and P. Kimberly (2010). *Volcanoes of the World: Third Edition*. University of California Press. 568 pp.
- Small, C. and T. Naumann (2001). "The global distribution of human population and recent volcanism". *Global Environmental Change Part B: Environmental Hazards* 3 (3–4), pp. 93–109. doi: 10.1016/S1464-2867(02)00002-5.
- Snively, N., S. M. Seitz, and R. Szeliski (2006). "Photo tourism: exploring photo collections in 3D". *ACM Transactions on Graphics* 25 (3), pp. 835–846. doi: 10.1145/1141911.1141964.
- Staron, L. (2008). "Mobility of long-runout rock flows: a discrete numerical investigation". *Geophysical Journal International* 172 (1), pp. 455–463. doi: 10.1111/j.1365-246X.2007.03631.x.
- Stevens, N. F., V. Manville, and D. W. Heron (2003). "The sensitivity of a volcanic flow model to digital elevation model accuracy: experiments with digitised map contours and interferometric SAR at Ruapehu and Taranaki volcanoes, New Zealand". *Journal of Volcanology and Geothermal Research* 119 (1–4), pp. 89–105. doi: 10.1016/S0377-0273(02)00307-4.
- Stirling, M., M. Bebbington, M. Brenna, S. Cronin, A. Christophersen, N. Deligne, T. Hurst, A. Jolly, G. Jolly, B. Kennedy, G. Kereszturi, J. Lindsay, V. Neall, J. Procter, D. Rhoades, B. Scott, P. Shane, I. Smith, R. Smith, T. Wang, J. D. L. White, C. J. N. Wilson, and

- T. Wilson (2017). “Conceptual Development of a National Volcanic Hazard Model for New Zealand”. *Frontiers in Earth Science* 5, p. 51. DOI: 10.3389/feart.2017.00051.
- Stirling, M. and C. Wilson (2002). “Development of a volcanic hazard model for New Zealand: first approaches from the methods of probabilistic seismic hazard analysis”. *Bulletin of the New Zealand Society for Earthquake Engineering* 35 (4), pp. 266–277.
- Swanson, F. and J. Major (2005). “Physical Events, Environments, and Geological—Ecological Interactions at Mount St. Helens: March 1980–2004”. *Ecological Responses to the 1980 Eruption of Mount St. Helens*. Ed. by V. Dale, F. Swanson, and C. Crisafulli. Springer New York. Chap. 3, pp. 27–44. DOI: 10.1007/0-387-28150-9_3.
- Tai, Y. C. and C. Y. Kuo (2008). “A new model of granular flows over general topography with erosion and deposition”. *Acta Mechanica* 199 (1-4), pp. 71–96. DOI: 10.1007/s00707-007-0560-7.
- Tang, C.-L., J.-C. Hu, M.-L. Lin, J. Angelier, C.-Y. Lu, Y.-C. Chan, and H.-T. Chu (2009). “The Tsaoling landslide triggered by the Chi-Chi earthquake, Taiwan: Insights from a discrete element simulation”. *Engineering Geology* 106 (1-2), pp. 1–19. DOI: 10.1016/j.enggeo.2009.02.011.
- Teufelsbauer, H., Y. Wang, S. P. Pudasaini, R. I. Borja, and W. Wu (2011). “DEM simulation of impact force exerted by granular flow on rigid structures”. *Acta Geotechnica* 6 (3), pp. 119–133. DOI: 10.1007/s11440-011-0140-9.
- Teufelsbauer, H., Y. Wang, M.-C. Chiou, and W. Wu (2009). “Flow-obstacle interaction in rapid granular avalanches: DEM simulation and comparison with experiment”. *Granular Matter* 11 (4), pp. 209–220. DOI: 10.1007/s10035-009-0142-6.
- Thomas, P. A. and J. D. Bray (1999). “Capturing nonspherical shape of granular media with disk clusters”. *Journal of Geotechnical and Geoenvironmental Engineering* 125 (3), pp. 169–178. DOI: 10.1061/(ASCE)1090-0241(1999)125:3(169).
- Thompson, M. A., J. M. Lindsay, T. M. Wilson, S. Biass, and L. Sandri (2017). “Quantifying risk to agriculture from volcanic ashfall: a case study from the Bay of Plenty, New Zealand”. *Natural Hazards* 86 (1), pp. 31–56. DOI: 10.1007/s11069-016-2672-7.
- Thompson, M., J. Lindsay, and J. C. Gaillard (2015). “The influence of probabilistic volcanic hazard map properties on hazard communication”. *Journal of Applied Volcanology* 4 (1), pp. 1–24. DOI: 10.1186/s13617-015-0023-0.
- Thompson, N., M. R. Bennett, and N. Petford (2009). “Analyses on granular mass movement mechanics and deformation with distinct element numerical modeling: implications for large-scale rock and debris avalanches”. *Acta Geotechnica* 4 (4), pp. 233–247. DOI: 10.1007/s11440-009-0093-4.
- Thornton, C., S. J. Cummins, and P. W. Cleary (2013). “An investigation of the comparative behaviour of alternative contact force models during inelastic collisions”. *Powder Technology* 233, pp. 30–46. DOI: 10.1016/j.powtec.2012.08.012.

- Thouret, J.-C., G. Enjolras, K. Martelli, O. Santoni, J. Luque, M. Nagata, A. Arguedas, and L. Macedo (2013). “Combining criteria for delineating lahar-and flash-flood-prone hazard and risk zones for the city of Arequipa, Peru”. *Natural Hazards and Earth System Sciences* 13, pp. 339–360. DOI: 10.5194/nhess-13-339-2013.
- Thouret, J.-C., S. Ettinger, M. Guitton, O. Santoni, C. Magill, K. Martelli, G. Zuccaro, V. Revilla, J. Charca, and A. Arguedas (2014). “Assessing physical vulnerability in large cities exposed to flash floods and debris flows: the case of Arequipa (Peru)”. *Natural Hazards* 73 (3), pp. 1771–1815. DOI: 10.1007/s11069-014-1172-x.
- Ting, J. M., L. Meachum, and J. D. Rowell (1995). “Effect of Particle-shape on the Strength and Deformation Mechanisms of Ellipse-shaped Granular Assemblages”. *Engineering Computations* 12 (2), pp. 99–108. DOI: 10.1108/02644409510799497.
- Tommasi, P., P. Campedel, C. Consorti, and R. Ribacchi (2008). “A discontinuous approach to the numerical modelling of rock avalanches”. *Rock Mechanics and Rock Engineering* 41 (1), pp. 37–58.
- Tonini, R., L. Sandri, D. Rouwet, C. Caudron, W. Marzocchi, and Suparjan (2016). “A new Bayesian Event Tree tool to track and quantify volcanic unrest and its application to Kawah Ijen volcano”. *Geochemistry, Geophysics, Geosystems* 17 (7), pp. 2539–2555. DOI: 10.1002/2016GC006327.
- Toyos, G., R. Gunasekera, G. Zanchetta, C. Oppenheimer, R. Sulpizio, M. Favalli, and M. T. Pareschi (2008). “GIS-assisted modelling for debris flow hazard assessment based on the events of May 1998 in the area of Sarno, Southern Italy: II. Velocity and dynamic pressure”. *Earth Surface Processes and Landforms* 33 (11), pp. 1693–1708. DOI: 10.1002/esp.1640.
- Tsai, T.-L. and J.-C. Yang (2006). “Modeling of rainfall-triggered shallow landslide”. *Environmental Geology* 50 (4), pp. 525–534. DOI: 10.1007/s00254-006-0229-x.
- Tuñgol, N. M. and M. T. M. Regalado (1996). “Rainfall, acoustic flow monitor records, and observed lahars of the Sacobia River in 1992”. *Fire and Mud: Eruptions and Lahars of Mt. Pinatubo, Philippines*. Ed. by C. Newhall and R. Punongbayan. Philippine Institute of Volcanology and Seismology.
- Ullidtz, P. (2001). “Distinct element method for study of failure in cohesive particulate media”. *Geomaterials 2001: Soils, Geology, and Foundations* (1757).
- UNISDR (2015). *Sendai Framework for Disaster Risk Reduction 2015-2030*. Tech. rep. United Nations Office for Disaster Risk Reduction. 32 pp.
- Vallance, J. W. (2000). “Lahars”. *Encyclopedia of volcanoes*. Ed. by H. Sigurdsson, B. F. Houghton, S. R. McNutt, H. Rymer, and J. Stix. San Diego: Academic Press, pp. 601–616.
- Vallance, J. W. and R. M. Iverson (2015). “Lahars and Their Deposits”. *The Encyclopedia of Volcanoes (Second Edition)*. Sigurdsson, Haraldur. Amsterdam: Academic Press. Chap. 37, pp. 649–664. DOI: 10.1016/B978-0-12-385938-9.00037-7.

- Vallance, J. W. and K. M. Scott (1997). "The Osceola Mudflow from Mount Rainier: Sedimentology and hazard implications of a huge clay-rich debris flow". *Geological Society of America Bulletin* 109 (2), pp. 143–163. doi: 10.1130/0016-7606(1997)109<0143:tomfmr>2.3.co;2.
- van Asch, T. W., J.-P. Malet, L. P. van Beek, and D. Amitrano (2007). "Techniques, issues and advances in numerical modelling of landslide hazard". *Bulletin de la Société Géologique de France* 178 (2), pp. 65–88. doi: 10.2113/gssgfbull.178.2.65.
- van Westen, C. J., T. W. J. van Asch, and R. Soeters (2006). "Landslide hazard and risk zonation—why is it still so difficult?" *Bulletin of Engineering Geology and the Environment* 65 (2), pp. 167–184. doi: 10.1007/s10064-005-0023-0.
- van Westen, C. J. and A. S. Daag (2005). "Analysing the relation between rainfall characteristics and lahar activity at Mount Pinatubo, Philippines". *Earth Surface Processes and Landforms* 30 (13), pp. 1663–1674. doi: 10.1002/esp.1225.
- Vargas Franco, R., J.-C. Thouret, G. Delaite, C. Van Westen, M. Sheridan, C. Siebe, J. Mariño, T. Souriot, and A. Stinton (2010). "Mapping and assessing volcanic and Flood hazards and risks, with emphasis on lahars, in Arequipa, Peru". *Stratigraphy and Geology of Volcanic Areas* 464, pp. 265–280. doi: 10.1130/2010.2464(13).
- Varnes, D. J. (1984). *Landslide hazard zonation: a review of principles and practice*. Vol. 3. Natural Hazards. Paris, France.
- Voight, B. (1990). "The 1985 Nevado del Ruiz volcano catastrophe: anatomy and retrospection". *Journal of Volcanology and Geothermal Research* 42 (1), pp. 151–188. doi: 10.1016/0377-0273(90)90075-Q.
- Volentik, A. C. M., C. B. Connor, L. J. Connor, and C. Bonadonna (2009). "Aspects of volcanic hazard assessment for the Bataan nuclear power plant, Luzon Peninsula, Philippines". Ed. by C. B. Connor, N. A. Chapman, and L. J. Connor, pp. 229–256. doi: 10.1017/CBO9780511635380.010.
- Waite, R. B., L. Mastin, and J. E. Beget (1995). *Volcanic-hazard zonation for Glacier Peak Volcano, Washington*. U. S. Geological Survey Open-File Report 95-499. 9 pp.
- Wang, T. and M. Bebbington (2012). "Estimating the likelihood of an eruption from a volcano with missing onsets in its record". *Journal of Volcanology and Geothermal Research* 243–244, pp. 14–23. doi: 10.1016/j.jvolgeores.2012.06.032.
- Watt, S. F. L., D. M. Pyle, and T. A. Mather (2013). "The volcanic response to deglaciation: Evidence from glaciated arcs and a reassessment of global eruption records". *Earth-Science Reviews* 122, pp. 77–102. doi: 10.1016/j.earscirev.2013.03.007.
- Williams, J. R. and A. P. Pentland (1992). "Superquadrics and modal dynamics for discrete elements in interactive design". *Engineering Computations* 9 (2), pp. 115–127. doi: 10.1108/eb023852.
- Williams, R. D., J. Brasington, M. Hicks, R. Measures, C. D. Rennie, and D. Vericat (2013). "Hydraulic validation of two-dimensional simulations of braided river flow with spatially

- continuous aDcp data”. *Water Resources Research* 49 (9), pp. 5183–5205. doi: 10.1002/wrcr.20391.
- Williams, R., A. J. Stinton, and M. F. Sheridan (2008). “Evaluation of the Titan2D two-phase flow model using an actual event: Case study of the 2005 Vazcún Valley Lahar”. *Journal of Volcanology and Geothermal Research* 177 (4), pp. 760–766. doi: 10.1016/j.jvolgeores.2008.01.045.
- Wilson, G., T. Wilson, N. Deligne, and J. Cole (2014). “Volcanic hazard impacts to critical infrastructure: A review”. *Journal of Volcanology and Geothermal Research* 286, pp. 148–182. doi: 10.1016/j.jvolgeores.2014.08.030.
- Wirtz, A., W. Kron, P. Löw, and M. Steuer (2014). “The need for data: natural disasters and the challenges of database management”. *Natural Hazards* 70 (1), pp. 135–157. doi: 10.1007/s11069-012-0312-4.
- Woessner, J. and S. Wiemer (2005). “Assessing the Quality of Earthquake Catalogues: Estimating the Magnitude of Completeness and Its Uncertainty”. *Bulletin of the Seismological Society of America* 95 (2), pp. 684–698. doi: 10.1785/0120040007.
- Wolfe, E. W. and T. C. Pierson (1995). *Volcanic-hazard zonation for Mount St. Helens, Washington, 1995*. U. S. Geological Survey Open-File Report 95-497. 12 pp.
- Woo, G. (1999). *The mathematics of natural catastrophes*. World Scientific, p. 304.
- Woodhouse, M. J., A. R. Thornton, C. G. Johnson, B. P. Kokelaar, and J. M. N. T. Gray (2012). “Segregation-induced fingering instabilities in granular free-surface flows”. *Journal of Fluid Mechanics* 709, pp. 543–580. doi: 10.1017/jfm.2012.348.
- Workspace (2014). *Workspace*. Computer Program.
- Wu, C. (2013). “Towards Linear-Time Incremental Structure from Motion”. *2013 International Conference on 3D Vision (3DV)*, pp. 127–134. doi: 10.1109/3DV.2013.25.
- Yamakoshi, T., Y. Doi, and N. Osanai (2005). “Post-eruption hydrology and sediment discharge at the Miyakejima volcano, Japan”. *Zeitschrift für Geomorphologie Supplement series* 140, pp. 55–72.
- Zanchetta, G., R. Sulpizio, M. T. Pareschi, F. M. Leoni, and R. Santacroce (2004). “Characteristics of May 5–6, 1998 volcanoclastic debris flows in the Sarno area (Campania, southern Italy): relationships to structural damage and hazard zonation”. *Journal of Volcanology and Geothermal Research* 133 (1–4), pp. 377–393. doi: 10.1016/S0377-0273(03)00409-8.
- Zeng, C., P. Cui, Z. Su, Y. Lei, and R. Chen (2015). “Failure modes of reinforced concrete columns of buildings under debris flow impact”. *Landslides* 12 (3), pp. 561–571. doi: 10.1007/s10346-014-0490-0.
- Zuccaro, G., F. Cacace, R. J. S. Spence, and P. J. Baxter (2008). “Impact of explosive eruption scenarios at Vesuvius”. *Journal of Volcanology and Geothermal Research* 178 (3), pp. 416–453. doi: 10.1016/j.jvolgeores.2008.01.005.

Appendices

A Validation of DEM prediction for granular avalanches on irregular terrain

Stuart Mead and Paul W. Cleary

Journal of Geophysical Research: Earth Surface

Volume 120, Issue 9, pp. 1724 - 1742

doi: 10.1002/2014JF003331

Abstract

Accurate numerical simulation can provide crucial information useful for a greater understanding of destructive granular mass movements such as rock avalanches, landslides and pyroclastic flows. It enables more informed and relatively low cost investigation of significant risk factors, mitigation strategy effectiveness and sensitivity to initial conditions, material or soil properties. In this paper, a granular avalanche experiment from the literature is re-analysed and used as a basis to assess the accuracy of Discrete Element Method (DEM) predictions of avalanche flow. Discrete granular approaches such as DEM simulate the motion and collisions of individual particles and are useful for identifying and investigating the controlling processes within an avalanche. Using a super-quadric shape representation, DEM simulations were found to accurately reproduce transient and static features of the avalanche. The effect of material properties on the shape of the avalanche deposit was investigated. The simulated avalanche deposits were found to be sensitive to particle shape and friction, with the particle shape causing the sensitivity to friction to vary. The importance of particle shape, coupled with effect on the sensitivity to friction highlights the importance of quantifying and including particle shape effects in numerical modelling of granular avalanches.

Keywords

Discrete Element Method · landslide · avalanche · super-quadric particle · depth averaged models · numerical model

A.1 Introduction

Geophysical mass flows such as rock avalanches, pyroclastic flows and landslides are characterised by their sudden onset and high energy which can cause significant damage to exposed infrastructure and populations (Hung, 1995; Crosta et al., 2006; Nadim et al., 2006). The unpredictable and evolving nature of these flows presents challenges for risk assessment, disaster management and hazard mitigation planning. This unpredictability also tends to limit field measurements to post-event surveys used in the development of landslide inventory maps (e.g. Duman et al., 2005; van Westen et al., 2006; Guzzetti et al., 2012). These landslide inventories provide little guidance on mitigation options such as building of protective structures or strengthening of vulnerable infrastructure (van Westen et al., 2006). In this context, predictive numerical models can enable a wide range of avalanche scenarios to be investigated at relatively low cost, providing information on the nature and progress of the event and allowing for informed development of hazard mitigation strategies (Chen and Lee, 2000; Crosta et al., 2006). Accurate numerical predictions should therefore be considered a key component in improving understanding and reducing the risk of these granular flows.

Computational prediction of granular flows have been performed using both continuum mechanics and discrete granular modelling approaches. Continuum mechanics models are typically based on depth averaged equations of motion similar to the shallow water equations. Depth averaged approaches are favoured for the comparable level of detail to field measurements, their ability to capture the flowing free surface and computational efficiency which enables large scale geophysical hazard assessment (Iverson and Ouyang, 2015). Savage and Hutter (1989) and Savage and Hutter (1991) derived one-dimensional depth averaged equations of motion by assuming that the granular material flows as an incompressible, shallow, finite volume of Coulomb-like material. The applicability of this approach, known as the Savage-Hutter (SH) method, can be limited by the five key simplifying assumptions explained in (Hutter et al., 2005):

1. incompressibility of the avalanche
2. small avalanche thickness and topographic curvature (the shallowness assumption)
3. Coulomb-like bed friction
4. simplified Mohr-Coulomb internal friction behaviour, causing preferential flow in one direction, and
5. uniformity of the vertical velocity profile.

Hutter et al. (2005) provided discussion and justification of these five assumptions. They noted that SH models can usually provide an accurate description of avalanche dynamics along nominally smooth beds where the assumptions of shallowness and uniform vertical velocity profiles are most valid. The simplification of the Mohr-Coulomb behaviour to cause

preferential flow in one direction was identified as the most critical assumption when considering avalanches over irregular, three dimensional terrain. To address the limitations of classic SH methods, Savage-Hutter and similar depth-averaged approaches have been developed to incorporate a more complete description of granular flow. These depth-averaged approaches have been modified and extended to multidimensional avalanches over more complex terrain (Hutter et al., 1993; Gray et al., 1999; Denlinger and Iverson, 2001; Pitman et al., 2003; Pudasaini and Hutter, 2003; Denlinger and Iverson, 2004), multi-phase flows with intergranular fluid (Iverson and Denlinger, 2001; Savage and Iverson, 2003; Pitman and Le, 2005; Pudasaini, 2012), erosion and deposition processes (Capart and Young, 1998; Bouchut et al., 2008; Tai and Kuo, 2008; Iverson, 2012) and dilatancy (Kowalski and McElwaine, 2013; Iverson and George, 2014). Gray et al. (2003) simplified a hydraulic theory for granular avalanches to develop a shallow-water like model for granular flow. These methods are able to use numerical schemes that capture shocks and model elements of flow around obstacles (e.g. Hákonardóttir and Hogg, 2005; Cui et al., 2007; Gray and Cui, 2007; Cui and Gray, 2013). A recent advance in depth-averaged approaches has been the implementation of the $\mu(I)$ rheology (Jop et al., 2006) by Forterre (2006) and Gray and Edwards (2014). This rheology is well suited to modelling dense granular flows. Despite being able to model the behaviour of complicated granular flows, these depth-averaged approaches are still limited by the shallowness assumption. While the shallowness assumption is valid for mass flows where the topographic curvature is small, natural landscapes can be steep and irregular with obstacles such as buildings in the flow path that may affect the accuracy of the depth-averaged predictions. In these instances, momentum transfer and forces need to be accounted for in three dimensions to fully capture the transitions between static and dynamic states (Denlinger and Iverson, 2004). To account for these three dimensional stresses, Denlinger and Iverson (2004) developed a quasi-three dimensional computational method and tested it against laboratory scale avalanche experiments in Iverson et al. (2004). While features of the avalanche such as the static stranding of sand behind an obstacle are reproduced, computational grid issues were observed to cause some errors (Iverson et al., 2004).

An alternative to continuum models of granular avalanches is to use discontinuous granular flow models such as the Discrete Element Method (DEM). DEM is a meshless method initially proposed by Cundall and Strack (1979) which models the motion of individual particles within a granular mass. Contacts and resultant forces within the granular mass are determined through representing each particle as a separate geometric entity. As particle scale dynamics are simulated, it is not limited by the same assumptions of continuum or depth-averaged methods. This makes DEM particularly useful for understanding the controlling processes in granular flow such as sorting, rheology changes with different flow regimes and the effect of particle shape and size (Thompson et al., 2009). DEM methods have also been applied to model landslides on full scale topography (e.g. Cleary and Prakash, 2004; Tang et al., 2009; Thompson et al., 2009; Lo et al., 2011), however computational limitations

usually requires upscaling of particle sizes. DEM simulations are computationally intensive as the simulation time scales with the number of particles being modelled and is influenced by the approach used for representing particle shape. The computational cost of DEM is a primary limitation of the method, particularly when simulating large real-world scenarios where particle shape is important and avalanche volumes are large (10^6 m^3). Simulations on this scale usually require upscaling of particle size with consequences for model accuracy that are not clear. Detailed grain-scale mechanical data on material properties and structure is also required for accurate DEM simulation. However, these are difficult to measure for natural grains, are often not recorded or reported as bulk measures. This can form a practical limitation to the level of confidence in simulation results and general applicability of DEM for modelling of natural avalanches.

Initial usage of DEM for geophysical mass flows was focused on explaining long run-out landslides. It was first considered in the study of landslides by Cleary and Campbell (1993). The apparent low friction observed in long run-out landslides was investigated using DEM to model a thin periodic slice of the landslide in two dimensions. The run-out distance was found to depend on energy dissipation within a basal shear zone and its relative thickness. Campbell et al. (1995) extended this investigation by studying run-out over large distances using a simplified two dimensional topography. The topography represented an idealised landslide on a mountain slope followed by long run-out across a valley or plain. This model confirmed the shear was concentrated in a thin basal layer leading to lower dissipation than expected by traditional models which assumed shear was uniform throughout the landslide depth. Calculated run-out distances were consistent with distances obtained through field data and particularly demonstrated the dependence of run-out distance on landslide volume. More recent investigations of fundamental mechanics and run-out distances using two dimensional DEM are given by Okura et al. (2000), Cleary (2007), Staron (2008), Thompson et al. (2009), and Liu and Koyi (2013). Two dimensional DEM is commonly limited to studying fundamental problems in highly simplified configurations, however some quasi-realistic avalanche scenarios have been attempted. For example, Li et al. (2012) simulated a historic landslide using oversized discrete particles and Salciarini et al. (2010) studied the effectiveness of a barrier as protection against rock avalanches. These types of two dimensional investigations cannot account for three dimensional interactions between particles or the effect of irregular topography and are therefore limited to special cases where there is a dominant flow direction with minimal lateral spreading.

Three dimensional investigations using DEM have highlighted the effect irregular topography and obstacles have on avalanche behaviour. The hypothetical collapse of a mountain peak and escarpment occurring on real topography was modelled in three dimensions by Cleary (2002), Cleary (2004), and Cleary and Prakash (2004). Irregular topography was shown to play a significant role in dissipating the avalanche energy since the topographic variation increases energy dissipation and reduces the run-out by expanding the shear zone

depth and disrupting the thin basal layers reported in Cleary and Campbell (1993) and Campbell et al. (1995). Lo et al. (2011) simulated the 2009 Hsiaolin landslide using a 40 metre resolution digital elevation model and spheres with a radius of 5-6 metres. A parallel bond model was used to represent the cohesion between the particles, and the simulation was used to understand the time varying velocities of the landslide. Despite using oversized particles, the simulated deposit matched the measured dimensions of the landslide deposit. On a smaller scale, three dimensional DEM simulations were compared to experiments on the interaction between granular flow and a simple obstacle by Teufelsbauer et al. (2009) and Teufelsbauer et al. (2011). They found that the flow and deposition pattern of their simulations was too disperse due to the low rolling resistance of spherical shaped particles. The effect of particle shape was accounted for by introducing artificial parameters to restrict the rolling behaviour of the spheres and this modification yielded comparable results between simulation and experiment.

In all of the above studies, the DEM particles were assumed to be circular in two dimensions or spherical in three dimensions. This neglects the critical role that the irregular shape of real particles has on the static and dynamic behaviour of granular materials. While approaches to restrict the rolling of spheres can represent the rolling resistance to some degree, it cannot represent the anisotropy and complex behaviour exhibited by non-round particles (Cho et al., 2006), both of which add strength to the material. The effects of particle shape and surface roughness on the strength of granular materials has been studied experimentally (e.g. Konishi et al., 1983; Oda et al., 1985; Chan and Page, 1997; Santamarina and Cascante, 1998; Cho et al., 2006) and numerically (e.g. Rothenburg and Bathurst, 1992; Ting et al., 1995; Thomas and Bray, 1999; Ullidtz, 2001; Cleary, 2008; Cleary, 2009). In general, particle eccentricity (aspect ratio), angularity and surface roughness all increase resistance to shear by creating anisotropy in the bulk material, making rotation more difficult and increasing the packing fraction. Cleary (2009) identified particle shape as having four key effects on granular flows - the most important of which for avalanches is the generation of increased resistance to shear arising from the greater interlocking of the grains. This is consistent with the experimental observations of Cho et al. (2006). The importance of shape in determining the behavior of simple shear flows was demonstrated by Cleary (2008) using simple studies of a two dimensional shear cell. It was also demonstrated for slow deformation of a granular slope by Owen et al. (2009). Spherical particles and non-round two dimensional particles failed to correctly predict slope failure and behavior. These observations are critical as they demonstrate that spherical particle DEM simulations cannot accurately predict the slope failures of a non-round granular material. The use of aspherical particles was found to increase the shear strength of the material allowing for a reasonably accurate prediction of the shear planes which are critical in determining the displaced volume of failing slopes. The same considerations apply to landslide prediction. Bonded particle models, which join clusters of circular particles to artificially create shaped particles have been used to represent particle

shape in DEM (e.g. Thomas and Bray, 1999; Lu and McDowell, 2007). In avalanche simulations, a two dimensional bonded particle model has been used by Tommasi et al. (2008), Banton et al. (2009), and Tang et al. (2009), however computational speed is impacted in the artificial bonding approach as a number of spherical particles is required to form one shaped particle.

An alternative approach to shape representation that is highly suited to DEM is that of the super-quadric (SQ). This was first proposed in two dimensions by Williams and Pentland (1992) and in three dimensions by Cleary (2004). The particles are defined as a level set of an algebraic expression, which in this case is the super-sphere or super-quadric given by the equation (Williams and Pentland, 1992):

$$\left(\frac{x}{a}\right)^m + \left(\frac{y}{b}\right)^m + \left(\frac{z}{c}\right)^m = 1, \quad (\text{A.1})$$

where a , b and c are the lengths of the principle axes in its canonical frame, and the power m determines the angularity of the particles. Lengths of the three axes can be set independently allowing particles to have any combination of aspect ratios. The power (m) represents the blockiness of the particle which can vary from rounded (spherical) to nearly cubical (for high powers). The super-quadric shape is able to represent most important shape attributes of rock particles. This approach of direct geometric representation of shape is better than alternative numerical devices such as employing artificial bonding (because of the impact on computational speed) or placing restrictions on angular rotation such as through using unphysically large values of rolling friction. Its use in DEM was demonstrated in three dimensions by Cleary (2004) and has since been used extensively to include shape in DEM models of industrial processes (see Cleary (2009) for details and examples). The use of such non-round particles for landslide modelling in three dimensions was introduced by Cleary (2009) and Cleary (2010) who investigated the effect of particle shape for one of the landslide scenarios taken from Cleary and Prakash (2004). The shape of the particles was shown to have a strong effect on the run-out distance and nature of the flow.

Although the level of DEM modelling available for predictions of landslides has now become quite sophisticated there is little in the way of validation of the predictions. Mead and Cleary (2011) compared results of a single laboratory scale avalanche from Iverson et al. (2004) to DEM simulations using SQ shaped particles in three dimensions. The simulations used particles which were larger than the experimental sand grains to reduce computational time. To quantify the range of uncertain particle properties Mead and Cleary (2011) developed a process which provided a range of DEM particle properties that were consistent with experimental results. Some agreement was found between the DEM simulations, using oversized SQ shaped particles, and the experimental avalanche. However, as the scope of the comparison was limited to a single simulation, it is unclear whether differences identified were caused by over-sizing of particles or incorrect material properties.

In this paper, we extend the work of Mead and Cleary (2011) to provide strong validation

of DEM predictions for avalanche flow. Again, the comparisons are made using a single laboratory avalanche experiment from Iverson et al. (2004). We use SQ shaped particles with the correct physical scale and a range of material properties and particle shapes based on those of the preliminary study of Mead and Cleary (2011). Detailed comparison of the avalanche flow, run-out time and deposit structure are made allowing assessment of the suitability of the material property choices and of the accuracy of the DEM avalanche predictions. The accuracy of the DEM method for avalanches and the sensitivity of the results to uncertainties in particle shape and frictional properties are separated from over-sizing effects. The relative influence of these properties on the DEM predictions is used to gain an insight into their impact on large scale landslides.

A.2 Experimental setup and materials

To test the predictions of granular avalanche models, Iverson et al. (2004) performed laboratory scale experiments of nominally dry sand avalanches across an irregular three-dimensional terrain designed to mimic the complexities of naturally occurring topography. Two different sets of flume experiments were undertaken with the main difference being the material properties and shape of the flume topography. The first experiment contained angular, high asperity grains with nominal diameters of 0.5 to 1.0 mm while the second experiment contained rounded, low asperity grains with nominal diameters of 0.25 to 0.5 mm. As the computational time of DEM scales with the number of particles (i.e. particle size in a fixed volume), the computational resources required to simulate the second experiment is currently too great. Therefore, in this paper we only consider the first experiment for comparison with DEM predictions.

Flume setup

A digital model of the flume used by Iverson et al. (2004) was constructed from published vertical contours measured using a laser cartography method. This configuration is shown in Fig. A.1. The same configuration was used in the preliminary simulations of Mead and Cleary (2011) and is used in this follow-on study. The flume is 0.2 m wide and 1.0 m long and was angled at a slope of approximately 30° . The surface of the experimental apparatus was constructed to mimic realistic terrain features. A reservoir at the top of the flume was filled with granular material and was the source of the avalanche. The front of the reservoir had a 12 cm wide central opening from which the material was allowed to flow when a movable gate was raised rapidly using a spring loaded release mechanism. The reservoir was filled with 308 cm^3 of sand which corresponds to a vertical depth of 4.35 cm at the head gate and the surface was graded to be flat. At the interface between the reservoir and terrain insert there was a small (0.2 mm from Iverson et al. (2004)) step which caused a thin layer of granular material to be retained behind the step. In our configuration this step

is assumed to be exactly 0.2 mm high. The shape of the terrain and restricted opening of the reservoir were designed to represent irregular terrain features found in the environment and promote behaviour such as convergence, divergence, stranding and self-forming boundaries commonly found in natural avalanches. The resulting complex flow makes this configuration suitable for simulation validation because the flow has many features against which to test the model.

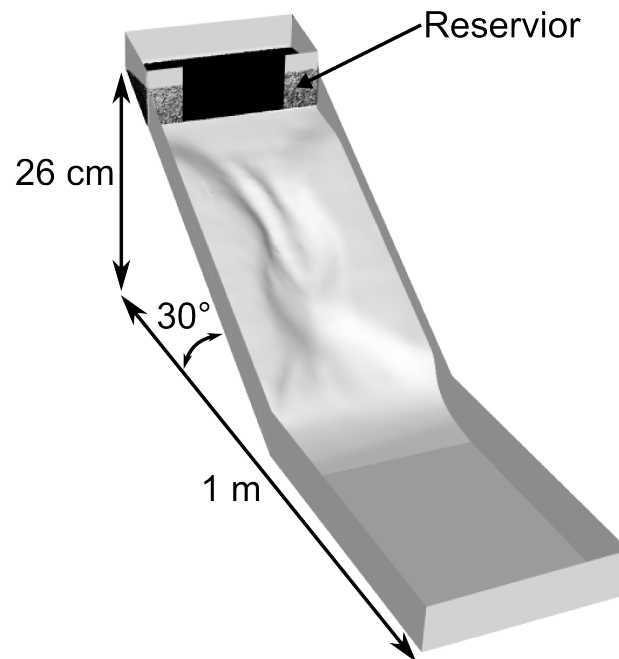


FIGURE A.1: Flume configuration used in the DEM simulations, based on digitized contours of Iverson et al. (2004). Particles are initially located behind the reservoir at the top of the flume. Reproduced from Mead and Cleary (2011).

The process for digitising the experimental surface (as reported by Iverson et al. (2004)) resulted in a surface terrain model with errors reported to be less than 3 mm in the direction along the flume, 1.5 mm transversely across the flume and 0.5 mm vertically. Large parallax errors due to the orthorectification process were removed in post-processing, however small errors may still be present, particularly near the edges of the flume (Iverson et al., 2004). These errors could cause some differences between the simulations and experiment. In areas with reasonable slope, such as along the middle of the flume, this uncertainty is expected to have little effect. The uncertainty could have some impact in shallower areas with smaller terrain gradients, such as near the reservoir. These differences may affect the local flow of particles and therefore the fine details of run-out extent in these regions. These terrain errors will be considered in the context of evaluating the differences between the experimental and simulation flow results.

Material properties

Relatively homogeneous quartz sand was used in the experiment. The sand was dried and sieved to retain grains with nominal diameters of 0.5–1.0 mm. This material was chosen by Iverson et al. (2004) as it provided the best reproducibility of friction angle measurements. The mono-disperse nature of particle size is not representative of actual geophysical flows, where the poly-disperse grain sizes can give rise to the formation of self-channelized flows and static levees (e.g. Pouliquen et al., 1997; Gray and Kokelaar, 2010; Johnson et al., 2012; Woodhouse et al., 2012). This may restrict the direct relevance to full scale, poly-disperse avalanches to some degree, however the experiment still creates several important features to test numerical predictions against. The internal and basal friction angles of the sand were measured using a tilting table test. The friction angle of the sand on the terrain material was reported to be 19.85° and internal friction angle of sand was 43.99° . The cohesion of the sand was assumed to be negligible, with efforts having been taken to reduce the electrostatic and liquid bridge (humidity) effects which could create attractive forces between the sand and terrain.

As the experiments of Iverson et al. (2004) were designed to test a continuum approach, some reported material properties, such as internal friction, are bulk measures. The internal friction angle reported by Iverson et al. (2004) is controlled by a combination of the particle shape (aspect ratios, size, angularity) and mechanical (contact friction, cohesion) properties. In DEM, the combination of particle shape and mechanical properties determine the shear strength of the granular material. This means that the measured bulk friction cannot be used directly in the simulations. Instead, the particle size, semi-major and semi-minor axis ratios, angularity and particle-particle contact friction need to be quantified in order to accurately construct the particles for a DEM model. These properties are difficult to measure and usually not required for non-DEM purposes (as in Iverson et al. (2004)), forming a critical practical limitation of DEM when using published historical or experimental particle data.

While the material property information published in Iverson et al. (2004) does not completely specify the particle shape and contact friction, some estimates can be made from the published data. The major axis length and aspect ratio of 25 individual grains was measured from a photomicrograph in Iverson et al. (2004). The measured grains had a major axis length in the range of 1.0–2.0 mm with aspect ratios of 0.54–1.0. However, as the photomicrograph is a two dimensional projection, only one aspect ratio from each particle can be obtained from the image. This means that the second aspect ratio for each particle is not available from the published experimental data. Some estimate of the angularity of the particles can be made from the photomicrograph, where the particle corners were observed to vary from fairly rounded to very sharp. We estimate that these can be approximated by angularities within the range of 2.5 to 6.0. The high visual surface roughness of the sand grains suggests that the particle-particle friction should be higher than the particle-terrain friction, but its magnitude is also not known.

As these input uncertainties are common in DEM studies, it is important to understand the sensitivity of the avalanche to these uncertain parameters. The experiment is first re-analysed to identify key behaviours that need to be replicated by the model. The probable ranges of the uncertain material properties using the experimental observations is estimated and discussed in section A.4. A sample of the experimental material, provided by the authors of Iverson et al. (2004), is then used to evaluate the effectiveness in representing particle shape.

A.3 Dilation of granular material during avalanche

The measured depths of sand from experiments A and B in Iverson et al. (2004) are used to calculate the volumes of sand retained in the reservoir, on the flume surface and in total. The point depths from Iverson et al. (2004) were interpolated onto a regular grid with a cell spacing of 0.2 cm using the method of Akima (1978). Volume was calculated from the depth grid by multiplying the cell area (0.04 cm^2) by the depth. While only experiment A is simulated using DEM, both experiment A and B are reanalysed here to examine avalanche compressibility and the effect particle shape and flume geometry can have on results. Figure A.2 displays the variation of measured bulk volumes with time for experiments A and B. Most material discharges from the reservoir in the first 2 seconds, decreasing the retained volume (dashed line) and increasing the volume of material flowing on the flume surface (dotted line). Discharge from the reservoir has largely ceased by 3 s, with more material remaining in the reservoir for experiment B due to the smaller gate width. The total bulk volume of sand (solid line) decreases over the first one second of the experiments. This decrease may partly be explained by the omission of regions containing dispersed and saltated grains (Iverson et al., 2004), which would be more prevalent in the early stages of the experiment as thin layers of grains travel down the flume. Over the course of the experiment the material dilates by approximately 6% in experiment A and compresses by 2% in experiment B. Some volume loss is expected due to the omission of saltated grains and the measured total volumes therefore provide a lower-bound estimate to the changes in bulk density, particularly for experiment B where the material was observed to have a tendency to saltate by Iverson et al. (2004). The net dilation of at least 6% in experiment A indicates that the avalanche does not behave as a purely incompressible mass, which has implications for methods that assume the material behaves as an incompressible granular mass. An advantage of the DEM approach for this experiment is that it is not limited by an incompressibility assumption and is able to predict thin layers and saltation of grains.

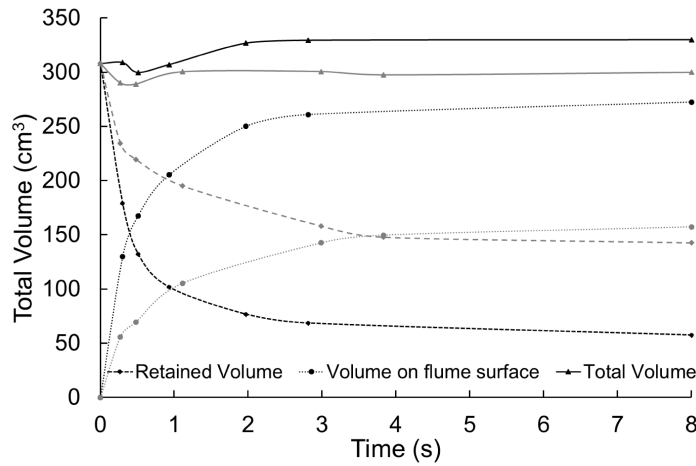


FIGURE A.2: Variation with time of the total sand volume (solid line), volume of sand on the flume surface (dotted line) and volume of sand retained in the reservoir (dashed line) for both experiment A (black) and experiment B (grey) of Iverson et al. (2004).

A.4 DEM method, particle properties and simulation

DEM method

DEM seeks to predict all inter-particle collisions as well as collisions between particles and their physical environment. The DEM software used in here is described in more detail in Cleary (1998), Cleary (2004), and Cleary (2008). Briefly, the particles are allowed to overlap where the amount of overlap Δx , normal v_n and tangential v_t relative velocities determine the collisional forces via a contact force law. In this work a linear spring-dashpot model is used in which the normal force is given by:

$$F_n = -k_n \Delta x + C_n v_n \quad (\text{A.2})$$

This spring component provides a repulsive force and the dashpot provides viscous dissipation of a proportion of the relative kinetic energy. The maximum overlap between particles is controlled by the normal spring stiffness k_n . The normal damping coefficient C_n is chosen to give the required coefficient of restitution ϵ (defined as the ratio of the post-collisional to pre-collisional normal component of the relative velocity). The equations for calculating C_n are given in Thornton et al. (2013).

The tangential force is given by an incremental linear spring which is limited by the Coulomb friction. Its general form is

$$\mathbf{F}_t = \min\{\mu F_n, \Sigma k_t \mathbf{v}_t + \Delta t + C_t \mathbf{v}_t\}, \quad (\text{A.3})$$

where the vector force \mathbf{F}_t and velocity \mathbf{v}_t are defined in the plane tangent to the surface at the contact point. The summation term is the tangential displacement which stores energy from the relative tangential motion and represents the elastic tangential deformation of the

contacting surfaces. The dashpot provides viscous dissipation and represents the tangential plastic deformation of the contact. The magnitude of the total tangential force \mathbf{F}_t is limited by the Coulomb frictional limit μF_n , at which point the surface contact shears and the particles begin to slide over each other. Other contact laws can be used in DEM but a linear model is the most commonly used. For details of alternative contact models for inelastic collisions and their relative performance for oblique single particle impacts, see Thornton et al. (2013).

In most applications, particles are typically not spherical or near spherical and so the shape needs to be included explicitly in the DEM particle geometry model. Super-quadric particle shapes (Eq. A.1) are used here. The ratios of the three semi-axis lengths (b/a and c/a) are the aspect ratios of the particles. The super-quadric power m determines the blockiness of the particle. For $m = 2$ a spherical particle is obtained. As m increases, the shape becomes progressively more cubical with the corners become sharper and the particle more blocky. By $m = 10$, the particle shape is essentially cubic (for aspect ratios of 1). This is a very flexible class of shapes, which varies continuously (m is not restricted to integer values). This allows plausible shape distributions to be represented and the shape can be made to change dynamically during simulation (for example with abrasion as measured by the shear energy dissipation on the particle). Many examples of applications using this shape are given in Cleary (2004) and Cleary (2009).

The DEM algorithm proceeds in three steps:

1. A search grid is used to regularly update a near-neighbour interaction list for all particle pairs and particle-boundary pairs that might participate in a collision in that given period.
2. In each timestep, this list is used to identify all collisions involving combinations of particles and boundary elements. The forces on particle pairs and boundaries are evaluated using the contact force model.
3. All the pair-wise collision forces and torques are summed to give net forces and torques. Newton's equations of motion using the net force on each particle and the matching kinematic equations are then integrated to give the changes in the position and speed of each particle. Similar equations are solved to give the current orientation and spin of the particles in response to the net torques.

Steps 2 and 3 are repeated sequentially stepping the system state forward in time until the search information is no longer valid. A new search (step 1) is then performed to update the interaction list.

Bulk material and numerical properties

The coefficients of restitution and spring stiffness parameters were found to have a negligible effect on the accuracy of the results (Mead and Cleary, 2011). So here, coefficients of

restitution for both particle-particle and particle-wall collisions were chosen to have mid-range values of 0.5. This makes the particles moderately inelastic, which is sensibly representative of sand materials. The spring stiffness (which controls the amount of overlap of the particles during collisions) was chosen to be 50 N/m which gave average overlaps of less than 0.5% throughout the simulation. This is generally a sufficient condition for accurate simulation, see Cleary (2004) for more details.

The particle-flume friction was set to 0.36, based on the measured friction angle between the sand and flume surface. In contrast to the preliminary simulations in Mead and Cleary (2011), for the simulations reported here the DEM particle sizes were chosen to match the experimental particle size with the major axis length in the range of 1 – 2 mm.

Characterising particle shape and internal friction

The uncertain material property inputs of particle aspect ratios, angularity and contact friction can have a significant effect on DEM predictions of avalanches and are commonly unreported in historical, experimental and field studies. This uncertainty can be reduced through direct measurement of the particle properties (e.g. through X-ray micro-tomography) or calibration of the particle properties to other measurements such as the bulk friction angles (as in Mead and Cleary (2011)). For the Iverson et al. (2004) experiments, Mead and Cleary (2011) quantified the probable range and sensitivity to the uncertain material properties using DEM simulations of discharge from the reservoir. The volume of sand retained within the reservoir was compared between simulations and the experiment. The results of the retained volume analysis was used to identify combinations of material properties that result in the right amount of material being discharged from the reservoir. Using the retained volume of sand in this way allowed the range of the uncertain properties to be narrowed without calibrating material properties to results of the down flume deposit.

Here we use the material property envelope established in Mead and Cleary (2011) to choose sets of material properties found to be consistent with the retained volume of material in the reservoir. Table A.1 provides the 27 sets of particle attributes used in DEM simulations of the avalanche. Individual particle shape and size properties were assigned from a random uniform distribution between the ranges specified according to table A.1, with a major axis length range of 1.0 to 2.0 mm.

The relative effects of the different particle shape attributes such as angularity and aspect ratio have been found to be coupled and exhibit problem dependence (Debroux and Cleary, 2001; Mead et al., 2012). To examine the sensitivity to particle shape and uncertain material properties in addition to validation, three levels of each of the angularity, aspect ratio range and friction coefficient were investigated in a fully factorial design:

- The angularity was estimated to be between 2.5 and 6.0. Two narrower angularity ranges were chosen to evaluate the effect of the more rounded (2.5-4.0) and more angular (3.0-6.0) particles within the original broad angularity range of 2.5-6.0.

TABLE A.1: Particle angularity, aspect ratio and internal friction used for DEM simulations of the avalanche.

Angularity	Case	Aspect ratio 1	Aspect ratio 2	Internal friction
2.5 - 4.0	1	0.7 - 1.0	0.55 - 0.8	0.45
	2	0.7 - 1.0	0.55 - 0.8	0.50
	3	0.7 - 1.0	0.55 - 0.8	0.55
	4	0.8 - 1.0	0.65 - 0.8	0.45
	5	0.8 - 1.0	0.65 - 0.8	0.50
	6	0.8 - 1.0	0.65 - 0.8	0.55
	7	0.9 - 1.0	0.8 - 0.95	0.45
	8	0.9 - 1.0	0.8 - 0.95	0.50
	9	0.9 - 1.0	0.8 - 0.95	0.55
3.0 - 6.0	10	0.7 - 1.0	0.55 - 0.8	0.45
	11	0.7 - 1.0	0.55 - 0.8	0.50
	12	0.7 - 1.0	0.55 - 0.8	0.55
	13	0.8 - 1.0	0.65 - 0.8	0.45
	14	0.8 - 1.0	0.65 - 0.8	0.50
	15	0.8 - 1.0	0.65 - 0.8	0.55
	16	0.9 - 1.0	0.8 - 0.95	0.45
	17	0.9 - 1.0	0.8 - 0.95	0.50
	18	0.9 - 1.0	0.8 - 0.95	0.55
2.5 - 6.0	19	0.7 - 1.0	0.55 - 0.8	0.45
	20	0.7 - 1.0	0.55 - 0.8	0.50
	21	0.7 - 1.0	0.55 - 0.8	0.55
	22	0.8 - 1.0	0.65 - 0.8	0.45
	23	0.8 - 1.0	0.65 - 0.8	0.50
	24	0.8 - 1.0	0.65 - 0.8	0.55
	25	0.9 - 1.0	0.8 - 0.95	0.45
	26	0.9 - 1.0	0.8 - 0.95	0.50
	27	0.9 - 1.0	0.8 - 0.95	0.55

- Three sets of aspect ratios were considered and are termed low (0.9-1.0, 0.8-0.95), intermediate (0.8-1.0, 0.65 - 0.8) and elongated (0.7-1.0, 0.55-0.8).
- The particle-particle friction coefficient was between 0.45 and 0.55.

These tests will be used to better understand the range of variation for input conditions which all satisfy the known bulk material and configuration conditions.

The dimensions of 30 individual grains were measured from a material sample provided by the authors of Iverson et al. (2004) to assess and cross-check the validity of the estimated properties. The range of particle shapes investigated here appears to reasonably match these additional measurements. The major-axis length was between 1.0 and 2.2 mm (average of 1.5 mm), the semi-major aspect ratio was between 0.6 and 1.0 (average of 0.83) and the semi-minor aspect ratio was between 0.3 and 0.9 (average of 0.65). The particle angularity was within the range of 2.5 to 6.0 but was not evenly distributed across all particles. Particles with lower aspect ratios (0.9 - 1.0) tended to be more rounded, with angularities between 2.5

and 3.5, while elongated particles were more angular. In the following simulations, particle angularities and aspect ratios are distributed uniformly and therefore do not exactly replicate the distribution of particle shapes found in the provided material sample. While it is possible to replicate the specific distributions of shape and size, the detailed particle measurements and particle statistics required makes it unfeasible with manual methods. Given these limitations, the additional measurements suggest that cases 19 to 21 have particle properties that are the closest match to the experiment. The lower bound of both aspect ratios are higher for these cases than the experimental material, however the average aspect ratios are similar between experiment and simulation.

DEM simulations and comparison to spherical particles

The reservoir was filled with DEM particles to a depth of 4.35 cm, replicating the initial experimental configuration of Iverson et al. (2004). The avalanche simulations contained between 250,000 and 300,000 particles and took 30 to 40 days to simulate 10 seconds of the avalanche on a single core on a 2.93 GHz processor. Proportional reductions in duration can be made by using more cores in parallel. The exact number of particles in each simulation varied depending on the particle shape properties.

To demonstrate the importance of particle shape, a spherical shaped particle simulation was run. The final deposit of the spherical particle simulation at 13 seconds is compared with the experimental final deposit in Fig. A.3. While some material has been retained in the reservoir, there are few similarities between the simulated and experimental results. Spherical shaped particles in DEM cannot replicate the experimental results due to the insufficient representation of experimental initial conditions and particle shape. The packing fraction of spheres is lower than that of aspherical particles (Delaney and Cleary, 2010), resulting in a lower initial bulk density and mass of material in the simulated reservoir than was used in the experiment. Spherical particles also have very little resistance to rolling, which causes contact (sliding) friction to have a minimal effect on dissipating the energy of the simulated avalanche. This lack of energy dissipation results in larger run out distances, a lack of coherent structure in the flume deposit and less material being retained behind the reservoir head gate when compared to the Iverson et al. (2004) experiments. While artificially increasing the resistance to rolling in the model may improve the comparison (as in Teufelsbauer et al. (2009) and Teufelsbauer et al. (2011)), the use of a better approximation of the experimental grain shape (e.g. using Super-Quadrics) would result in a more accurate representation of both the initial conditions and the material properties.

A.5 Comparison of experimental and DEM avalanches

Several of the DEM avalanche simulations from Table A.1 produced results that were very similar to the experiment. Case 19 has the closest match to the experiments and is therefore

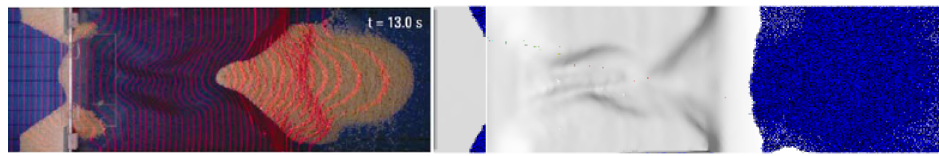


FIGURE A.3: (left) Final deposit of the Iverson et al. (2004) experiment and (right) spherical particle simulations at 13 seconds.

used as the reference case. A comparison of the experimental avalanche progression and DEM simulation of case 19 is shown in Fig. A.4. The DEM particles are shaded by speed and appear in the right column alongside the corresponding orthophotograph from Iverson et al. (2004) in the left column.

Upon exiting the reservoir, the avalanche front is separated into two streams at 0.30 s by a ridgeline approximately 1/3 of the way down the flume. At 0.51 s, the front of the avalanche has reached the base of the flume with a large amount of material travelling along the right side of the flume (lower part of the image). A small ‘u’ shaped depression in the back of the reservoir is present as a result of the discharge of sand from this area. By 0.93 s, the leading grains have started coming to rest and there are fewer particles flowing along the right side of the flume. By 1.97 s, the discharge of material from the reservoir has reduced significantly, with two separate streams of material flowing down the flume. At 2.81 s, most of the material has come to rest. The two streams of material flowing down the flume have become smaller and more distinct. A small amount of material is trapped at the interface between the terrain and reservoir where it has been retained behind the step. At 13.0 s, when all motion has ceased, there are two separate final deposits of material. The sand within the reservoir has a distinct V shape, with small volumes of material retained behind the topographic step and ridges below the reservoir in the flume. The distal edge of the deposit has not moved further down the flume since 0.93 s with most of the material accumulated upstream of this location.

The shape and features of the simulated and experimental avalanche are qualitatively very similar at all times with minor differences observable in small scale features. At 0.51 s, the small ‘u’ shaped depression of sand in the reservoir is not observed in the DEM simulations. The reason for this is unclear, since by 0.93 s the shape of the sand in the reservoir is similar between experiment and simulation, suggesting that this is a timing effect. The main difference between the experiment and simulation is in the upper sections of the flume, where more material is retained behind the topographic ridges. These differences may not be fully explained by differences in material properties between the experiment and simulation, as the more extreme aspect ratio (in the experiment) would be expected to retain more material behind the ridges. These differences could be due to errors in the digital model of the flume topography. The depressions behind the ridges appear to be larger in the simulation flume geometry compared to the physical one. This results in slightly more material retained in these areas, however does not appear to affect the down flume deposit.

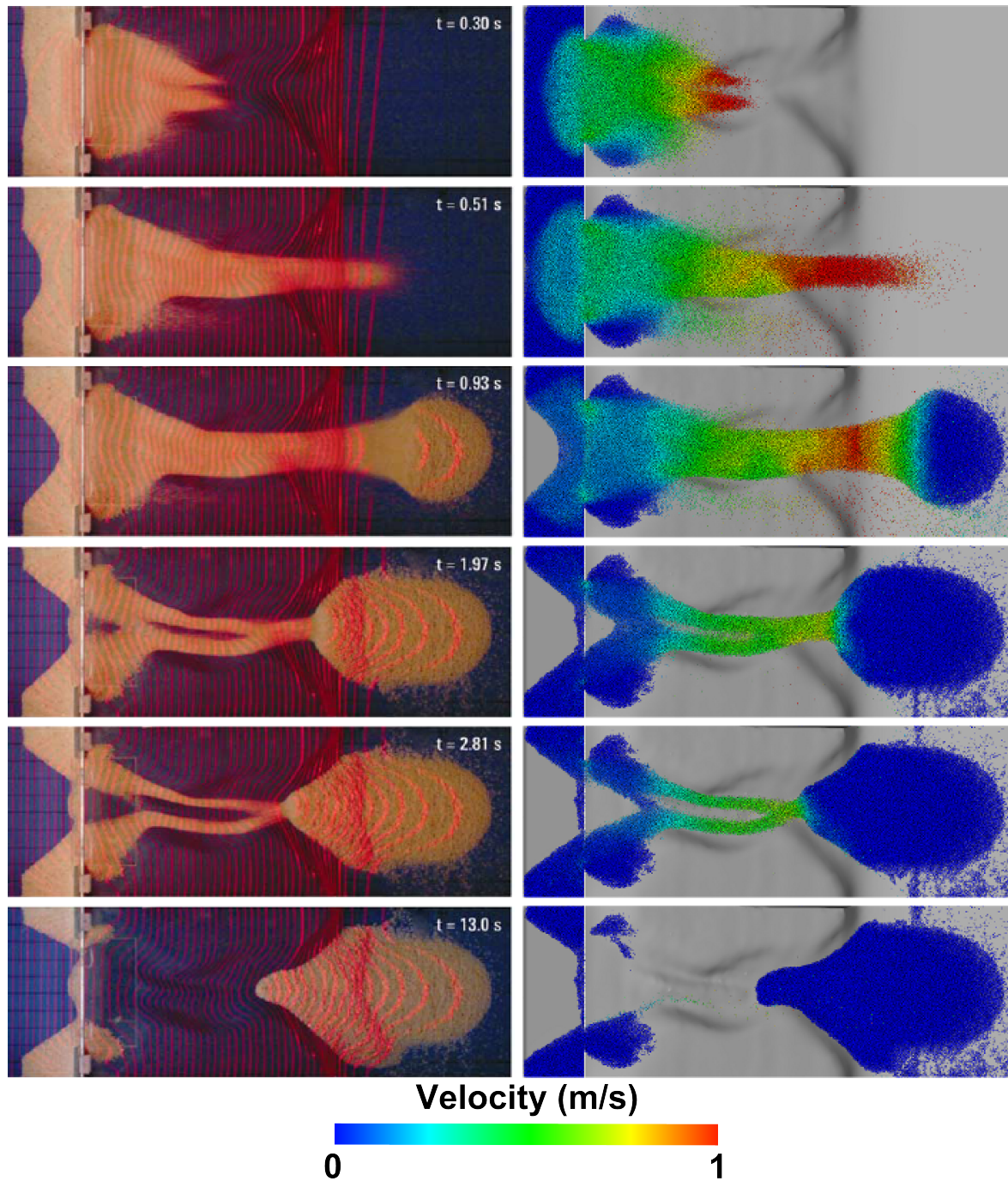


FIGURE A.4: (left) Vertical orthophotographs depicting the avalanche experiment of Iverson et al. (2004), and (right) DEM simulation for case 1. Timestamps show the time elapsed since the opening of the head gate. Particles in the simulation are coloured by speed. Red laser contours are projected at 5 mm intervals in the experiment.

Iverson et al. (2004) extracted a series of avalanche depth measurements to enable comparisons of vertical avalanche thickness between the experiment and numerical models. These were obtained through a laser cartography method and Kriging algorithm for smoothing and clean-up of the resulting data. The errors along and across the flume were estimated to be approximately 1.5 mm and 3 mm respectively, with vertical errors of 0.5 mm. These depths were used to quantitatively compare between the Denlinger and Iverson (2004) quasi-three dimensional model and the experiment of Iverson et al. (2004), and will also be used for comparison with our DEM simulations. Comparison of the original orthophotographs and the isopach maps (both from Iverson et al. (2004)) reveals observable discrepancies between them. The isopach margins were determined as the point where vertical sand thickness was greater than 0.5 mm, which results in regions of saltated grains being omitted and a slightly smaller avalanche extent Iverson et al. (2004). Since the DEM approach can predict the motion of saltated grains, here we compare the simulated results to both the isopach outline and a manually extracted outline from the orthophotographs. The isopach contours are considered as a lower bound estimate and the orthophotograph outline gives an upper estimate of the avalanche margins.

The thickness of the final deposit for the DEM avalanche was calculated on a regularly spaced grid for comparison with the experiment. Particles with fewer than 5 neighbours within an 8 mm distance (i.e. 2 particle diameters) were neglected in the DEM thickness calculation. This distance was chosen as it removed most of the grains that are visually separated (saltated) from the bulk granular mass without incorrectly filtering out particles which were clearly part of it. The removal of saltated grains from the DEM depth measurements provides a fairer comparison between DEM results and the isopachs of Iverson et al. (2004) which also ignored grains separated from the main avalanche mass.

Figure A.5 shows outlines of the avalanche obtained from the isopach data (black dashed line) and orthophotographs (blue line) and the DEM simulation (red) for case 19 at six times from soon after initiation to the final deposit. The largest difference between the manually extracted and isopach outlines occur at 0.51 and 0.93 s when a thin layer of material travels over the ridgeline on the right of the flume, marked as B in the image. This is consistent with the observations of Iverson et al. (2004).

Over the first 1.0 s all three outlines are very similar. The simulation extent is slightly larger at almost all locations but this difference is generally less than 1% of the flume length (approximately 7 average particle diameters). The largest difference is in the reservoir at 0.51 s where the simulated outline lacks the depression upslope of the head gate. This is likely to be a matter of timing for the drainage from the reservoir in the DEM simulation, since by 0.93 s the profile within the reservoir matches closely to all three outlines.

At 0.3 s, the simulation extent is slightly larger, but reproduces the separation of the material into two fronts well. At 0.51 s, there is close agreement along the middle of the flume indicated as A on Figure A.5. A large depression in this area restricts the avalanche,

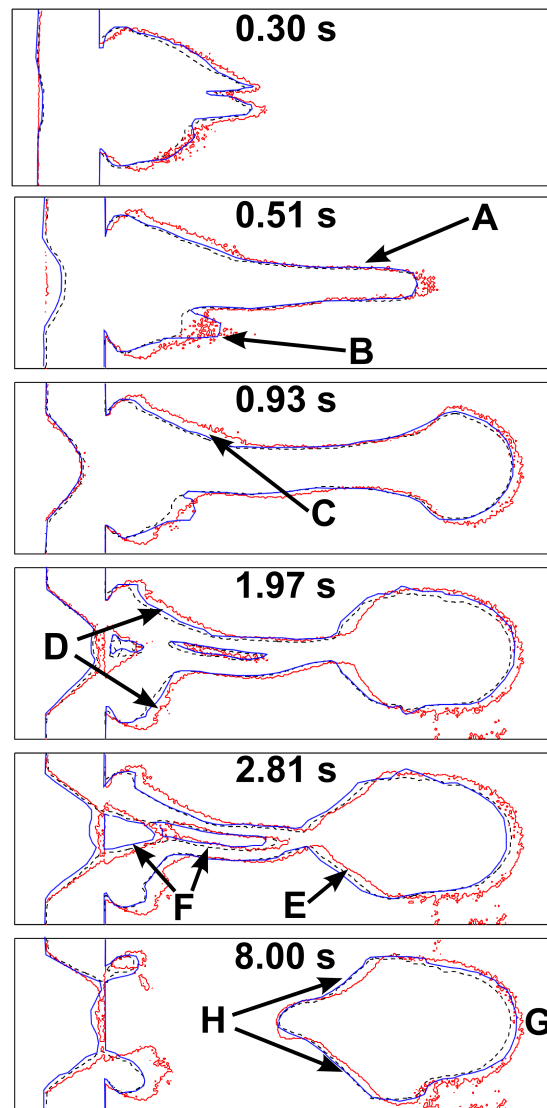


FIGURE A.5: Outline of sand from the avalanche experiment isopachs (black, dashed line), extracted from the experimental images (solid blue line) and DEM simulation for case 1 (red, solid). Timestamps show the time elapsed since the opening of the head gate.

causing it to be thicker, resulting in smaller comparison errors between the three outlines. In the upper half of the flume, the width of the simulated avalanche is broader by around 12 mm (7.5% of the avalanche width). The leading edge of the avalanche is slightly further down the flume by about 15 mm. Saltated grains are not captured in the isopach outline along the upper right area of the flume (marked B). This feature is visible in both the photographic images of the experiment and the DEM results, demonstrating the ability of DEM to predict saltated grains and thin layers of material.

At 0.93 s, there is good agreement with the experimental curves in the reservoir and along the middle of the flume. On the left of the flume (marked C), the DEM extent is slightly larger which is a difference persisting from 0.51 s and with a similar magnitude. The distal edge of the avalanche has broadened significantly into a bulbous shape, which is well tracked by the

DEM simulation, with a small uniform difference around the entire front of the avalanche. The width of this difference is 10 mm (7 particles), which is a small systematic error likely caused by differences in the material properties between the DEM and simulation. This suggests that the simulated material is slightly more mobile than the experimental granular material.

At 1.97 s, the outlines in the upper section of the flume and reservoir match closely. The shape of the two separate streams and voids in the upper region of the flume are predicted well by the DEM simulation. These are complex structures whose prediction demonstrates the strengths and accuracy of the DEM approach. Just below the reservoir, the DEM avalanche outline is slightly wider than the experimental outline (indicated as E). This error is visible at all times to a varying degree and is most likely to be a result of errors in the digitisation of the topography, discussed earlier in this section. At the base of the flume, the distal edge and front of the avalanche deposit is further down the flume than the experiment (indicated as D). On the left side of the distal deposit, the simulated outline is in close agreement with the extracted experimental outline, and both are larger in extent than the isopach outline. This indicates the magnitude of the difference between the isopach map and avalanche extent. On the right side of the deposit, the simulated extent is further down the flume. This difference is relatively minor and the width of the deposit is very close between experiment and simulation.

At 2.81 s, the outlines are again similar in the upper region of the flume, near the reservoir, and only slightly different along the sides of the deposit at the base of the flume. In particular, the voids below the reservoir (indicated by F) are predicted well. There is also good agreement along the centre of the flume, where two narrow streams of material are travelling down the flume. Accurate prediction of these thin and narrow features is difficult for most numerical models, so the ability of DEM to reproduce these small scale features is encouraging. The trailing edge of distal deposit (D in the 1.97 s frame) is still slightly further down flume. The leading edge of the DEM deposit, marked G, and the trailing edge of the DEM deposit sits slightly further down the flume than both experimental deposits. This indicates a small error, most likely related to the increased mobility of the DEM material properties compared to the experimental material.

By 8.0 s, when most of the material has stopped moving, particles in the long streams behind the distal mass have caught up with the deposit and there is little change in the shape of the reservoir deposit. The retained mass in the reservoir is very similar between the experiment and simulation. The two small deposits just below the reservoir have some small differences with more material retained in the simulation compared to the experiment. The deposit on the left is of a similar size to the experimental one but is disconnected from the reservoir which we attribute to small gradient errors in the local topography. The deposit on the right of the simulation is almost double the size of the experimental one. This difference is also expected to be a result of the difference between the digitised and experimental terrain models, however this does not appear to result in a significant change in the avalanche behaviour or shape of the final deposit. The outlines of the main deposit at the base of the flume show a high degree

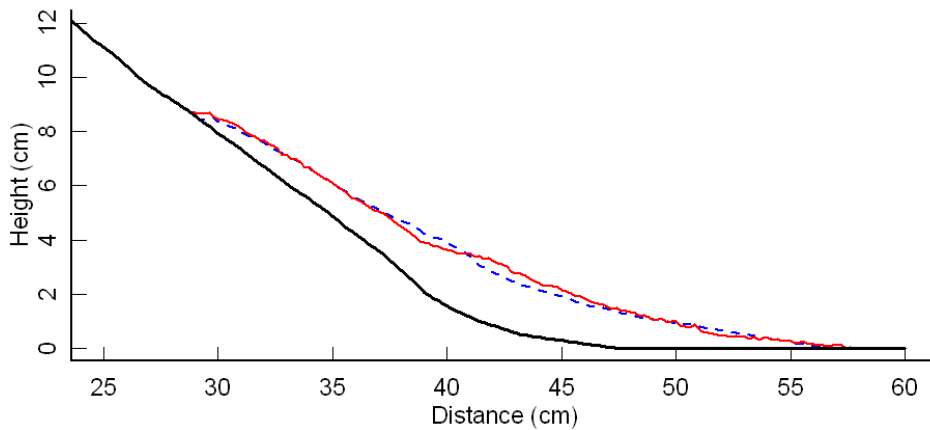


FIGURE A.6: Cross-section along the centreline of the final avalanche deposit for the experiment (dashed blue line) and DEM case 1 (solid red line). The base of the flume is the thick black line.

of agreement between the DEM prediction and the experiment. The width of the deposit is very similar. Along the trailing edge of the deposit (marked as H), the DEM outline is closer to the extracted (blue) outline from the experiment than the isopach (black dashed) outline. There is some difference in the deposits at the leading edge of the deposit (marked as I). This difference is around than 17 mm (11 particle diameters), which is the largest difference in the deposit but is still small in absolute terms.

The mass distribution and vertical profile of the avalanche are also important in determining the spread of the avalanche. Figure A.6 shows vertical cross-sections of the final deposit with the experimental deposit being shown by the dashed line and the DEM case 19 deposit being shown by the solid line. The cross-section is taken along the flume centreline. There is good agreement between the experimental and DEM depth profiles. The start and end points of the deposit are within 1 particle diameter of each other. There are some minor differences in the depth of the deposit between 35 and 45 cm along the flume. These differences are of the order of a particle diameter, meaning the differences are likely within the uncertainty range of the material properties.

Figures A.5 and A.6 demonstrate that, with close to correctly characterised material and particle shape inputs, DEM can be expected to predict static and transient features of laboratory scale, idealised granular avalanches with a reasonable accuracy. This includes prediction of the detailed shape of the avalanche mass at each time and its rate of propagation down slope. Accurate prediction of the run-out and lateral spreading are most useful in determining the likely impacts of an avalanche so it is important that models be able to accurately predict these details. The accuracy of the DEM results compared to the experiment indicates that the method is suitable for studying the effects and dynamics of granular avalanches. Both the retained deposit and final avalanche results are sensitive to the choice of particle attributes such as shape and inter-particle friction and that correct measurement or estimation of these is important for accurate avalanche prediction. The sensitivity of the results to these properties is now investigated in order to determine how much uncertainties or variations in inputs can

affect the model outcomes.

A.6 Sensitivity of avalanche deposit to particle attributes

Sensitivity to particle shape properties

Particle shape controls the bulk properties of granular materials, directly affecting the shear strength, bulk density (packing fraction), failure and repose angles. These properties directly influence the dynamics of avalanches and the shape and location of the final deposits. Depth-averaged continuum methods are able to represent the effect of particle shape in the macroscopic frictions (basal and internal), however shaped particle DEM requires a direct specification of aspect ratios and angularity. In the previous section, the final avalanche deposit predicted by DEM did not precisely match the experiment, which we predominantly attribute to the material properties not exactly matching those of the real material. We therefore now explore the sensitivity of the final avalanche deposit to particle shapes within the range identified in section A.4 to understand the effects of particle shape and contact friction on avalanche deposits.

The centre of mass of particles along the flume in the down slope direction (X_{com}) is a useful way of characterising the final avalanche deposit. The final location of the avalanche is more sensitive to input changes than the deposit shape and therefore is a useful quantification of the deposit variability. It can also be used as a measure of run-out distance, with larger values for the centre of mass indicating that the run-out distance of the material is longer. Figure A.7 shows the variation of X_{com} with particle aspect ratios for three different particle angularities, namely rounded (2.5 – 4.0), mildly angular (2.5 – 6.0) and highly angular (3.0 – 6.0). The inter-particle friction for all cases was 0.45. The rounded particles (solid line) result in much larger run-out distances compared to the other two angularities and is consistent with findings of Cleary (2004) for full scale landslides and the experimental observations of Iverson et al. (2004). This suggests that particles with angularities less than 3.0 cause the avalanche to travel much further. The consistent trend with aspect ratio shown in Fig. A.7 is that decreasing elongation of particles leads to increases in the run-out distance.

The effect of aspect ratio on the final deposit shapes is shown in Fig. A.8, which displays the thickness of the final avalanche deposit for cases 19, 22 and 25 from Table A.1. The particles are mildly angular with an inter-particle friction coefficient of 0.45. The final deposit is very similar for the elongated (aspect ratios 0.7 – 1.0 and 0.55 – 0.8) and intermediate (aspect ratios 0.8 – 1.0 and 0.65 – 0.8) cases, with slightly less material retained behind the topographic step and ridges of the flume for the intermediate aspect ratio case. As the aspect ratio decreases, more material is released from the reservoir and the deposit sits slightly further down the flume and is slightly wider. This change is more significant between the intermediate and low aspect ratio particle cases. The volume retained behind the topographic step and ridges has also decreased by a larger amount. The increasing roundness of the particles at lower aspect

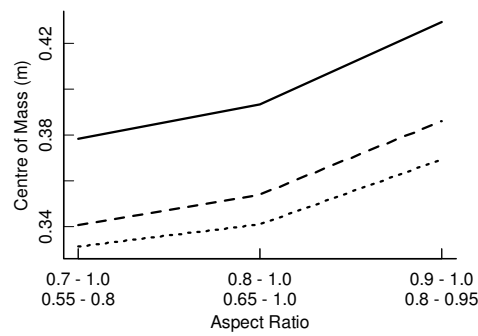


FIGURE A.7: Variation of the centre of mass position (X_{com}) of the DEM particles in the final deposit in the downhill direction along the flume for three aspect ratio combinations with a friction coefficient of 0.45. Each curve shows a different amount of angularity with rounded particles given by the solid line, mildly angular particles by the dashed line and highly angular particles by the dotted line.

ratios causes the particles to flow more freely, which results in a larger proportion of grains being disconnected from the main body.

Figure A.9 shows the thickness of the final avalanche deposit for cases 4, 13 and 22, where the angularity differs. The particles have an intermediate aspect ratio and an inter-particle friction coefficient of 0.45. The rounded particles (Fig. A.9a), sit much further down the flume than the higher angularity cases. This is similar to the observations that more rounded particles travel further and flow more freely in both the experiments of Iverson et al. (2004) and simulations of dragline bucket filling by Cleary (2000). There is a larger amount of loose particles that are disconnected from the main mass for the rounded case, and the extent of the lateral spread decreases as the particle angularity increases. The closeness of the thickness contours also indicates that the overall slope of the granular pile is steeper in the higher angularity cases. This is again consistent with the experimental observations of Iverson et al. (2004), where the higher angularity particles from experiment A had a much steeper slope than the low angularity particles from experiment B.

These results demonstrate that the final deposit shape and location of the avalanche is moderately sensitive to the particle shape. As the particles become more rounded, due to either decreasing angularity or aspect ratio, the resistance to shear in the avalanche is reduced. As a result, the energy dissipation rate within the avalanche is reduced leading to both more run-out and more lateral spread which influence the centre of mass and shape of the final deposit.

Sensitivity to inter-particle friction

The inter-particle friction is a function of the surface roughness of the particles. Smooth particles can slide over other particles with less resistance while particles with rougher surfaces resist sliding more strongly, leading to a greater granular shear strength. The range of potential inter-particle friction coefficients that gave correct retained volumes was moderate

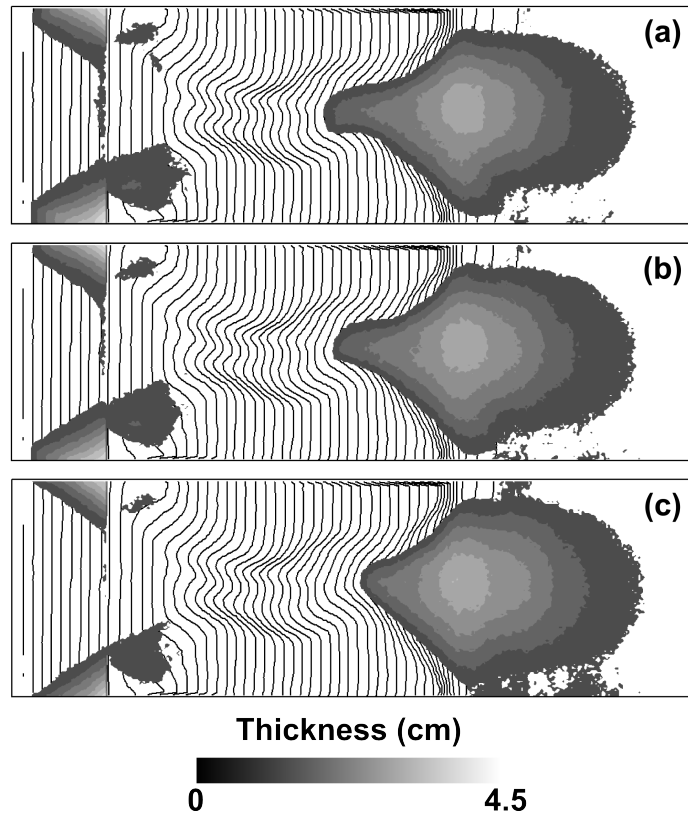


FIGURE A.8: Final avalanche deposit thickness for DEM simulations with mildly angular particles for (a) elongated, (b) intermediate, and (c) low aspect ratios.

in size (varying from 0.45 to 0.65).

Figure A.10 shows the thickness of the final avalanche deposit for different inter-particle friction coefficients for mildly angular, elongated particles (cases 10, 11 and 12 from Table A.1). The leading edge of the avalanche (distal margin) moves progressively higher up the flume as friction increases. For the friction coefficient of 0.45, there are two separate deposits of sand with one around the reservoir and the main deposit near the base of the flume. However for friction coefficients of 0.50 and 0.55 (Figs. A.10b and A.10c), the deposit remains as a single contiguous body spread along much of the whole length of the flume. The width of the distal edge of the deposit is also consequently narrower. The upper parts of the deposit lie in two branches reflecting the two main flow channels in the topography. For the highest friction coefficient case (Fig. A.10c) a large amount of material is retained in the reservoir, leading to a much thinner avalanche deposit.

Figure A.11 shows the X_{com} for all simulation cases. The overall trend, evident in all cases, is that X_{com} (run-out) decreases with increasing friction, however the degree of sensitivity to friction is dependent on the particle shape. Particles with the lowest angularity (solid line) travel the furthest down the flume, followed by the mildly angular (dashed line) particles with the highly angular particles (dotted) travelling the shortest distance. The difference in X_{com} is much smaller between the mildly and highly angular particles than between the rounded and mildly angular particles. The sensitivity of X_{com} to friction is dependent on the aspect

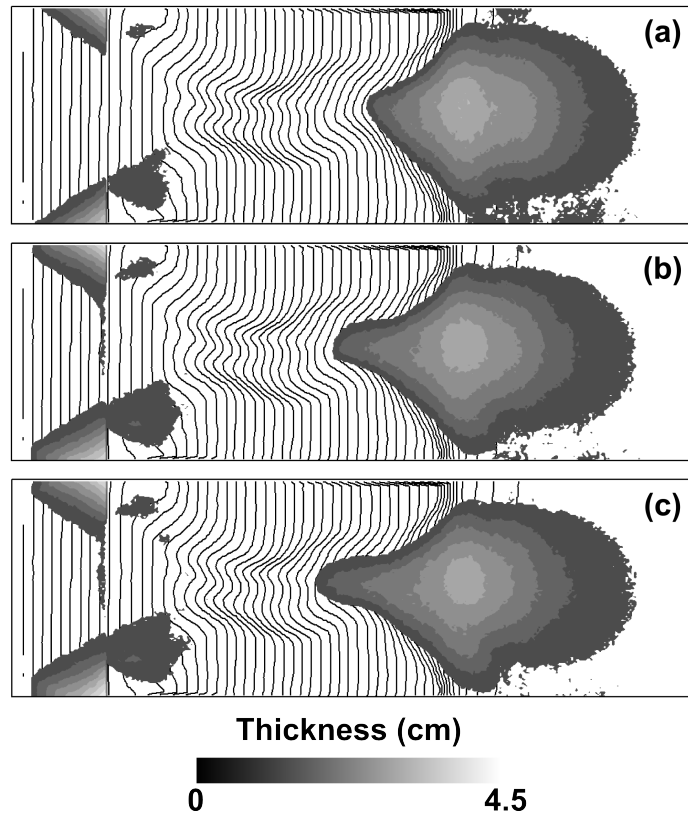


FIGURE A.9: Final avalanche deposit thickness for DEM simulations with an intermediate aspect ratio range for: (a) rounded, (b) mildly angular, and (c) highly angular particles.

ratio. The change in X_{com} with friction is less than 10% at low aspect ratios, but increases to 28% and 42% for the intermediate and elongated particles respectively. At lower aspect ratios, the effect of friction is relatively minor which results in less energy dissipation and further run-out distances, however friction has a larger effect on the energy dissipation for higher aspect ratio particles, resulting in reduced run-out distances.

The angularity of the particles also affects the sensitivity to friction changes by a reasonable degree, but to a lesser amount than was found for aspect ratio. This demonstrates that the particle shape causes the effects of friction to vary. This type of behaviour has also been observed by Mead et al. (2012) in a DEM investigation of particle properties on the angles of repose and failure.

A.7 Conclusions

The granular avalanche experiments of Iverson et al. (2004) were re-analysed and the results of a single avalanche experiment were compared to DEM predictions of the avalanche. Uncertainties in reported material properties were identified, and their importance to flow prediction highlights the need for experimental sensitivity studies and detailed measurements of experimental inputs for DEM studies. Re-analysis of the experimental depth measurements from Iverson et al. (2004) highlighted moderate compressibility in the avalanche as it travelled

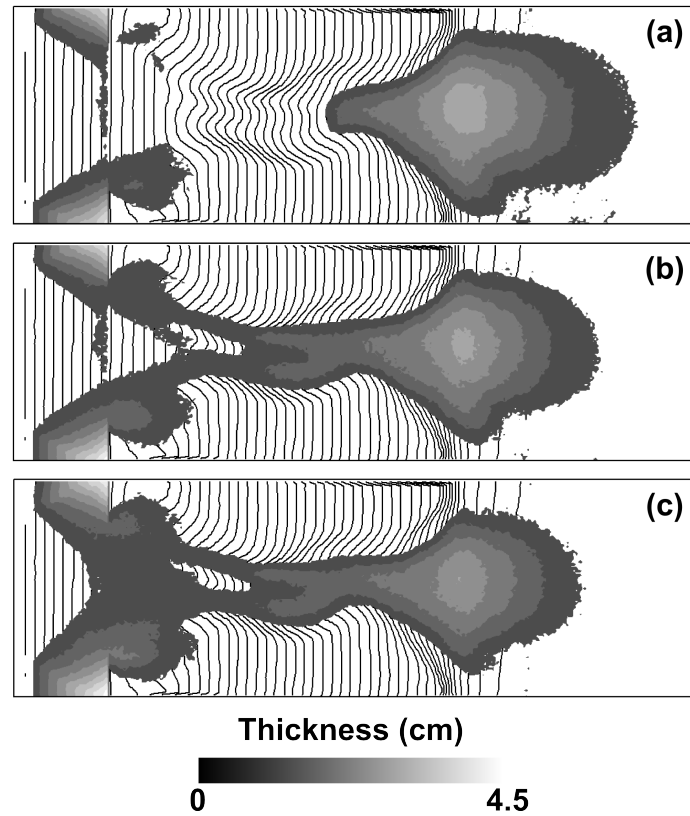


FIGURE A.10: Final avalanche deposit thickness for DEM simulations for elongated, mildly angular particles with friction coefficients of: (a) 0.45, (b) 0.50, and (c) 0.55.

down the flume. The bulk density of sand in these experiments was found to have increased by more than 6% during the avalanches. It is also possible that the bulk density of the material varied spatially (along the flume) in addition to the temporal variation identified. This compressibility has implications for methods that assume granular avalanches travel as incompressible masses. The DEM approach presented in this paper does not suffer from the limiting assumption of incompressibility. The dilation, compression and saltation of the granular material is handled naturally in DEM as the motion of individual particles (which collectively determine the bulk density) is predicted. The key limitations of the method for avalanche modelling, particularly at full scale, are the computationally intensive nature of the method and the challenges in measurement of material properties.

Results of the DEM retained volume simulations from Mead and Cleary (2011) provided a small envelope of realistic material properties that were investigated further by comparing the behaviour of the avalanche along the entire flume. The sensitivity of the avalanche to three sets of particle angularity (2.5-4.0, 2.5-6.0 and 3.0-6.0), aspect ratio (low, intermediate and elongated) and friction (0.45, 0.50 and 0.55) were investigated through a fully factorial design. Several of the DEM avalanche simulations produced results that were very similar to the experiment. DEM simulations of case 19, which contained particles with a low aspect ratio, moderate angularity of 2.5 – 6.0 and a friction coefficient of 0.45 produced results that were very close to the experiment. Additional measurements of the experimental material

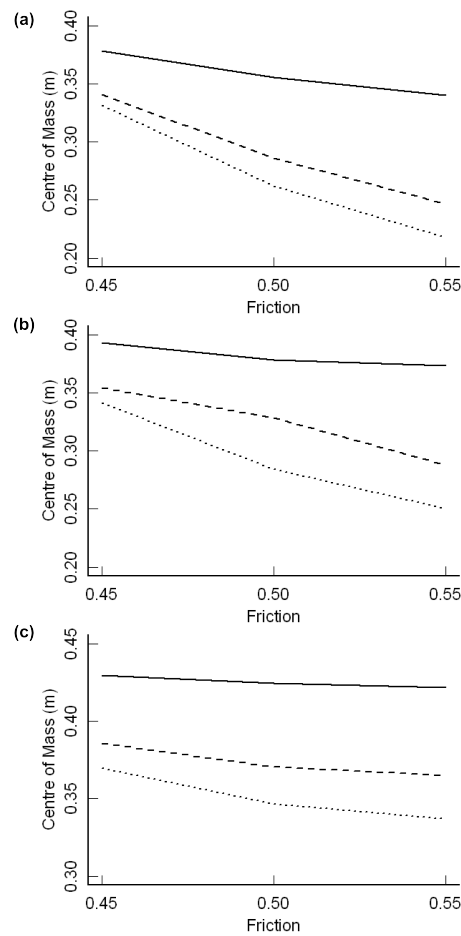


FIGURE A.11: Centre of mass of DEM particles in the down slope direction for friction coefficients between 0.45 and 0.55, for (a) elongated, (b) intermediate and (c) low aspect ratios at rounded (solid line), mildly angular (dashed line) and highly angular (dotted line) angularities.

suggested that cases 19 to 21 had the most similar particle shape properties to the experimental samples, providing confidence in the estimation of DEM particle shape.

The transient and static avalanche features of the simulated and experimental avalanche were found to be qualitatively very similar throughout the avalanche, with only minor observable differences that can be attributed to errors in the digitisation of the topography or a small difference in material properties. Outlines of the experimental isopach data, experimental photographs and DEM simulation at six times during the avalanche were compared. A substantial fraction of the key features were matched closely for all three outlines, indicating that DEM is capable of predicting complex avalanche behaviour such as separation and convergence when particle shape is included in the model. In particular the thin granular streams which formed in the latter part of the experiment were in close agreement. These features are generally difficult to capture in numerical models. The most notable difference between experiment and simulation was for the final deposit, which was located slightly further down the flume in the best DEM prediction. This is attributed to having slightly

different material properties (of either friction or shape) between the experiment and simulation. Other small magnitude errors were observed in the DEM predictions, these are also attributed to differences in material properties and flume configuration between experiment and simulation.

The DEM predictions were found to be sensitive to both the particle shape (aspect ratios and angularity) and friction values. The shape and location of the avalanche deposit was moderately sensitive to the particle shape. Rounded particles, caused by decreasing angularities or aspect ratios, have a lower resistance to shear as opposed to elongated and high angularity particle shapes. The lower shear resistance decreases the energy dissipation within the avalanche, leading to greater run-out distances and lateral spread. The avalanche was sensitive to the DEM contact friction coefficients. A higher contact friction increases the shear strength of the bulk material, leading to deposits sitting further up the flume and having less lateral spread. A key observation of the sensitivity to friction was that it is highly dependent on the particle shape, particularly aspect ratio. At low aspect ratios, the friction coefficient only affected the avalanche centre of mass by 10%, however this increased to 42% for elongated particles. This leads to the conclusion that not only does particle shape have an important effect on avalanche dynamics in its own right, but it also moderates the effects of other material properties (such as friction). This again highlights the importance of correct particle shape determination and representation.

A.8 Acknowledgements

Experimental data used in this paper are available from the auxiliary material of Iverson et al. (2004), accessed at <ftp://agu.org/jf/2003JF000084/>. The authors would like to thank Richard Iverson and Matt Logan for making samples of the experimental material available to us and Clement Leroy for identifying this validation case study and creating the initial geometry used in the DEM simulations.

B Supplementary images for Chapter 6

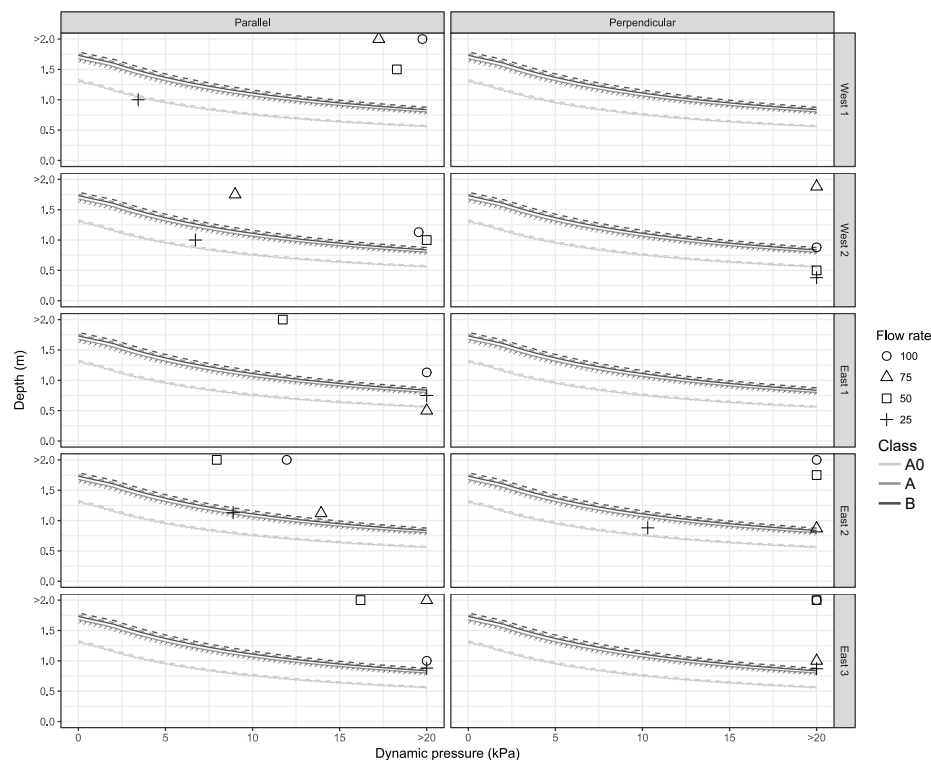


FIGURE B.1: Critical depth-pressure curves for building classes A0, A and B with brick widths of 0.25 m subjected to Newtonian flow. Peak normal pressures and corresponding depths applied to each city block are plotted as points for each flow rate.

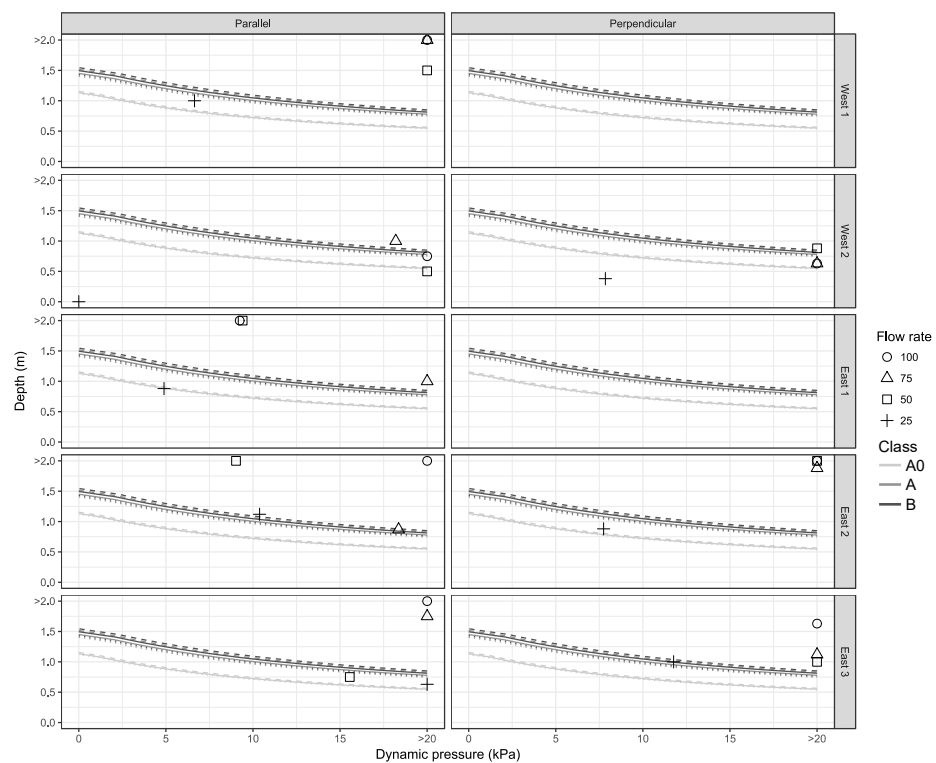


FIGURE B.2: Critical depth-pressure curves for building classes A0, A and B with brick widths of 0.25 m subjected to a hyper-concentrated flow. Peak normal pressures and corresponding depths applied to each city block are plotted as points for each flow rate.

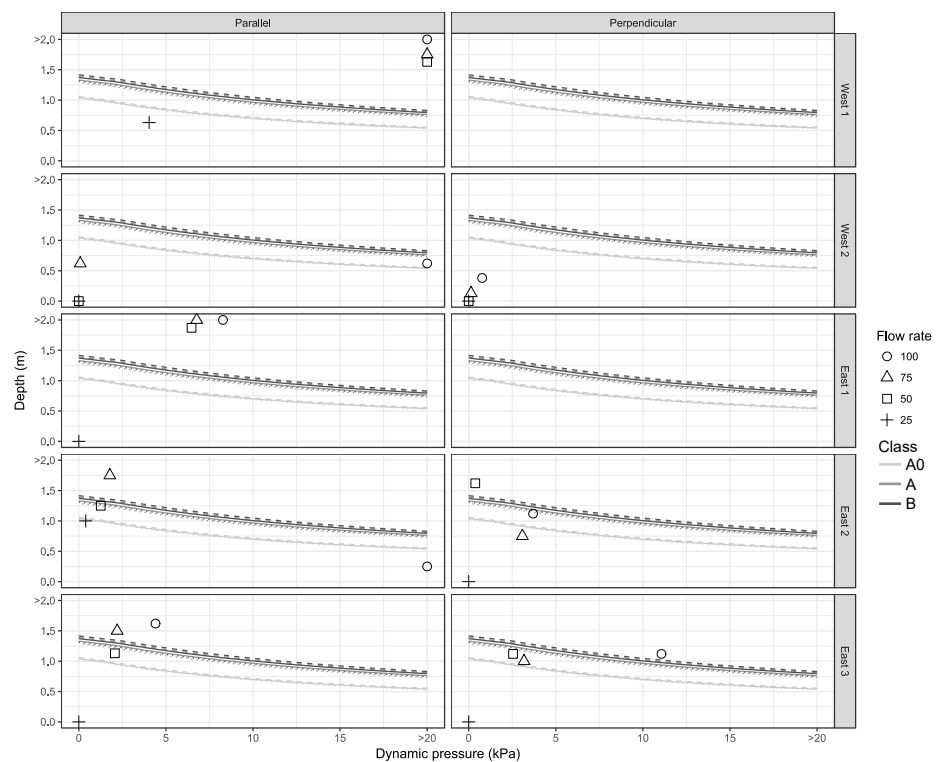


FIGURE B.3: Critical depth-pressure curves for building classes A0, A and B with brick widths of 0.25 m subjected to a debris flow. Peak normal pressures and corresponding depths applied to each city block are plotted as points for each flow rate.